Advanced techniques for the study of membrane proteins in complex and native lipid environments.

By

James Matthew Hutchison

Dissertation

Submitted to the Faculty of the

Graduate School of Vanderbilt University

in partial fulfillment of the requirements

for the degree of

DOCTOR OF PHILOSOPHY

in

Chemical and Physical Biology

September 30, 2021

Nashville, Tennessee

Approved:

Hassane S. Mchaourab, Ph.D.

Lauren Buchanan, Ph.D.

Walter Chazin, Ph.D.

Jens Meiler, Ph.D.

ACKNOWLEDGEMENTS

I would like to take some time to thank my many scientific mentors over the years. I will always be appreciative of my undergraduate advisor, Dr. Jason DeRouchey, who gave me a research position and opened my eyes to the frustration and joy of working in research. My post-baccalaureate advisor, Dr. Don Rau at NICHD, devoted himself to the pursuit of science and mentoring. Don was a scientist in the purest sense, and I will never forget his kindness and our lengthy discussions about classical science-fiction over chocolate. Finally, I would like to thank my PhD advisor Chuck Sanders for his mentorship and patience over the past six years. Chuck has always been supportive and allowed me to develop independence and confidence in my research. I have had the pleasure of working with a wide array of brilliant and passionate collaborators over the years and I would not be here without their help. I of course would also like to acknowledge my funding from training grants NIH T32 CA00958229 and by F31 AG061984 and the lab RF1 AG056147.

I personally want to thank my partner in crime, Olivia, for putting up with the late nights in lab and always being by my side. My parents and friends have always supported me and offered a reprieve from the day-to-day grind. I also want to thank the denizens of Mega-lab and their helpful insights and amusing banter. I will miss seeing everyone at holiday parties, seminars, and cookouts, ... but the longing signifies that Vanderbilt was a great scientific home.

TABLE OF CONTENTS

LIST OF FIGURES

I. Introduction

Statement of Purpose

The biophysical and biochemical study of membrane proteins (MP) is uniquely challenged by the lipid bilayer environment in which MPs reside. While fantastic methods have been developed over the years, there is still a dearth of techniques to study MPs in their complex *in vivo* lipid environments. Study of MPs in their native lipid environment is critical because the lipid environment is known to influence the structure, function, and processing of MPs. The purpose of this dissertation is to characterize and implement novel biochemical and biophysical tools for the study of MPs in biomedically important or native lipid environments; a short review relevant to the methods developed below will be covered in **Chapter 1**. **Chapter 2** serves as a steppingstone and will characterize a previously understudied non-ionic detergent, n-Dodecyl-β-D-Melibioside (DDMB), and its application ins MP studies.

The role of phase-phase separation in biology has recently become a critical focus of biochemistry and biophysics. Lipids are known to undergo lipid-lipid phase separation and the biological poster child for this, the raft hypothesis, is continually refined in the biological context. This thesis describes the first isotropic particle, e.g. detergent micelles, that are capable of dissolving significant amounts of sphingomyelin and cholesterol, key components of the aforementioned lipid-raft hypothesis. The resulting new sphingomyelin and cholesterol rich bicelles (SCOR Bicelle) enable detailed studies of the impact of lipid composition on MP structure and function. In **Chapter 3**, we explore the morphological characterization of SCOR bicelles and the impact of a SCOR environment on the amyloid beta (Aβ) precursor protein, C99. SCOR bicelles are an exciting step towards recreating a lipid raft environment but lack the chemical complexity and heterogeneity of the native bilayer.

It is critical to remember that living systems represent entropy machines which constantly use energy to maintain bilayer lipid leaflet asymmetry and change lipid bilayer composition in response to stimuli. Therefore, it is important to develop new methods in which MP structure and function can be studied while embracing the full complexity of the lipid environment in living systems. Single pass transmembrane proteins (SPTPs) generally have the largest ratio of bilayer-exposed surface area per transmembrane segment (TM), and I posit that this ratio makes them uniquely susceptible to changes in bilayer composition. (Granted, this dissertation does not directly assess this hypothesis in living cells and only establishes methods for future studies on this topic.) I here describe two novel methods for delivering recombinant SPTPs to mammalian cells. **Chapter 4** explores how amphipathic polymers can deliver the severe acute respiratory syndrome 2 virus (SARS-CoV-2) envelope protein (S2-E) to the mammalian cell plasma membrane (PM) and follow its subsequent retrograde trafficking to the perinuclear space. The other delivery method leverages the ability of SPTPs to oligomerize and form unique particles that are water soluble without the need of membrane mimetics. The biophysical characterization of these detergent free particles and their uptake by mammalian cells are explored in **Chapter 5**. **Chapter 6** describes results in which we tested for binding between C99 and another key Alzheimer's disease (AD) protein, tau. Overarching conclusions and future directions for this thesis work are covered in the final **Chapter 7**.

1.1 The vast complexity of the lipid bilayer.

In order to appreciate the importance of current scientific pursuits, it is immensely helpful to have historical perspective on the hypothesis at hand. Tchaikovsky's *Swan Lake* premiered the same year (1877) that Wilhelm Pfeffer posited that a then-unseen plasma membrane (PM) acted as a cellular barrier to water and certain solutes (1). A pioneering work in 1959 by Robertson used electron microscopy to visualize this hypothesized barrier and showed that the PM has a single lipid bilayer with electron dense proteins on each side of the bilayer (2). The Nicolson "fluid mosaic model" was published in 1972 and underpins our modern understanding of how proteins, lipids, and carbohydrates all fit into the overall structure of the PM lipid bilayer (3). The fluid mosaic model highlights how amphipathic and MPs interact with and can span the "sea" of the lipid bilayer. The 1970s also contained some of the first studies on lipid bilayer asymmetry and lipid phase heterogeneity (4,5). These historical works set the foundation for modern studies of MPs in the complicated environment of mammalian lipid bilayers.

There are three main classes of lipids in eukaryotic cells: glycerophospholipids, sphingolipids, and sterols (6). However, these three classes belie the true chemical complexity found in the lipid bilayer (7). Lipidomics recently identified over 8000 lipid species in human platelets (8), highlighting the vast variety of lipids found *in vivo*. The lipid bilayer complexity is further complicated when one considers that organelles have varied lipid compositions (9,10) and different tissues have specific lipodomes (11). Certain lipid species, such as phosphatidylinositol phosphates, have defined functions and can act as a ligand for proteins (12-14) while most non-annular or "bulk" lipids do not have a known purpose and their wider roles within the bilayer are even more obscured. Determining the impact (or lack thereof) of changes in "bulk" lipid on MP structure and function (15) is challenged by a dearth of methods when trying to study complex lipid phenomena such as leaflet asymmetry (16) and lipid-lipid separation (17). The methods presented in **Chapter 4 and 5** aim to expand our ability to study MPs in the context of in an *in vivo* lipid environment while enabling application of chemical biological approaches originally developed for *in vitro* studies.

1.2 Lipid heterogeneity and rafts

Lipid-lipid spatial heterogeneity has been observed in complex lipid environments of organelles (18), bacteria (19), and in simple ternary lipid artificial bilayers (20,21). Lipids can form several different phases depending on properties such as temperature, hydration, headgroups, and hydrocarbon chain lengths (22). There are two lipid phase transitions pertinent to this dissertation, the gel (S_o) to liquid disordered (L_d) transition and liquid ordered (L_o) to liquid disordered (L_d) transition. Lipids in the S_o phase are dominated by Van der Waals (VDW) forces and therefor have tight lateral packing, limited translational diffusion, and fully extended fatty acid chains (23). L_d phase lipids do not possess ordered acyl chains or lipid packing (22) and allow for rapid lateral diffusion (24). The S_o to L_d transition temperature (T_m) increases as a function of chain length since more energy is required to overcome the increased VDW forces (25). Likewise, the kinks found in unsaturated fatty acids disrupt packing and lower this T_m (26). The L_o phase is unique and can form when high concentrations of sterols are present in the lipid bilayer (21). As shown in **Figure 1.1,** the L_o phase can be thought of as having properties that are intermediate between the S_o and L_d phases since it exhibits increased lipid order due to packing of hydrocarbon tails against the rigid sterol structure while also allowing some lateral diffusion of lipids (27,28).

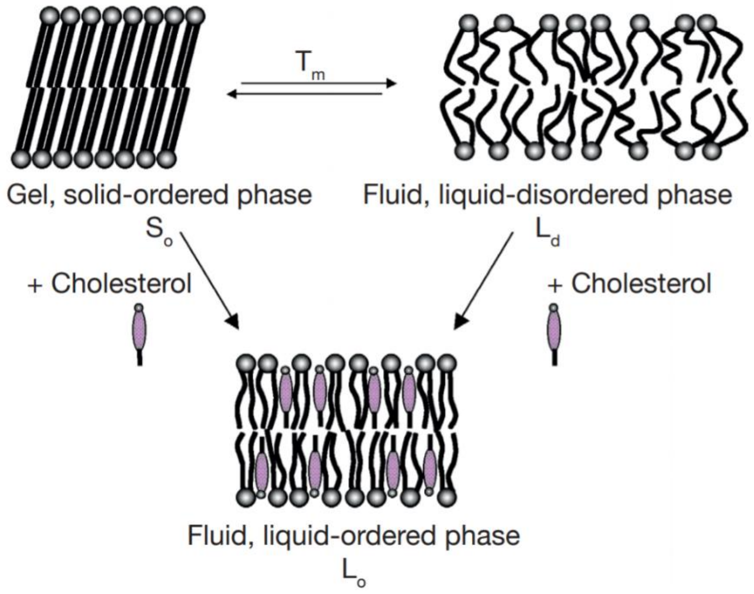

Figure 1.1. The liquid ordered phase has properties that are intermediate between gel and disordered phases. *Addition of cholesterol to either the gel or disordered phase can result in the liquid ordered phase. Figure adapted under CC BY 4.0 from Marc Eeman & Magali Deleu, «From biological membranes to biomimetic model membranes», BASE [En ligne], numéro 4, Volume 14 (2010), 719-736 URL : https://popups.uliege.be/1780-4507/index.php?id=6568.*

Sphingolipids and sterols are often discussed in the same breath when referring to a specific L_o phase known as a lipid raft (29-31). Cholesterol and sphingomyelin have been shown to form an energetically favorable complex that is stabilized by the higher T_m of sphingolipids and by a hydrogen bond between the cholesterol hydroxyl headgroup and sphingomyelin amide-linked acyl chain (32,33). This distinctive sphingomyelin and cholesterol affinity likely drives clustering of these two lipids *in vivo.* Lipid rafts have an increased bilayer thickness due to sterol-induced straightening of the lipid chains(28,34). L_o and L_d can coexist on a Gibbs phase diagram (21) and form spatially separated domains where the domain sizes and lifetimes are dependent on composition and temperature (27,35,36). Simple artificial membrane studies in Giant Unilamellar Vesicles (GUVs) set the foundation for lipid-lipid separation *in vivo (30)* where, remarkably, the lipid and protein components of mammalian cell membranes can also form coexisting L_o and L_d phases. (It is astounding that despite of the vast chemical complexity of plasma membranes, their bilayers occupy only a small number of definable phases.) In order to directly visualize the phase separation, the mammalian lipids must be removed from the live cells through a membrane-oxidizing blebbing process to form Giant Plasma Membrane Vesicles (GPMVs) (37,38).

Before GPMVs, lipid raft-like domains known as detergent resistant membranes (DRMs) were isolated from cells via lysis with non-ionic detergents under cold temperatures (39). DRMs and GMPVs have both shown that MPs have an affinity for the L_o or L_d phases (17,40). I often find myself agreeing with the Leventhal lab notion of MP phase preference: the L_o phase excludes many MPs, but is permissive of certain MPs. However, it does not actively enrich L_o preferring proteins (41). The L_o phase preference of proteins along with their slower diffusion (42) within the L_o phase had led to the idea that rafts function as a spatially sequestered signaling and processing platform (30,43,44). The PM has the highest concentration of cholesterol and sphingomyelin (6) and yet obvious L_o and L_d phases are not observed in living mammalian cells. This failure of the PM to phase separate into long-lived and microscopically visible phases is likely intentional since long lived L_o and L_d lipid phases would possibly limit signaling flexibility and lead to undesirably large and sustained signaling domains. Moreover, clearly separated L_o and L_d phases have a sharp line tension boundary that contrasts the gradients often observed in living systems (45). The PM likely exists near the critical point of the L_o and L_d phases such that both phases are small and short lived. This idea is supported by studies that show GPMVs need to be cooled below the growing temperatures of their source cell lines in order to stably phase separate, presumably because PMs tune their lipid compositions to be near the critical miscibility temperature (27,36,46). It is important to reiterate that there is a substantial body of evidence that lipid-lipid heterogeneity and changes in lipid order do occur in living cells. However, it is not yet obvious how lipid rafts or the L_o phase manifest in living cells and the extent to which they control cellular processes. Regardless of how important lipid rafts end of being in biomedical research, the case can be made that mammalian MP structure and function should be studied in membranes that contain all three classes of lipids found in cells: glycerophospholipids, sphingolipids, and sterols.

2.1 How do we study membrane proteins?

Ideally all investigations on MP structure would be done or validated *in vivo*, but this is not possible for most modern structural methods. Most biophysical and structural methods were originally developed for soluble proteins and then adapted for MPs. Adapting MPs to these methods often involves replacing the native lipid bilayer with a simpler alterative, referred to as a “membrane mimic” or “model membrane”, (47-49) and dividing up the MP into soluble and membrane-bound fragments, colloquially referred to as divide and conquer. It should be noted that removing a MP from the native lipid environment represents another split in the divide and conquer approach. Structural biologists are aware of the importance of the native bilayer and there is a strong drive to study MPs in their native membrane environment as highlighted in an extensive collaboration on *in vitro* full-length EGFR in mammalian cell derived vesicles (50).

The lipids surrounding a MP were historically thought of as a solvent without much attention being placed on the ability of bulk lipids to impact protein structure and function (12-14). (Hence the fluid in the fluid mosaic model) The easiest way to study the impact of lipids on MPs would be to use bilayered vesicles. However, due to their large size, vesicles tend to settle in solution or complicate many spectroscopic structural and biophysical methods that are reliant on optically clear solutions (51). This desire for transparent solutions biases MP studies towards stabilizing the hydrophobic domains of MPs with smaller membrane-mimetic particles. There are additional technical advantages of using small particles such as tumbling rate and orientation bias. As shown in **Figure 1.2**, some examples of small membrane mimics commonly used today are detergents (47), bicelles (47,52,53), nanodiscs (48,54,55), and amphipols (56,57).

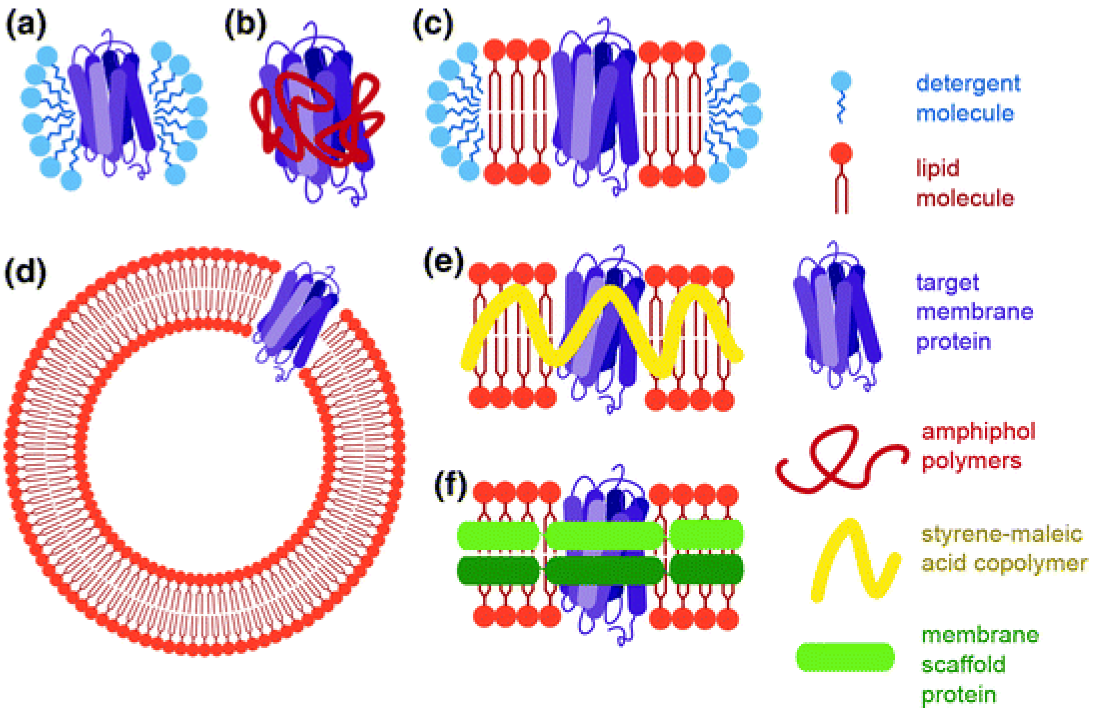

Figure 1.2. Common membrane mimics for in vitro membrane protein work. *Cartoon rendition of an integral membrane protein in* ***A)*** *detergent micelle,* ***B)*** *amphipol polymer,* ***C)*** *bicelle,* ***D)*** *vesicle,* ***E)*** *SMALP, and* ***F)*** *nanodisc. Figure adapted with permissions from Yeh V. (2019) Introduction. In: Study of Bacteriorhodopsin in a Controlled Lipid Environment. Springer Theses (Recognizing Outstanding Ph.D. Research). Springer, Singapore. https://doi.org/10.1007/978-981-13-1238-0_1*

2.2 Detergents

Detergents are routinely used as a membrane mimic due to their ease of use and comparatively low cost. Lipids and detergents are both amphiphiles and therefore contain a hydrophilic head group and a hydrophobic chain (58). Glycerophospholipids generally have two hydrocarbon chains while detergents usually only have a single hydrophobic chain. This results in lipids having an overall cylinder structure opposed to the cone structure associated to detergents (59). This conical shape causes detergents to form a hydrophobic-core spheroid, referred to a micelle, when trying to balance their hydrophobic and hydrophilic needs. The formation of these micelles requires the detergent to be at a a concentration above the critical micelle concentration (CMC)(60). The CMC varies based on detergent properties such as headgroup and hydrocarbon chain length. Another important factor in micelle size and shape is the number of detergent molecules in each individual micelle, this is referred to as the aggregation number (61,62). The CMC and aggregation number can be used to estimate the molar concentration of micelle in any given solution. It is imperative to consider the protein to micelle ratio when doing MP studies because it is deceptively easy to artificially crowd MPs together with a small number of micelles.

There are many factors one must consider when choosing a detergent for MP studies. Detergents broadly have three types of head groups and their general denaturing tendency from highest to lowest are: ionic, zwitterionic, and non-ionic (47). There is rarely an obvious choice of detergent for any given MP and so a significant amount of effort should be devoted to finding the right surfactant. This task appears daunting but structural biology sub-communities often gravitate towards a short list of detergents that are well suited for their technique or protein. For example: cryo-electron microscopy (Cryo-EM) MP structures are often solved in non-ionic detergents (63) whereas solution NMR studies are biased toward use of anionic and zwitterionic detergents (64). Interestingly, some groups have used detergents and organic solvents to carry out protein studies in reverse micelles where the hydrophobic tails are facing the solvent and hydrophilic headgroups line the interior (65,66). **Chapter 2** will go into further detail about a non-ionic detergent, DDMB, that was found to be suitable for NMR and has several physical characteristics that improve on the commonly used n-Dodecyl-B-D-maltoside (DDM).

A great advantage of detergents is their ability to easily dissolve small amount of most lipids (59). Lipid and detergent mixtures are referred to as mixed micelles and lack spatial separation between the lipid and detergent phases (67). As highlighted with bacterial diacylglycerol kinase (DAGK), DAGK in detergent alone is not active, whereas solubilization in lipid (cardiolipin) and detergent mixed micelles supports DAGK enzymatic activity (68). Incorporating higher ratios of lipid to detergent or complex lipid compositions sometimes result in lipid precipitation or odd phase behavior where spheroid particles are no longer present (69). On the other and certain combinations of detergent and lipid do not generate mixed micelles and instead form unique particles with a defined lipid bilayer and detergent annulus; these particles are known as bicelles.

2.3 Bicelles: A versatile membrane mimic.

In work starting during his postdoctoral studies in the James Prestegard lab at Yale, bicelles were characterized and pioneered by my advisor Charles Sanders (70-72). Ideal bicelles are comprised of a detergent and lipid mixture with a lipid bilayer core surrounded by a rim of detergent. The main determinant for bicelle size and morphology is the lipid to detergent molar ratio, referred to as the q ratio (52). High q bicelles, q of 2.5 or more, are large and display complex phase behavior such as elongated (ribbon-like) or perforated bilayers (69). These high q ratio bicelles are used in NMR with soluble proteins due to their ability to align with the of magnetic field (73,74) and have also found use in MP x-ray crystallography (75). Bicelles with a q ratio between 0.25 and 1.0 are isotropic in nature and commonly used in the study of MPs by NMR and optical spectroscopy due to their small size and optically clear solutions (76). There is a long-running debate on whether these low q bicelles possess a true lipid bilayer core with a detergent rim or are a mixed micelle (67,77).

Bicelles have traditionally used the short chain lipid 1,2-dihexanoyl-sn-glycero-3-phosphocholine (DHPC) or detergent 3-([3-cholamidopropyl]dimethylammonio)-2-hydroxy-1-propanesulfonate (CHAPSO) as the detergent/rim component and a wide array of glycerophospholipids have been used to make bicelles, with the most popular being 1,2-dimyristoyl-sn-glycero-3-phosphocholine (DMPC). Bicelles have successfully incorporated glycerophospholipids with *either* sphingolipids or sterols (78-81), but it was not previously possible for isotropic particles to co-dissolve mixtures with appreciable amounts of *all three* classes of lipid (82). (The difficulty is likely due to the special complex that is known to form between cholesterol and sphingomyelin (32,33)) **Chapter 3** describes the first-in-class creation of sphingomyelin and cholesterol rich (SCOR) bicelles that exhibit the ideal bicelle morphology and are suitable for a wide range of common structural biology techniques. Detergents will always be an integral component of bicelles and this has driven others to develop detergent-free ways to stabilize MPs with lipids, as we describe below.

2.4 Nanodiscs and SMALPs

Nanodiscs (54,83) and styrene-maleic acid lipid particles (SMALPs) (84,85) represent two popular alternatives to bicelles, which replace the detergent rim of bicelles with either a protein or polymer respectively. Nanodiscs use a membrane scaffold protein that mimics the high-density lipoprotein apolipoprotein A1 to encircle a lipid bilayer in a belt-like fashion (54,86,87). For nanodisc assembly, MPs must first be removed from their natural bilayer and put in detergent/lipid mixed micelle. Detergent is then removed from the system to force the lipids, apolipoprotein scaffold, and membrane protein of interest to form nanodiscs. The assembly and detergent removal process usually requires significant optimization. The Sanders lab had previously attempted to make SCOR nanodiscs but the resulting particles were unstable and resulted in lipid vesiculation. SMALPs offer a distinct advantage for those looking to study MPs in their native membrane environment. The SMALP polymer acts like a strong detergent and can be used to lyse cells and remove MPs along with their surrounding lipids (88-90). As with detergent resistant membranes, SMALPs were recently shown to solubilize cellular membranes and density gradient ultracentrifugation was used to isolate large >250 nm raft-like and small <20 nm non-raft lipid environments from T cells (91)

2.5 Amphipols

Amphipols are another class of polymer commonly used in the study of MPs. Amphipols act like a weak detergent and can solubilize MPs in the absence or presence of lipids, but amphipols are not capable of dissolving membranes (56,57,92). These weak detergent properties allow amphipols to be well tolerated by animals and have been used in antibody development (93,94). The ability to solubilize MPs but not dissolve membranes makes amphipols an ideal method to deliver MPs to preformed artificial lipid bilayers (95). In **Chapter 4**, we show that this MP delivery idea can be extended to live mammalian cells. We show that S2-E can be delivered directly to the PM of mammalian cells and the delivered S2-E is trafficked back to disease relevant organelles.

2.6 Purification of membrane proteins without membrane mimics.

It is assumed that an integral MP requires a lipid bilayer, organic solvent, or one of many membrane alternatives discussed above to remain soluble in aqueous environments. However, a small set of studies has aimed to buck this trend and developed methods to study MPs lacking conventional membrane mimics in aqueous environments. The properties that make the apolipoprotein A1 protein useful for nanodiscs also allows for solubilizing integral MPs when fused to the MP (96). Other groups have asked the question: Can we make a MP soluble if we replace the lipid-facing residues with hydrophilic ones? Remarkably yes. Computational guided mutagenesis has led to water soluble versions of the KcsA potassium channel (97,98) and DsbB (99) that was able to catalyze disulfide bonds *in vivo*.

Interestingly, not all MPs need to undergo significant mutation or fusion to become water soluble. Magnetotactic bacteria are able to synthesize magnetic nanoparticles out of iron oxide within a unique vesicle/organelle known as a magnetosome (100). Several magnetosome proteins, such as Mms6, are known to reside within the organelle lipid bilayer but appear to be amphiphiles when recombinantly expressed in other bacteria (101). Recombinant magnetosome MP Mms6 forms protein micelles with the C-terminus exposed to water and N-terminus buried like a micelle hydrophobic core (101). (Although it should be noted that the term micelle may be misappropriated here since it us unknown if a CMC of proteins exists as monomers in solution outside the particles). These odd protein-only micelles bind iron and are likely important to magnetosome formation since addition of iron ions changes the shape of aqueous Mms6 particles (102). Several other magnetosome MPs (103,104) have been found to form water soluble micelles but this phenomenon is not known to occur in proteins of higher order organisms.

Integral MPs in higher order organisms could conceivably form protein micelles, but this is overlooked since all integral MPs are presumed *a priori* to be insoluble in the absence of a membrane mimic. Mms6 is an integral MP and proteins with a simpler membrane topology should also be able to form protein "micelles" as well. Single pass proteins would be an ideal candidate given their resemblance to a double-headed detergent or bolaamphiphile (105). **Chapter 5** will characterize and discuss how human single pass proteins can form protein micelles or membrane mimic free protein particles (MeMFs).

3.1 Proteins

The main focus of this dissertations is the development of methods that allow MPs to be studied in challenging lipid environments and *in vivo*. However, it is desirable to use relevant and biomedically important proteins when developing these novel methods. Use of disease relevant MPs can forcefully demonstrates the true usefulness of novel methods for using in solving modern biomedical problems. The following section provides a brief introduction to the main proteins used in this dissertation and their associated human diseases.

3.2 The Severe acute respiratory syndrome coronavirus two (SARS-CoV-2)

Much of my last year at Vanderbilt was dominated both scientifically and personally by the coronavirus SARS-CoV-2 pandemic. This pandemic has shown how powerful science can be when many diverse groups of scientists focus on one disease. Powerful vaccines to combat the current pandemic were rapidly developed (106,107) but it will take years to manufacture and provide to the worldwide population. Coronaviruses are positive-sense single stranded RNA viruses (108) present in a wide range of species including avians, humans, and their companion animals (109). Given the previous prevalence of coronavirus zoonotic events (110,111), it is critical to develop other therapies that can be generally applied to coronavirus infections during future novel coronavirus infections. Due to safety, there are several avian and mouse model viral systems used for the study of coronavirus, but it is not clear to what degree conclusions in these model systems can be extrapolated to human β coronavirus (112). This is one of the main reasons why it is important to develop methods which can allow experimental study of human pathogen proteins while limiting risk from infectious diseases.

The spike (S), membrane (M), nucleocapsid (N), and envelope (E) proteins are the structural proteins that form the mature viral particle. SARS infection in humans begins with the binding of the S protein to the host angiotensin converting enzyme 2 (ACE2) (113) and the bulk of early structural biology work was focused on this interaction (114,115). Impressively, electron microscopy was recently able to combine low resolution S protein structures in intact virions with *in vitro* high-resolution structures (116). The main function of the N protein is to form a compact complex with viral genomic RNA and be loaded into in mature viral particles (117). The M protein is the main structural protein that is responsible for viral assembly and shape (118). E proteins are also important for viral assembly since both M and E are needed to form particles that resembles a virus without genetic material known as virus-like particles (VLPs) (119-121). Both the M and E proteins are highly expressed during infection but only a small fraction of the E protein is incorporated into the mature viral particles (122). The limited incorporation of E into the mature viral particles implies that E carries out important functions aside from physical-viral assembly.

For coronavirus assembly, the aforementioned structural proteins are translocated into the endoplasmic reticulum (ER) and nascent viral particle assembly occurs in the ER to Golgi intermediate compartment (ERGIC) (123). Assembled progeny virus move through the Golgi stacks and accumulate in the *trans*-Golgi network (TGN) where they undergo post translational modifications such as glycosylation (124). Traditionally, mature coronavirus particles were thought to egress via a traditional biosynthetic pathway (125), but recent work has highlighted the possibility that egress occurs via deacidified lysosomes (126); it is of course possible and likely that both pathways are used. Recent non-peer reviewed EM work has shown viral particles present in both pathways during SAR-CoV-2 infection (127).

3.3 Coronavirus envelope protein

The function of E outside of viral assembly is poorly understood due to a lack of enzymatic activity and multiple oligomeric states (128). E is important for viral fitness and deletion of E results lowers viral titers by two orders of magnitude (129-131). E proteins are between 75-109 amino acids long and there is significant sequence variability between coronaviruses (132) however, despite this sequence variance, coronavirus E isoforms are thought to have the same general functions (128). E populates both low order and higher order oligomeric state during infection, presumed to be monomers and homopentamers respectively (133). The homopentameric form of E is a cation selective ion channel referred to as a viroporin (134-136) and may represent a druggable target, analogous to the influenza M2 protein and FDA approved amantadine (137,138). Viroporin formation is often associated with changes in pH and it is documented that E is able to increase the pH of the Golgi and TGN (139,140). The E viroporin can also transport calcium and this calcium transport is linked to inflammation and the related acute respiratory distress syndrome (ARDS), a major cause of COVID-19 fatalities (141,142). Given its potential as a drug target and functional readout, most studies have focused on the homopentameric E with few studies looking at the function of monomer.

SARS-CoV-1 and SARS-CoV-2 E share over 95 % sequence similarity and so structural results for S1-E can likely be extrapolated to S2-E (134,135). It was originally unknown if E was a single pass or hairpin-like double pass MP in the thinner membranes of the ER and Golgi, but NMR structures found both oligomeric states of E to be a single pass protein, as determined in both detergents and in ERGIC-mimicking lipid bilayers (134-136,143-145). In agreement with these structures, glycosylation studies found E to be a single pass protein with the carboxyl terminus facing the cytosol and the amino terminus facing the organelle lumen (146). S2-E contains three cysteine residues in the juxta membrane region that do not form disulfide bonds *in vivo* (147) and are not required for homopentamer formation (135,143). In model systems, mutation of two or three but not one cysteine to alanine resulted in reduced VLP formation and reduced viral yield (147). The cysteines of E can be palmitoylated but the function of palmitoylation is unknown (147,148). It is important to note that palmitoylation does not appear to impact the strict E localization to the ERGIC/Golgi/TGN (148). E is strongly retained at sites of assembly and budding by the ER retention sequence DLLV (149). Exporting E from the perinuclear space to the plasma membrane requires deletion of DLLV and a Golgi export signal (140). The DLLV sequence in E is also proposed to increase virulence by disrupting the tight junction via binding and relocating multiple tight junction proteins including the PALS1 protein (150,151).

It is convenient to think that viroporin channel formation is the main non-structural role of the envelope protein. However, we observe in **Chapter 4** that E viroporins have a low open state probability and a recent publication found that the E-associated organelle pH increase is correlated with the *monomeric* E concentration (139). Regardless of oligomeric state, it is documented that the E is able to increase the pH of the Golgi and TGN(139,140). The increase in pH is thought to prevent overprocessing of the spike protein during viral maturation (139). The E protein is also able to slow down secretory pathways in the host cell but it is unclear if this is due to E-based pH changes or interaction with host proteins (152). Given the complexity in oligomeric state and function of E, we wanted to develop a novel method where S2-E could be studied *in vivo*. In **Chapter 4** describes the purification and delivery of recombinant S2-E to mammalian cells with amphipols.

3.4 Alzheimer's Disease.

AD was first described in 1901 by Alois Alzheimer when observing short term memory loss in Auguste Deter. Upon the death of Auguste, Alois identified the neurological amyloid plaques and neurofibril tangles that we still associate with the AD (153). Auguste was only 55 when she died, and she likely suffered from the familial early onset version of AD (FAD). FAD is often diagnosed before 65 and is associated with mutations in gamma secretase (GS) subunits presenilin 1 (PSEN1), presenilin 2 (PSEN 2), or amyloid precursor protein (APP) (154). Modern medicine has extended life expectancy which also highlights the far more common late-onset sporadic version of AD (LOAD) (155). AD represents the largest cause of dementia and will become a far more acute public health problem as life expectancy continues to increase. Despite concerted efforts, there is still a dearth of therapy options for AD, as most current treatments are palliative in nature (156). 2021 saw the approval of a contentious monoclonal antibody curative therapy (aducanumab) that aims to rid the brain of amyloid plaques (157). Creating therapies for AD has been difficult because the exact etiology of AD is not specifically known, but a dominant hypothesis in the field, referred to as the amyloid cascade hypothesis (158-161), focuses on the production of the Aβ peptides which ultimately forms the plaques for associated with the disease.

The amyloid hypothesis states that the accumulation of Aβ peptide oligomers and resultant plaques are the primary cause of Alzheimer's disease. APP can be processed in several ways (162) but as shown in **Figure 1.3**, there are two major pathways (163): the majority of APP is processed in the non-amyloidogenic pathway via initial cleavage by alpha secretase to produce the C83 fragment and a minority of APP is subject to amyloidogenic processing via beta secretase to produce the C99 fragment. Both the C83 and C99 TM fragments are then cleaved in the membrane by GS to yield either the non-toxic p3 or plaque forming Aβ respectively. It should be highlighted that that the initial alpha or beta secretase cleavage is often described as deterministic, however, alpha secretase can also cleave the C99 to generate C83 (164).

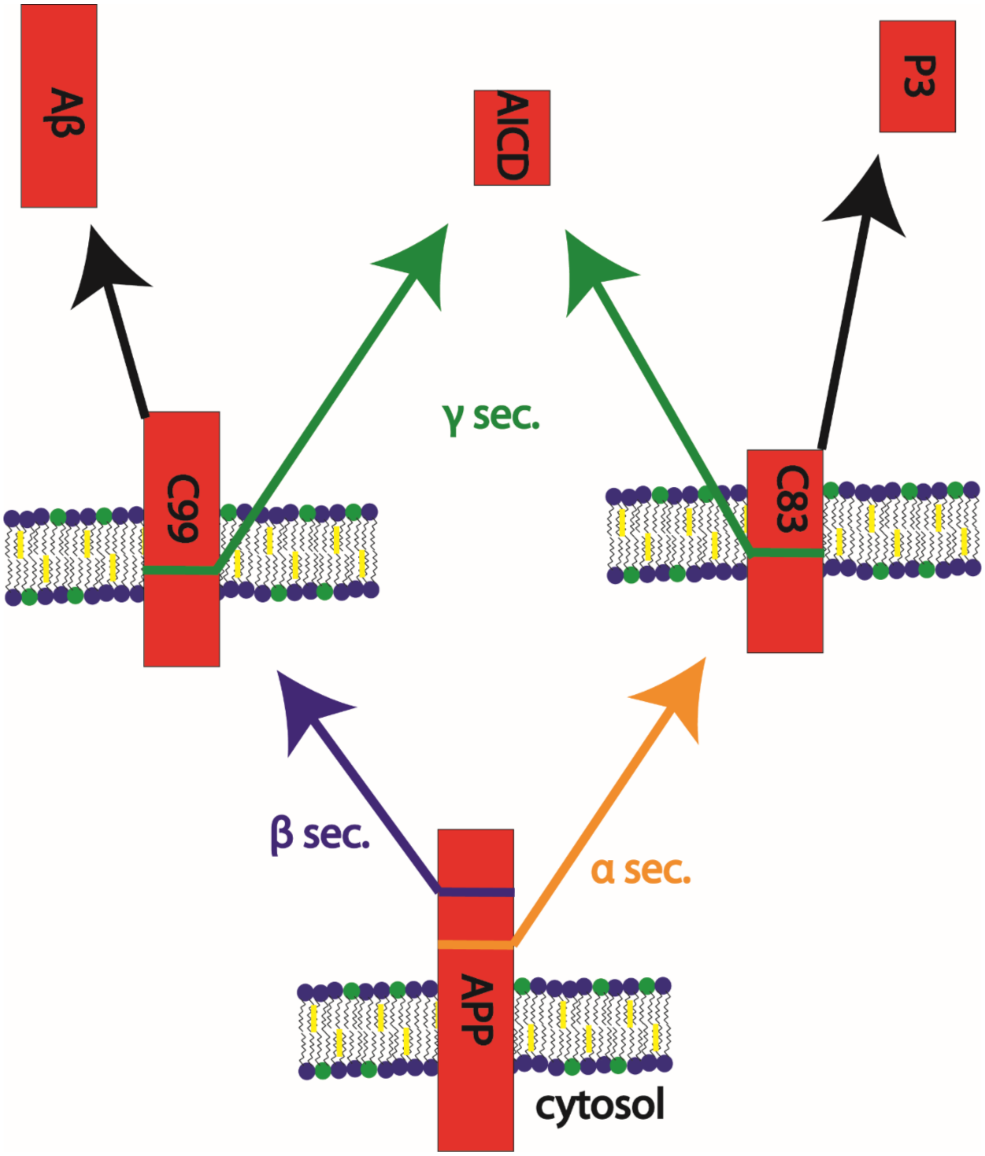

Figure 1.3. Processing of APP. *APP amyloidogenic is represented by the left pathway as APP is initially cleaved by beta and then gamma secretase. The non-amyloidogenic pathway is shown on the right with cleavage by alpha secretase before gamma secretase. Both pathways create the amyloid intracellular signaling domain (AICD) after cleavage by gamma secretase.*

FAD associated germline mutations are found within three critical proteins involved in APP processing that ultimately result in altered Aβ production and plaque formation (154,165). FAD mutations associated with APP are found within the C99 fragment and cluster at the GS cleavage sites and in the Aβ peptide (https://www.alzforum.org/mutations/app). The other two sets of FAD mutations are within subunits PSEN1 and PSEN2 of the multi-subunit GS (154). Generally, mutations in the Aβ sequence result in either increased Aβ production or increased Aβ plaque forming potential. Mutations near the GS cut site result in increased production of Aβ42 over Aβ40 (166,167). Aβ42 is the main species of Aβ found in amyloid plaques (168-170) and it contains additional hydrophobic residues isoleucine and alanine on the C-terminus which increases the aggregation rate and toxicity of Aβ42 over Aβ40 (171). Although Aβ

40/42 are the most commonly discussed, longer variants of Aβ are generated by GS due to variability in the initial cut site and subsequent processivity (172). There is a known protective “Icelandic” Aβ mutation (173) that protects against AD associated cognitive decline, further solidifying the genetic link between Aβ and AD etiology.

The tau hypothesis is an alternative prominent hypothesis for AD etiology (174,175). While Aβ plaques are found in the extracellular space, abnormal tau structures are often found within neurons in AD brains (176). Tau is normally a microtubule binding protein that, upon hyperphosphorylation, forms large aggregates referred to as a neurofibrillary tangles or paired helical filaments in tauopathies (177). Since both Aβ and tau induce aberrant aggregates, it is tempting to try and link the two pathologies and studies have shown that the presence of increased Aβ results in aberrant tau aggregation (178-180). It is unclear if the impact of Aβ on tau is due to a direct binding and several studies have looked for a physical interaction between tau and peptide fragments of Aβ, C99, and APP (181-185). Residues 713-724 of C99 were previously found to bind tau(183-185), but are always found within or against the lipid bilayer during structural studies(186-188). Recent studies had failed to affirm the C99-tau interaction (182) and in **Chapter 6**, we confirmed the lack of a C99-tau interaction by conducting solution NMR titrations with detergent solubilized C99 and soluble tau.

The genetic link between APP processing and Aβ in FAD is undeniable, but it is not clear if Aβ is the causal agent in LOAD. The exact function of APP is in healthy humans is not well understood due to ubiquitous expression in human tissues and the presence of three main isoforms. The isoform associated with AD is APP695 (189,190). Further complicating understanding, deletion of APP in mice results in only a mild phenotype due to the presence of APP like proteins 1 and 2 which can partially compensate for the loss of APP (191). In addition to Aβ production, GS cleavage always releases the APP intracellular domain (AICD) which is believed to act as an important signaling domain (192). AICD is rapidly degraded once produced (193) and the short half-life of AICD increases the difficulty in understanding APP function in healthy patients.

3.5 The C99 protein fragment and AD.

Aducanumab is a highly controversial AD therapy (157) that will require additional clinical trials, post FDA authorization, to fully assess its efficacy. All other therapies targeting Aβ and GS are currently in clinical trials or failed in the clinic due to intolerable side effects and failure to prevent worsening cognition (156). Some of these failed therapies, and aducanumab, succeed in removing Aβ form the brain and cerebral spinal fluid. The ability to remove Aβ from the brain but not prevent cognitive decline has led some to question the amyloid hypothesis and there is now a shift in funding towards other etiological possibilities (194). There also is growing interest in the idea that the direct precursor to Aβ, C99 is a significant contributor to AD outcomes (195).

The APP gene is located on chromosome 21 and trisomy 21, also known as Down syndrome (DS), is associated with early onset Alzheimer’s disease and Aβ plaques (196,197). Fibroblasts from both DS patients and mouse model systems have shown C99 to cause impaired endosomal trafficking and endosomal swelling (198). C99 accumulation in endosomes ultimately results in failure of lysosomal and autophagic functions (199,200) and rescue experiments using beta secretase deletions and inhibitors show that these endosomal and lysosomal perturbations were not caused by Aβ accumulation (198-200). The poisoning of lysozymes is especially problematic for neurons which cannot divide in order to remove insoluble aggregates. In line with this idea, C99 and not Aβ plaques have recently been shown to accumulate and correlate with neuronal vulnerability (201). Moreover, the ability of neurons to degrade misfolded protein aggregates deteriorates with time, making C99-induced issues with catabolism become more apparent with age (202,203).

An important causal link between C99 and AD relevant to this dissertation is elevated cholesterol (186,204,205). Hypercholesterolemia has been proposed as a risk factor for AD(206,207), although this has been challenged (208). C99 has been shown to bind cholesterol *in vitro (186),* regulate cholesterol trafficking (209), and cholesterol is known to compete with C99 homodimerization (204). The impact of cholesterol on C99 dimerization is likely important because C99 oligomeric state has been reported to impact Aβ production (210-217). Small amounts of cholesterol in addition to cholesterol and sphingomyelin rich environments have both been shown to increase the production of Aβ (218). (Although it should be noted that the impact of cholesterol on Aβ production can be biphasic and do not lend itself to simple descriptions.) The literature has posited that the amyloidogenic processing pathway for APP dominantly occurs in raft like environments (219,220) since alpha secretase is excluded from the raft-like environment (221) and it was hypothesized that the C99-cholesterol complex would allow for C99 localization within liquid rafts. In opposition to this idea, studies of C99 phase preference have shown that in both synthetic GUVs (222) and neuron-derived GPMVs (223) that C99 localizes in the bulk lipid disordered phase and is strongly excluded from the liquid ordered or raft phase. It is possible that protein-protein interactions not found in GPMVs are required to drive C99 into raft-like environments *in vivo.*

Mitochondrial dysfunction and associated increases in reactive oxygen species have long been associated with AD (224,225). C99 expressing mice can be found to have mitochondrial defects that are made worse with gamma secretase inhibitors (226). Recent work found C99 to be a regulator of cholesterol synthesis and trafficking in the ER mitochondrial associated membrane (MAM) (209). They propose that the failure to cleave C99 in the MAM results in dysregulated cholesterol trafficking and synthesis. This study is particularly exciting since it bridges the ideas of C99-cholesterol interactions and mitochondrial dysfunction. Regardless of the exact relationship between AD and C99, there is growing link between the two and this has led to many structural studies on C99 *in vitro* in a variety of membrane mimics.

3.6 C99 structural studies

There is heightened interest in understanding the impact of cholesterol and sphingomyelin on C99 structure due to the known impact of a SCOR environment on Aβ production (218). Since C99 is a small single pass fragment of APP, it is too small for cryo-EM and too flexible for X-ray crystallography (227). Solution NMR is ideal for small proteins and the main experimental technique used to study small integral MPs (228). There are several solution NMR C99 or C99 fragment structures published (204,229,230) and the first full length C99 structure was determined in 2012 by the Sanders lab (186). LMPG, an anionic detergent, was used as the membrane mimetic and as shown in **Figure 1.4,** C99 was found to possess a random coil N-terminus followed by a short amphipathic helix and TM. After the TM, a long intracellular random coil C-loop is capped by an amphipathic helix at the C-terminus. A detergent-hybrid of cholesterol known as chobimalt (231) was used to show that C99 may bind cholesterol(232). The cholesterol C99 interaction was later validated in the more bilayer-like DMPC/DHPC bicelle using true cholesterol. The cholesterol-laden bicelles were not stable over a long period of time and prevented structural studies beyond demonstrating cholesterol binding.

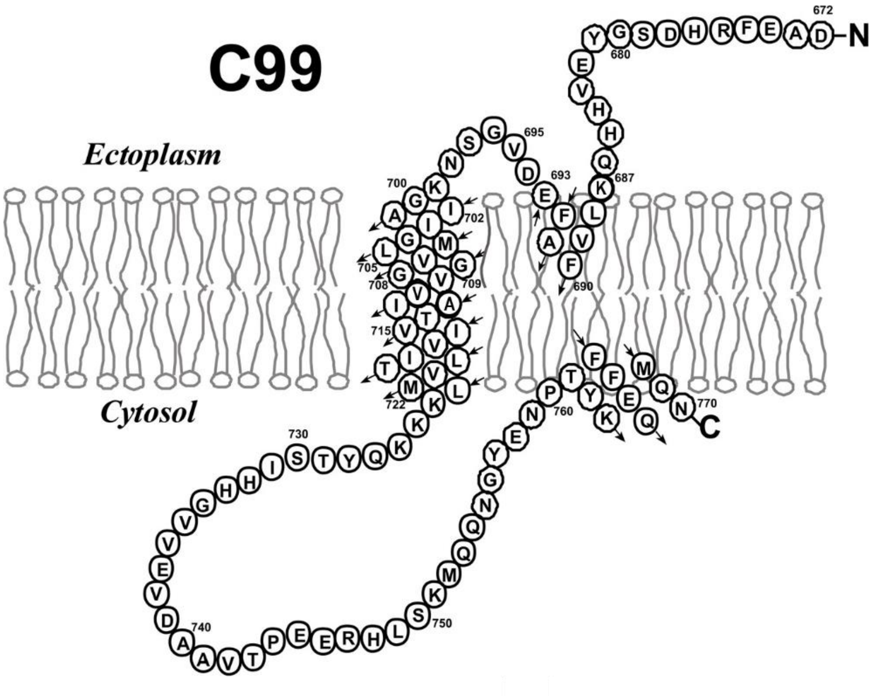

Figure 1.4: C99 sequence and topology. *C99 sequence and topology determined in LMPG, DHPC/DMPC bicelles, and SCOR bicelles. Adapted with permission from Song, Y., Hustedt, E. J., Brandon, S., and Sanders, C. R. (2013) Competition Between Homodimerization and Cholesterol Binding to the C99 Domain of the Amyloid Precursor Protein. Biochemistry* ***52****, 5051-5064.*

It is important to note that there were no structures of C99 in a SCOR environment due to the absence of a suitable membrane mimic (82). SCOR lipid compositions are traditionally restricted to vesicles which are not suitable for solution NMR due to their large size/correlation times. Computational studies on C99 in a SCOR environment have been published in the last few years and are based on experimental structures determined in the absence of sphingomyelin and cholesterol (205,233-235). In **Chapter 3**, we explore the impact of a SCOR environment on C99 structure using SCOR bicelles. A wealth of structural information on C99 in membrane mimetics bereft of cholesterol and sphingomyelin allows for a thorough comparison against C99 in a SCOR environment.

There is much interest in understanding the structure of the C99 oligomeric state due to the potential impact on Aβ production. Dimerization of the full-length APP can be induced by heparin and mediated by the extracellular ectodomains (236,237), but it is not clear what residues comprise the interface for TM dimerization (212,215,238,239). All previous solution NMR structural studies of C99 dimerization relied on the use of C99 fragments with only the TM or C55 fragment which lacks the C-loop and C-terminal amphipathic helix (229,230). Some studies found that TM dimerization is mediated through GXXXG motifs located on the N-terminal side of the TM (210,214,240-242) while others found dimerization to be mediated by a GXXXA near the middle of the TM (230,243). The membrane mimic used likely dictates the interface of dimerization (234) and this idea agrees with computational studies that highlight all plausible C99 dimerization methods (244). The Xu lab determined *in vivo* that that the TVIV motif in the C-terminal side of the C99 TM mediates dimerization (238); this is also where GS can make the initial cleavage of C99. We show in **Chapter 3** that C99 readily forms oligomers in a SCOR environment, and the oligomers are mediated by both previously known and unknown C99 interfaces.

4. Summary

The following chapters in this dissertation focus on novel methods to study recombinant MPs in unique detergents and native/complex lipid environments. These new methods were demonstrated with disease relevant proteins in order to demonstrate the methods suitability in addressing important biomedical questions. **Chapter 2** examines the use of an underutilized non-ionic detergent, DDMB, for solution NMR and membrane protein studies. **Chapter 3** characterizes the morphology and stability of DDMB-based SCOR bicelles and uses a wide variety of techniques to study the structure of C99 in a SCOR environment. Delivery of SARS-Cov-2 E to live mammalian cells via amphipol and subsequent E retrograde trafficking is described in **Chapter 4**. **Chapter 5** highlights how single pass MPs can be purified without any membrane mimic and their subsequent characterization. **Chapter 6** does not utilize any novel methods but uses solution NMR to see if soluble tau and C99 form a complex. The final Chapter will provide a brief summary of this dissertation and future directions for others wanting to implement or develop these methods and studies further.

II. Dodecyl-β-Melibioside Detergent Micelles as a Medium for Membrane Proteins

This chapter is adapted from ***Dodecyl-β-Melibioside Detergent Micelles as a Medium for Membrane Proteins*** *published in Biochemistry and has been reproduced with the permission of the publisher. Hutchison JM, Lu Z, Li GC, Travis B, Mittal R, Deatherage CL, Sanders CR. Dodecyl-β-melibioside Detergent Micelles as a Medium for Membrane Proteins. Biochemistry. 2017 Oct 17;56(41):5481-5484. doi: 10.1021/acs.biochem.7b00810. Epub 2017 Oct 9. PMID: 28980804; PMCID: PMC5685800.*

Introduction

Spectacular advances in membrane protein structural biology over the past 20 years have been enabled, in part, by the development of new and improved model membranes for solubilizing and stabilizing these difficult-to-study biomolecules. (47,53,58,64,245-249) Such media include nanodiscs, bicelles, new classes of detergents, and lipidic cubic phases. Despite these advances, there remains room for innovation. For example, there are few examples of successful use of non-ionic detergents in NMR studies of membrane proteins. Given the widespread use of uncharged detergents such as n-dodecyl-β-maltoside (β-DDM) in crystallization/diffraction studies of many different membrane proteins, the fact that β-DDM, lauryl maltose neopentyl glycol (MNG), and other uncharged detergents have thus far been of limited use for NMR has been vexing. This paper was originally motivated by the desire to find an uncharged detergent that can be used to solubilize membrane proteins for NMR studies. This led one of the authors of this work to recall an alkyl glycoside first synthesized and subjected to preliminary characterization many years ago, n-dodecyl-β-melibioside (β-DDMB, **Figure S2.1**). (250) The disaccharide melibiose is distinct from maltose and most other disaccharide in that its galactose and glucose units are connected by an α(1➔6) glycosidic linkage, conferring a much higher conformation freedom between the two sugar groups than is possible for non-1➔6 glycosides. We hypothesized that this enhanced conformational flexibility might attune its micelle properties and interactions with membrane proteins in a way that would promote its utility in both biochemical and biophysical studies, including solution NMR spectroscopy. Preliminary testing of this hypothesis is presented herein.

Results and Discussion

DDMB was synthesized and purified as described in the **Appendix 1** and **Figure S2.2**. Using an ANS dye-based fluorescence method (251) the critical micelle concentration of β-DDMB at 25 °C was determined to be 0.3 mM. This is higher than for β-DDM (0.2 mM (252)) and matches the value previously determined for an unresolved mixture of α and β mixtures of DDMB. (253) Dynamic light scattering (DLS) was employed to assess the size and aggregation number of β-DDMB micelles based on the assumption that they are spherical. Our DLS measurements for micelles of pure β-DDMB at 25°C and at concentrations <100 mM (**Figure 2.1**) indicate that the radius of hydration (Rh) for β-DDMB micelles is 2.9 nm and the aggregation number is roughly 84, corresponding to an aggregate molecular weight of 42 kDa. These results are similar to those previously reported for an α + β anomeric mixture of DDMB in the 20–40 mM concentration range. (253) Multi-angle light scattering (MALS) was used to confirm the DLS result. MALS determines the molecular weight of particles without needing a shape factor or modeling. The MALS result of 46 kDa for the β-DDMB micelle (**Table S2.1**) was in good agreement with the value determined by DLS.

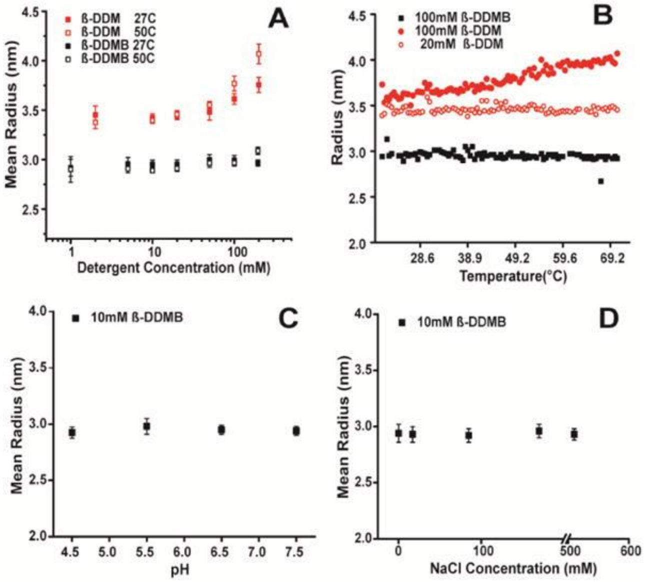

Figure 2.1. Use of DLS to characterize the mean radius of hydration (Rh) of β-DDMB and β-DDM micelles. *A) 10mM DDMB (black) or 10mM DDM (red) detergent was dissolved in water and subjected to a 1°C/min temperature ramp. B) Example of a temperature ramp used in panel A. C) β-DDMB micelle size as a function of pH. The buffer was either 25mM imidazole buffered at either pH 7.5 or 6.5, or 25mM sodium acetate at pH 5.5 or 4.5. D) β-DDMB micelles as a function of salt concentration.*

β-DDM(254) has previously been shown to form micelles in the range of 69–76 kDa, (255) significantly larger than the ca. 42 kDa micelles formed by β-DDMB (see also the Rh comparisons in **Figure 2.1A–B**). β-DDM micelles also exhibited a linear temperature-dependent increase in size at higher concentrations (i.e. 100mM) not seen for β-DDMB micelles at 100 mM (**Figure 2.1B**). The Rh of β-DDMB micelles was also independent of both pH and ionic strength (**Figure 2.1C and 2.1D**). The constancy of the properties of β-DDMB micelles across a wide range of relevant pH, temperatures, concentrations, and ionic strengths is useful because β-DDMB micelles can be employed in a wide range of conditions without concern about major changes in micellar properties.

To test whether β-DDMB micelles are smaller than those of β-DDM in the presence of a membrane protein we used SEC-MALS to examine the sizes of micelles containing *E. coli* diacylglycerol kinase (DAGK), a 42 kDa homotrimeric mostly-helical protein with three transmembrane segments per subunit. The β-DDMB/DAGK complex is roughly 30kD smaller than the βDDM/DAGK complex (**Table S2.2**), indicating that the smaller micelle size of β-DDMB extends to its complex with DAGK.

We next tested the ability of β-DDMB to maintain the stability of a membrane protein. DAGK was purified into β-DDMB and into each of four commonly used detergents (n-dodecylphosphocholine: DPC, n-decyl-β-maltoside: β-DM, MNG, and β-DDM) and incubated at 70°C. Aliquots were removed as a function of time and subjected to the standard DAGK activity assay (in DM/cardiolipin mixed micelles) to determine $t_{1/2}$ values for irreversible inactivation of the enzyme—a measure of thermostability.(256) As shown in **Figure 2.2**, DAGK is much more stable in β-DDM and β-DDMB ($T_{1/2}$ of 8.5±0.5 h and 9.9±1.7 h respectively) than in DPC or β-DM, where $T_{1/2}$ in both cases was < 4 hours. In the case of MNG there seem to be two populations of DAGK-MNG mixed micelles: a ca. 40% population in which DAGK is sensitive to thermal degradation ($T_{1/2}$ of 5.6 hours), while the other 60% population appears to be resistant to thermal degradation over a period of many hours. This heterogeneity may reflect the fact that the properties of MNG are close to the borderline between being detergent-like and being lipid-like, such that MNG may be able to form more than one type of kinetically stable complexes with some membrane proteins. In any case, these results indicate that β-DDMB is similar to β-DDM in terms of its ability to suppress irreversible thermal inactivation of DAGK and much better than DPC or β-DM.(256)

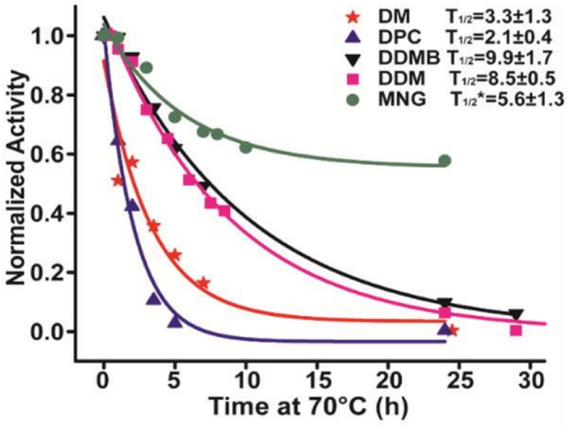

Figure 2.2. Thermal stability of DAGK in β-DDMB and other detergents. *DAGK samples (0.2 mg/ml) were incubated at 70°C, with aliquots being removed at time points and assayed in the standard β-DM/cardiolipin mixed miceller DAGK activity assay.* (257) T1/2* of MNG represents the DAGK population that sensitive to thermal inactivation in MNG/DAGK mixed micelles.

We next tested the degree to which β-DDMB can serve as a medium that supports the native functionality of a membrane protein. We again employed DAGK, which was purified into lipid-free β-DDMB, MNG, β-DDM, and β-DM. Aliquots from these stock solutions were then transferred into DAGK assay mixtures prepared using several different types of micelles or detergent-cardiolipin mixed micelles, including β-DM/cardiolipin mixed micelles (the traditional standard assay condition). As can be seen in **Figure 2.3**, DAGK has only low activity (ca. 1 unit/mg) when assays are carried out in lipid-free β-DDMB micelles, as is also the case for lipid-free β-DM, MNG, and β-DDM. However, the presence of cardiolipin (CL) in the assay mixtures as a lipid activator dramatically enhances DAGK activity in β-DDM, MNG, and β-DDMB. The activities observed in β-DDMB/CL and β-DDM/CL are not as high as for the corresponding reactions carried out in β-DM/CL or MNG/CL, suggesting subtle differences in DAGK structure and/or dynamics that result in sub-optimal catalytic properties in β-DDMB/CL and β-DDM/CL mixed micelles relative to β-DM/CL and MNG/CL conditions. When the same DAGK stock is used MNG with cardiolipin gives a higher activity compared to DM with cardiolipin. A surprising observation is that DAGK prepared in β-DDMB and then aliquoted (≥250-fold diluted) into either β-DM/CL, β-DDM/CL, or β-DDMB/CL mixed micelle assay mixtures yielded higher activities than the corresponding assays initiated using small aliquots of DAGK prepared in β-DM, β-DDM, or MNG micelles and then transferred to these same detergent/CL mixtures. Indeed, the observed specific activity of 166±15 U/mg for DAGK purified into β-DDMB and the aliquoted into β-DM/CL mixed micelles is much higher than the highest previously reported 30°C mixed micellar specific activity for DAGK, which is 120 U/mg. (258,259) This suggests that DAGK prepared in β-DM (and, most likely, many other detergent types) micelles is susceptible to irreversible misfolding, a problem that is avoided when the enzyme is prepared in β-DDMB. Indeed, DAGK has long been known to be prone to misfold in detergent micelles. (258,260) These results show that not only does β-DDMB provide a medium that supports the thermal stability of DAGK, but it also seems to enhance its efficiency of folding during and following purification (see **Appendix 1**). On the other hand, β-DDMB is typical of most detergents (261,262) in that it cannot itself satisfy the requirement of DAGK requirement for the presence of a lipid cofactor for maximal catalytic activity. (263,264)

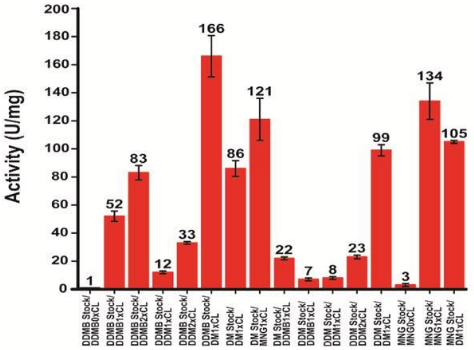

Figure 2.3. DAGK activity assays started with detergent aliquots of DAGK diluted various micelle and mixed micelle assay mixtures. *DAGK was purified into β-DDMB, β-DM, β-DDM, or MNG micelles (stock) and then assayed using reaction mixtures at 30°C. The "standard" assay condition is labeled DM1×CL. "1×CL" refers to the fact that the mole fraction of CL in the mixture is the same (1×) as in the standard assay procedure. (257)*

We next examined β-DDMB micelles as a medium for NMR studies of membrane proteins. TROSY-HSQC were collected for three different membrane proteins: (i) the human Notch1 transmembrane domain (Notch-TMD) residues 1721–1771 (a single span protein), (ii) the 99-residue C99 domain of the human amyloid precursor protein, the immediate precursor of the amyloid-β polypeptide (also with single transmembrane segment), and (iii) the 160 residue human peripheral myelin protein 22 (a mostly helical protein with 4 transmembrane segments). Each of these proteins was purified into β-DDMB micelles, into β-DDM micelles, and into the micelle type previously observed to yield the most favorable NMR spectra for each protein following extensive screening. (232,265,266) A TROSY-HSQC spectrum was collected for each sample. **Figure 2.4** shows that β-DDMB yields spectra for C99 and the Notch-TMD that are comparable in quality with the detergents previously shown to yield the best spectra for these proteins (lyso-myristoylphosphatidylglycerol, LMPG, for C99 and lyso-myristoylphosphatidylcholine, LMPC, for the Notch-TMD). **Figure 2.4** also shows that β-DDMB also yields better spectra for C99 and the Notch-TMD than β-DDM. In both cases certain peaks observed when the proteins are in β-DDMB are too broad to detect in β-DDM. For example, there are a pair of black peaks near 111 PPM in the ^{15}N dimension for the Notch-TMD in β-DDMB for which there are no corresponding red peaks from β-DDM.

The average ^{15}N linewidths for Notch in the β-DDM micelle are ~32% larger than the linewidths for Notch in β-DDMB, most likely reflecting the significantly larger size of β-DDM micelles compared to β-DDMB micelles (see **Table S2.2**). The ^{15}N linewidths of C99 in a β-DDM micelle were ~12% larger than the linewidths in the β-DDMB micelle.

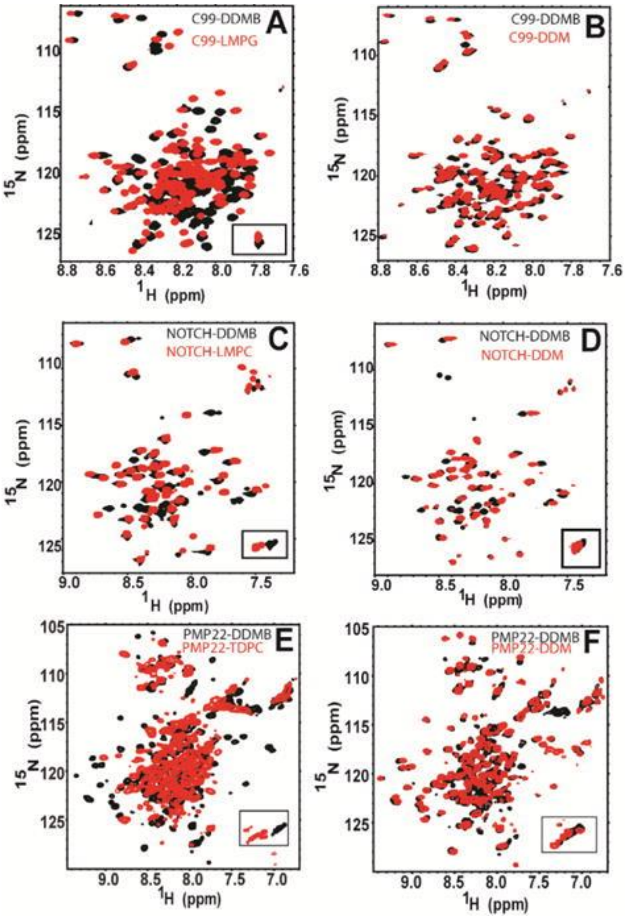

Figure 2.4. NMR spectra of single span membrane proteins in β-DDMB and in other detergents. *A) 400μM C99 in 9% β-DDMB (black) and 400μM C99 in 9% LMPG (red). B) 400μM C99 in 9% β-DDMB (black) and 300 μM C99 in 9% β-DDM (red). C) 230μM Notch-TMD in 5% β-DDMB (black) and 300μM Notch-TMD in 1% LMPC (red). D) 230μM Notch-TMD in 5% β-DDMB (black) and 300μM Notch-TMD in 4.5% β-DDM (red). E) 350μM PMP-22 in 20% β-DDMB (black) and 700μM PMP-22 in 20% TDPC (red). F) 350μM PMP-22 in 20% β-DDMB (black) and 400μM PMP-22 in 20% β-DDM (red).*

A more demanding test case for NMR is provided by the human PMP22, a tetraspan membrane protein. Despite over a decade of effort to optimize NMR conditions for this disease-linked protein the best NMR spectra acquired to date have been in tetradecylphosphocholine (TDPC) micelles and these are highly unsatisfactory, characterized by the absence of many peaks and considerable heterogeneity of linewidths among the peaks that can be observed. (265,266) As shown in **Figure 2.4E**, PMP22 presents an improved spectrum when purified in β-DDMB relative to TDPC. The quality of the spectrum from β-

DDM and β-DDMB are more similar (**Figure 2.4F**), however, the β-DDMB spectrum exhibits more peaks in the crowded region between 8.5 and 7.5 H ppm.

Conclusion

To conclude, detergents remain a nearly ubiquitous tool in biochemical and biophysical studies of membrane proteins, usually being employed during purification and reconstitution, as well as often being a component of the final model membrane system in which the membrane protein is characterized. Here, studies of β-DDMB that show that it forms smaller micelles than the commonly used β-DDM, even though both detergents have n-dodecyl tails and disaccharide head groups. β-DDMB is just as good as β-DDM at maintaining the thermal stability of a complex membrane enzyme, DAGK. Moreover, β-DDMB is better than any detergent yet tested as a medium in which to purify DAGK in a way that avoids misfolding. Finally, for three different membrane proteins β-DDMB was seen to yield NMR spectra of similar or even higher quality than previously observed for the best of the previously tested detergents. This is an important development for non-ionic detergents, which have rarely been used as membrane-mimetic media in previous NMR studies. We hope these observations will encourage both further characterization of β-DDMB and exploration of applications for which it may be uniquely well suited.

III. Bicelles Rich in both Sphingolipids and Cholesterol and Their Use in Studies of Membrane Proteins

This chapter is adapted Bicelles Rich in both Sphingolipids and Cholesterol and Their Use in Studies of Membrane Proteins published in JACS and has been reproduced with the permission of the publisher. Hutchison JM, Shih KC, Scheidt HA, Fantin SM, Parson KF, Pantelopulos GA, Harrington HR, Mittendorf KF, Qian S, Stein RA, Collier SE, Chambers MG, Katsaras J, Voehler MW, Ruotolo BT, Huster D, McFeeters RL, Straub JE, Nieh MP, Sanders CR. Bicelles Rich in both Sphingolipids and Cholesterol and Their Use in Studies of Membrane Proteins. J Am Chem Soc. 2020 Jul 22;142(29):12715-12729. doi: 10.1021/jacs.0c04669. Epub 2020 Jul 8. PMID: 32575981; PMCID: PMC7924963.

Introduction

The plasma membrane (PM) of mammalian cells and related endosome and lysosome membranes is distinguished from other organellar membranes by its high levels of both cholesterol (Chol) and sphingolipids, lipids that are well known to undergo unusually strong lipid-lipid interactions in the membrane that result in local membrane clustering and ordering. (267) The observation of local ordering of membrane lipids has led to the lipid raft hypothesis, which posits that phase separation can occur in PMs, resulting in Chol and sphingolipid-rich ordered phase nanodomains ("lipid rafts") surrounded by disordered phase bilayers. (29-31) While the lipid raft hypothesis has been controversial, (268) there is no question that PMs are rich in Chol and sphingolipids. (6) To test the impact of the unique mammalian PM composition on protein structure and dynamics, there is a need for model membranes that are rich in both Chol and sphingolipids that can be used in biochemical and biophysical studies of isolated membrane proteins and complexes. However, except for bilayered lipid vesicles (liposomes), no such model membrane system has previously been available, mainly due to difficulties in co-solubilizing large molar fractions of Chol and sphingolipids to form mixed micelles, bicelles, nanodiscs, or lipodisqs (the latter also known as SMALPs).

Both sphingolipid-rich bicelles and Chol-rich bicelles have been reported, (78-81) but not bicelles that are rich in both these lipids. Chol-rich "native" eukaryotic bicelles have been used in studies of peptide structures, but were not morphologically characterized and contained only ~ 1 mole % sphingomyelin (SM). (269) Reinforcing the idea of poor SM/Chol co-solubility, recent work by Kot et al. showed that SM and Chol mixtures are recalcitrant to the detergents traditionally used to form bicelles. (82) Peptide-based nanodiscs have used to co-solubilize lipid mixtures containing SM and Chol, but only to 7 and 4 mol % respectively. (270) The difficulty of dissolving sphingolipid-Chol mixtures may be related to energetically-favorable complex formation between these two lipids. (32,33) In this work we set out to develop a model membrane system that is rich in both SM and Chol and that involves formation of assemblies small enough to be monodisperse and optically clear, such that they can be employed in a wide range of biophysical and biochemical applications requiring these properties. Here, we describe the development and characterization of SM and Chol-rich SCOR bicelles. To demonstrate the utility of this new model membrane system we also report reconstitution and biophysical characterization of the transmembrane C99 domain of the human amyloid precursor protein (APP) into SCOR bicelles. It is shown that this protein exhibits structural properties in this medium that are distinct from what has previously been observed in more conventional model membrane media.

Results

Screening for a Detergent That Can Solubilize Phosphatidylcholine-Sphingolipid-Chol Mixtures

A screen of over 200 mixtures was conducted in search for a detergent that can co-solubilize Chol and SM mixtures in the presence of phosphatidylcholine at a total detergent:lipid of 3:1 molar ratio (q = 0.33), with results summarized in **Table S3.1**. The choice of lipid mixtures tested was heavily weighted towards lipid mixtures that either are known to form ordered phase bilayers at near-physiological temperatures or are predicted to do so. Among the cross-section of 35 detergents tested we found a number that could could solubilize *either* Chol or SM, tested. However, only the recently introduced(68) n-dodecyl-β-melibioside (DDMB) was successful at solubilizing mixtures of various forms of phosphatidylcholine with both Chol *and* egg SM (eSM). eSM is predominantly (~86 %) composed of the saturated C16-amidated form (*https://avantilipids.com/product/860061*). It is notable that DDMB, with its melibiose (galactose-α(1→6)-D-glucose) head group, was effective, while n-dodecyl-β-maltoside, with its less flexible glucose-α(1→4)-D-glucose headgroup was not. DDMB was seen to be able to solubilize a range of phospholipid-Chol-sphingomyelin mixtures. We chose DMPC as the glycerophospholipid for the SCOR bicelles focused on in this work because of its extensive prior use in well-characterized classical bicelle mixtures, including work involving our test protein for this study, C99.(186,187,204,205,230,235,240,271-274) Accordingly, there is a wealth of previous data for classical DMPC-based bicelles that can be compared to our results for the new SCOR bicelles.

Solid-State NMR Characterization of 4:2:1 DMPC:eSM:Chol Bilayered Vesicles

From the numerous mixtures tested (Table S1) we selected SCOR bicelles composed of DDMB and 4:2:1 DMPC:eSM:Chol SCOR to focus on in this study. Because detergent-free 4:2:1 DMPC:eSM:Chol lipid bilayers have not previously been characterized, we examined vesicles of this composition using solid-state NMR spectroscopy. The goal was to illuminate the bilayer phase properties of the parent lipid mixture used for the SCOR bicelles. First, static ^{31}P NMR spectra were acquired as a function of temperature, as shown in **Figure 3.1A**. All spectra for the 20 to 50°C temperature range exhibited a single powder pattern characterized by an axially symmetric chemical shift anisotropy tensor spanning ~50 ppm, in which the individual ^{31}P NMR contributions of DMPC and eSM are indistinguishable. Such an NMR powder pattern lineshape is characteristic of lipids undergoing rapid axially symmetric motional averaging, as is typical for lamellar membranes in either the ordered or disordered but not the gel phase.(23,275) Next, ^{2}H NMR spectra of the mixture containing chain-perdeuterated DMPC-d_{54} were measured as a function of temperature (**Figure 3.1B**). The typical superposition of quadrupolar Pake powder patterns from all deuterons along the myristoyl chains is observed, where each quadrupolar splitting provides information on the degree of molecular order of a particular methylene or methyl segment in the lipid chain. Close inspection of the innermost (and most intense) terminal methyl group splitting reveals the appearance of a second Pake doublet at temperatures below 30°C (**Figure 3.1C**). This indicates that DMPC populates two different environments (as would be the case if DMPC is distributed between two different phases).(27) No spectral features indicative of a gel (Pβ) or solid-ordered (So) phase were observed even at 20°C, where pure DMPC membranes are well known to form a gel phase. As expected, the widths of the ^{2}H NMR quadrupolar Pake doublets decreased with increasing temperature due to increased motional disorder of the C-D bond vectors along the chain, as also seen in a plot of the first spectral moment as a function of temperature (**Figure 3.1D**). The slight discontinuity seen at a temperature of ~30°C coincides with the spectral changes observed for the methyl groups, also consistent with a transition from the ordered Lo phase to the disordered Ld phase above this temperature.(275) Above 30°C, the spectral resolution is sufficient for dePakeing(276) the ^{2}H NMR spectra, resulting in the order parameter profiles along the carbon chains shown in **Figure 3.1E**. These profiles are consistent with a somewhat disordered phase state at temperatures above 30°C. As temperature increases, the order in the acyl chain decreases.

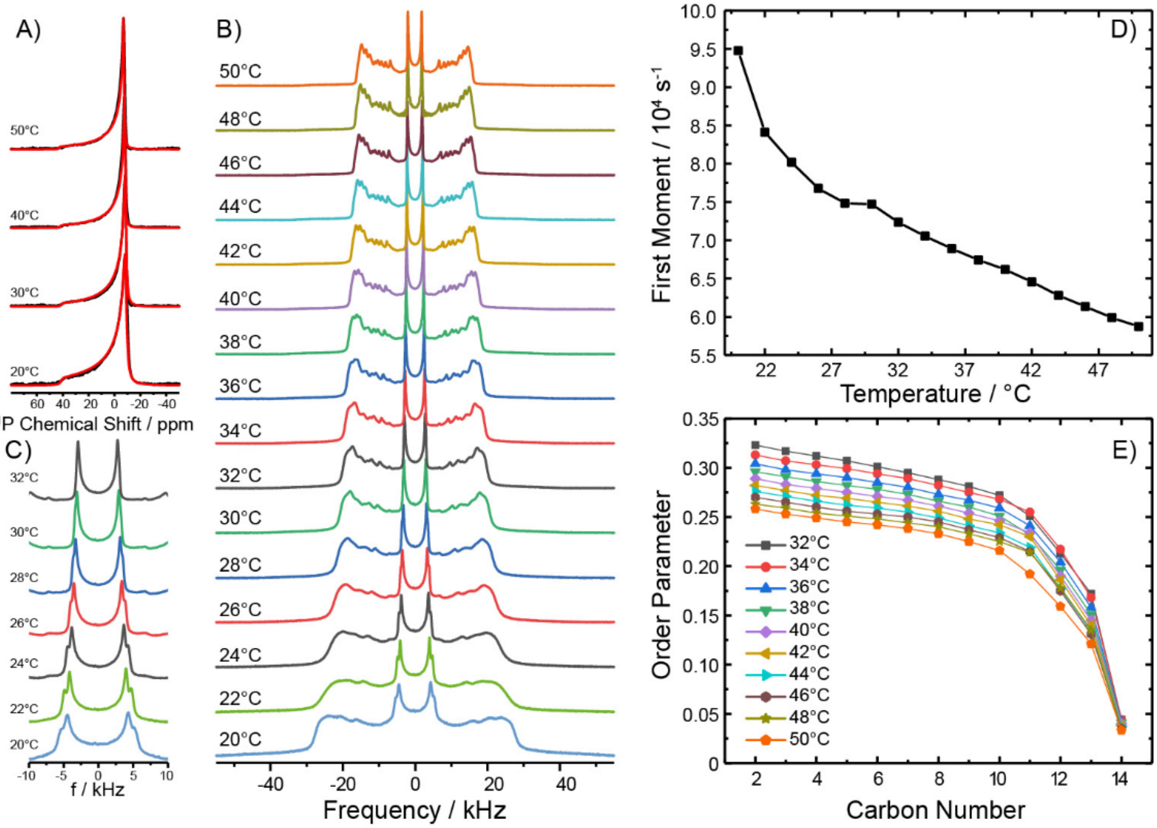

Figure 3.1. Static ^{31}P and ^{2}H NMR spectra of fully hydrated DMPC-d$_{54}$/eSM/Chol (4/2/1 mol/mol/mol) vesicles at various temperatures. *A) Static ^{31}P NMR spectra exhibiting powder patterns reflecting axially symmetric motional averaging of the lipid in the Lo phase at low and Ld phase at high temperatures. The widths of the ^{31}P NMR spectra exclude that DMPC is in a gel phase. Red lines indicate best fit simulations of the spectral line shape. Samples were observed to be slightly field-oriented. Spectra were simulated using an ellipsoidal distribution function with aspect ratios of 0.65 – 0.75. B) ^{2}H NMR spectra of chain perdeuterated DMPC-d$_{54}$ in the ternary lipid mixture as a function of temperature. C) Enlarged view of the chain-terminal methyl group quadrupolar splitting of the ^{2}H NMR spectra shown in B, which highlights two sets of quadrupolar splitting at temperatures from 20 to 30°C. D) Plot of the 1st spectral moment of the ^{2}H NMR spectra shown in B as a function of temperature. E) DMPC chain order parameters as a function of chain position in the ternary mixture at various temperatures, as determined after dePakeing the NMR spectra shown in panel B.*

It has previously been seen that lipids in the Lo phase share a property with those in the Ld phase by undergoing unhindered lateral diffusion and also long axis rotational diffusion around the bilayer normal. (27,28) However, the Lo phase state differs from Ld by featuring a dramatic decrease in the number of *gauche* dihedrals angle along the hydrocarbon chains due to strong ordering interactions imposed by proximal Chol. (27,28) This trend is reflected by the wider span of the ^{2}H NMR spectra below

30°C relative to spectra from Ld phase bilayers, as was observed here. The population of *gauche* conformers can be estimated from the average DMPC chain length determined from each ^{2}H NMR spectrum. (277,278) Each *gauche* excursion reduces the chain length by 1.1 Å. (279) At 20°C, the maximum quadrupolar splitting of DMPC in the mixture is 56 kHz, which is close to the maximum of 62.6 kHz, which would indicate fully extended all *trans* chains undergoing axially symmetric reorientation along the long axis of the DMPC molecule, as expected for an ideal Lo phase state. The average chain order parameter of DMPC-d_{54} in the mixture at 20°C can roughly be determined to be $\langle S \rangle = 0.36$ given the broad nature of the ^{2}H NMR spectrum at this temperature. From the average order parameter of 0.36, the average length of DMPC chains in the mixture was estimated to be 13.1 Å, which can be compared to 15.2 Å for an all *trans* chain. This suggests that the DMPC chains in the mixture exhibit on average ~2 *gauche* defects at 20°C. At temperatures above 30°C, the chain length can be determined precisely from the dePaked spectra, yielding chain lengths varying from 11.6 Å at 32°C to 10.7 Å at 50°C. This would correspond to 3.3 to 4.1 *gauche* defects, which is in agreement with the population of the liquid disordered (Ld) phase state in that temperature range. These results therefore suggest that the 4:2:1 DMPC:eSM:Chol mixture occupies an Lo-like phase state between 20 and 30°C and the Ld state above 30°C. The transition between these phases is somewhat gradual.

The conclusion that the phase occupied by 4:2:1 DMPC:eSM:Chol at lower temperatures is Lo-like, but not to an ideal extreme, is not surprising. Pure Lo phase formation is most often described only at Chol contents higher than the 14 mol% of the current mixture. (27,280) To confirm that the 4:2:1 mixture truly occupies a Lo-like phase below 30°C we applied ^{1}H MAS NMR to gain additional information. **Figure S3.1** shows a series of ^{1}H MAS NMR spectra of this mixture as a function of temperature. Particularly at 20 - 24°C, the observed NMR spectra closely resembles what has been defined as the pure Lo phase ^{1}H NMR spectrum. (280)

Taken together, the solid-state NMR characterization of the DMPC/eSM/Chol (4:2:1 mol/mol/mol) mixture indicates the bilayers form are in a Lo-like phase state at temperatures below ~30°C and that there is a transition to the Ld state above 30°C. The transition between these states is gradual. The fact that the mixture appears to have properties that are at the borderline between Lo and Ld phases over the 20-40°C temperature range is well suited for mimicking mammalian PMs, which also appear to exhibit properties that also are borderline between these two phases. (35)

Small Angle Scattering Characterization of SCOR Bicelles

Small angle X-ray and neutron scattering (SAXS & SANS) methods are powerful tools for resolving the ensemble morphology of particles. We therefore used these methods to characterize the shape and structural organization of SCOR bicelles. Measurements were made for mixtures with lipid-to-DDMB q ratios (q is the lipid-to-detergent mole ratio) ranging from 0.25 to 1.0, a range of q in which the bicelles are small and monodisperse. **Figure 3.2** shows that a simultaneous fit of the SAXS and SANS scattering curves with a core shell bicelle model (**Figure S3.2**) for both q = 0.33 and 1.0 SCOR bicelles supports the ideal bicelle model in which a discoidal lipid bilayer region is surrounded by a toroid of DDMB detergent. It is noted that the deviation from fit at $Q < 0.02$ Å^{-1} in **Figure 3.2B** (SAXS data where Q is the scattering vector) was likely due to the presence of air bubbles, but that this did not impact the best fitting parameters, as the simultaneous fit with both SAXS and SANS data greatly reduced the uncertainty. Over q ratios of 0.25 to 1.0, SCOR bicelles were seen to conform to the classical detergent edge-stabilized bilayer disc model with a near constant bilayer thickness of 4.7 nm at q = 0.25 to 5.3 nm at q = 1.0, and with disc diameters ranging from ~7 nm at q = 0.25 to ~11 nm at q = 1.0 (**Figures 3.2C and S3.2**).

Due to the higher electron density of the phosphate groups, SAXS can provide model-free information about headgroup-headgroup distances in bicelles (along the axis orthogonal to the plane of the bicelle) via analysis of the second maxima, referred to as the Q_{Max} (**Figure 3.2D**). (62) As highlighted in **Figure 3.2E**, the mean headgroup-to-headgroup distance in the SCOR bicelles increases from 4.6 nm at q = 0.25 to 5.0 nm at q = 1.0 (~ 9 %), while for DMPC-DHPC bicelles the mean headgroup-to-headgroup distance increases by ~44% over a very similar q range. (67) Mean headgroup-headgroup distances are understood to approximate bilayer thickness and the SCOR bicelles are seen to exhibit only a slight increase in bilayer thickness as a function of q. The SCOR bilayer thickness of ~5.0 nm at q = 1.0 is significantly larger than the ~4.3 nm bilayer thickness of pure DMPC. (67) This increase is likely because Chol increases the bilayer thickness, as it is known to do in DMPC vesicles.(34) The thicker SCOR bilayer is also consistent with the higher order of the bilayered domain of the SCOR bicelles, meaning a higher proportion of trans conformations for the acyl chains of DMPC and eSM, as corroborated by our solid state ^{2}H NMR results for vesicles. The limited change in bilayer thickness of SCOR bicelles over a range of q ratios implies minimal detergent penetration into the lipid core, even at low q ratios. Moreover, the decay transition from the low-Q intensity plateau moves toward lower Q values, suggesting that the size of bicelles increases with higher q ratios, as expected. In summary, combined SAXS and SANS results demonstrate that SCOR bicelles have the bilayered disc morphology of ideal bicelles with limited detergent penetration into the ~5 nm thick bilayer core.

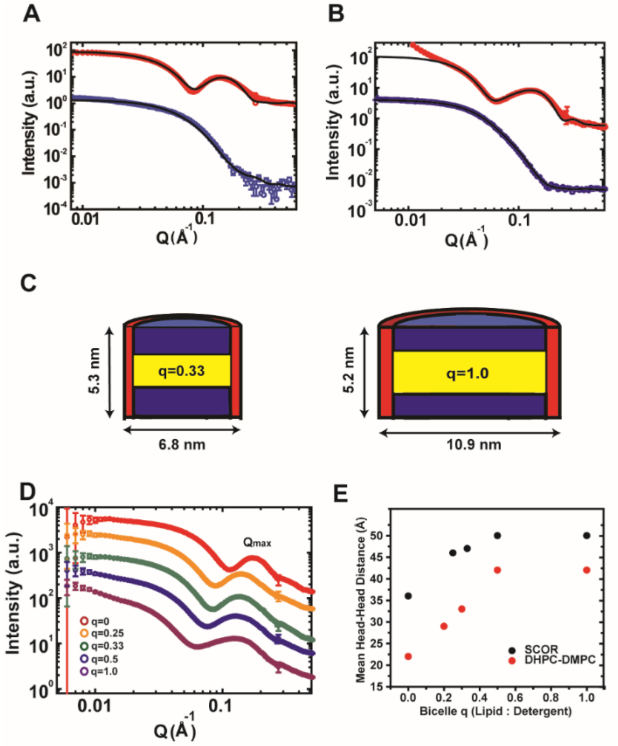

Figure 3.2. Small angle X-ray and neutron scattering of SCOR bicelles. *A) Small-angle scattering measurement for q= 0.33 SCOR bicelles at a total lipid+detergent concentration of 0.5 wt %, a concentration at which bicelles were confirmed to persist (see later section of Results devoted to dynamic light scattering). Fully protonated SCOR bicelles were prepared in H2O (SAXS) or in 100 % D2O (SANS), with scattering results shown in red and blue, respectively. B) Small angle scattering measurements for fully protonated q=1.0 SCOR bicelles at 0.5% w/v prepared in* H_2O *(SAXS) or in 100 %* D_2O *(SANS), shown in red and blue respectively. C) Models of SCOR bicelles at q=0.33 and q=1.0 (left and right, respectively) based on small angle scattering core-shell bicelle model fitting of panels A and B (see* ***Figure S3.2 and Appendix 2*** *for a description of the model). D) SAXS scattering curves for 0.5 wt % DDMB micelles (red) and for SCOR bicelles at lipid:detergent mole (q) ratios of 0.25 (orange), 0.33 (green), 0.5 (blue), and 1.0 (purple) buffered with 10 mM imidazole pH 6.5, 0.1 mM EDTA, and 0.3 mM DDMB. The Qmax peak is around ~ 0.12. E) Mean headgroup-to-headgroup distance determined from scattering results shown in panel D using Qmax ratios for classical and SCOR bicelles at various q ratios. The classical bicelle—DMPC/DHPC—ratios are from Caldwell et al. (67)*

Cryo-Electron Microscopy Visualization of SCOR Bicelles

We used transmission cryo-electron microscopy (cryo-EM) on SCOR bicelles frozen in vitreous ice to see if it was possible to obtain direct visualization of bicelle discs. **Figures 3.3A and B** show cryo-EM micrographs for q = 0.33 and 1.0 SCOR bicelles.

The cryo-EM micrographs did not reveal any self-association of the bicelle assemblies. SCOR bicelles exhibit a hollow discoidal shape reflecting their electron-poor hydrocarbon interior and electron-rich head group surface. Bicelle image populations were sufficiently uniform to be picked and class-averaged, with orthogonal views of the same reconstructions being shown for q = 0.33 and q=1.0 bicelles in **Figures 3.3C and 3.3D**, respectively. As can be seen, for both compositions the discoidal morphology is confirmed. Moreover the dimensions seen for both the q=0.33 (thickness of 5.3 +/- 0.7 nm, diameter of 6.9 +/- 0.8 nm) and q= 1.0 (thickness of 5.5 +/- 0.4 nm, diameter of 12.8 +/- 1.9 nm) bicelles are in good agreement with the SAXS and SANS results (**Figure 3.3E**). It is important to note that the q = 0.33 SCOR bicelle sample, (**Figures 3.3A and C**), contained the C99 protein, a small single-span membrane protein (see later section of Results). We could not resolve any protein density, which was as expected given the small (14 kDa) size of our C99 construct and its dynamic oligomeric state (see below). These results confirm the conclusions of the scattering experiments and demonstrated that SCOR bicelles are well-behaved in vitrified conditions, suggesting that they may be suitable for use in cryo-EM studies of larger integral membrane proteins and their complexes, especially those with less dynamic structures. We used the q = 0.33 SCOR bicelle for the C99 studies described below and estimated the aggregate molecular weight of q = 0.33 SCOR bicelles to be around 100kD with roughly 185 lipid and detergent molecules in each bicelle (**see Appendix 2**).

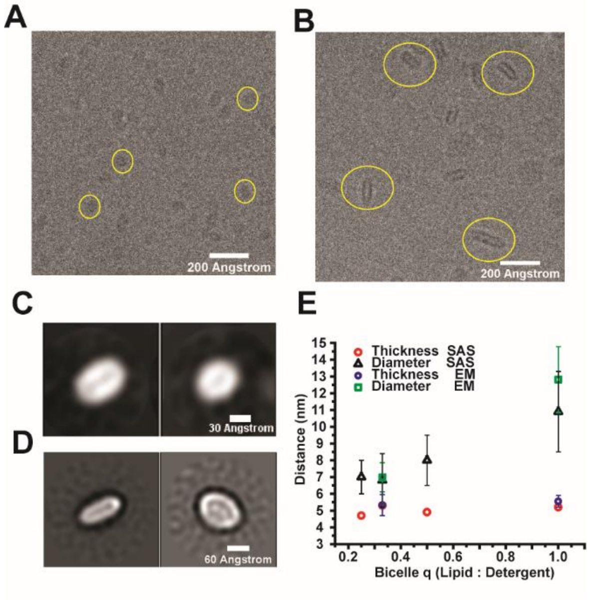

Figure 3.3. Cryo-Electron microscopy of SCOR bicelles. *A) Contrast-enhanced cryo-EM image of q= 0.33 SCOR bicelles with yellow circles highlighting individual particles. B) Contrast-enhanced cryo-EM image of q= 1.0 SCOR bicelles with yellow circles highlighting individual particles. Samples in A and B are 0.64 wt % bicelle samples (at both q = 0.33 and q = 1.0) in 75 mM NaCl, 1 mM EDTA, 25 mM sodium acetate, pH 4.5. C) and D) are orthogonal views of class averages for the q = 0.33 and q = 1.0 bicelles, respectively. q=0.33 samples contained the C99 protein at a ~ 2:3 protein-to-bicelle ratio. C99 is not observed owing to its small size. E) Comparison of SCOR bilayer thickness and diameter as determined from cryo-EM (n=50), and small angle scattering fits.*

Use of Dynamic Light Scattering to Test the Resilience of SCOR Bicelles to Changes in Concentration, pH, Salt and Temperature.

Dynamic light scattering was employed as a convenient way of exploring the range of conditions in which the integrity of SCOR bicelles persists (**Figure 3.4**). **Figure 3.4A** shows that the radius of hydration (R_h) determined from dynamic light scattering is in general agreement with the radius of gyration (R_g) determined by SAXS from the Guinier region. It was also seen that SCOR bicelle size is not affected by bicelle concentration (total lipid+detergent) above 0.25 wt%, but does exhibit a slight increase in radius of hydration when the total bicelle concentration is reduced to 0.125 wt% (**Figure 3.4B**). The persistence of SCOR bicelles at such low concentrations is likely due to the low critical micelle concentration (CMC) of DDMB (0.3 mM(68)) relative to the higher critical micelle concentration of the most commonly used detergent in conventional bicelles, dihexanoylphosphatidylcholine (DHPC, CMC of 10-15 mM (281)). It was also seen that SCOR bicelle size is not significantly affected by pH, ionic strength, or temperature. This robustness is well-suited for the possible utility of SCOR bicelles as a membrane mimetic medium (**Figure 3.4B-D**).

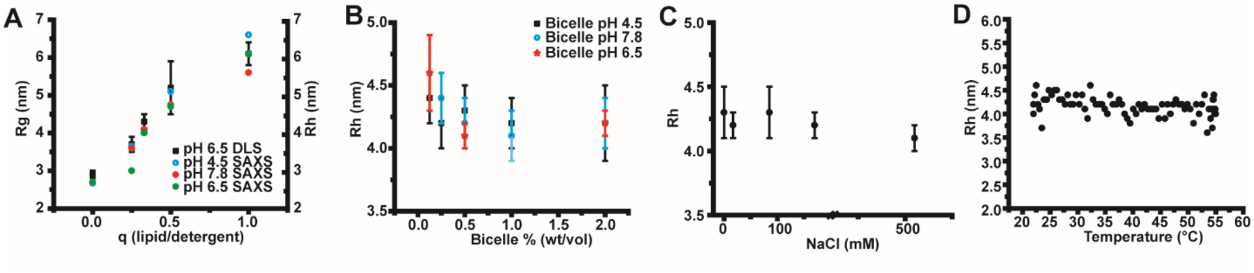

Figure 3.4. Dynamic light scattering of SCOR bicelles. *(A) DLS-determined apparent hydrodynamic radii (R_h) values are compared to SAXS and SANS-determined apparent radius of gyration (R_g) values for SCOR bicelles at various q (lipid:detergent) ratios. Error bars reflect the standard deviation of R_h values determined from three repetitions of 10 DLS acquisitions for each q ratio. (B) DLS-determined R_h for SCOR bicelles at a q of 0.33 for various pH values as a function of bicelle solution wt %. Bicelles at pH 4.5 were buffered with 10 mM sodium acetate, while bicelles at pH 6.5 and 7.8 were buffered with 10 mM imidazole. (C) DLS-determined R_h values for SCOR bicelles at a q of 0.33 as a function of ionic strength. (D) DLS-determined R_h values for SCOR bicelles at a q of 0.33 as a function of temperature. Temperature ramps to and from 22 to 55 °C were conducted at rate of 1 °C/minute.*

Assignment of Backbone NMR Resonances for the Amyloid Precursor C99 Protein in SCOR Bicelles.

To demonstrate the utility of SCOR bicelles as a medium for biophysical studies of a membrane protein, we selected for study the 99-residue C-terminal domain of the human amyloid precursor protein (APP), the immediate precursor of the amyloid-beta polypeptides that are associated with Alzheimer's disease. C99 has previously been subjected to structural studies in micelles, bicelles, and lipid vesicles. (186,187,204,205,230,235,240,271-274) When initially screening SCOR bicelle lipid compositions for NMR studies of C99, we found that the 4:2:1 DMPC:eSM:Chol mixture at a q of 0.33 yielded $^{1}H,^{15}N$-TROSY NMR spectra of reasonably high spectral quality, reminiscent of previous work with C99 in DHPC/DMPC bicelles.(187) Using uniformly $^{2}H,^{13}C,^{15}N$-lableled C99 we assigned its backbone ^{15}N and ^{13}C NMR resonances in SCOR bicelles using traditional 3D NMR approaches supplemented with data from amino acid-specific labeling experiments. Assignments were also facilitated by transferring some previously-completed assignments from DDMB micelle conditions (**Figures S3.3-S3.5**). The $^{1}H,^{15}N$-TROSY spectrum of C99 in SCOR bicelles is shown in **Figure 3.5**. Over 90 % of C99 backbone resonances were assigned, with the main hindrance for the remaining resonances being that some transmembrane or juxtamembrane sites yield only very broad peaks.

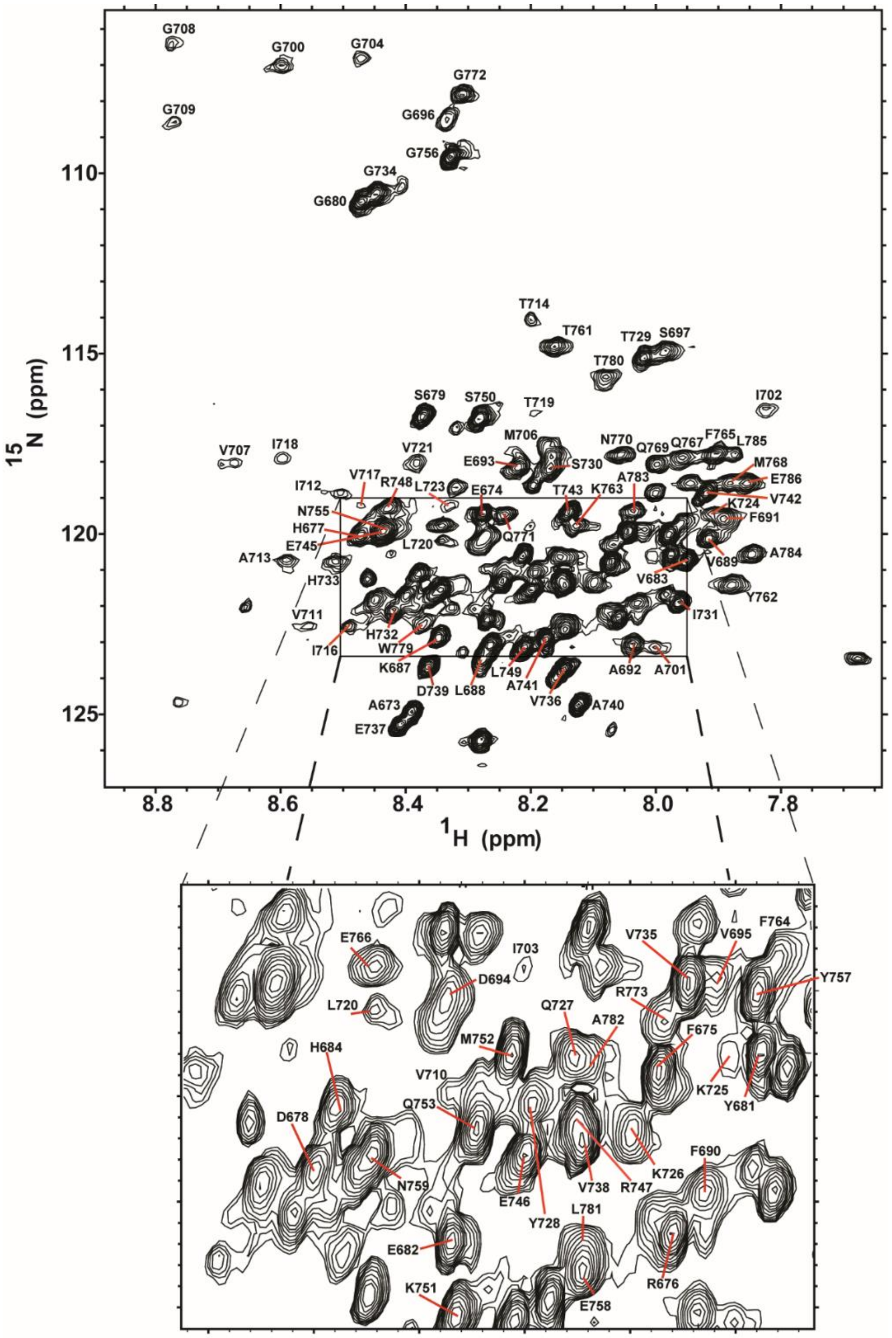

Figure 3.5. Assigned ^{1}H,^{15}N-TROSY NMR spectrum of C99 in SCOR bicelles. *The backbone amide ^{1}H-^{15}N peaks are labeled according to amino acid number. This spectrum was collected on a 400 µM C99 sample in 10 wt % SCOR bicelles, q=0.33, in NMR buffer in a shaped tube at 45 °C and 900 MHz.*

Structural Studies of C99 in SCOR Bicelles

TALOS-N was used to analyze chemical shifts from C99 to map its secondary structure in SCOR bicelles. In addition to the helical transmembrane domain, there is a short extracellular amphipathic “N-helix” separated from the N-terminus of the transmembrane domain (TMD) by only a few linking residues. There also is an amphipathic “C-helix” at the extreme C-terminus separated from the TMD by a 35 residue “C-loop”. A summary of the secondary structure elements and sequence is shown in **Figure 3.6A**. The overall secondary structure of full length C99 in SCOR bicelles is nearly identical to what was previously been seen for full length C99 in micelles and in classical bicelles. (186,187)

To probe both the membrane topology and possible quaternary structural interfaces for C99 in SCOR bicelles, TROSY NMR spectra were acquired in the presence of paramagnetic probes. The presence of the lipophilic paramagnetic probe, 16-DOXYL-stearic acid (16-DSA), broadens NMR signals from residues in direct contact with the membrane interface or hydrophobic interior. Conversely, the presence of the water-soluble probe gadopentetic acid (Gd-DTPA) broadens the NMR signals from water-exposed sites. Together, these probes permit mapping of which residues are exposed to the membrane and extramembrane regions. As shown in **Figures 3.6B and S3.6**, resonances from both the N- and the C-terminal helices (sites 690-697 and 761-770) were broadened by the presence of 16-DSA and are partially protected from broadening by Gd-DTPA, indicating that these helices are amphipathic and interact with the bicelle surface, similar to what has previously been seen for C99 in micelles, (232) vesicles, (186) and in DMPC/DHPC bicelles. (187) However, a more surprising result for C99 in SCOR bicelles is that a number of sites located in the C-terminal half of the C99 TMD (sites 710-720) were seen to be protected against 16-DSA broadening, while sites in the N-terminal half (sites 700-709) of the TMD were broadened (**Figure 3.6B**). This protection of transmembrane sites against access by a lipophilic probe indicates the location of quaternary structural interface. This oligomeric interface does not involve the GXXXG (residues 700-704) motifs seen to be critical for dimerization of C99 in some previous experimental structural studies (214,240,282) all of which were conducted in conventional model membranes bereft of Chol and SM. Instead, the transmembrane oligomerization sites are located in the cytosolic half of the TMD.

Unusual paramagnetic probe NMR results were observed for residues 673-678 at the N-terminus and for residues 735-745 in the C-loop that connects the TMD to the surface-associated C-helix. While analysis of the NMR chemical shifts indicates random coil structure for the 37 residue C-loop (residues 724-760), it was seen those residues 735 to 745 located midway through the loop were protected from both lipophilic and water-soluble probes, while being flanked on each end by water-exposed segments (**Figure 3.6B**). To verify these results, we collected an NMR spectrum after adding very high concentrations of *both* Gd-DTPA and 16-DSA probes. As is shown in **Figure 3.6C**, this segment of the C-terminal loop is the only part of the protein that was seen to be completely resistant to paramagnetic broadening by the combined influence of excess levels of both probes. Residues 673-678 do not show the same strong protection from excessive paramagnetic probes, indicating that these sites exhibit a weaker or less populated state of the phenomenon occurring for residues 735-745.

To better elucidate the behavior of the C-loop, backbone amide proton exchange with water was probed using the CLEANEX-PM experiment, (283) with the results being shown in **Figure 3.6D**. As expected, the helical segments of the protein were resistant to amide exchange, while the seemingly random coil segments (much of the N-terminus and C-loop) underwent facile exchange. The notable exception was the 735-745 residue segment of the C-loop. Even though this segment appears to adopt a random coil-like secondary structure, it was seen to be resistant to amide exchange (**Figure 3.6D**), results that complement the observation that this segment is inaccessible to both paramagnetic probes (**Figures 3.6B and C**). N-terminus residues 673-678 are random coil and also exhibit, albeit to a lesser degree, the same type of probe protection and reduced backbone hydrogen exchange as seen for loop residues 735-745.

To gain further insight into the structure and dynamics of the paramagnetic probe-resistant and amide exchange-resistant segment of the C-terminal cytosolic loop, we collected ^{15}N NMR relaxation and ^{1}H-^{15}N NOE data for C99 in SCOR bicelles. The measured T1/T2 ratios and ^{1}H-^{15}N NOE values for the cytosolic domain of C99 are shown in **Figures 3.6E and F**, respectively. The relatively high order of the surface-associated C-terminal helix (sites 762-770) is evident from these measurements as is the gradual increase in order as the TMD-anchored N-terminus of the cytosolic domain is approached. Notably, these measurements also reveal that sites 735-745 of the C-loop are extremely mobile. While consistent with the chemical shift/TALOS analysis showing that these sites appear to adopt random coil-like structure, these are also the same sites that were seen to be resistant both to amide exchange and to line broadening by lipophilic and water-soluble paramagnetic probes, which in both cases is suggestive of significant tertiary or quaternary structure. The only previous experimental studies of the C99 cytosolic domain in the context of full-length C99 (186,187,232) indicated that the C-loop is largely disordered and revealed no anomalies for the 735-745 segment. Interestingly, previous NMR studies of the isolated cytosolic domain of C99 or of fragments of this domain (284-288) in aqueous buffer (no model membranes) led to the conclusion that this segment does exhibit transient structural properties. We also point out that the unusual observations seen in the C99 735-745 segment in SCOR bicelles are not unprecedented in structural and dynamic studies of proteins. For example, a recent paper by Borgia et al.(289) describes structural and dynamic studies of the interactions of human proteins histone H1 and its nuclear chaperone, the prothymosin α protein. It was shown that these two intrinsically disordered proteins form a high affinity heterodimeric structure stabilized by electrostatic interactions, while remaining disordered.

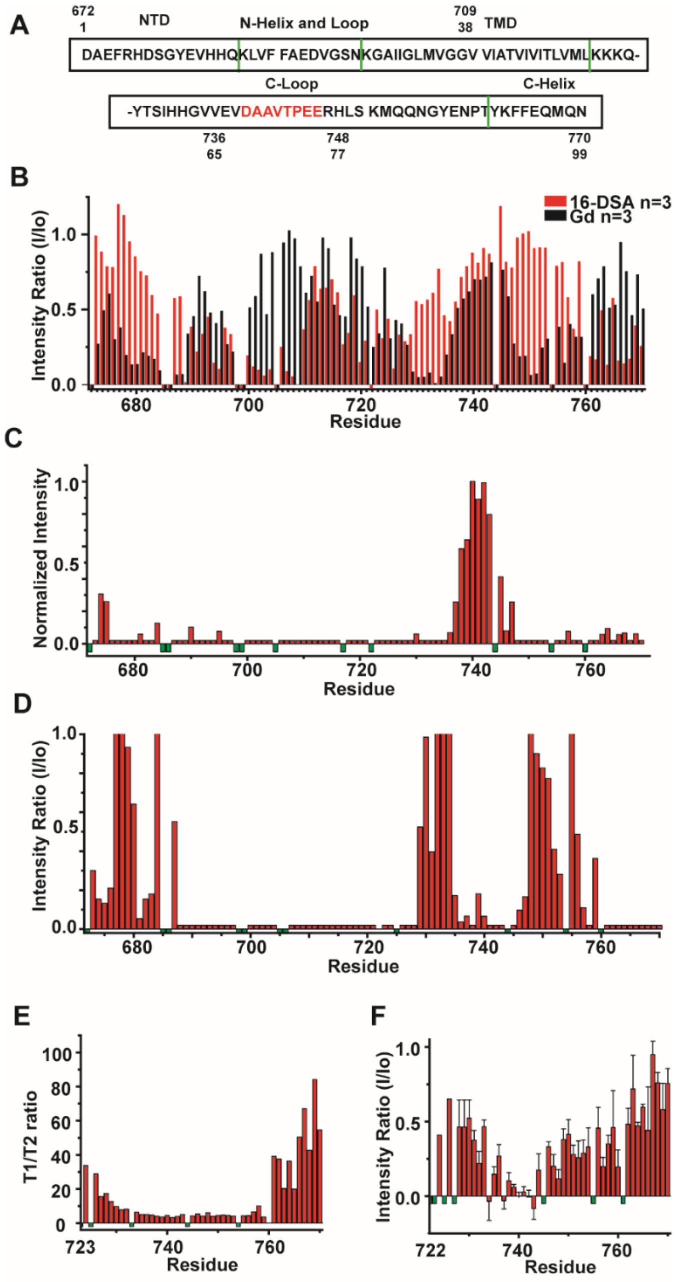

Figure 3.6. Use of NMR to probe the topology and dynamics of C99 in SCOR bicelles. *A) Sequence of human C99 with numbering based either on C99 only (sites 1-99) or on the parent full-length amyloid precursor protein (672-770). Green lines indicate boundaries of secondary structural elements as determined in this work from analysis of the backbone NMR resonance chemical shifts and paramagnetic data. Amino acids in the C-loop previously identified as being involved in transient amide backbone hydrogen bonding are identified in red. (287) B) Topology of C99 in SCOR bicelles as mapped by site-specific TROSY NMR peak linebroadening due to site access by lipophilic (16-DSA) or aqueous (Gd-DTPA) paramagnetic probes. Mean intensity ratios (probe-exposed versus control peak height) are presented for 16-DSA (red) and Gd-DTPA (black). The U-^{15}N-C99 concentrations for all experiments were between*

~200 and 400 μM in 5-10 wt% SCOR bicelles, q = 0.33, in NMR buffer. Error bars for these n=3 data are not shown here (to avoid clutter), but are displayed in ***Figure S3.6.*** *C) Effect on C99 peak intensities of adding both excess 16-DSA (to 12 mol %), and Gd-DTPA (to 3mM) to a 300μM U-^{15}N-C99 sample in 7 wt % SCOR bicelles and NMR buffer at 45 °C. n=1 D) CLEANEX-PM amide exchange analysis of peak height ratios for a 50 ms mixing time experiment. Ratios are of 50 ms mixing time versus no mixing time. E) NMR ^{15}N T1/T2 relaxation time ratios for the cytosolic domain of C99. T1 and T2 analyses are derived from a 300 μM U-^{15}N-C99 sample in 5 wt % SCOR bicelles q=0.33 in NMR buffer at 45 °C. n=1 F) Intensity ratios for ^{1}H-^{15}N NOE signals from a 300 μM C99 sample in 10 wt % SCOR bicelles, q=0.33, in NMR buffer at 45 °C. n=2 Small negative values in B are residues which were not assigned or were too broad; for C-F, these values are represented by small negative green bars.*

Oligomeric State of C99 in SCOR Bicelles

C99 has previously been seen to be either a monomer (186,204) or a homodimer, (214,240,282,290) depending on the model membrane medium used and whether C99 was studied as the full length protein or in a truncated form—most often the residues 1-55 fragment that lacks most of its cytosolic domain. Based on the paramagnetic probe-protection results, it seems likely that C99 forms dimers or some other oligomer in SCOR bicelles. Determining the oligomeric state of a small integral membrane protein in a complex model membrane medium is often not straightforward, (291) so determination of the C99 oligomeric state offered an ideal opportunity to test the suitability of SCOR bicelles to applications involving a range of biochemical and biophysical techniques. Most measurements were conducted under conditions in which the C99-to-bicelle ratio was carefully controlled to avoid non-specific C99 interactions in crowded bicelles ("forced co-habitation" (292)). Specifically, sample compositions were usually fixed in the range of 1 C99 molecule for every 1-2 SCOR bicelles. Moreover, all experiments probing oligomerization employed SCOR bicelles with a q of 0.33 so that results using different methods could be compared with each other and with the solution NMR results already presented in this work. Here, we describe experiments conducted using Förster resonance energy transfer (FRET) spectroscopy, electron paramagnetic resonance (EPR) double electron electron resonance spectroscopy (DEER), chemical crosslinking/SDS PAGE, and native ion mobility - mass spectrometry.

FRET was previously used to detect C99 dimerization in POPC/POPG vesicles. (204) The C99 H732C mutation was used to provide a labeling site for IAEDANS (FRET donor) and for IANBD (FRET acceptor). This site is in an unstructured region of the cytosolic loop and outside the C-loop paramagnetic probe-protected region. IADEANS-C99 and IANBD-C99 were mixed in SCOR bicelles at various ratios using conditions in which both the donor-tagged C99 concentration and overall protein:lipid concentration were held constant. A linear relationship between FRET efficiency and the donor-to-acceptor ratio affirms that C99 forms oligomers (**Figures 3.7A and B**), but poor labeling efficiency (**see Appendix 2**), makes the identification of a specific oligomeric state difficult. (293) Nevertheless, the FRET results confirm that C99 does form oligomers in SCOR bicelles. We next turned to EPR DEER measurements.

C99 with single cysteine sites located at either N- (K699C) or C-terminal (L723C) sides of the transmembrane helix were spin-labeled with MTSL, followed by DEER measurements in SCOR bicelles, as shown in **Figures 3.7C and D**. For both labeled forms, the observation of the DEER phenomenon supports oligomerization and indicates a broad distribution of spin label/spin label distances. We did not observe any evidence of aggregation and only one peak is observed in the P(r) distribution, which implies a dimer or trimer oligomeric state. (294) The P(r) distribution for each form was centered at ~31-32 angstroms, which is slightly longer than expected for a tight dimer mediated by a transmembrane interface. While some of the distance distribution almost certainly reflects spin label motions, (186) side chain mobility cannot account for the full distance distribution for a tight dimeric state. However, either a flexible dimer or a trimer can account for the slightly larger-than-expected P(r) distances. Another way to determine oligomeric state with DEER is to reference the depth of modulation, (295) but we did not implement this because of incomplete C99 labeling with MTSL. Neither the FRET nor EPR DEER results rule out the possibility that there is also a population of C99 that remains monomeric. Since the FRET and DEER results are consistent with the possibility that C99 may populate either or both dimers and trimers in SCOR bicelles, we next turned to the use of chemical cross-linking in an attempt to covalently trap C99 in dimer and/or trimer forms.

Chemical crosslinking combined with SDS-PAGE is an expeditious way to screen oligomeric states, although results must be validated with an independent technique due to significant risk for false positives/negatives. We cross-linked C99 with glutaraldehyde under near-NMR conditions followed by SDS-PAGE and found that monomer, dimer, and trimer are all observed following cross-linking at high glutaraldehyde concentrations (above 1 % w/v), as shown in **Figure 3.7E**. We observed an enrichment in the trimer form as the cross-linker is increased and also confirmed the absence of significant concentrations of higher order oligomers or aggregates. The cross-linking results clarify the FRET and DEER results by suggesting that C99 populates monomer, dimer, and trimer oligomeric states in SCOR bicelles.

In order to understand how the protein-to-lipid ratio affects C99 oligomerization in SCOR bicelles, we also carried out crosslinking experiments at constant C99 but with increasing concentrations of SCOR bicelles present. As shown in **Figure 3.7F**, increasing the bicelle concentrations increased the relative population of monomer seen following crosslinking and also led to a reduction in the rate of crosslinking efficiency as the glutaraldehyde concentration was increased. While 1:180 and 1:360 protein-to-(lipid+detergent) ratios show only modest levels of monomer, crosslinking to dimers and trimers appears to be far less efficient at and above 1:720. The monomer/dimer/trimer ratio is responsive to the protein-to-lipid ratio with the ratio shifting to favor monomer when the protein is diluted with additional bicelles. This suggests that monomer, dimer, and trimer forms of C99 are in equilibrium in SCOR bicelles.

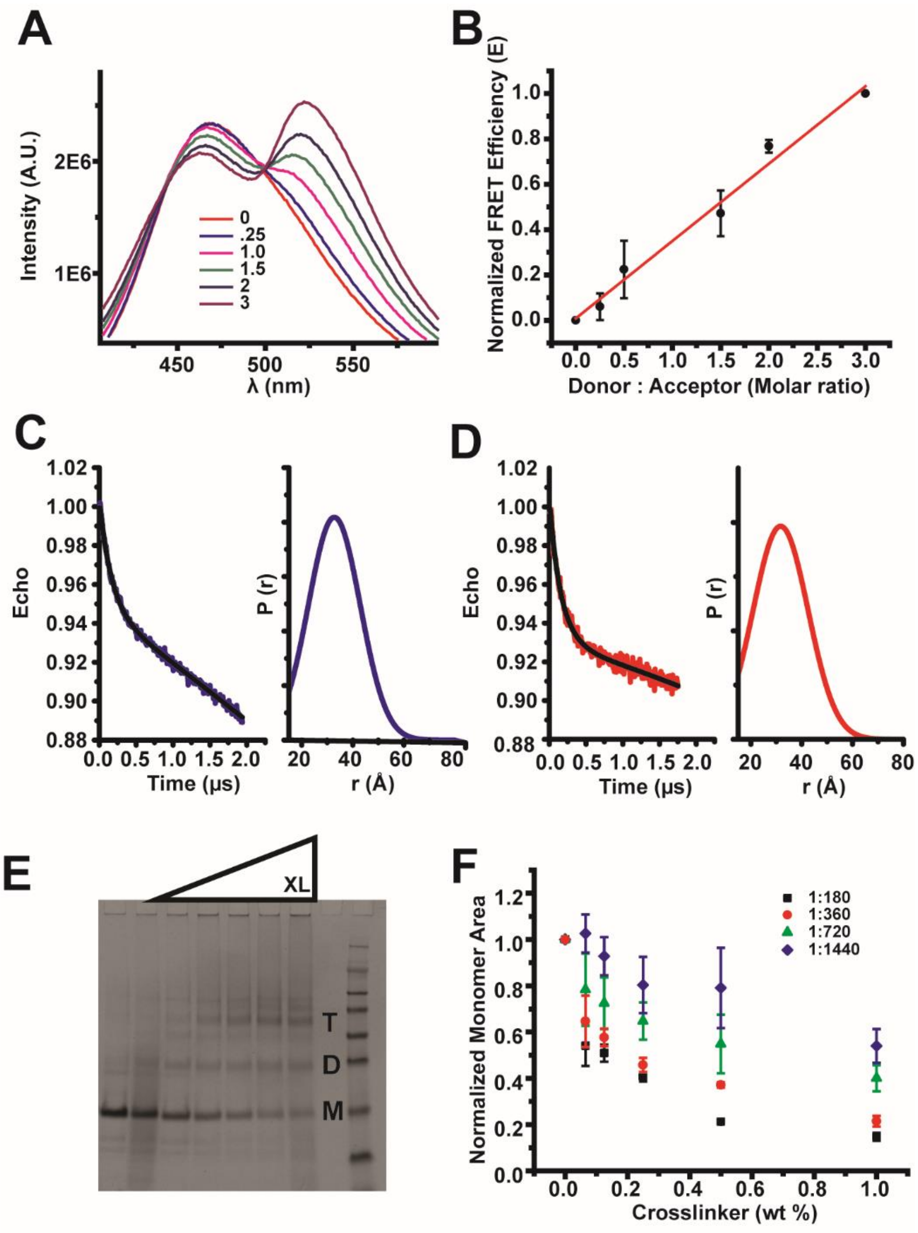

Figure 3.7. C99 forms oligomers in SCOR bicelles. *A) FRET spectra of IAEDANS-labeled C99 at a fixed protein to bicelle concentration ratio in the presence of increasing amounts of IANBD-labeled C99. The mole:mole ratios for each scan, in order of decreasing donor intensity, are (donor: acceptor): 1:0, 1:0.25, 1:1, 1:1.5, 1:2, and 1:3. B) Linear fit of normalized FRET efficiency from scans in A. Error bars represent the error in determination of the FRET transfer efficiency. C) DEER spectra of MTSL-labeled 200 µM C99 (L723C mutant) in 5 wt% SCOR bicelles, q=0.33. D) DEER spectra of MTSL-labeled 200 µM C99 (K699C mutant) in 5 wt % SCOR bicelles, q=0.33. E) Example SDS-PAGE (coomassie staining) of purified C99 following glutaraldehyde crosslinking of C99 in SCOR bicelles. Monomer, dimer, and trimer bands are indicated by M, D, and T respectively. F) Quantification of monomeric C99 from SDS-PAGE crosslinking experiments with C99, where the purification tag has been shortened and moved from the C to N terminus. Experiments were conducted with 50 µM C99 and various concentrations of SCOR bicelles in NMR buffer at 25 ° C n=3. The legend indicates the protein to lipid ratio.*

We were intrigued that crosslinking revealed that C99 can populate monomer, dimer, and timer oligomeric states in SCOR bicelles over a wide range of both C99-to-bicelle ratios and as detected over a wide range of glutaraldehyde concentrations. These results are fully consistent with both the FRET and DEER EPR results. Given the pitfalls that can accompany the interpretation of chemical cross-linking studies, we turned to one last method, native ion mobility – mass spectrometry (nMS) (296,297) to validate the chemical cross-linking results.

To our knowledge, bicelles of this complexity have not previously been used to study proteins via native mass spectrometry. We were pleased to observe that, with optimization of instrument parameters, intact C99 and C99 complexes could be readily liberated from SCOR bicelles. In agreement with previous experiments there are clear trends in the ion mobility – mass spectrometry data, which can be attributed to monomer, dimer and trimer oligomeric states of C99 liberated from SCOR bicelles (**Figure 3.8A**). As shown in **Figure 3.8B**, the C99 oligomer populations were found to be impacted by the protein-to-lipid ratio (here defined to include both detergent and lipid), as indicated by a transition from mostly trimer in 0.5 wt % bicelles to mostly monomer in 2.0 wt % bicelles under conditions in which the C99 concentration was held constant. The native MS results are in excellent agreement with the chemical crosslinking data as noted by the high monomer population seen by native mass spectrometry at a protein to lipid ratio of ~1:1200 (~30 µM C99 in 2 wt % bicelle), as supported by observation of inefficient crosslinking at ~1:1440 (~50 µM C99 in 4 wt % bicelle).

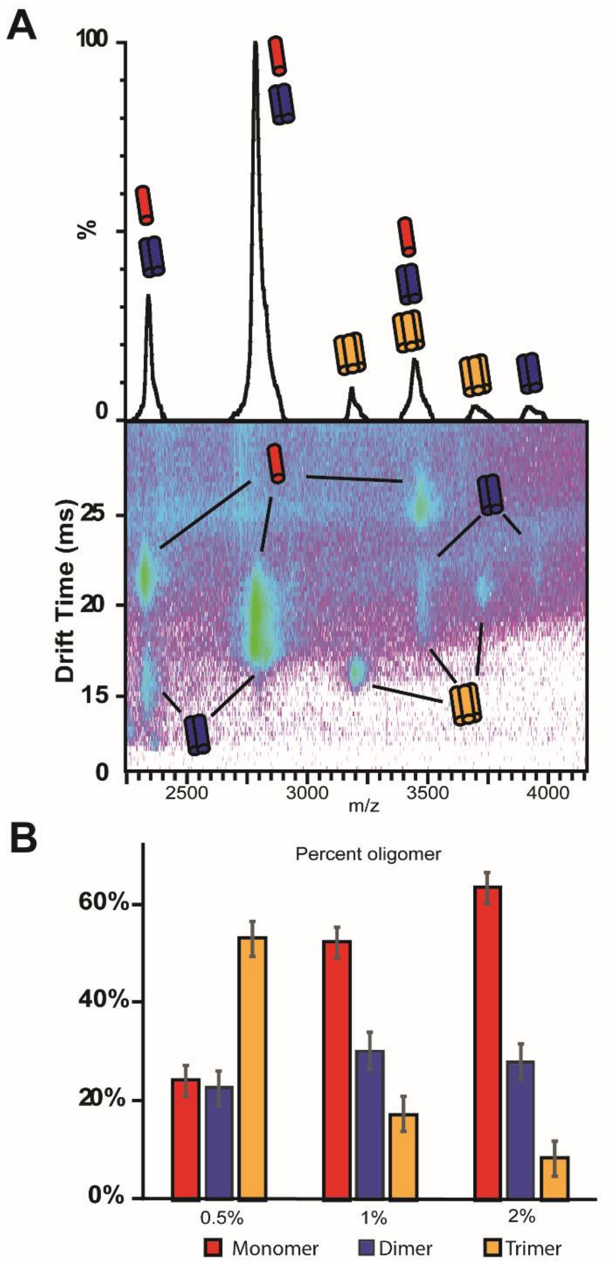

Figure 3.8. Determination of the oligomeric composition of C99 in SCOR bicelles with ion mobility – mass spectrometry (native mass spectrometry). *A) Mass spectra of C99 complexes liberated from SCOR bicelles (29 µM C99 in 1% wt/v SCOR bicelle q=0.33) show signals corresponding to the masses of monomer, dimer, and trimer C99 complexes (top). Ion mobility mass spectrometry data sets, which report on the mass, charge, and orientationally averaged size of an analyte, are used to deconvolute signals for which the mass-to-charge ratio alone is ambiguous between C99 complexes and monomer species (bottom). For example, the signal corresponding to 2822 m/z is observed to be comprised of monomeric and dimeric C99 from the ion mobility – mass spectrum shown. This approach also ensures that any lipid noise produced by dissociated bicelles is removed from analysis. B) The relative intensities*

of each deconvoluted species were used to calculate the percent of each oligomeric species for 29 µM C99 at 0.5%, 1%, and 2% w/v q= 0.33 SCOR bicelles.

DISCUSSION

SCOR Bicelles Represent a New Class of Bicelles

The development and characterization of SCOR bicelles described in this work provides the first isotropic and optically clear model membrane system that is rich in both SM and Chol. It was shown that the parent lipid mixture used for SCOR bicelle formation, 4:2:1 DMPC:eSM:Chol, forms bilayers that are more highly ordered than DMPC-only bilayers and exhibit a Lo to Ld phase transition temperature close to 30°C. It was observed that SCOR bicelles differ from conventional DMPC/DHPC bicelles both by being significantly thicker and in that the bilayer thickness of SCOR bicelles is nearly independent of the q (lipid-to-detergent mole) ratio. This confirms that the increased order of this membrane composition observed in bilayered lipid vesicles composed of 4:2:1 DMPC:eSM:Chol is maintained in SCOR bicelles. The lipid composition of mammalian PMs is, of course, vastly more complex than the lipid composition of SCOR bicelles. However, the inclusion of both Chol and SM in SCOR bicelles leads to increased order in their bilayer domain, representing a significant step closer to native PMs than conventional bicelles formed with glycerophospholipids only. It is interesting to note that some conventional isotropic bicelles have recently been shown to undergo lipid phase transitions (82) and that we are actively working to understand whether SCOR bicelles exhibit any such phase transitions. We are also planning to investigate whether there is any segregation of lipid types within the bilayered domains of SCOR bicelles or if the three types of lipid are uniformly mixed.

Among the 35 detergents tested (see **Table S3.1**), DDMB was seen to be the only detergent that was capable of solubilizing a range of lipid mixtures containing both Chol and eSM. Why β-n-dodecylmelibioside (DDMB) has this capability and not other detergents is not yet clear. It does seem instructive that, in contrast to DDMB, β-n-dodecylmaltoside (DDM) is not a good Chol/eSM co-solubilizer. This strongly suggests that the extra degree of conformational flexibility associated with the α(1→6) linker between the galactoside and glucoside units in the melibiose headgroup of DDMB is key to the effectiveness at co-solubilizing Chol and eSM.

Besides the DMPC-based 4:2:1 SCOR bicelles that were the focus of this paper, DDMB was found to be capable of solubilizing a range of other Chol and eSM-rich lipid mixtures that also appear to form SCOR-class bicelles, such as 4:1:1 POPC:eSM:Chol and 6:3:1 DPPC:eSM:Chol. This compositional flexibility is advantageous when trying to optimize conditions to suit a particular protein or method. This property will also enable studies to determine if either Chol and/or SM individually or only as a mixture modulates membrane protein structure and function (32,33)

SCOR bicelles in focus on a 4:2:1 DMPC:EggSM:Cholesterol lipid mixture but it must be noted that DDMB can dissolve a wide array of SCOR lipid compositions. SCOR bicelles can accommodate more complex common lipids such as POPC with 16:0-18:1 chains, compared to the 14:0 of DMPC. Diverse headgroups also are accommodated, for example: DMPC:DMPG:EggSM:Chol at a molar ratio of 2:2:2:1. DLS was used to confirm that these mixtures resulted in SCOR bicelles and that the size of the resulting bicelles were not drastically different than the main 4:2:1 mixture. Oddly enough, the lipid mixture of

POPC:POPG:EggSM:Chol at a 2:2:2:1 ratio was not able to form SCOR bicelles. SCOR lipid mixtures that failed to form bicelles resulted in either an obvious lipid precipitate or a transparent gel with a viscosity similar to honey. The normal 4:2:1 SCOR mixture can also form this transparent gel at q ratios >1. Generally, the higher the q ratio the lower the transition temperature from bicelle to transparent gel. Heating of SCOR bicelles past this gel phase would result in a cloudy white precipitate that would settle and become transparent again when cooled. The upper and lower phases were separated by an obvious change refractive index and did not remix without agitation. Both phases contained bicelle-sized isotropic particles, but the composition of each phase is unknown. I posit that the two phases could represent a separation into bicelles containing majority DMPC/EggSM vs DMPC/Chol since DDMB is not capable of solubilizing EggSM/Chol only mixtures. Low q bicelles used for structure determination did not have an obvious gel phase and heating was beneficial for redissolving trace lipid vesiculation that occurred when the SCOR bicelles sat at room temperature for a week or more. The above statements are practical tips for successful use of SCOR bicelles but also highlight the highly complex phase behavior available to SCOR bicelles. Traditional DMPC/DHPC bicelles at large q are capable of aligning in a magnetic field(73,74) and have been used to calculate residues dipolar couplings for protein NMR studies. As highlighted above, SCOR bicelles possess odd phase behavior and it is unknown if SCOR bicelles can align in a magnetic field. Future studies will be required to determine if these non-bicelle phases are biomedically useful or colloidal curiosities.

SCOR Bicelles Have an Idea Bilayered-Disc Morphology at Low q

It is generally accepted that classical DMPC/DHPC bicelles at q ratios between 2 and 6.5 form a true discoidal morphology with spatial separation between lipid and detergent, with mixtures at even higher q values adopting a “Swiss cheese”-like morphology. However, these “high q” bicelles are not commonly used in solution state NMR studies of integral membrane proteins because of their large size and/or because they fail to tumble isotropically, even sometimes aligning in strong magnetic fields.(52,53,69) Recent work has indicated that at low q ratios suitable for solution NMR—generally less than q = 0.7—DMPC/DHPC bicelles are discoidal but exhibit significant penetration of DHPC into the bilayer core and, as q is reduced, become akin more to classical mixed micelles than ideal DHPC-edge-stabilized bilayered discs. (67,76) Nevertheless, it should be noted that evidence also exists for near-ideal bicelles at low q. (78,281) In this work SAXS, SANS, and cryo-EM are all in accord that the SCOR bicelles contain an ideal discoidal morphology even at a q ratio of 0.33. As expected for ideal bicelles, the diameters of the bilayered discs increase as q is increased from 0.33 to 1.0, while maintaining a relatively stable bilayer thickness of ~5 nm. This consistency of membrane thickness with changing q implies minimal detergent penetration into the bilayer domain. We hypothesize that the higher order of the bilayered domain of SCOR bicelles relative to classical bicelles makes it more energetically unfavorable for cone-shaped detergents such as DDMB to partition into the bilayered domain, such that detergent molecules are efficiently relegated to the edges of the discs. In this regard, SCOR bicelles resemble nanodiscs (54,83) and lipodisqs/SMALPs, (84,85) where bilayer discs are edge-stabilized by either amphipathic proteins or amphipathic polymers that do not penetrate the bilayer interior.

SCOR Bicelles are Robust and Compatible with a Wide Array of Experimental Methods

It was observed in this work that SCOR bicelles are stable over a range of concentrations, pH, ionic strengths, and temperatures. This robustness makes SCOR bicelles well-suited for use as a membrane mimetic, because it will permit biophysical and biochemical investigations may require varying temperature, pH, or ionic strength to approximate the natural conditions of a membrane protein or to investigate the effects of these parameters on a membrane protein. We found, for example that SCOR bicelles are morphologically stable down to 0.25 wt % (total lipid + detergent) and only slightly increase in size upon further dilution to 0.125 wt %. Indeed, even at 0.06 wt % (for q = 0.33) we did not observe vesicle formation, although in this case it was not possible to obtain consistent sizes from sample to sample after dilution, likely due to errors in determining detergent concentration (relative to CMC) that become insignificant at higher bicelle concentrations. The working concentration range of classical DHPC and CHAPSO-based DMPC (and other) bicelles is much more limited because DHPC and CHAPSO have CMC values that are on the order of 40X higher than that of DDMB, such that vesicles begin to form when the bicelle concentrations are lowered below ~ 2 wt % (see(298)).

The stability and constancy of SCOR bicelles over a range of conditions enabled successful use of this medium in our studies of the human APP C99 protein using a range of biophysical and biochemical methods, including NMR, DEER, FRET, NMS, and chemical crosslinking. We anticipate that it should be possible to reconstitute many other membrane proteins in SCOR bicelles for analogous studies. Moreover, retention of the bilayered disc morphology even at low concentrations should allow SCOR bicelles to be used in studies that require a high level of dilution, such as cryo-EM. Cryo-EM has recently yielded spectacular progress in determining high resolution structures of large membrane proteins.(299) The authors are unaware of any examples of membrane protein structures being determined in bicelles using cryo-EM, likely because conventional bicelles vesiculate when diluted to concentrations suitable for rapid sample vitrification. The fact that we were able to directly image SCOR bicelles using cryo-EM methods suggests they are suitable model membranes in which to solubilize larger membrane proteins and complexes for cryo-EM analysis.

The Structure of C99 in SCOR Bicelles Exhibits Some Unexpected Features

The structure of the APP C99 protein or transmembrane domain-containing fragment has been examined by a number of labs in various conventional model membrane systems. (186,187,204,205,229,230,232,235,240,241,271-274) This previous body of work made C99 an ideal test protein for study in SCOR bicelles. Full length C99 in SCOR bicelles exhibits a similar secondary structure as seen in previous studies, where it has been shown to exhibit a disordered water-exposed N-terminus followed by a short surface-associated amphipathic helix linked via a short loop to the transmembrane domain. The helical transmembrane segment of C99 in SCOR bicelles is slightly longer than in DMPC/DHPC bicelles, (187) but is similar in length to what was previously seen in DHPC-based POPC/milk sphingomyelin bicelles. (187) This result is reasonable in light of the increased thickness of SCOR bicelles relative to DMPC/DHPC bicelles and because DHPC/POPC/milk SM bicelles are also thicker (POPC has longer fatty acids than DMPC and the most common fatty amide chain in milk SM is 23 carbons long, *https://avantilipids.com/product/860063*). Following the TMD of C99, there is a ~35 amino acid random coil intracellular loop followed by a C-terminal surface-bound amphipathic helix.

While the secondary structure of full length C99 in SCOR bicelles is similar to what has previously been observed, there were three aspects of its structure in SCOR bicelles that are surprising. The first is the fact that nearly all previous studies of C99 have, variously, observed that C99 is either a monomer, a dimer, or a mixture of monomer and dimer, depending on sample conditions. In contrast, the results of this work indicate that C99 in SCOR bicelles appears to populate an equilibrium mixture of monomer, dimer, and trimer. This observation is not completely unprecedented, as Higashide et al. previously observed that following mixture of mammalian CHO cells with the non-ionic detergent DDM, C99 was seen to run as a mixture of monomer, dimer, and trimer on blue native PAGE, results that are strikingly similar to those of this paper. (215) We do not know why SCOR bicelles promote formation of C99 trimer along with monomer and dimer, but we do note that a common feature of the Higashide study and that of this paper is the presence of Chol and SM in the C99 samples. Recent computational work by Sun et al. suggested that the C99 TM dimer is less stable in a raft-like environment but did not look at trimer. (239) Of course, the fact that C99 populates three oligomeric states in SCOR bicelles is vexing from a practical standpoint, as it means that most of the C99 samples examined in this work involve a mixture of three different forms of the protein, hindering attempts to interpret the data, especially the NMR data, in terms of a single structural state. At the required protein concentration for NMR, C99 exists in a dynamic mixture of oligomeric states, which—along the relatively large bicelle size—is likely the cause for the additional NMR signal broadening compared to the DDMB micelles environment.

A second important structural observation for C99 in SCOR bicelles concerns the *location(s)* of its oligomeric interface(s). There has previously been much interest in the dimerization of C99 due the possibility that dimerization is linked to its cleavage (either promoting or hindering amyloid β (Aβ) production). (211,213,290,300-303) Previous biophysical studies in which dimerization of C99 or of derived TMD-containing fragments have usually pointed to $G_{700/704}XXXG_{704/708}$, (210,214,240-242) $G_{709}XXXA_{713}$, (230,243) or both (233,234,282) motifs located in the C99 TMD as being the location of the dimerization interface. (210,211,214,240-243,282,303) Studies highlighting the GXXXA oligomerization motif often additionally implicate the following TV_{715} residues. (230,233,234,243,282) These previous experimental studies were often conducted in conventional model membranes bereft of Chol and SM and often did not use full length C99. However, in the present work with SCOR bicelles, paramagnetic probe accessibility studies indicated that the oligomer interface is located in the cytosolically disposed C-terminal half of the TMD, roughly spanning residues 710-716. The fact that C99 populates both dimer and trimer states in SCOR bicelles makes exact identification of the specific residues involved difficult, but our results are very clear that the upper end of the TMD containing the GXXXG motifs is not involved. (230,233,234)These conclusions are strongly supported by previous biochemical (Tango assays) and biophysical (BRET) studies of C99 oligomer formation (assumed to be dimer) in mammalian cells. (238) In that study, Yan et al. showed that C99 oligomerization is mediated by residues 714-717, in agreement with the results in SCOR bicelles. A computational work study of the C99 TM dimer in a raft-like environment also found the dimer is mediated by residues V711 and V715, (239) in close agreement with our SCOR bicelle data. The fact that the oligomerization interface for C99 in SCOR bicelles appears to be similarly located to the interface observed in mammalian PMs supports the notion that SCOR bicelles may be a better mimic for mammalian plasma membranes than conventional model membranes.

A third surprising structural observation made in this paper is that there is a segment within the long cytosolic loop of C99 (resides 735-745, based on full length APP numbering), that seems to populate a highly dynamic random coil ensemble of conformations and yet is both inaccessible to paramagnetic probes and also resistant to backbone amide-water hydrogen exchange. N-terminal residues 673-678 indicate a similar phenomenon, albeit to a lesser degree and this region is likely sampling beta sheet secondary structure as seen in previous simulations (235) and known amyloid beta structure. (304) We hypothesize that these results reflect participation of these segments in a dimer and/or trimer interface that is predominantly random coil but can sample alpha helical and beta sheet states. (235) It should be added that previous solution NMR studies of a soluble APP intracellular domain (AICD) fragment found that residues $V_{742}TPEER_{747}$ of AICD forms a transient N-terminal helix capping box(287,288), hinting at a predilection of this segment for complex dynamics. Moreover, the non-conventional nature of the dynamic structure formed by this segment is likely reflected by the fact that the PEER segment yielded only broad and assignable resonances in our previous NMR studies of monomeric C99 in detergent micelles. (186,187,232)

While unusual, the formation of non-canonical tertiary or quaternary structure seen for the C-loop 735-745 segment is not unprecedented. Borgia et al recently reported a high-affinity heterodimeric structural ensemble where two oppositely charged IDPs, histone H1 and its nuclear chaperone, the prothymosin α protein, interact while retaining structural disorder. (289) They report a lack of peak dispersion in the HSQC spectrum upon complex formation and no obvious indication of secondary structure in the Cα chemical shifts, both classic indications of random coil. We find that the C99 C-loop also possesses these classic random coil-like traits, and yet paramagnetic and hydrogen exchange experiments indicate the presence of structure for residues 735-745. The C99 C-loop does not contain the high charge densities found in Borgia et al; however, it is likely that the transmembrane oligomerization facilitates co-localization of the C-loop interfaces. Our homo-oligomeric C99 C-loop interface and the work of Borgia et al on a hetero-dimeric system appear to be similar in nature as both represent oligomeric interfaces that lack classical structure.

Many proteins are known to interact with the intracellular portion of APP/C99 and we posit that this paradoxical C-loop interaction may play a role in a regulatory mechanism that modulates interactions of the 735-745 segment with cytoplasmic binding partners such as caspases and trafficking adaptor proteins. (305) Phosphorylation in the C-loop oligomeric interface at T743 has been shown to impact Aβ production (284,285,306) and it will be interesting to explore how the unstructured and dynamic oligomeric interfaces impacts its interaction with other proteins and how this impacts Aβ production. A summary of the oligomeric interfaces and dynamic oligomeric states found for C99 in SCOR bicelles is highlighted in **Figure 3.9**.

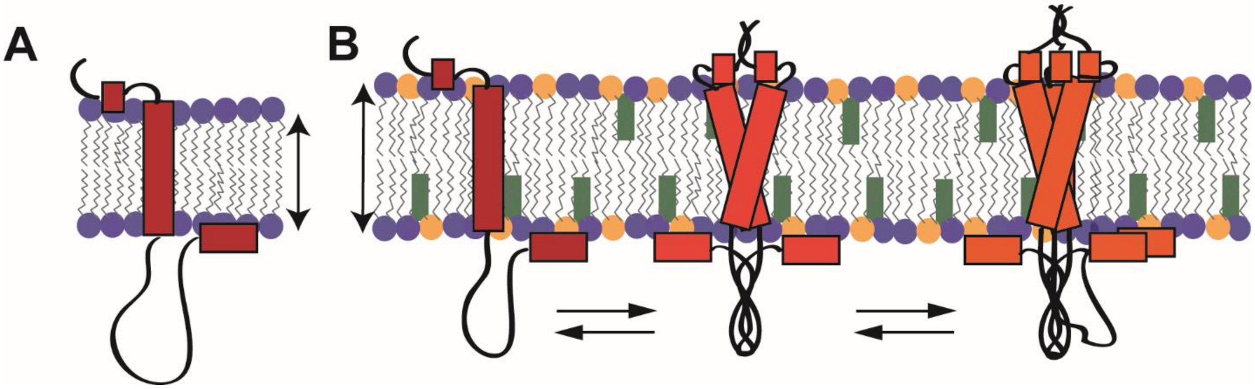

Figure 3.9. Schematic model for C99 in SCOR Bicelles. *A) Model for monomeric C99 based on previous studies of C99 in conventional DMPC/DHPC bicelles. (186) B) C99 in SCOR bicelles populates a dynamic mixture of monomer/dimer/trimer. Two oligomeric interfaces were identified, one in the cytosolic half of the TM and another in the disordered C-loop. The double headed arrow highlights that the bilayer thickness of the SCOR lipid bilayer shown in B is thicker than the DMPC-only bilayer shown in A (not to scale). The blue and orange lipids symbolize DMPC and eSM respectively. Green blocks represent Chol.*

Conclusions

Here, we introduced a new phosphatidylcholine bicelle platform that is eSM and Chol-rich (SCOR). The bicelles are ~5 nm thick and are edge-stabilized by a DDMB annulus. We found the SCOR bicelles to be well-behaved, even at concentrations as low as 0.25 % w/v, making them highly suitable for cryo-EM studies. SCOR bicelles are stable over a wide range of pH, ionic strength, concentration, and temperature, such that they are well-suited for implementation of a wide range of biochemical and biophysical techniques, as demonstrated in this manuscript on the well-characterized protein C99. Moreover, the detergent used to form SCOR bicelles, DDMB, can support a wide array of other Chol and eSM-rich lipid mixtures, potentiating future studies to examine how variations in lipid composition impact membrane protein structure and function. Our studies of the C99 protein in SCOR bicelles indicate notable differences in the structure and dynamics of this important protein relative to what had previously been documented from studies of C99 in micelles, conventional bicelles or glycerophospholipid vesicles. Moreover, the differences observed for the C99 oligomeric interfaces present in SCOR bicelles seems to closely approximates the oligomeric interface documented in recent studies of the protein in mammalian plasma membrane. This raises the possibility that the presence of abundant Chol and sphingolipids in membranes may sometimes significantly alter the structure and dynamics of some membrane proteins, and that SCOR bicelles may be a closer mimetic for some biological membranes than conventional model membrane systems.

IV. Recombinant SARS-CoV-2 envelope protein traffics to the trans-Golgi network following amphipol-mediated delivery into human cell.

This chapter is adapted from Recombinant SARS-CoV-2 envelope protein traffics to the trans-Golgi network following amphipol-mediated delivery into human cell. *Published in Journal of Biological Chemistry and has been reproduced with the permission of the publisher Hutchison JM, Capone R, Luu DD, Shah KH, Hadziselimovic A, Van Horn WD, Sanders CR. Recombinant SARS-CoV-2 envelope protein traffics to the trans-Golgi network following amphipol-mediated delivery into human cells. J Biol Chem. 2021 Jul 5:100940. doi: 10.1016/j.jbc.2021.100940. Epub ahead of print. PMID: 34237302; PMCID: PMC825665.*

Introduction

The severe acute respiratory syndrome 2 virus (SARS-CoV-2) became a focal point of science and society in 2020. It is to be hoped that the ongoing vaccine development and delivery programs will soon allow the world to return to an approximation of normalcy (106,107). However, previous coronavirus (CoV) epidemics, including Middle East respiratory syndrome (MERS) (110) and SARS (111) from 2002-2003 foretell that future CoV zoonotic events (109) are likely to afflict humankind. Fundamental studies of the molecular underpinnings of CoVs may help to mitigate the current and future pandemics.

Within CoVs, there are four critically conserved structural proteins (307,308), each of which is of possible therapeutic importance due to their critical functions (309). Among these is the envelope (E) protein. The E protein is a single-pass transmembrane protein whose roles in pathogenesis are incompletely understood (128). However, its importance is highlighted by cellular studies showing that the CoV E and M proteins alone are sufficient to produce a budding virus-like particle (VLP) (119-121). Moreover, deletion of E dramatically lowers viral fitness (310-312) and growing evidence suggests that E is directly responsible for acute respiratory distress syndrome (ARDS) occurring in conjunction with CoV infections (313). E is highly expressed in infected cells, but only a small fraction is incorporated into mature viral particles, implying functions beyond its role as a mature capsid structural protein (122). Supporting this idea, E is known to populate both monomer and oligomer forms *in vivo* (133). Most biophysical measurements have focused on the homopentamer form that functions as a cation-selective ion channel (134-136,144), which is analogous to a well-studied and validated drug target, the influenza M2 protein (137,138).

A distinct feature of coronavirus assembly is that their nascent particles (314) accumulate in the *trans*-Golgi network (TGN) (124) before a unique cellular egress pathway via deacidified lysosomes (126). The E protein is critical to viral maturation (119,122,149). Localization of SARS E protein to these membranes is remarkably stringent, likely a consequence of Golgi-targeting motifs present in E protein (149). Since E functions in multiple roles that are critical to viral fitness (129-131), it is desirable to develop methods to further characterize key E-dependent pathogenic mechanisms. Current methods to study the E protein in mammalian cells are reliant on transfection of genetic material encoding the protein into cells and its subsequent transcription and translation. Here, we sought to develop a robust method for exogenous delivery of purified SARS-CoV-2 envelope protein (S2-E) into human cell lines to enable chemical biological methods for studies of S2-E function and possibly to potentiate novel therapeutic approaches.

Results and Discussion

We developed a straightforward bacterial expression and purification protocol that yields ~100 µg per liter of culture of 90-95% pure full-length S2-E under conditions in which it is bereft of detergent and lipid, with its aqueous solubility being maintained by complexation with the zwitterionic amphipol PMAL-C8 (95,315) (**Figure S4.1 and Appendix 3**). This purification protocol has been streamlined to a single gravity column and does not require semi-automated chromatography or an ultracentrifuge. Once purified into lipid/detergent-free amphipol solution, the S2-E/amphipol complexes remain stable and soluble in aqueous solution even following removal of excess un-complexed amphipols. Amphipols are a class of amphipathic polymers that exhibit weak detergent properties, in that they can solubilize and stabilize membrane proteins but cannot solubilize or even permeabilize membranes (56,93). Additionally, some amphipols are well tolerated by animals (316) and have been used in vaccine development (93,94) because at least some forms do not elicit the production of anti-amphipol antibodies (57).

Planar lipid bilayer electrophysiology was used to test if amphipols can deliver the S2-E protein to a membrane environment to form ion channels without otherwise disrupting the lipid bilayer (**Figure 4.1*A***). It was seen that amphipol-based S2-E delivery resulted in ion channel activity that is consistent with previous SARS-CoV-1 E (317) and preliminary S2-E (318) channel measurements in terms of current amplitudes, sodium cation selectivity, and open probabilities. (**Figures 4.1*B,C*, and S4.2, and Appendix 3**). The S2-E-dependent currents and similarity to other planar bilayer measurements support the idea that S2-E is released spontaneously from amphipols into membranes. The bilayer integrity during amphipol delivery and exposure was monitored through membrane capacitance measurements. The bilayers remained stable throughout the recordings with an average value of 58 ± 3 pF. These results demonstrate that recombinant S2-E can be delivered into pre-formed lipid bilayers using amphipols, where the protein not only inserts into the bilayers, but also retains ion channel function, without significantly compromising the bilayer integrity.

We next tested whether S2-E can be delivered from amphipol complexes to the membranes of human cells. To this end, S2-E was irreversibly tagged at one of its three native cysteine residues with fluorophores nitrobenzoxadiazole (NBD) or Alexa Flour 488 (AF488). The native cysteine residues do not form disulfide bonds *in vivo (147)* and are not required for ion channel formation (143,319), although substituting two or three cysteines to alanine results in reduced viral fitness (147). NBD-labeling S2-E at roughly one cysteine site per protein did not significantly lower the channel open state probabilities (P-values of 0.125 at -100 mV and 0.055 at 100 mV) and did not change channel conductance properties (**Figure S4.3**). (320,321). The solvatochromic properties of NBD (320) were better for observing the deposition of S2-E on the plasma membrane at early time points (**Figure S4.4**) while the environment insensitivity of AF488 (321) was more suited for S2-E colocalization experiments. No significant difference was observed between S2-E labeled AF488 or NBD when quantifying colocalization (**Figure S4.5**).

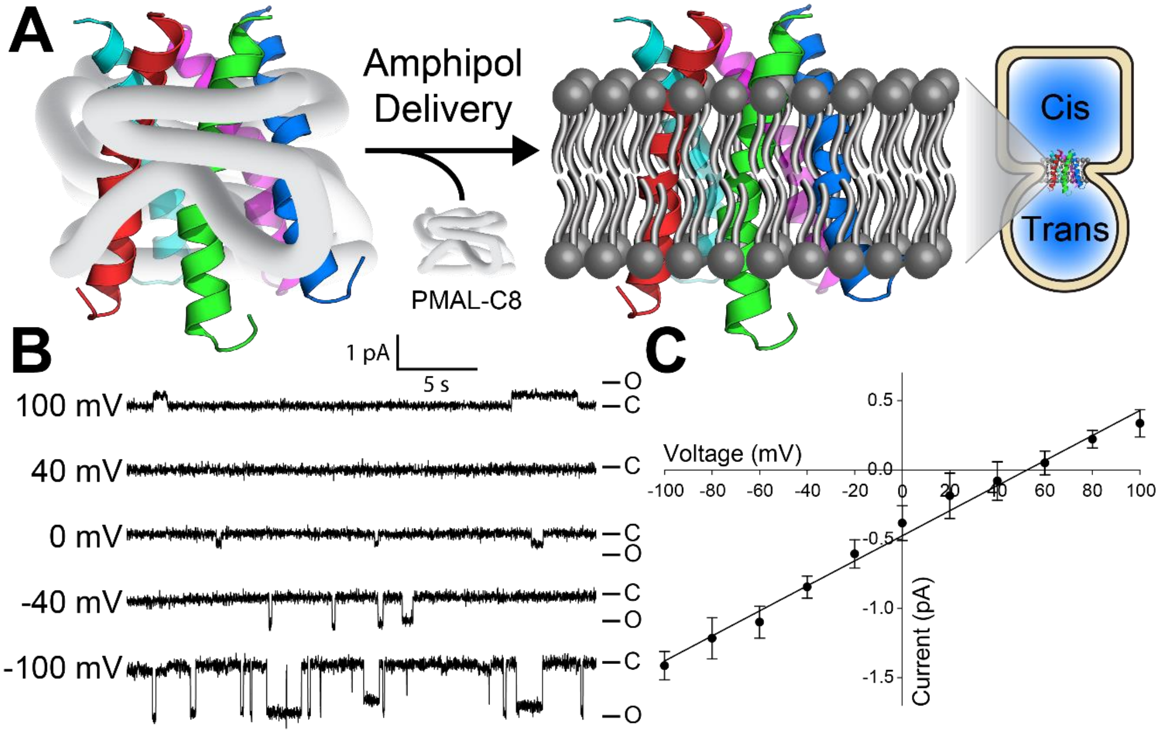

Figure 4.1. Functional delivery of SARS-CoV-2 envelope protein from amphipol complexes to planar lipid bilayers. (A) *Schematic of SARS-CoV-2 envelope protein (S2-E) delivered using amphipols for membrane protein insertion into planar lipid bilayers.* ***(B)*** *Representative single-channel current recordings of PMAL-C8 amphipol-delivered S2-E as a function of transmembrane electrical potential showing ion channel activity in POPC:POPE (3:1) planar bilayers, where S2-E fluctuates between closed (C) and open (O) states.* ***(C)*** *The S2-E current-voltage relationship identifies a conductance of 9.0 ± 0.3 pS and a reversal potential of 53 ± 3 mV in an asymmetric NaCl buffer, indicative of cation selectivity. Data represent three replicates. Error bars are standard deviation from the three distinct amphipol delivery experiments on different days (For open state probabilities see* ***Figure S4.2****). Single-channel current recordings using S2-E-NBD also show similar conductance, see* ***Figure S4.3****. The trans-compartment is the chamber with the command/input Ag-AgCl electrode whereas the grounded chamber is the cis-compartment. Planar bilayer control experiments in which PMAL-C8 only was added (no S2-E), did not exhibit channel activity at amphipol concentrations 1x or 50x relative to those used in these S2-E and S2-E-NBD planar bilayer experiments.*

As shown in **Figures 4.2 and S4.6**, the S2-E-NBD protein was delivered from amphipol complexes to HeLa cell membranes, with all cells exhibiting NBD signal within 30 min (**Figure 4.2*B***). **Figure 4.2*C-F*** shows the 8 hour progression of the S2-E-NBD protein from the plasma membrane to a predominately perinuclear intracellular location. After 16-18 hours nearly all the S2-E was observed in the vicinity of the nucleus, with a clear focal area on one side of the nuclear compartment (**Figure 4.2*G,H***). Delivered S2-E was typically more diffuse at early time points but becomes punctate as it traffics towards the perinuclear space.

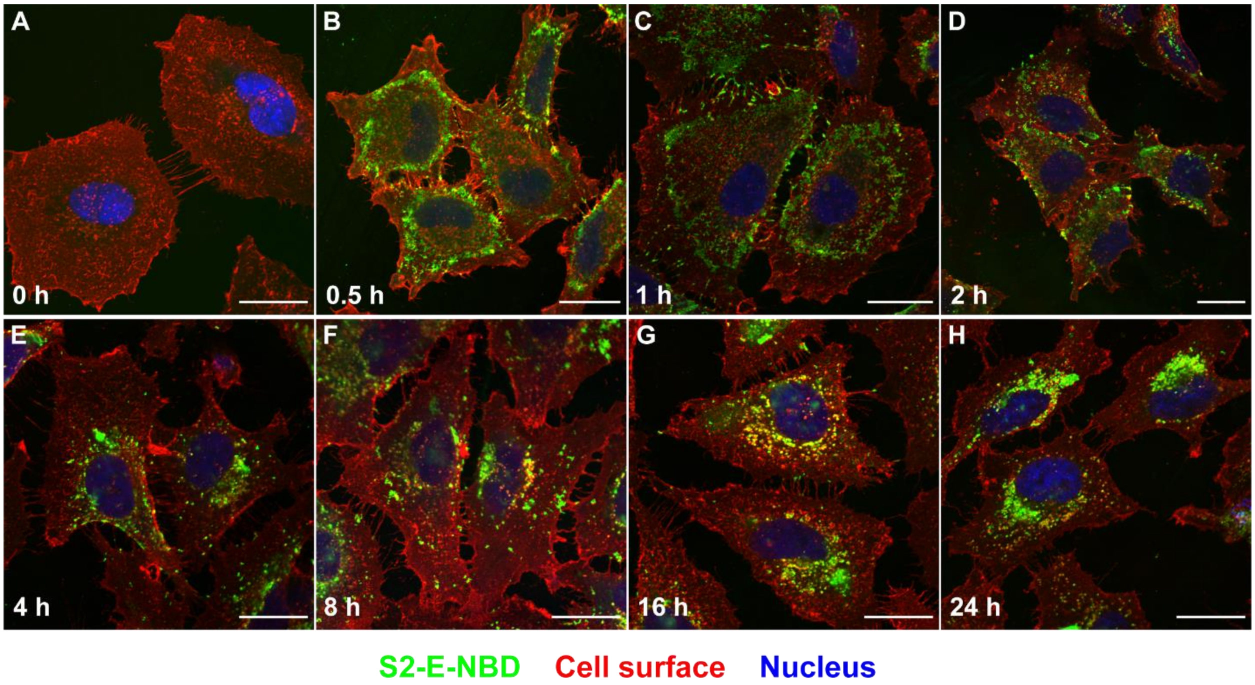

Figure 4.2**. **Membrane incorporation and uptake of amphipol delivered SARS CoV-2 E protein by cells and subsequent intracellular trafficking of the protein.** Representative confocal microscopy images of HeLa cells at various time points following treatment with amphipol-complexed 2.5µM S2-E labeled with NBD (S2-E-NBD). Color markers are: green, S2-E-NBD; red, cell membrane (we used WGA-AF555; wheat germ agglutinin or WGA is an N-acetyl-glucosamine and sialic acid binding lectin, here conjugated to AF555; blue, cell nuclei (we used DRAQ5, a cell permeable, far-red emitting fluorescent anthraquinone DNA dye, that stains dsDNA). (A) is the untreated (0 µM) sample and 0 h time point, (B) is cells 0.5 h after treatment, (C) is following 1 h, (D) 2 h, (E) 4 h, (F) 8 h, (G) 16 h, and (H) 24 h. The S2-E-NBD signal migrates from the cell plasma membrane (see panel B) toward the perinuclear space (see panels G and H). Time course experiments using the same cell markers were independently repeated 3 times using 3 different S2-E-NBD preparations. All scale bars are 25 µm. See further details **Appendix 3** and **Figure S4.6.

The amount of S2-E signal in cells was dependent on the applied amphipol/S2-E dose (**Figures S4.7**). It was verified that NBD did not drive S2-E internalization and perinuclear aggregation (**Figure S4.7**). To ensure that we were microscopically tracking intact NBD labelled S2-E (S2-E-NBD) instead of dye freed from full length S2-E by degradation, we confirmed S2-E localization following cell fixation and permeabilization with a polyclonal anti-S2-E antibody (**Figure S4.5**). We observed consistent strong co-localization between S2-E labeled with either AF488 or NBD and the polyclonal anti-E signal. Cysteine-reacted NBD was used as an S2-E degradation control and was found to stain all cellular membranes (**Figure S4.8**). Therefore, delivered S2-E is not extensively degraded during the 24-hour treatment since the level of anti-S2E and S2-E-dye colocalization remained strong at both short and long time points. (**Figure S4.5**). We observed unspecific binding of the anti-E antibody in the nucleus and determined the dye-tagged S2-E to be a better reporter of S2-E localization. (**Figure S4.5**) While amphipols have previously been reported to deliver select membrane proteins to artificial lipid bilayers (92,95), this study represents the first use of amphipols to deliver a protein to mammalian cells. Elucidation of the pathway(s) taken by the S2-E protein to dissociate from its soluble amphipol complex to then insert into the membrane and adopt a trans bilayer configuration will require further study.

To ensure that the observed S2-E delivery and perinuclear trafficking was not unique to HeLa cells, we also examined possible delivery of S2-E from amphipol solutions into SW1573 human alveolar cells, a COVID-19-relevant cell line (322). We observed (**Figure S4.9**) that S2-E is indeed taken up by these cells and similarly undergoes surface-to-perinuclear retrograde trafficking as seen in HeLa cells.

The fact that delivered S2-E retrograde traffics proximal to one side of the nucleus (**Figure 4.2*G,H***) is consistent with its localization at or near the Golgi compartments. To gain further insight into the final cellular location of S2-E, we used organelle-specific monoclonal antibodies and wheat germ agglutinin (WGA) to pinpoint the locations of the *cis*- and *trans*-Golgi, TGN, early endosomes, lysosomes, endoplasmic reticulum (ER), aggresomes, and ERGIC relative to delivered S2-E in the perinuclear space at late timepoints. In agreement with **Figure 4.2*B-E***, S2-E does not strongly colocalize with markers of ER/Golgi space at early time points and takes 18-24 h for the protein to accumulate in the perinuclear space via retrograde trafficking (**Figure 4.2*G,H***). At 18-24 h after initial delivery, S2-E was not found in the ER, ERGIC, or *cis*-Golgi (**Figures 4.3*D-F* and S4.10-S4.12**). Instead, S2-E was seen to partially overlap with the *trans*-Golgi marker Golgin 97 (323) in the area surrounding the Golgi, but not within the Golgi (**Figures 4.3*A-C* and S4.9**).

The partial co-localization of S2-E with the *trans*-Golgi and exclusion from the *cis*-Golgi indicated that delivered S2-E ultimately resides in the TGN and associated vesicles. WGA is an N-acetyl-glucosamine and sialic acid binding lectin (324,325) that is often used in conjunction with fixed cells to stain the plasma membrane (326). In live cells, WGA is rapidly endocytosed to the Golgi and specifically accumulates in the endocytic TGN (**Figure S4.13**) (327-330). We observed strong colocalization between WGA and delivered S2-E between 16-24h, indicating that S2-E accumulates in the TGN (**Figures 4.3*G-I* and S4.10***)*. WGA and S2-E travel to the TGN independently and WGA does not induce S2-E TGN colocalization. There is significant bi-directional traffic between the TGN and endosome/lysosome systems (331) and we wanted to determine if delivered S2-E was accumulating in endosomes and lysosomes at later timepoints. We did observe some colocalization of S2-E with early endosome marker EEA1 (332) at late timepoints (**Figure S4.14**). Additionally, we observed colocalization of S2-E with late endosomes and lysosomes as indicated by the overlap in S2-E and LAMP1 signals (**Figure S4.15**) (199). Perinuclear S2-E containing LAMP1 positive vesicles were enlarged while peripheral LAMP1 positive vesicles remained unchanged.

The localization of delivered S2-E to swollen TGN vesicles is likely disease relevant given that progeny coronaviruses are known to accumulate in the TGN before cellular egress (124,140). Lysosomes have long been associated with coronavirus infection (333) and recent work showed that coronavirus is unique in its use of deacidified lysosomes for cellular egress (126). In line with these ideas, E increases the pH of the Golgi (140) and TGN (139), apparently to protect the spike protein from premature processing. E also has been shown to slow cellular secretory pathways (152).

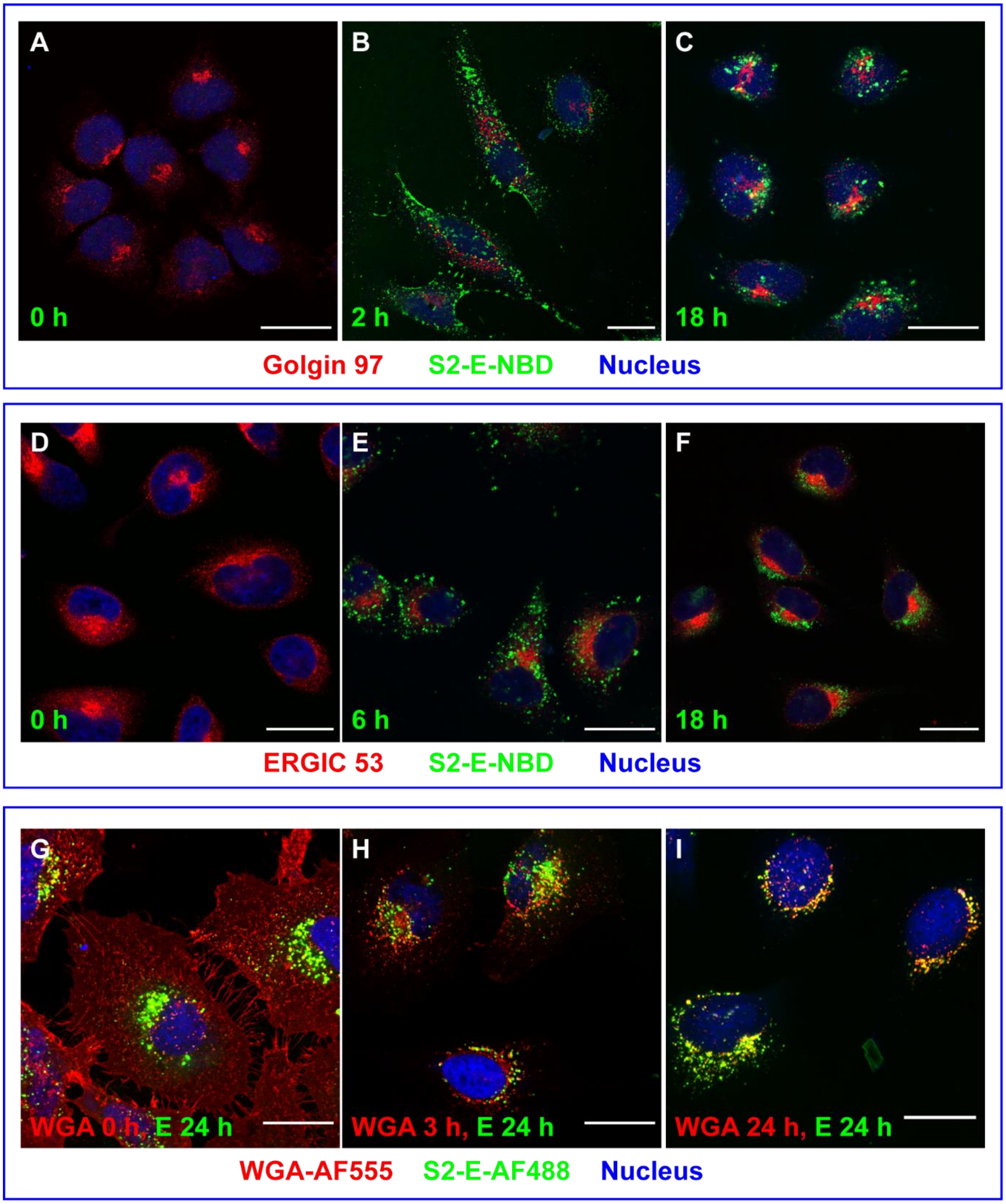

Figure 4.3. SARS-CoV-2 envelope protein traffics to the perinuclear space and accumulates in the trans Golgi network (TGN). *Representative confocal microscopy images showing HeLa cells treated with 2.5 μM S2-E labeled with either NBD or AF488. Panels* ***A-C*** *and* ***D-F*** *show S2-E localization relative to the Golgi (A-C) and ERGIC (D-F) as a function of increasing S2-E treatment time. Panels* ***G-I*** *shows cells that were treated with S2-E-AF488 for 24h and labeled with WGA-AF555, the latter added either: (i) 24 hours*

after S2-E-AF488 treatment followed by immediate fixation (G, 0 h of WGA), (ii) 21 hours after S2-E-AF488 treatment followed by an additional 3 hours of WGA incubation followed by fixation (H, 3 h of WGA), or (iii) at the same time (0 h) S2-E-AF488 was added to the cells followed by 24 hours of incubation followed by fixation (I, 24h of WGA). Notice how WGA accumulates and colocalizes with S2-E over time. Note how WGA moves to the perinuclear space at a faster rate than S2-E; i.e. compare 3 h WGA (H) versus S2-E at 2 h (B) or 6 h (E). Color scheme: green, S2-E labeled with NBD (A-F) or AF488 (G-I); blue is the fluorescent dye DRAQ5, marking the cell nucleus; red, in panels A-C, is from an antibody to Golgin-97, a Golgi marker; in panels D-F, red is from an antibody to ERGIC-53, a defining marker for the ERGIC region and panels G-F is from WGA-AF555, a common marker for plasma membrane for fixed cells. Panels A and D are the control samples where cells were not treated with S2-E-NBD. Panels A-I were treated with labeled S2-E for the time indicated in green fonts, while WGA in panels G-I was added for the stated time shown in red fonts, right before cell fixation. Co-localization analysis of panel I between WGA-AF555 and S2-E-AF488 channels result in Pearson correlation coefficients (> 0.7, ***Figure S4.5****). All experiments shown were repeated 3 times in panels A-F were using 3 different E-NBD preparations, while in panels G-I twice with S2-E-NBD and once with S2-E-AF488. All three repeats show comparable behaviors. Scale bars are 25 µm. Further details in* ***Appendix 3 Figure S4.10****.*

It is likely that the Golgi-localization motifs (149) in S2-E drive its retrograde trafficking in a way closely related to the mechanism that facilitates E protein perinuclear retention during viral infection. However, we also considered the possibility that amphipol-mediated extracellular delivery of S2-E triggers ER stress and unfolded protein response (UPR)-related retrograde trafficking, leading to deposition of S2-E in perinuclear aggresomes. Aggresomes are ordered protein aggregates that form following transport of certain proteins along microtubules by dynein to perinuclear microtubule-organizing centers (334) and are often detected by the formation of vimentin cages (334). We looked but did not observe the induction of vimentin cages with our delivered S2-E (**Figure S4.16**). The lack of aggresome formation suggests that our delivered S2-E does not induce an obvious UPR stress, likely because the S2-E accumulates in the TGN and not in the ER (335-337).

We did not observe an obvious enrichment of S2-E in the ERGIC or ER compartments before the accumulation in the TGN. However, it is important to note that we focused on identifying the final location of externally delivered S2-E and not its location in earlier timepoints. Additionally, further studies will be required to understand by which pathways S2-E is trafficked to the TGN.

Conclusions

We have shown that the S2-E protein can be stripped of lipid and detergent and purified into aqueous solutions in which its solubility is maintained solely by complexation with amphipols. The protein can then be delivered to lipid bilayers, in which the protein spontaneously inserts into the membrane to form ion channels. As proposed in **Figure 4.4**, addition of the S2-E protein to living human cells results in plasma membrane integration and subsequent retrograde trafficking deep within the cell, ultimately occupying enlarged LAMP1 positive vesicles derived from the TGN, which are believed to be critical for coronavirus egress and pH dysregulation. The S2-E protein-to-cells approach established by this work should be exploitable as a route to delivering chemically modified full length S2-E to cells in culture or possibly even to cells under physiological conditions. This capability enables a wide range of chemical biological tools to explore the biological function of this protein or to test whether chemical warheadarmed S2-E can play the role of a Trojan horse to interfere with SARS-CoV-2 replication, potentially as an anti-COVID therapeutic or prophylactic. The results of this work also establish a general paradigm for using amphipols to deliver membrane proteins to living cells, although whether numerous other membrane proteins can be successfully delivered using this approach remains to be explored.

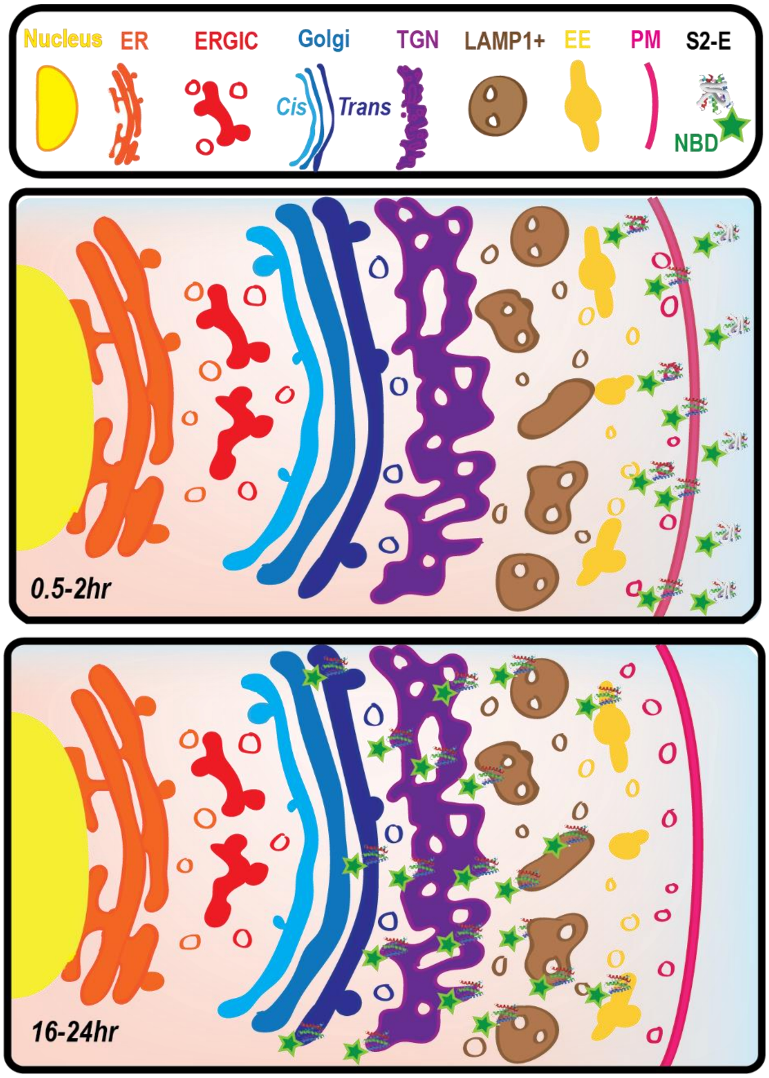

***Figure 4.4**. **Schematic of amphipol-delivered S2-E and its localization within HeLa cells at early and late timepoints.** Top Panel) Legend of cellular markers tested for colocalization with S2-E. Middle Panel) S2-E is mainly localized on the plasma membrane at early time points. Bottom Panel) After 16-24 hours, delivered S2-E is enriched within the TGN and LAMP1 positive vesicles. S2-E is also partially found within early endosomes and the trans-Golgi. Organelles and S2-E are not to scale.*

V: Purification of Membrane Proteins Bereft of Membrane Mimics

Introduction

Integral membrane proteins (IMPs), by definition, contain highly hydrophobic transmembrane (TM) domains that are inserted in the lipid bilayer *in vivo* and have very limited solubility in aqueous environments. In order to prevent IMP aggregation, *in vitro* experiments use amphipathic membrane mimetics to stabilize the TM domains (55,63,75,338). Detergents are the most commonly used mimic due to their low cost and ease of use (47,63,339), but IMPs are only solubilized by detergents when they are surrounded by a detergent micelle (340,341). Detergent micelles form when the detergent concentration is above its critical micelle concentration (CMC), which reflects the free energy of micellization (342,343). Membrane protein stability and oligomerization are sensitive to the protein: micelle ratio and membrane proteins can be artificially "crowded" by limiting the micelle concentration (344). However, diluting the detergent concentration below the CMC results in demicellization and rapid IMP precipitation.

Significant effort is often required to find a suitable detergent that maintains IMP function and stability (340,341,345). There are alternatives to pure detergents that are capable of dissolving lipids, including nanodiscs (54,83), amphipols (57,338), Styrene maleic acid lipid particles (SMALPs) (84,85) and bicelles (48,52). Some groups have employed more radical approaches, seeking to solubilize IMPs without the need for any lipid bilayer mimic. Computer-aided mutagenesis studies have revealed that IMPs can be made water soluble (97,98) and functional (99) if lipid-facing hydrophobic residues of a membrane protein are mutated to hydrophilic residues. Other groups have fused the apolipoproteins such as those used in nanodiscs directly to the IMP in order to greatly increase recombinant yield and water solubility (96). Interestingly, there is a class of IMPs in the magnetosome organelle of Magnetotactic bacteria (MTB)(346) that act as amphiphiles and form water soluble "protein micelles" when recombinantly expressed (103,104). These protein micelles are able to bind iron and are likely an important step in magnetosome formation (103). It is impressive that these magnetosome proteins, such as *Mms6* are unique in their ability to form water-soluble protein micelles without any modification (101,102). Small water-soluble *peptides* such as the 26 residue melittin are able to conform to their environment and readily form a monomer or tetramer in aqueous solutions (347) and aggregate in membranes to form pores(348). The phenomenon of IMPs forming micelles in the absence of a membrane mimetic is unknown in higher order organisms, but this is likely due to a lack of effort due to the *a priori* assumption that IMPs require detergent.

Single-pass TM proteins(227) have the simplest membrane topology and are conceptually similar to a double headed detergent connected by an alkane chain, or bolaamphiphile (105). It seems plausible that some single pass transmembrane proteins might be able to self-associate and satisfy their own hydrophobic and hydrophilic requirements in the absence of membrane mimic. However, this has not been previously reported, most likely due to rapid IMP aggregation after demicellization in aqueous solutions. We posit that controlled removal of detergent from a sterically isolated IMP can prevent "runaway" aggregation and promote the formation of water-soluble protein "micelles". We here show, for the first time, that some human single pass TM proteins can indeed form stable water-soluble particles lacking any detergent, lipid, or membrane mimic. These particles are referred to as membrane mimetic free particles (MeMFs) and are reversible upon addition of detergent to form normal protein-detergent micelle complexes (PDC).

Several, but not all single pass membrane proteins tried were able to form MeMFs. The amyloid precursor protein (APP) TM fragment and direct amyloid beta (Aβ) precursor, C99, forms MeMFs that are stable in solution for months at 4 °C. The high stability and wealth of structural knowledge on C99 in detergent and lipid bilayer systems(186-188,204,235) makes it an ideal test case for MeMF characterization and comparison to normal PDCs. In addition to their interesting biophysical properties, MeMFs are readily taken up by mammalian cells and accumulate at a perinuclear location. It is currently unknown if these internalized C99 MeMFs are processed in biologically relevant pathway or simply catabolized.

Materials and Methods

Expression and purification of C99

As previously reported (186,188,232,349), C99 was expressed in a pET-21a vector in BL21(DE3) cells and grown in M9 minimal media. For NMR experiments, cells were grown on $^{15}NH_4Cl$-supplemented M9 medium at 37 °C with shaking at 230 rpm to an OD_{600} of ~ 0.6 before being induced with 1 mM IPTG. Induced cells grew overnight at 18 °C with same shaking and were harvested the next morning by centrifugation before being flash frozen in liquid N_2 and stored at -80 °C. Day 1 of purification involved thawing ~6L worth (13-18 g wet cell mass) of the frozen cells to RT and resuspension in 140 mL of lysis buffer, (75 mM Tris pH 7.8, 300 mM NaCl, 5 mM Mg-Acetate and 0.2 mM EDTA), before being enzymatically lysed (RNase, DNase, and lysozyme) by tumbling at 4 °C for 2-4 hours. Lysed cells were then sonicated on ice for 12 minutes with 5 second pulses, a 50 % duty cycle, and 60 % power. The C99-continaing inclusion bodies were then separated from the soluble lysate by centrifugation at 25,000 xg for 20 minutes at 4 °C. The pellet was resuspended in another 140 mL of lysis buffer with a Dounce homogenizer and again sonicated and centrifuged. The clean inclusion body pellet was suspended in 140 mL of lysis buffer containing 3 % Empigen and DPC, protease inhibitor (P8849 Sigma), and 1mM DTT (if purifying a cysteine mutant of C99). The C99 was extracted from the inclusion bodies overnight tumbling at 4 °C.

On day 2, the inclusion body solution was spun down at 25,000 xg for 45 minutes at 4 °C in order to remove insoluble precipitates. While centrifuging, a small volume of Ni-NTA resin, 0.5-1.5 mL, per 6L of starting culture was equilibrated with 1×Tris-buffered saline (TBS, 20 mM Tris pH 7.5 140 mM NaCl pH 7.8). After centrifugation, the supernatant was combined with the resin and tumbled at 4 °C for ~1-2 hour at 4 °C before being loaded in a gravity column. When developing the protocol for preparing MeMFs, aliquots of the washes and elution were collected for Dynamic light scattering (DLS), SDS-PAGE, and ^{31}P NMR analysis. To remove impurities, the column was washed with 40 column volumes (CV) of 30 mM imidazole and 0.05 wt/v LMPG in TBS. Then excess detergent was removed from the column with 20 x 10 CV of detergent-free TBS, with occasional bulb pipette agitation. C99 MeMFs were then eluted with 10 mL of 250 mM Imidazole in TBS pH 7.8. Most of the C99 MeMFs elute in this first elution step, deemed E1. Additional MeMFs can be nudged off the column with a second elution, E2, that contains a small ~2x CMC amount of detergent—0.025 wt/v LMPG. The E2 elution contained MeMF particles of comparable size to E1 and could be extensively dialyzed against detergent free solutions without precipitation occurring. An aliquot from E1 was removed for DLS and SDS-PAGE analysis and the elution was stored at 4 °C in a conical tube until needed. A typical yield was ~1-2 mgs of C99 MeMFs per purification. All other MeMF IMP purifications we attempted (on human KCNE1, KCNE3, the SARS coronavirus Envelope protein, diacylglycerol kinase, which we expressed as described in (68,350-353)) were conducted using essentially the same protocol as developed for C99; limited Ni-NTA resin was used for a normal on-resin purification followed by an extensive detergent-free TBS wash before elution in detergent-free solution. The protein sequences used for these studies are listed below with the transmembrane segment being highlighted in red.

C99

MDAEFRHDSGYEVHHQKLVFFAEDVGSNKGAIIGLMVGGVVIATVIVITLVMLKKKQYTSIHHGVVEVDAAVTPEERHLSKMQQNGYENPTYKFFEQMQNQGRILQISITLAAALEHHHHHH

Notch 1 TM

MGHHHHHHVQSETVEPPPPA QLHFMYVAAAAFVLLFFVGC GVLLSRKRRRQHGQLWFPE

KCNE1

MGHHHHHHGMILSNTTAVTPFLTKLWQETVQQGGNMSGLARRSPRSGDGKLEALYVLMVLGFFGFFTLGIMLSYIRSKKLEHSNDPFNVYIESDAWQEKDKAYVQARVLESYKSCYVVENHLAIEQPNTHLPETKPSP

KCNE3

MGHHHHHHGMETTNGTETWYESLHAVLKALNATLHSNLLCRPGPGLGPDNQTEERRASLPGRDDNSYMYILFVMFLFAVTVGSLILGYTRSRKVDKRSDPYHVYIKNRVSMI

S2-E

MYSFVSEETGTLIVNSVLLFLAFVVFLLVTLAILTALRLCAYCCNIVNVSLVKPSFYVYSRVKNLNSSRVPDLLVLESSGGGSILVPRGSGGSHHHHHHHHHH

DAGK

MANNTTGFTRIIKAAGYSWKGLRAAWINEAAFRQEGVAVLLAVVIACWLDVDAITRVLLISSVMLVMIVELLNSAIEAVVDRIGSEYHELSGRAKDMGSAAVLIAIIDAVITWCILLWSHFG

MeMF fluorophore labeling.

A cysteine mutant in the cytosolic loop of C99, H732C, was previously used as a fluorophore labeling site and this construct was again used here (188,204). The labeling reaction was carried out in a traditional PDC since it was unknown if MeMFs would sterically occlude labeling. C99 H732C inclusion bodies were solubilized in Empigen as above, but the centrifuged supernatant was tumbled with 2-3 mL of Ni-NTA resin in order to increase the overall yield of C99 for the labeling step. To remove impurities, the column was washed with 20 column volumes (CV) of 30 mM imidazole and 0.1 % wt/v LMPG in TBS. C99 in LMPG was eluted with 10 mL of 250 mM Imidazole and 0.1 % wt/v LMPG in TBS. The eluted C99 was then immediately reacted with a >10x molar concentration (~1.5 mg) of IANBD thiol-reactive N,N'-dimethyl-N-(iodoacetyl)-N'-(7-nitrobenz-2-oxa-1,3-diazol-4-yl)ethylenediamine (IA-NBD) (Thermo Fisher) dissolved in 300 µL of DMSO. The reaction vessel was covered with aluminum foil and tumbled at RT for one hour before being placed at 4 °C overnight. The following morning, the imidazole was removed by extensive buffer swapping with a Amicon Ultra-4 10KDa molecular weight cut-off filter (Millipore) into TBS containing a 1x CMC of LMPG. The fluorophore labeled C99 was then bound normally to Ni-NTA resin, stripped of detergent, and purified into MeMFs as indicated above. C99 MeMFs were stored unconcentrated at 4 °C until concentrated immediately before tissue culture experiments. C99 MeMFs were concentrated with an a Amicon Ultra-4 10kDa cartridge and the final labeling efficiency was determined by comparing the protein concentration (A280 = 11400 M−1 cm−1) to the NBD label concentration (the latter determined by measuring absorbance at 472 nm with an excitation coefficient of 23700 M−1 cm−1).

Dynamic Light Scattering

DLS was the main method used to quickly determine the presence and quality of DLPs present in solution after purification. Samples and a detergent-only reference were filtered through a 0.22-micron syringe filter in order to remove dust, trace protein aggregates, and shedding from the agarose column. Filtered MeMFs were added to the inner chamber of a disposable cuvette and loaded into a Wyatt DynaPro NanoStat DLS. Samples were allowed to equilibrate at 25 °C for 5 minutes before conducting three readings consisting of 10 acquisitions with a five second integration window. Dynamics 7.5 software (Wyatt Technologies) uses the diffusion coefficient to calculate an apparent hydrodynamic radius (Rh) via the Stokes-Einstein equation. MeMFs were always larger than micelles formed by detergents used at the early stages of purification. MeMFs were usually exhibited an Rh of 7-20 nm compared to 2-4 nm for most detergent micelles(62,255). We wanted to understand how stable MeMFs were against mild denaturing conditions, urea, and if MeMFs would revert to a traditional PDC upon addition of excess detergent. DLS was used for this purpose since it is a quick an effective way to screen many conditions while requiring small sample volumes. The detergent to protein ratio and the urea stability DLS experiments (below) used ~10 µM C99 MeMFs that had been extensively dialyzed into TBS using a 6-8 kD molecular weight cut-off (MWCO) dialysis tubing (SpectraPor, part number 132660). Samples were then mixed 1:1 with various concentrations LMPG or urea in TBS so that the final volume for all samples was 200 µL. To reach equilibrium, samples sat at RT for at least half an hour before being measured in the DLS instrument at 25 °C. Dynamics software was used to correct for changes in viscosity urea containing samples.

NMR

^{31}P 1D NMR was carried out to determine detergent concentrations an on a 500 MHz Bruker spectrometer equipped with a 5mm BBFOplus probe, with 1024 scans at 25 °C. 1H, 15N, TROSY-based HSQC experiments were carried out using a 900 MHz Bruker Avance III spectrometer equipped with a cryoprobe at 45 °C for experiments at either pH 7.8 or pH 6.5. The impact of detergent on C99 MeMF samples was explored by running a TROSY-HSQC on 50 µM C99 MeMF in 25 mM Imidazole 75 mM NaCl pH 7.8 and then adding 2.5 % wt/v LMPG and running a duplicate experiment. Experiments looking at C99 MeMF hysteresis started with 50 µM C99 in 25 mM Imidazole 75 mM NaCl pH 7.8, followed by addition of 2.5% LMPG before changing the pH to 6.5 with 1M HCl. The TROSY-HSQC of this sample was compared against that from an identical TROSY-HSQC experiment run on a C99 sample that had never been in the MeMF state, see fluorophore labeling above for how this sample was purified. Spectra were processed using TOPSPIN 3.2 and analyzed using NMRFAM-SPARKY version 1.413.

Negative stain EM

Homemade negative stain grids were glow discharged immediately prior to staining. 5 µL of 1 µM C99 MeMF in 25 mM Imidazole 75 mM NaCl pH 7.8 either with or without 2.5 % wt/v LMPG was applied to the grid for 30 seconds. The excess sample was then removed with filter paper and the grids were washed twice in water. The grids were then quickly washed once in uranium acetate stain with stain being blotted away on filter paper before being stained again for 60 seconds before excess stain was blotted away. Vacuum was then used to dry the grids in preparation for imaging on a Morgagni, 100kV TEM.

Chemical Crosslinking

Glutaraldehyde crosslinking was previously used to accurately assess the oligomeric states of C99 (188) and a modified version of that protocol is used here. ~ 40 µM C99 in MeMFs was filtered through a 0.22-micron filter before being crosslinked with 0.01, 0.1, and 1.0 wt/v fresh glutaraldehyde for 30 minutes at room temperature. Samples were run on SDS-PAGE and stained with SimplyBlue Coomassie alternative (Invitrogen).

Circular Dichroism

Before CD, C99 MeMFs were extensively buffer swapped into phosphate buffer (25 mM $NaPO_4$ and 75 mM NaF pH 7.8) with an Amicon Ultra-4 10KDa molecular weight cut-off filter and filtered through a 0.22-filter. Filtered C99 MeMFs were diluted down to 25 µM with or without 2.5 % wt/v LMPG and allowed to sit at room temperature for half an hour before being loaded into Jasco J-810 spectropolarimeter (Jasco) in a 1 mm pathlength cuvette. Three acquisitions from 185-260 nm taken at 25 °C and averaged with buffer subtraction before being converted to molar ellipticity.

2D-IR

C99 MeMF samples for 2D-IR were extensively buffer swapped into phosphate buffer (25 mM $NaPO_4$ and 75 mM NaF pH 7.5 99 % D2O) with an Amicon Ultra-4 10KDa molecular weight cut-off filter (Millipore). Samples were then concentrated to ~70-200 µM and filtered through a 0.22-micron syringe filter before being stored on ice. Chain deuterated LMPG detergent (Anatrace) was used for all 2D-IR experiments.

Results

How to make MeMFs

There are examples of limiting detergent in order to artificially crowd IMPs (344,354), but we are not aware of any methods that aim to strip *all* the IMP of all detergent or membrane mimic. We attempted to make MeMFs with two methodologies: method one involved dialysis of normally purified C99 solubilized in LMPG against buffer lacking detergent. Using a dialysis membrane with a molecular weight cutoff below the mass of the detergent micelle allows for the slow removal of non-micelle associated detergent i.e., the CMC. Extensive dialysis resulted in a large amount of C99 precipitation, likely due to de-micellization when the detergent concentration fell below the CMC. C99 precipitation does not occur during dialysis if the CMC of detergent is maintained in all buffers. While it is possible to *slowly* remove the detergent from the system via dialysis, the CMC or demicellization event likely occurred quickly and allowed for rapid C99 nucleation and subsequent aggregation.

Nucleation based protein aggregation in solution is often thought to contain a lag, exponential growth phase, and plateau(355). We hypothesized that immobilizing the C99 on the stationary phase during chromatography prior to detergent removal would allow us to prevent exponential aggregation upon demicellization. As normal with C99 purification, C99 was extracted from *E. coli inclusion bodies* with a harsh detergent and then bound to a gravity IMAC column. We used a very small amount of Ni-NTA resin (~0.1mL resin/gram wet cell mass) compared to previous literature (~2.0 mL resin/gram wet cell mass)(186,232) in order to limit impurities and greatly enhance the concentration of C99 on the resin. Empigen is a harsh detergent that is normally used to extract C99 from inclusion bodies, but it lacks phosphorus. DPC was used instead of empigen for select experiments since it is observable by solution NMR and is still harsh enough to extract C99 from inclusion bodies. The first part of the purification swaps the harsh detergent in for a mild surfactant (LMPG) during impurity removal. The free detergent was then removed from the system with a large excess of detergent-free washes before elution. ^{31}P NMR indicated that 150-200 CV of washes are required to completely remove the free detergent as shown in **Figure 5.1**, this is likely due to the IMAC column substrate, agarose, acting as a "detergent sink". C99 MeMFs were eluted off the column in a buffered solution lacking any detergent and were stable for months when refrigerated. MeMF yields are significantly lower than from previously reported purification in LMPG: 0.33 mg/L of C99 MeMF vs 20 mg/L C99 in LMPG(232). C99 MeMFs can be concentrated to over 150 µM C99 and can be extensively dialyzed against solutions lacking detergent without visible precipitation. We also attempted to make MeMFs by removing the detergent with urea, a strong chaotropic agent that can unfold proteins(356,357) and exponentially increase detergent CMC values (358). MeMFs did not elute from the column after being washed in buffered urea lacking detergent, likely due to unfolding of the C99 secondary structure by urea in the absence of a detergent.

To test if MeMF formation was unique to C99 we attempted to make MeMFs using multiple different single pass IMPs (KCNE1, KNCE3, Notch1 TM and SARS-2 envelope protein) and one topologically complex trimeric triple-pass IMP (DAGK). The Notch1 TM and KCNE3 both formed MeMFs while the SARS-2 envelope protein, KCNE1, and DAGK did not. Proteins that failed to form MeMFs either did not elute off the column after detergent removal or precipitated within seconds of elution and formed aggregates with a Rh > 300 nm. DAGK contains a topology that is likely too complex for MeMF formation. It is unclear at this time why some single pass IMPs can form MeMFs while others do not. KCNE1 did not form MeMFs even though it had significant hydrophilic domains on the amino and carboxyl terminus like C99 and KCNE3. The Materials and Methods section lists the sequences of all proteins tested for MeMF formation. For clarity and potential importance in AD etiology, as well as ease of feasibility, this work focuses on the extensive characterization of C99 MeMFs.

MeMFs are larger than most micelles.

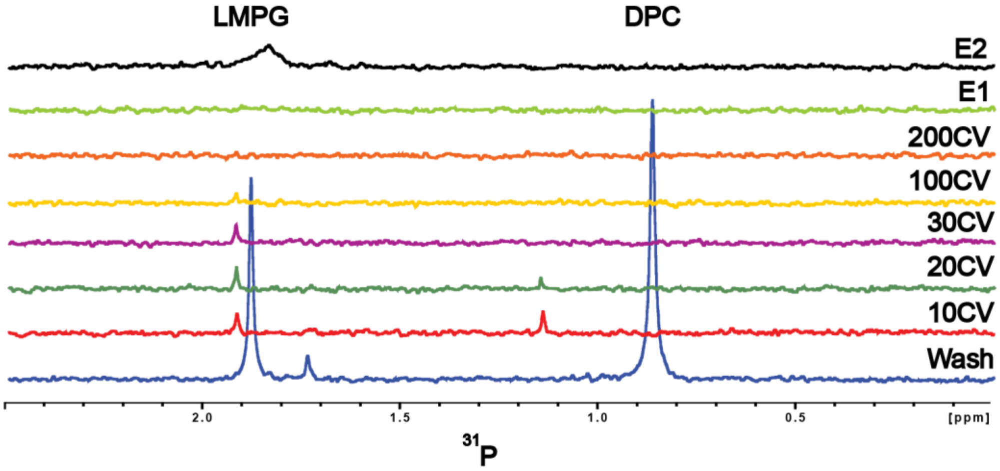

Figure 5.1: Removal of excess detergent prior to elution of C99 MeMFs. *Overlaid ^{31}P NMR spectra track the removal of detergent prior to MeMF elution in the impurity removal (wash), and detergent removal (CV), and elution steps (E1 and E2). All experiments had the same number of scans, 1024, so that the detergent concentrations can be compared. For reference, the LMPG concentration is the wash step is 0.05 wt/v (~ 1mM). N=2*

A unique feature of the MeMFs is their increased size compared to that of a normal protein-detergent complex (PDC) (62,255). Dynamic light scattering (DLS) determines diffusion coefficients in order to estimate the size of particles in solution and is very sensitive to aggregation. DLS showed that the freshly eluted C99 MeMFs were significantly larger (Rh ~7-14 nm) than the normal C99 in LMPG or DPC micelles (Rh ~3 nm) (**Figure 5.2**). Importantly, DLS rarely found large aggregates to be present in the C99 MeMF samples, indicating that extensive aggregation was not occurring. Chemical crosslinking of C99 was previously used to accurately determine its sometimes-complex set of oligomeric states in bicelles(188) and we wanted to see if C99 MeMFs formed a specific oligomer. Glutaraldehyde crosslinking and subsequent SDS-PAGE revealed that the C99 MeMFs represented a distribution of molecular weights with the majority being between the range 98 and 188 kD, representing between 7-14 C99 molecules per MeMF (**Figure 5.2**). Negative stain EM was used to confirm the size of non-crosslinked C99 MeMFs, **Figure 5.3.** EM showed the C99 MeMFs to be spherical and pairs of MeMFs would often appear to be touching, helping to explain the large mass distribution observed in the crosslinking experiment. The EM staining procedure did not include any detergents in the washing steps and so the detergent concentration would plunge the detergent concentration of PDC solutions of C99 below the CMC. **Figure 5.3** re-affirms the dialysis finding that C99 in PDC solutions precipitates when demicellization occurs and does not lead to formation of spherical MeMFs.

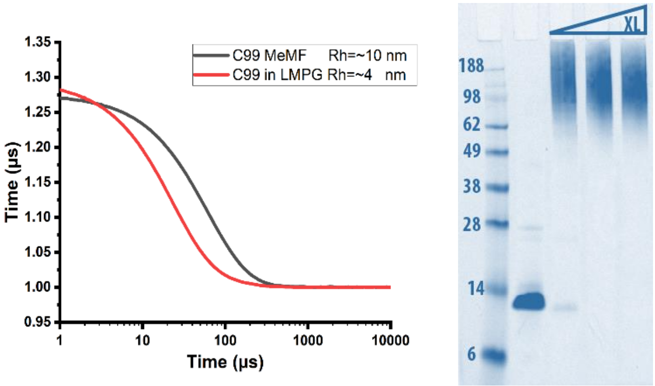

***Figure 5.2. C99 MeMF particles are larger than the traditional detergent-protein complex.** Left Panel: Dynamic light scattering autocorrelation curves showing that ~10 µM C99 MeMFs are larger than 10 uM C99 in LMPG micelles, indicated by the shift to the right in the autocorrelation curve. Right Panel: SDS-PAGE of ~ 40 µM C99 in MeMFs crosslinked with 0.01, 0.1, and 1.0 wt/v fresh glutaraldehyde. Crosslinking reveals a high molecular weight population corresponding to ~150kD, (right lanes) instead of monomer in the absence of crosslinker (first lane after ladder). This experiment was replicated 3 times.*

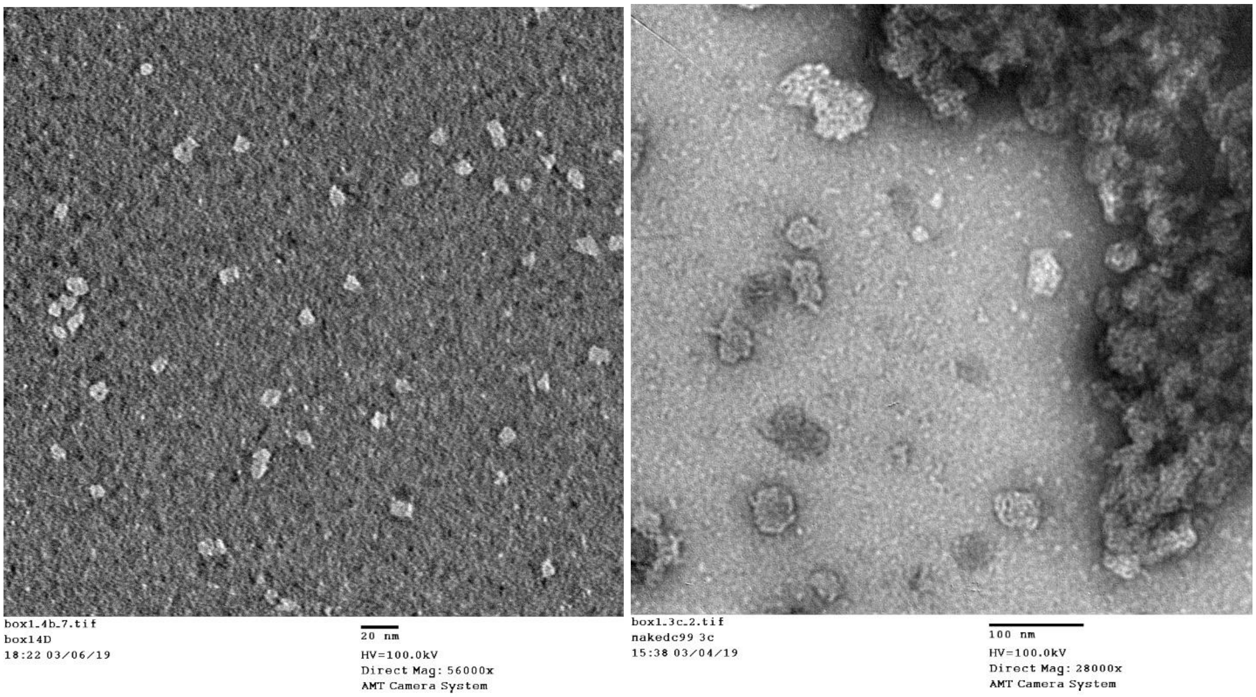

***Figure 5.3 Negative stain shows C99 MeMFs form spherical particles that do not aggregate upon dilution.** Left Panel: Negative stain of 1 µM C99 MeMF in 25 mM Imidazole 75 mM NaCl pH 7.8 without 2.5 % wt/v LMPG. Diluted C99 MeMFs are spherical or crescent particles that do not aggregate. The particle sizes observed approximately agree with DLS. Right Panel: 1 µM C99 MeMF in 25 mM Imidazole 75 mM NaCl pH 7.8 with 2.5 % wt/v LMPG. C99 in LMPG diluted below detergent CMC during the*

staining process shows large aggregates that are commonly observed when detergent is quickly removed from C99. N=1

MeMFs are reversible.

We tested if MeMF particles were reversible and able to revert to a traditional PDC upon the addition of exogenous detergent. DLS reveals (**Figure 5.4)** that addition of LMPG detergent to C99 MeMFs resulted in the MeMF particles getting smaller as a function of the C99: LMPG ratio. The decrease in particle size is likely due to free detergent splitting MeMFs and stabilizing lower order C99 oligomers. With increasing LMPG addition, these lower order oligomers are broken down until only LMPG micelle-sized particles were visible. DLS was also used to test MeMF stability upon addition of chaotropic denaturing agents. Up to 2.5 M urea was added to MeMFs without inducing aggregation (**Figure 5.4**). The protein to detergent ratio and urea trends are not C99 MeMF-specific and were also replicated for Notch 1 TM MeMFs.

DLS established that the MeMFs can be broken down by the addition of detergent, but it was unclear if C99 suffered any hysteresis from being in the MeMF state. Solution NMR is sensitive to changes in the chemical environment of every residue and can act as a “fingerprint” for a protein in defined conditions. Due to the structural heterogeneity and large size of MeMFs, the majority of backbone amide resonances in a 1H,15N TROSY-HSQC spectrum are broadened beyond detection for C99 in MeMFs (**Figure 5.5**). However, it is interesting to note that a few residues are still observable in the spectrum. These residues likely correspond to flexible portions of C99 that are more dynamic than those present in the core of the C99 MeMF particles. Addition of excess LMPG detergent resulted in over 100 peaks appearing, indicating the formation of the smaller, traditional PDC. The flexible residues in C99 MeMFs could not be identified since this spectrum was collected at pH 7.8 and C99 was previously assigned in LMPG at pH 6.5. The calculated pI of our C99 construct is 6.4 and, like many soluble proteins, MeMFs rapidly precipitates at pH 6.5 when no charged detergent is present. Addition of excess LMPG to MeMFs at pH 7.8 and then lowering the pH to 6.5 keeps C99 in solution and gives an excellent quality spectrum (**Figure 5.5**). The spectrum of a C99 sample previously purified into MeMFs followed by detergent addition overlayed nicely with a spectrum of C99 in LMPG micelles that had never been stripped of detergent; indicating that the NMR “fingerprints” matched, and that no hysteresis was induced by MeMF purification.

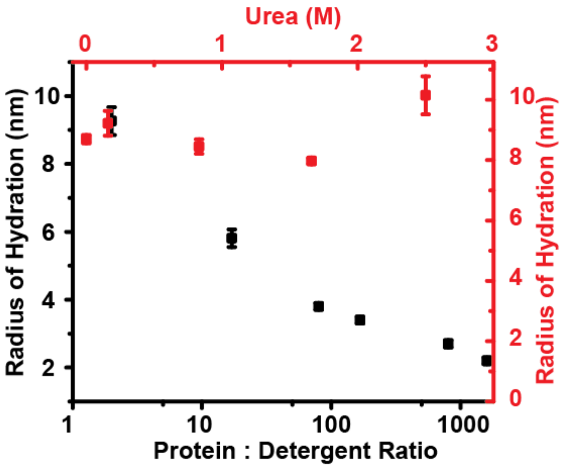

Figure 5.4. MeMFs are broken up by detergent and resistant to addition of denaturing agents. *Addition of detergent to ~10 μM C99 MeMFs in TBS decreases their size in a concentration-dependent manner, likely due to the conversion of the MeMFs back into traditional C99-detergent complexes. Urea does not obviously impact the size of 10 μM C99 MeMFs in TBS. (N =2)*

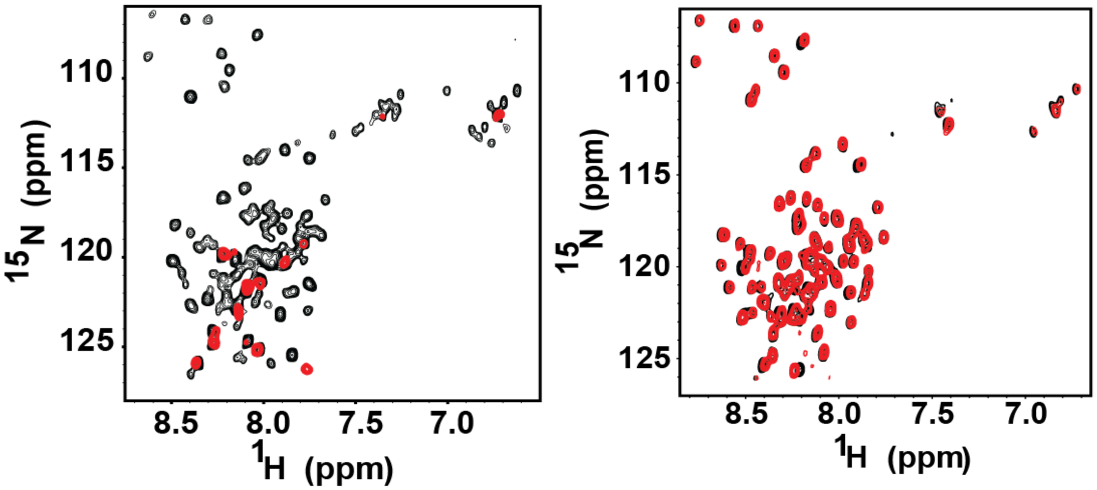

Figure 5.5. MeMFs can be fully reversed to traditional protein-micelle complexes. *Left Panel: TROSY-HSQC of 50 µM U-15N-C99 MeMF in 25 mM Imidazole 75 mM NaCl pH 7.8 in red and spectrum following addition of 2.5 % wt/v LMPG and running a duplicate experiment in black. Right Panel: TROSY HSQC of 50 µM C99 MeMFs in 25 mM Imidazole 75 mM NaCl pH 6.5 that had 2.5% LMPG added in red, overlaid on a TROSY HSQC of 50 µM C99 in 25 mM Imidazole 75 mM NaCl pH 6.5 2.5% LMPG that had never been purified as a MeMF in black. Notice how some residues are still visible for C99 in its MeMF form, left panel. N=1*

C99 MeMFs possess altered secondary structure.

The C99 TM is flanked by juxtamembrane regions that are thought to have significant beta sheet (βS) secondary structural propensity. The Aβ sequence that is liberated from C99 by gamma secretase cleavage is responsible for the amyloid plaques associated with AD. Aβ plaques are dominated by β 2° secondary structure (297,304); however, no stable β 2° structure is observed in monomeric C99 in LMPG micelles (186,232). Aβ Residues 16-22 and 30-42 on the amino terminus of C99 are normally buried within or associated with the lipid bilayer or detergent micelle, where they are helical. The membrane association of these residues likely limits the ability of Aβ for form strong β sheet 2° structure. The C-terminal cytosolic domain of C99 in LMPG micelles can participate in homo-oligomer transient hydrogen bonding that samples beta sheet structure (286,287). Both N- and C-terminal C99 juxtamembrane regions contain high amounts of random coil in a traditional PDC, but we hypothesized that βS would become a prominent secondary structural feature of the detergent-free C99 MeMF assemblies (7-14mers).

Circular dichroism (CD) is a traditional method for looking at protein secondary structure (51) and the spectrum of C99 in LMPG is dominated by alpha helical secondary structure as indicated by peak at 192 nm and troughs at 208 nm and 222 nm (359). As shown in **Figure 5.6,** C99 MeMFs do not give an obvious alpha helical spectrum and β-sheet structure appears to be present as indicated by the dip at 218 nm(360). As predicted by the solution NMR above, addition of detergent to MeMFs reverts the CD spectrum back to one dominated by alpha helix secondary structure. Quantification of secondary structure from CD spectra relies on a reference database of paired structures and spectra that should include similar structures (361). Membrane protein secondary structure quantification based on soluble protein databases often leads to errors due to phenomena such as the solvent shift (362,363) that are corrected by including membrane proteins in the database (364). While it can be argued that C99 MeMFs are similar to a soluble protein, CD databases do not contain particles similar to MeMFs and therefore quantification of secondary structure prediction within MeMFs based on CD would lead to possibly questionable results.

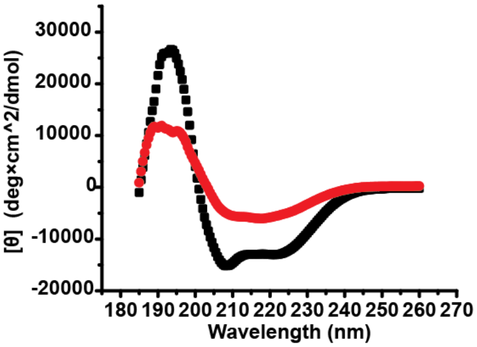

Figure 5.6. C99 MeMFs do not exhibit traditional C99 secondary structure. *CD spectra of 25 µM C99 MeMF in 25 mM NaPO$_4$ and 75 mM NaF pH 7.8, red, vs 25 µM C99 MeMF in 25 mM NaPO$_4$ and 75 mM NaF pH 7.8 that had 2.5 % wt/v LMPG added to make a traditional protein-micelle complex, black.*

2D-IR spectroscopy is another commonly used technique to examine protein secondary structure, unlike CD, 2D-IR is based on amide backbone vibrations (365). C99 MeMFs give a strong resonance signal that indicated the presence of βS. Similar to what was observed with CD, subsequent addition of excess LMPG detergent then greatly diminishes the βS peak intensity and an alpha helical/random coil peak appears. Once we had confirmed the presence of βS in C99 MeMFs, we were interested in understanding their transition to traditional PDC upon addition of detergent.

Both CD and DLS require tens of minutes in order to collect high quality data and one advantage of 2D-IR over CD is its higher sensitivity, conferring the ability to measure kinetics (366). The transition of C99 MeMFs to traditional PDCs occurred quickly and was complete within ten minutes. The speed of this transition upon addition of mild detergents implies that MeMFs are not similar to Aβ amyloid, which are also dominated by βS. Amyloid monomerization requires strong denaturing agents such as fluorinated solvents (367,368). DLS indicated that the MeMF particles gradually get smaller as a function of detergent concentration, and we wanted to see if this correlated to a gradual change secondary structure. Surprisingly, the addition of detergent to MeMFs did not have a drastic impact on the secondary structure below a detergent to protein ratio. The transition between βS-dominated and α-helix-dominated spectra occurred in a step function-manner. It is important to note that this transition ratio roughly corresponds to one C99 protein per detergent micelle in solution (62,255).

Delivery of C99 MeMFs to mammalian cells.

A distinctive trait of MeMFs is that they provide a mode of membrane protein solubilization that eliminates the need for use of model membranes such as potentially cytotoxic detergents or undegradable polymers. We posited that MeMFs might enable the delivery of recombinant membrane proteins into the membranes of live mammalian cells. For tracking purposes, we covalently labeled C99 MeMFs with a fluorophore, (NBD), via modification of H732C in the unstructured C99 cytosolic loop. As shown in **Figure 5.9,** C99-MeMFs-NBD are taken up by HeLa cells overtime accumulate labeled signal, likely protein "dose" resulting in increased cell-internal fluorescence. With time, it was seen that the C99 signal accumulates in a perinuclear intracellular location. The exact C99-MeMFs localization is now subject to additional investigation by other members of the Sanders Lab. These studies include use of anti-C99 antibodies to ensure that we are tracking C99 and not a degradation-liberated fluorophore-containing fragment of C99.

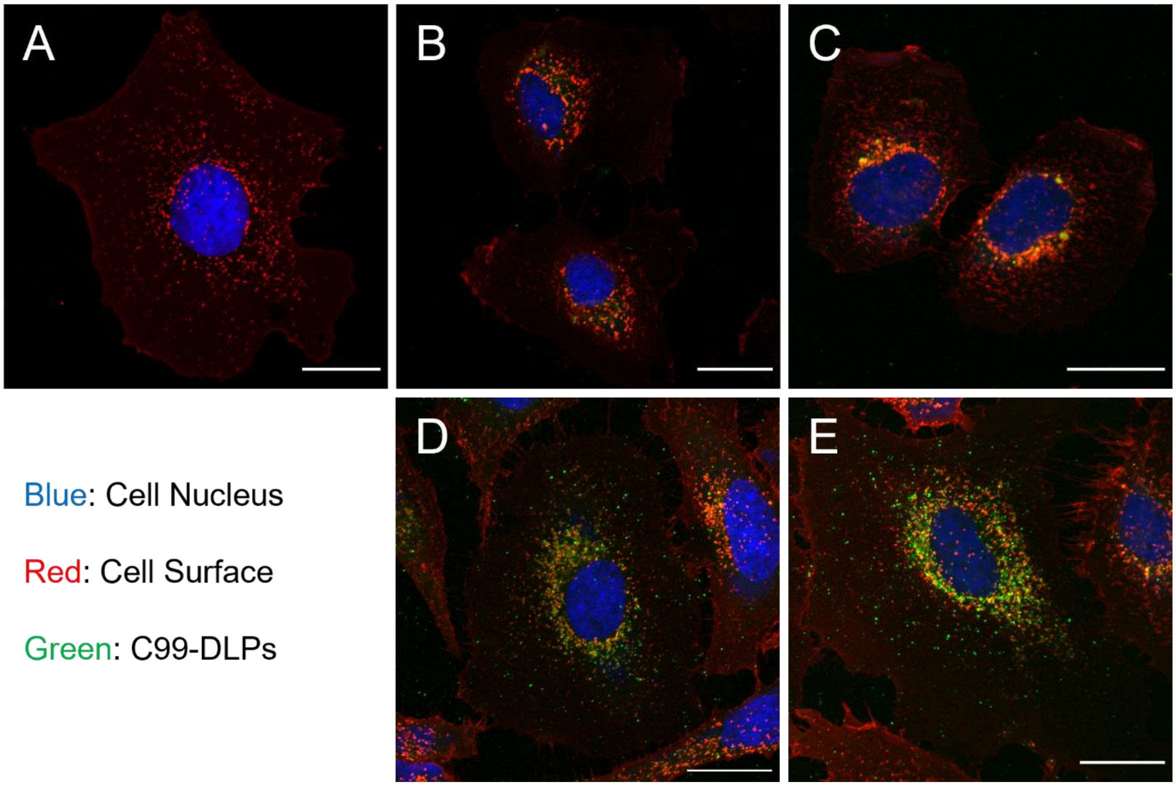

Figure 5.7. Time course of HeLa cells treated with 2.5μM C99 DLPs labeled with NBD. *Panel A shows untreated cells and therefore also represent the zero timepoint for DLP treatment. Panel B-E shows cells at various times after addition of DLPs to the culture. B) 1h, C) 2h, D) 18h, and E) 23h. N=1*

Discussion

MeMF formation requires steric immobilization.

MTB make a variety of magnetosome IMPs that form “protein micelles” when recombinantly purified in the absence of detergent (101-104). We hesitate to refer to them as “micelles” since it is not obvious if a CMC of monomeric protein is detected in solution. We are not aware of any reports of protein micelles occurring in higher order organisms, but this is likely due to a lack of effort since most would assume *a priori* that a detergent or some other membrane mimetic is required to solubilize an IMP in aqueous environments. Single pass membrane proteins can be abstractly thought of as a double headed detergent or “bolaamphiphile” (105) and we wanted to see if human single pass membrane proteins could also form MeMFs or “protein micelles”.

It is generally assumed that the removal of detergent from a membrane protein results in rapid precipitation when the detergent concentration goes below the CMC and demicellization occurs. Indeed, we observed that aggregation does indeed occur when detergent is removed from C99 in solution. We hypothesized that attaching micellar C99 to a stationary phase (chromatography resin) and only then stripping off the detergent would prevent exponential aggregation and create conditions that , upon elution, would allow time for C99 to form smaller aggregates that represent a local minimum in the energy landscape between unfolded and native states (369). Immobilizing the IMP during demicellization appears from our results to be the key methodology that facilitates MeMF formation. It is acknowledged that the formation of MeMFs is inefficient compared to traditional PDC purifications, indicating that only a fraction of the C99 is able to form these water soluble MeMF particles, with most C99 crashing out on the column. Maintenance of secondary structure also likely plays an important role in MeMF formation since urea washes before elution prevented C99 MeMFs from eluting off the column (356,357). We explore the unique details of MeMF secondary structure below.

MeMF Shape and Size

Mammalian TM proteins generally have an alpha helical TM segment that is far more rigid than the hydrocarbon chain of a detergent or lipid. Due to this and their large mass, it is expected that MeMFs would be larger than a normal C99 PDC or detergent micelle since MeMFs cannot easily bend their transmembrane to efficiently accommodate their hydrophobic needs. Chemical crosslinking in **Figure 5.2** indicates that multiple C99 proteins pack together to satisfy each other’s hydrophobic transmembrane needs. The packing of the C99 in MeMFs is observed by negative stain EM to create a spheroidal or crescent shaped particles. All linear amphipathic molecules such as lipid and detergents are subject to packing geometries that are generally described as the molecular packing parameter (MPP)(370,371). The MPP compares the area of the hydrophilic head groups and hydrophobic chain volume and length in order to determine what shape of macromolecular-particle an amphipathic molecule will form. Lipids generally have a cylindrical shape that form bilayers while most detergents, have a conical shape and forms spherical, oblate, or prolate particles. Single pass membrane proteins such as C99 often have large and disordered hydrophilic juxtamembrane regions that would occupy a large area, and this is contrasted against the relatively compact α-helical TM. This overall shape would resemble a hyperboloid and similar to bolaamphiphiles (371), would favor the formation of a spheroidal particle. The TM of C99 likely passes straight through the MeMF center of mass, but it is also possible that the C99 TM di-glycine hinge would allow for the U-shaped bending through the center of mass.

C99 MeMFs Stabilize β-Sheet Structure

Previous solution NMR structures in LMPG showed monomeric C99 to have a random coil amino terminus followed by a short amphipathic helix and helical transmembrane segment. The TM segment contains a di-glycine hinge and is followed by a large random coil cytosolic loop ending in an amphipathic helix at the carboxyl terminus (186,232). No obvious β-strand/sheet structure was observed in monomeric C99 which is interesting given that C99 contains the Aβ sequence that is known to form βS-based amyloid plaques *in vivo*. A separate study used FTIR to show the Aβ portion of C99 is capable of forming βS under conditions that are expected to contain significant C99 dimer (372). Moreover, solution NMR studies on the isolated cytosolic loop reported the presence of transient β-sheet hydrogen bonding patterns (286,287). We recently published the characterization of C99 as a mixture of monomer, dimer, and trimer in a cholesterol-rich plasma membrane-like environment and observed that TM-mediated oligomerization of C99 enabled random coil residues 673-678 and 735-745 on both sides of the TM to form transient hydrogen bond networks (188). This study did not present evidence that the transient hydrogen bond networks formed β-sheet structure, but this is a logical assumption given that previous structural work showed that these regions are prone to β-sheet formation. The work presented below, and previous studies imply that C99 oligomers form β-sheet in oligomeric interfaces in the juxtamembrane regions while monomeric C99 does not.

Both the CD and 2D-IR indicate that C99 MeMFs contain a significant amount of β-sheet structure that is not present in the α-helix and random coil-dominated spectra of C99 in LMPG. It is doubtful that the TM α-helix would unfold into β-strands since it is still buried in the MeMF hydrophobic core. This idea is supported by the plateau in the CD spectrum which represents a mixture of α-helix and β-sheet secondary structure in C99 MeMFs. We hypothesize that MeMFs are a defined oligomeric form of C99 and the C99 juxtamembrane regions are likely forming a β-sheet shell around the hydrophobic helical TM core and that the β-sheet shell is what makes C99 MeMFs impressively stable (on the order of months). Addition of excess detergent to C99 MeMFs resulted in a complete loss of βS secondary structure. The transition is completed quickly, in under 10 minutes, and highlights that C99 MeMFs are easily reversed to a traditional PDC with mild detergent. This MeMFs-to-PDC transition is not reversible in solution since demicellization of C99 in solution results in exponential aggregation. It should be noted, that once formed, amyloid plaques are very difficult to break up/monomerize and require harsh denaturing agents (367,368). Thus, even though C99 MeMFs contain the Aβ sequence and βS secondary structure, they *are not* thermodynamic dead ends like amyloid fibrils.

DLS showed that addition of detergent to MeMFs results in smaller particles, and we expected a gradual loss of beta sheet secondary structure as C99 transitioned out of MeMFs and into traditional PDCs. Instead, 2D-IR indicated that there is a step-like transition in secondary structure that occurs at a certain detergent to protein ratio, as detergent is added to a constant level of protein. This ratio is satisfying because it is near the condition where each C99 would have its own detergent micelle. There is significant interest in understanding the impact of C99 dimerization on Aβ production (211,213). The majority of those studies focus on the on the N-terminal plus TM domain fragment of C99 (214,230,240,290) , which contains both the amyloid Aβ domain and all γ-secretase cleavage sites (373,374). My work here and previous works imply that any forced colocalization of C99 within single micelles results in β-sheet formation. The complex secondary structures of C99 should be considered when studying the impact of C99 dimerization on Aβ production.

MeMFs are readily taken up by mammalian cells

C99 is linked to cholesterol regulation (209), lysosomal dysfunction (198,199,375), and AD etiology (190,195), and there is a growing interest in developing methods to study the impact and function of C99 *in vivo*. C99 is rapidly degraded *in vivo* and is difficult to study since multiple protease inhibitors are required (223). Delivery of C99 to mammalian cells via MeMFs allows for a novel transcription-free way to study C99 *in vivo*. Here, C99 MeMFs were labeled with a fluorophore in order to track the delivered C99 without the need for complex labeling schemes (376). We chose to the C99 H732C mutant because this site is outside regions identified to have secondary structure in monomeric and oligomeric C99 (186,188). Moreover, this site was successfully labeled with a variety of fluorophores previously, including NBD (204).

Delivery of the C99-MeMFs-NBD to HeLa cells resulted in internalization of MeMF that increases as a function of exposure time. As shown in **Figure 5.9**, the uptake process appears to be slow, requiring at least an hour to detect minor intracellular NBD fluorescence. However, internalized fluorescent signal is readily observed in the perinuclear space after 18 h. Based on appearance, we predict that perinuclear location occupied by C99-NBD will turn out to be the ER, but this will need to be determined in future experiments. Localization of MeMF-derived C99 in the ER would open the door to an exciting approach for studying the trafficking and function of C99 in cells and its contribution to AD etiology (377-379). If the MeMFs were simply being catabolized as cell food, one may expect the C99 to be enrich in the lysosomes distributed throughout the cell and not trafficked back to the perinuclear space. This is not seen. Future work should focus on establishing the nature of the perinuclear localization of the C99 MeMFs and determination of whether exogenously-added C99 can be processed in biologically relevant pathways, such as the amyloidogenic pathway.

Conclusions

Here, we show for the first time that mammalian single pass transmembrane proteins can be purified in an aqueous environment without any model membranes. These particles are referred as MeMFs and are larger than traditional PDCs. MeMFs can be converted back to a PDC with the addition of sufficient detergent and suffer no hysteresis. C99 MeMFs were found to have β-sheet character that was not observed in previous studies of monomeric C99. We posit that the βS enhances their stability by forming a shell around the α-helical TM core of the MeMF. We do not yet know why some single pass proteins are able to form MeMFs while others (so far) do not. It was seen that the C99 MeMFs were readily taken up by mammalian cells and accumulate in the perinuclear space, in a yet unknown cellular location. We speculate that the perinuclear location of C99 MeMFs is the ER, but this will need to validated in future work. Another focus of future work should be to understand if the C99 delivered by MeMFs is viewed by cells an endogenous protein and trafficked and processed as such, or instead is simply catabolized.

VI. The Transmembrane Amyloid Precursor Protein C99 Fragment Exhibits Non-Specific Interaction with Tau

Introduction

Hallmarks of Alzheimer's disease (AD) include the widespread deposition of extracellular amyloid-β (Aβ) peptide aggregates derived from the amyloid precursor protein (APP) and intracellular neurofibrillary tangles (NFTs) composed of the hyperphosphorylated microtubule associated protein tau (158,380,381). Aβ plaques and NFTs have historically dominated AD research since they are clinical biomarkers (161). The amyloid hypothesis posits that the pathological cascade of events in AD is initiated by the abnormal aggregation of Aβ peptide (158). Aβ is generated by amyloidogenic proteolytic processing when APP is initially cleaved by β-secretase (BACE1) to generate the soluble ectodomain, sAPPβ, and the 99-residue transmembrane C-terminal fragment, CTFβ, referred here as C99. Subsequent γ-secretase cleavage of C99 yields 38-43 amino acid Aβ peptides (190,382) and the soluble APP intracellular domain fragment (190,305). The healthy function of APP and its fragments are still not well understood, partly due to heterogeneity in the exact processing pathways and functional overlap with associated APP-like proteins (189). The tau protein stabilizes and promotes the assembly of axonal microtubules in healthy neurons (177) and has six isoforms ranging from 352-441 amino acids in length, each distinguished by either three of four microtubule binding domains (383). All tau isoforms, when hyperphosphorylated, have been observed to form paired helical filaments which comprise the characteristic NFTs in AD (384). Tau phosphorylation is known to reduce its affinity for microtubules, which may drive NFT formation; however, the exact mechanism of aggregation and propagation to other cells is not well understood (174).

It is tempting to explore the relationship between APP and tau given their coincident aberrant aggregates in AD. While there is evidence that Aβ and tau pathologies are connected, the definitive link between these two hallmarks of AD remains elusive. Broadly, detectable Aβ plaque precedes tau fibrillation during AD progression, and this has promoted the idea that the presence of Aβ aggregates in the extracellular space somehow induces or enhances NFT formation in the cytosol (160). In support of this, intracellular tau aggregation has been shown to be enhanced by extracellular Aβ deposition *in vivo* and in mouse models (178-180,385,386). Moreover, Aβ amyloid plaques have been shown to exhibit a prion-like seeding effect on paired helical filament (PHF) tau aggregates in an *in vivo* preclinical study (387). Several studies have looked at colocalization of Aβ and other APP fragments with tau. Immunohistology analyses suggest that both monomeric and oligomeric Aβ interact with phosphorylated tau in extracellular Aβ plaques and intracellularly as AD progresses in AD-affected neurons (388). However, some studies do not detect widespread intracellular Aβ-tau colocalization and instead observe colocalization at pre- and postsynaptic terminals (389) and synaptic compartments (390). In the classical model for AD, extracellular Aβ forms toxic oligomers that go on to seed plaques and that somehow then trigger intracellular tau fibrillization, a process that would appear to require the mediation of an extracellular to intracellular signaling pathway. A number of different membrane proteins or complexes have been considered as the transducers of this Aβ to tau signaling pathway (391-394). However, it is also possible there is a direct interaction between Aβ and tau, is the trigger of intracellular tau fibrillization.

In this regard, it is interesting to consider that extracellular Aβ may be able to bind to APP or C99 in the plasma membrane (395-397), which is not surprising given that both C99 and Aβ (which share the Aβ sequence) form homo-oligomers. It is therefore conceivable that C99 (or possibly even full length APP) could serve not only as the precursor of Aβ, but also as a receptor for Aβ. Given that C99 has a mostly-disordered 45 residue C-terminal domain, there is much potential for C99 interaction with intracellular tau. One can speculate, for example, that tau might not bind to the well-documented homodimeric form of C99, but that binding of extracellular Aβ to dimeric C99 might drive C99 into a tau binding-competent monomeric form.

Direct interaction of C99 and tau was reported in 1995 by Smith, et.al. (183) They found that tau bound to extracellular senile plaques *in situ* and that binding efficiency was independent of tau phosphorylation state (183). Several studies have previously mapped the binding of tau to APP residues 713-724 (183-185) which are in the cytosolic side of the transmembrane of APP and its derived C99 fragment (187,188). Residues 713-724 span a segment that is proteolytically processed by gamma secretase during Aβ generation and a peptide representing residues 713-724 is not known to exist outside of the lipid bilayer (374,398,399). Based on this work, the proposed APP-tau interface *in vivo* is thought to only be present in the cytosolic-proximal half of transmembrane fragments of APP or C99. A follow up study confirmed binding between full length APP and water-soluble tau via crosslinking (182) *in vitro* but determined residues 390–412 in the APP ectodomains are responsible for tau binding.

To our knowledge direct interaction of *full length* C99 and tau has not been tested. It is reasonable to wonder how the water soluble tau could bind APP/C99 at transmembrane residues 713-724 since the binding site is buried within the lipid bilayer (185). However, given the importance of AD, we sought to directly test whether tau and C99 bind each other. Titrations of C99 into tau and vice-versa were performed using purified recombinant proteins. In both cases the titrand was uniformly 15N-isotopically labeled so that individual amino acid chemical shifts could be tracked using 1H,15N TROSY-HSQC NMR spectroscopy. We find that C99-residues 713-724 do not interact with tau and the interaction between monomeric C99 in LMPG micelles and water-soluble tau is weak and non-specific.

Methods

Bacterial Expression of Full Length Tau$_{1\text{-}441}$

The purification of recombinant tau employed in this work draws heavily upon previous methods (400). Recombinant pET-29b plasmid (Addgene) with the gene for full-length tau (2N4R isoform, 441 residues) was transformed into a BL-21 (DE3) *E. coli* strain and plated overnight on a LB/agar plate supplemented with kanamycin (30 µg/mL). A 60 mL LB starter culture grown overnight at 37 °C was used to inoculate 6 x 1L of M9 minimal media supplemented with kanamycin (30 µg/mL). The culture was grown at 37 °C on a platform shaker at 230 rpm. Expression was induced with the addition of 0.5 mM isopropyl β-d-1-thiogalactopyranoside (IPTG) once cells reached OD_{600nm} between 0.6-1.0. Cells were allowed to continue shaking post-induction for 3 hours at 37 °C before being harvested by centrifugation at 5000 x g for 30 min. Cell pellets were, combined and flash frozen in liquid N_2 and stored at -80 °C.

The resulting pellet was thawed and resuspended in 10 mL phosphate buffer (50 mM sodium phosphate, 2.5 mM EDTA, 2 mM DTT, 0.5% Triton X-100, pH 6.2) per gram of wet cell mass supplemented with protease inhibitor cocktail (P8849, Sigma). The suspension was sonicated on ice for 10 minutes (5 on/5 off cycle) at 60% power. After sonication, the suspension was stirred at 80 °C for 15-20 minutes with a hot plate and then allowed to cool to room temperature. Precipitates were removed via centrifugation at 25,000 x g for 30 minutes. The pellet was discarded and the supernatant was filtered with a 0.2 µm syringe filter. The supernatant was then exchanged into cation exchange chromatography buffer A (50 mM sodium phosphate, pH 6.4, 2 mM EDTA) using an Amicon 30 kDa MW cutoff centrifuge filter (Millipore). Cation exchange chromatography was then conducted using the ATKA Start system and the HiTrap SP HP 5 mL column (Cytivia). Protein was eluted using a gradient of 0-80% Buffer B (50mM sodium phosphate, pH 6.4, 2mM EDTA, 2M NaCl) over 4-6 column volumes (CV). Fractions were collected and run on SDS-PAGE, and fractions containing pure tau were pooled together. $Tau_{1\text{-}441}$ expression was confirmed via Western Blotting using anti-tau antibody (Cell Signaling #4019S).

Bacterial Expression of APP-C99

Expression and purification of C99 was carried out as previously described (188). Recombinant pET-21b plasmid carrying His_6-tagged C99 I109W (Tryptophan added to purification tag to aid UV-Vis detection) was transformed into BL-21 (DE3) *E. coli*. 60 mL LB starter culture grown overnight at 37 °C was diluted into 6x1L of M9 minimal media with ampicillin (100µg/mL). The culture was grown at 37 °C with 230 rpm shaking. Expression was induced with the addition of 1 mM IPTG once cells reached OD_{600nm} 0.6-1.0. Cells were harvested via centrifugation at 5000 x g for 30 min after overnight induction at 18 °C. Harvested cell pellets were flash frozen in liquid nitrogen and stored at -80 °C.

Cell pellets were thawed to room temperature and resuspended in lysis buffer (75 mM Tris pH 7.8, 300 mM NaCl, 0.2 mM EDTA) before being enzymatically lysed by tumbling the suspension with lysozyme, DNAse, RNase mixture for 1-2 hours. The lysate was then sonicated on ice at 60 % power for 10 minutes at 50% duty cycle, followed by centrifugation at 25,000 x g for 20 minutes at 4 °C. The supernatant was discarded and the inclusion body pellet was resuspended in lysis buffer with a Dounce homogenizer. The sonication/centrifugation/resuspension cycle was carried out twice more to further remove contaminants from the inclusion body pellet. 3% Empigen was added to the final inclusion body resuspension and tumbled overnight at 4 °C to extract proteins.

The following morning, the insoluble fraction was removed via centrifugation at 25,000 x g for 30 minutes. The soluble fraction was tumbled for 45 minutes with 1-2 mL Ni-NTA resin that was pre-equilibrated in Tris-buffered saline (TBS, 20 mM Tris pH 7.5 140 mM NaCl). After tumbling, the resin was loaded onto a gravity column and rinsed with 10 CV of 3% Empigen (BOC Sciences) in TBS. Weakly-bound impurities were removed and the protein was exchanged into lyso-phosphatidylglycerol (LMPG) detergent with two 10 CV washes of 0.5 wt% LMPG in TBS containing 10 mM and 30 mM imidazole pH 7.8, respectively. Finally, C99 was eluted with an elution buffer of either 0.1 wt % or 0.5 wt % LMPG, 250 mM imidazole pH 7.8 in TBS.

Preparation of Sample for NMR Spectroscopy

For all experiments, both eluted proteins were first swapped into NMR buffer consisting of 25 mM buffering agent (sodium acetate for pH 4.5, imidazole for pH 6.5), 75 mM NaCl, 2 mM EDTA and the critical micelle concentration (CMC) of detergent (LMPG). Buffer swapping was performed using Amicon MW cutoff filters (Millipore, 10kDa for C99, 30kDa for tau). Final concentrations for both proteins were measured via UV absorption at 280 nm using their extinction coefficients (11,400 $M^{-1}cm^{-1}$ for C99 I109W and 7450 $M^{-1}cm^{-1}$ for $tau_{1\text{-}441}$). Titrations of unlabeled (0 to 300 µM) tau into 50 µM U-15N-C99 were buffered with 25 mM imidazole, pH 6.5, 75 mM NaCl, 2 mM EDTA, 1% LMPG. Titration of unlabeled (0 to 200 µM) C99 into 50 µM U-15N-tau was buffered with 25 mM sodium acetate, pH 4.5, 75 mM NaCl, 2 mM EDTA, 1% LMPG. All titration samples maintained the same concentration of LMPG in order to prevent detergent based artifacts.

NMR Spectroscopy

Proton 1D and 1H,15N TROSY-HSQC NMR spectra were acquired at 45 °C on a cryoprobe-equipped 800 MHz Bruker Avance III spectrometer. NMR data was processed with Topspin 3.2 and analyzed using NMRFAM-SPARKY. Chemical shift perturbations were measured according to equation 1.

Eq. 1

$$CSP_x\ (\Delta\delta) = \sqrt{(\delta[^1H_0] - \delta[^1H_x])^2 + (0.14(\delta[^{15}N_0] - \delta[^{15}N_x]))^2}$$

where $\delta\ [^1H_0]$ and $\delta\ [^{15}N_0]$ are the chemical shifts for a given peak in the 1H,15N TROSY-HSQC spectrum prior to the start of the titration and $\delta\ [^1H_X]$ and $\delta\ [^{15}N_X]$ are the chemical shifts for that same peak at a given titration point, assuming fast exchange conditions on the NMR timescale, where each peak reflects the populated-weighted average peak between free and complexed conditions.

Results

We started by conducting a tau into U-15N-C99 titration in LMPG detergent because the structure of C99 was previously determined in LMPG at pH 6.5 by solution NMR (186). This previous work allowed for the transfer of C99 resonance assignments to this titration experiment. In order to avoid detergent and buffer-based artifacts, both tau and C99 were buffer swapped into the same buffer. A concentration of 1 % LMPG detergent did not unfold soluble tau, as indicated by preserved peak dispersion in the HSQC proton dimension (data not shown). Moreover, a ratio of 50 µM C99 and 1 % LMPG concentration does not force C99 oligomerization by maintaining a 1 :8 ratio of C99 to LMPG micelle.

As shown in **Figure 6.1**, addition of 0-300 µM tau into 50 µM C99 solution was seen to induce small chemical shift perturbations (CSPs) in 19 peaks, mostly from residues near the protein-micelle interface or in the unstructured soluble C-terminal loop. C99 CSPs were linear as a function of tau concentration are therefore reflect a K_D of >300µM, consistent with non-specific tau interaction with C99.

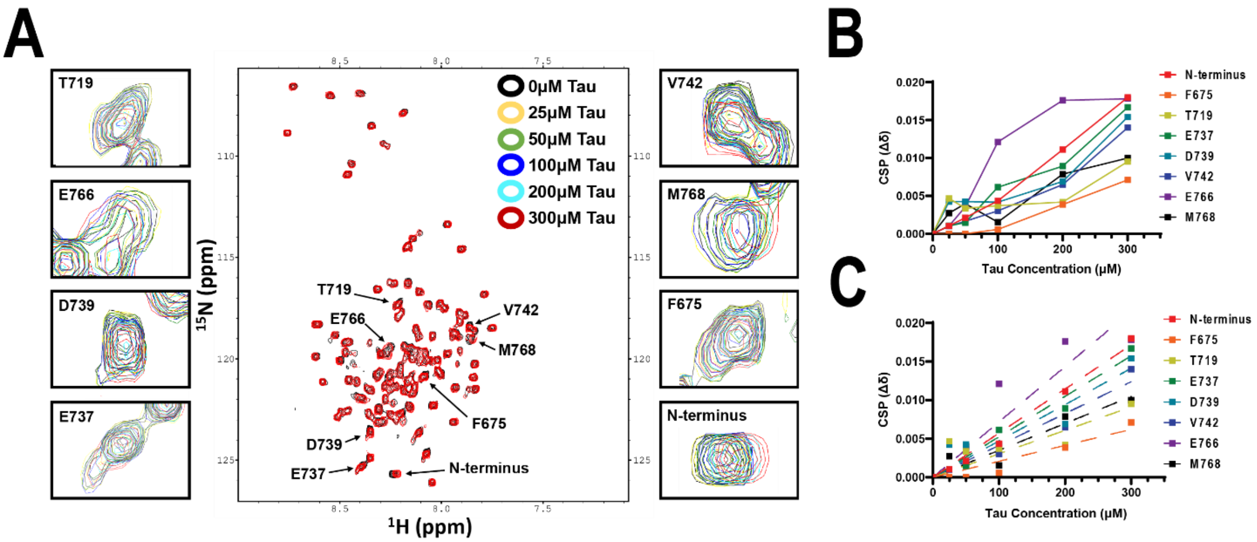

Figure 6.1. Titration of unlabeled tau into uniformly 15N-labeled C99. A) *Overlaid 1H,15N TROSY spectra of 50 μM 15N C99 in the presence of 0, 25, 50, 100, 200, and 300 μM unlabeled tau. The titration was performed in 25 mM imidazole, pH 6.5, 75 mM NaCl, 2 mM EDTA, 1% LMPG. Several C99 resonances shifted as a function of varying tau concentration. The titration series for eight of these resonances are highlighted with their transferred assignment.* ***B)*** *Resonances highlighted in* ***A*** *have their CSPs plotted as a function of tau concentration.* ***C)*** *Linear regression of* ***B*** *in order to highlight the non-saturating nature of the CSP plots, indicative of non-specific binding. The CSPs for the resonance associated with E766 appears non-linear, but this is likely due to poor resolution, see insert in* ***A****.*

We also conducted the reverse titration of unlabeled C99 into U-15N-tau for completeness. The reverse titration was conducted at pH 4.5 because the TROSY spectrum of tau exhibited more peaks and increased spectra dispersion at this reduced pH relative to pH 6.5 and previous work showed a strong C99 peptide-tau interaction at pH 5.0(183). C99 is known to maintain its structure at pH 4.5 (188). We observed large CSPs in many resonances as a function of C99 concentration however, as shown in **Figure 6.2**, the CSPs were again linear in nature, confirming only weak and likely non-specific binding between soluble tau and C99. Backbone assignments for tau$_{1\text{-}441}$ have been reported previously in different buffer conditions (401). We did not think the non-specific nature of the tau-C99 interaction warranted the significant effort that would be required to transfer assignments between conditions.

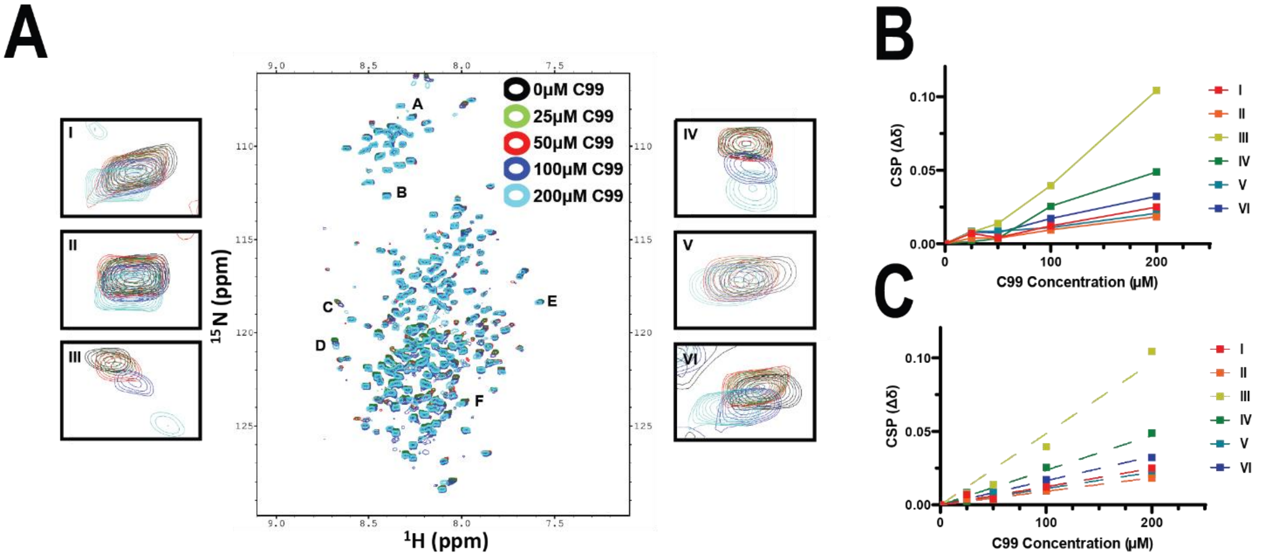

Figure 6.2. Titration of unlabeled C99 into uniformly-15N-labeled soluble tau$_{1-441}$. A) *Overlaid 1H,15N TROSY spectra of 50 µM U-15N tau in the presence of 0, 25, 50, 100, and 200 µM unlabeled C99. The titration was performed in 25 mM sodium acetate, pH 4.5, 75 mM NaCl, 2 mM EDTA, 1% LMPG. Several tau resonances shifted as a function of C99 concentration. The titration series for six of these unknown amino acid resonances are highlighted by I-VI in* ***A***. ***B)*** *Resonances highlighted in* ***A*** *have their CSPs plotted as a function C99 concentration.* ***C)*** *Linear regression of* ***B*** *in order to highlight the non-saturating nature of the CSP plots, indicative of non-specific binding.*

Discussion

Previous work suggested that tau binds to a short peptide derived from APP at a K_D of 9.6 nM (183) with the binding interface on APP including residues located on the cytosolic end of its transmembrane segment spanning residues 713-724 (183-185). Interestingly, these studies did not try and map any binding interface to tau. All of these studies (183-185)- used either Nonidet P-40 (185) or Tween-20 (183,184) detergents at pHs ranging from 5 to 8; these non-ionic detergents are commonly used when studying protein-protein interactions but lack a phospholipid-like structure. It is unclear if these detergents are suitable when trying to determine binding of a transmembrane fragment to a large soluble protein. A more recent work found no binding between APP residues 713-724 and tau (182), however, these results should be regarded with caution since *no* detergent use was reported when working with a transmembrane $APP_{713-730}$ fragment. All previous studies used short peptides to investigate APP-tau binding interfaces and did not validate the $APP_{713-724}$ interfaces with full-length APP or C99. Moreover, these studies used either no detergent or non-ionic detergents that lack a phospholipid-like structure. We therefore decided to carry out quantitative NMR-monitored titrations of C99 and tau in a non-denaturing model membrane environment (LMPG micelles) to determine whether these two proteins associate under conditions that are more physiological than in the previous studies.

Titration of tau into C99 and the reverse titration led to results indicating only weak and likely non-specific binding between C99 and tau, as indicated by observation of only linear CSPs for a limited number of peaks in the spectrum of the 15N-labeled protein as a function of the concentration of the other (unlabeled) protein. Both titrations were conducted in the presence of 1 % LMPG, a mild and non-denaturing detergent, in order to provide C99 with a membrane-mimetic environment without unfolding tau. We also carried out one titration at acidic (pH4.5) and the other at neutral (pH 6.5) pH in order to try and recreate the pH range used in previous work (183-185). It is unlikely that another detergent or membrane model system would have yielded qualitatively different results. The lack of interaction reported here is in contrast to the K_D of 9.6 nM reported previously by Smith et al (183). The study by Smith and colleagues reported that the tau-C99 binding assay was done under buffer conditions that lacked detergent and the strong binding affinity they observe is likely due to aggregation of the APP transmembrane peptide.

Our results suggest that tau and *full length* C99 has little affinity for each other, at least under the conditions of our study, which involved C99 in its monomeric form and both proteins in forms where they have not been post-translationally modified. We cannot yet exclude the possibilities that the affinity of tau for the dimeric form of C99 could be higher, or that higher affinity dependent on post-translational modification in one or both proteins. We also cannot rule out the possibility that there is a C99-mediated signaling pathway leading to tau, but that there are other proteins in the chain of response from C99 to tau.

Conclusion

In summary, we find that soluble Tau and *full length* C99 in model membranes do not bind each other with significant affinity. This is inconsistent with previous peptide-based only results that indicated C99 residues 713-724 bind tau in Tween-20 and Nonidet P-40, detergents that lack phospholipid-like structure. Given that residues 713-724 of C99/APP will always be buried in the lipid bilayer under physiological conditions, the lack of interaction observed here is not surprising. While our results cannot rule the possibility that there may be conditions that we did not test in which these two proteins interact with high affinity, the unmodified and monomeric forms of these two proteins do not avidly interact under model membrane conditions.

VII. Discussion and Future Directions

Amphipols

MPs *usually* must have a lipid bilayer mimic in order to stay soluble in aqueous environments and detergents are often used for *in vitro* studies due to their ease of use and low cost (47). However, detergents are problematic for *in vivo* work due to their ability to dissolve membranes and resulting high cytotoxicity (402). The Sanders lab previously showed that amphipols could be used to deliver a membrane protein to synthetic vesicles (95) and very high concentrations of amphipols are required to observe *in vivo* cytotoxicity (57). An amphipol-quantum-dot complex had previously delivered siRNA to live cells (403) and we advanced this idea further by delivering S2-E to multiple immortalized live mammalian cell lines. As shown in **Figure 7.1**, we have successfully delivered other single pass MPs with more complicated membrane topologies to mammalian cells. It is highly likely that this method of protein delivery would work for many model organisms and could be used to quickly see how a membrane protein functions in evolutionary distant organisms. DNA transfection of mammalian cells is often toxic and certain cell lines are nearly impervious to transfection (404). The weak detergent properties of amphipols allow them to be well tolerated by mammals and also would likely enable studies of membrane protein delivery to entire small organisms such as *C. elegans.* Amphipols were used to deliver recombinant protein to multiple mammalian cell types and amphipol delivery could be a great way to “transfect” difficult immortal or primary mammalian cell lines. I personally think one great potential application of the amphipol delivery method would be to deliver MPs of interest to heterogeneous cellular environments such as organ slices.

A common complication of studying a protein of interest *in vivo* is the need to add a fluorescent tag such as green fluorescent protein (GFP)(405). GFP and other fluorescent proteins are over 200 amino acids and can be significantly larger than the protein of interest, as is the case with the 75 amino acid S2-E. The large size of GFP can introduce artifacts like blocking important protein-protein interactions or driving dimerization (406). Labs have started to address this concern and have developed much shorter fluorescent tags that require arsenic dyes or terminal labeling such as the FlAsH (376) or STELLA systems (407). Delivery of MPs with amphipols allows one to easily add small high-intensity fluorophores to any position on the protein. It should also be possible to attach method specific tags for EPR (408) studies of membrane protein in native lipid environments or ROS-generating photosensitizers (409).

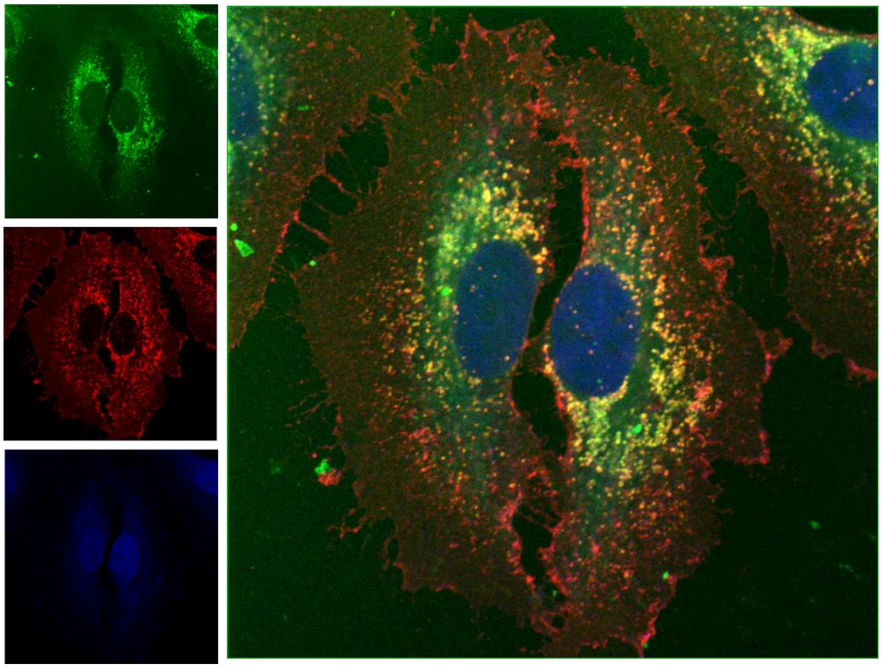

Figure 7.1. Delivery of C99 to HeLa cells with amphipols. *Confocal image of fixed HeLa cells after 16hr exposure to C99 in amphipols. Nuclei in blue are stained with DRAQ5, a DNA intercalator; PM is stained in red with WGA, a AF555 conjugated lectin; and C99 is in green due to NBD covalent labeling. Individual channels are shown on the left panels and the large right panel is the composite image.*

It must be acknowledged that the advantages mentioned above are best case scenarios and there are many unknowns when working with more complex MPs. Anionic amphipols are known to aggregate in the presence of multivalent ions (316,410,411). Even for zwitterionic amphipols we observed polymer and S2-E aggregation at higher doses in complete tissue culture media and future studies should explore use of non-ionic amphipols that are supposed to resist aggregation (412). Jean Luc Popot, a pioneer and advocate for amphipol use, posited that MPs with complex folds would have a problematic insertion/folding pathway when transitioning from amphipol to membrane (338). In support of this idea, a previous study on DAGK found that DAGK delivered to membranes from amphipols was less efficient than DAGK in amphipol mixed micelles. The lowered efficiency of DAGK in vesicles is possibly due to the unfolding/incorrect insertion during the amphipol to vesicle transition (95). Lasty, amphipols are well tolerated by cells, but cells are unlikely able to efficiently break down the polymer and it is unknown if the polymer is endocytosed along with MPs and accumulates in cells.

Membrane mimic free protein particles

Solubilization of an integral MP without detergents or lipids has traditionally required extensive computer aided mutagenesis (97-99) or fusion to an apolipoprotein scaffold (96). Magnetosome organelle integral MPs are an odd exception and can form protein "micelles" when recombinantly expressed (100-103). We here showed for the first time that several mammalian SPTPs are capable of forming water soluble membrane memetic free (MeMFs) particles. This idea is initially perplexing until one considers a SPTP to resemble the hydrophobic and hydrophilic architecture of a bolaamphiphile, a double headed detergent that can form micelles (105). MeMF particles self-satisfy their own hydrophobic and hydrophilic needs and therefore do not require any detergent to remain stable in solution. It important to highlight that MeMF particles are reversible upon addition of detergent and do not suffer hysteresis as indicated by solution NMR and CD. Structural and functional studies of MPs often require empirical screening of detergent types and buffer conditions. This can be a laborious process since a separate purification is needed for each detergent tested. The MeMF particles are easily reversed with detergent and could consequently be very beneficial during the detergent screening process.

Our work did not explore why certain SPTPs can form MeMFs and other do not. There are the many generic factors that play a role in general protein stability such as hydrogen bonding, charge distribution, and hydrophobicity. However, the high stability of C99 MeMFs and extensive previous research provides future studies with unique testable hypotheses. Both juxtamembrane regions of C99 are capable of forming transient beta sheet structure when oligomerized (188). The crowding of C99 in MeMFs results in additional beta sheet structure that is reversed upon the addition of detergent. It is possible that the beta sheet secondary structure in the juxtamembrane regions result in a stabilizing "shell" around the transmembrane core. C99 is also known to have a TM di-glycine hinge that allows for bending in the lipid bilayer (186). The additional conformational flexibility afforded by this hinge may be highly beneficial in MeMF formation and stability. All of the SPTP sequences used in this dissertation were based on *in vivo* proteins and future studies on what allows or prevents MeMF formation will undoubtably benefit from the use of more simplistic sequences.

Fluorescently labeled C99 MeMFs are readily taken up by immortalized mammalian cell lines and often appear as puncta within the cytoplasm. We are currently working to understand if the delivered C99 inserts into the lipid bilayer and is recognized like endogenous C99 via γ-secretase cleavage. It is also possible the C99 MeMF particles are catabolized and accumulate in lysosomes. Regardless, the C99 MeMFs act as a proof of concept for cellular entry. Future studies will be required for the potential of MeMFs to be fully realized.

Coronavirus envelope (E) protein

E is retained in the perinuclear space when produced by a host cell (122) but the protein/mechanism that retains E is unknown (128). It was initially unclear if our delivered recombinant S2-E would stay on the PM of mammalian cells or be trafficked back to the perinuclear space. Without knowledge of the mechanism or pathways, we observed the delivered S2-E traffics back to the TGN and is enriched in perinuclear LAMP1 positive vesicles. WGA also accumulates in the TGN and late endosome/lysosome (327,328) and showed good colocalization with S2-E. It is possible that S2-E and WGA use the same retrograde transport pathways, but this seems unlikely since WGA retrograde transport to the perinuclear space was much faster, less than 3 hours, compared to the trafficking time of S2-E, 18-24 hours. In any case, much more work needs to be done to understand how the S2-E is trafficked form the PM to the TGN.

We intended for the delivery of S2-E to act as a proof of concept for future studies on the pathogenic functions of S2-E. VLPs lack viral genetic material and offer a safe way to test if the delivered S2-E can function in its normal structural role of viral assembly. VLPs can be formed with only the M and E protein (119-121) and so delivery of S2-E to an M expressing host cell could easily test for successful S2-E incorporation into VLPs. Moreover, delivery of S2-E may allow for nuanced studies of non-structural roles for E. pH dysregulation is one of the main non-structural roles attributed to E (139,140) and the next logical step would be to determine if delivered S2-E increases organelle pH. pH dysregulation can be visually identified as swollen lysosomes in AD (198,199,375) and I think that this is likely occurring in HeLa cells when we deliver S2-E. Perinuclear lysosomes that contain S2-E appear swollen while peripheral lysosomes remain unchanged. There is some evidence that the E monomer, and not viroporin, drives the TGN pH dysregulation (139). It is easy to imagine delivering non-conducting channel mutants to cells to try and determine the contribution of viroporin formation on E function and viral fitness.

Our delivered S2-E contained a substantial C-terminal tag that did not interfere with channel function but likely does mitigate some host-E protein-protein interactions. The DLLV sequence on the C-terminus of S2-E is able to bind the tight-junction protein PALS1 (150,151) and retain PALS1 in the perinuclear space; it is thought that this retention can ultimately disrupt the tight junction and increase overall coronavirus virulence (413). Crystallographic structures indicate that the C-terminal tag on our delivered S2-E prevents this PALS1 interaction (150,151). N-terminus tagged S2-E purification protocols are now published and delivery of N-terminally tagged S2-E (414) could allow for a greater understanding of how SARS-CoV-2 can manipulate tight junctions in human airway epithelium.

The strong TGN localization of delivered S2-E opens up the possibility of using it as a retrograde trafficking tag as mutations that inhibit ion channel function are discovered. It is plausible to attach the 75 amino acid S2-E to a recombinantly expressed soluble or MPs and deliver the protein to cells with a S2-E “anchor”. If the anchor is able to auto insert or is delivered by amphipols, then there is a good chance that the protein would be endocytosed into the cell and trafficked to the TGN. Deletion of the C terminal S2-E DLLV sequence and attachment of an export sequence is required to remove S2-E from the perinuclear space (140). Therefore, any protein wanting to take advantage of the S2-E retrograde trafficking would need to be linked to the N-terminus of the protein. Previous studies of E discovered mutations that bias E towards the monomeric instead of pentameric oligomers *in vivo* and these mutations could be potentially used with an S2-E tag to control colocalization of a protein of interest.

DDMB

There is currently a dearth of solution NMR structures solved in non-ionic detergent since non-ionic detergents normally have a larger micelle than their ionic counterparts (62). The DDMB micelle is significantly smaller ~20-30kD than other commonly used non-ionic detergents like DDM (68). It was therefore straightforward to assign the TROSY-HSQC of C99 in DDMB and future studies could use DDMB to study membrane protein structure. It is now realized that the commonly used ionic dodecylphosphocholine (DPC) detergent can induce significant artifacts in MPs structures (339). Non-ionic detergents are thought to be less denaturing (63) and can be used in ligand binding experiments where ionic strength or charge repulsion of the detergent is an issue. We found that DAGK purified in DDMB had increased enzymatic activity compared to other non-ionic detergents (68), indicating that DDMB is likely less denaturing of MPs than many other commonly used detergents.

SCOR bicelle phases

Prior to our work on SCOR bicelles, there was a lack of isotropic particles that could incorporate significant amounts of both cholesterol and sphingolipids (82). DDMB was the key to the creation of SCOR bicelles and is chemically similar to commonly used non-ionic detergents such as DDM. Over 35 different detergents including DM and DDM were not able to dissolve SCOR lipids. We attribute the

SCOR-dissolving properties of DDMB to the unusual headgroup flexibility conferred by increased degrees of freedom afforded by the α(1➔6) glycosidic linkage present in the melibiose headgroup (68).

We showed in **Chapter 3** that the 4:2:1 lipid composition in detergent-free vesicles is capable of lipid-lipid phase separation near physiological temperatures but it is unknown if lipid-lipid phase separation occurs in the detergent-rich conditions of a bicelle. As shown in **Figure 7.2**, DLS solubility experiments showed that DDMB requires DMPC to solubilize both EggSM and Chol. I hypothesized that the DMPC acts as a physical buffer to mitigate repulsive forces between a DDMB rim and EggSM/Chol inner lipid core. We are currently collaborating with ORNL and the Mu-Ping lab to carry out contrast variation SANS experiments that will determine if lipid-lipid separation is present in SCOR bicelles. If lipid-lipid separation is present, it will be hard to determine if the lipid-lipid separation is due to DDMB-SM/Chol repulsive forces or to SM/Chol complex formation. Future MD simulations may be able to discern the driver of lipid-lipid separation by varying the ratios of the SCOR bicelle lipid composition. In summary, lipid-lipid separation in SCOR bicelles may not faithfully recreate the L_o-L_d phases observed in lipid bilayers but is a promising start.

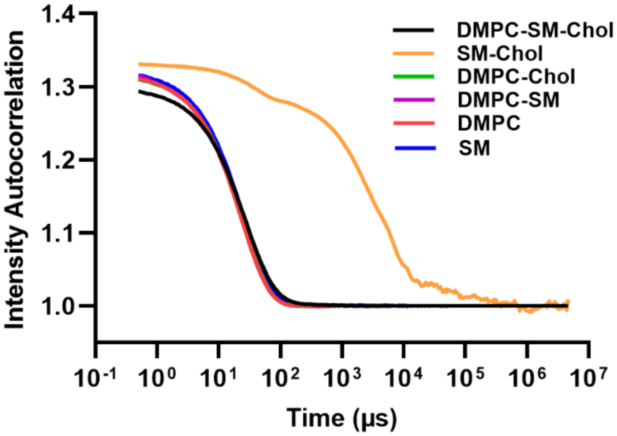

Figure 7.2: Dynamic light scattering of SCOR bicelles with various lipid compositions. *Autocorrelation curves collected for fully protonated 0.5 % wt % DDMB-based bicelle solutions of varying lipid compositions at a constant q ratio. All bicelles with the exception of DDMB-SM-Chol (no DMPC) formed bicelle particles as indicated by their overlapping curves. DDMB-SM-Chol mixtures did not form an optically clear solution as highlighted by the right-shifted curve with multiple populations, as indicated by humps in the curve.*

Future applications of SCOR bicelles

The process of assigning the NMR spectrum of C99 in SCOR bicelles was very difficult due to the large size of the SCOR bicelle and the complicated oligomeric state of C99 (188). We have looked at other MPs in SCOR bicelles and found that small MPs such as our Notch construct (350,415) give good 1H,15N TROSY-HSQC but that larger MPs such as PMP22 (40,265) do not. The size of the SCOR bicelles likely limits their overall usefulness for membrane protein structure determination via solution NMR, but it cannot be understated how SCOR bicelles were effortlessly compatible with many biophysical techniques as highlighted in **Chapter 3**. This section will focus on potential applications of SCOR bicelles that are able to leverage their beneficial and unique properties.

The most commonly used bicelle detergents have a high CMC (DHPC is 14 mM) and are not suitable for cryo-EM studies on MPs due to vesiculation upon dilution to below their CMC (298,416). DDMB has a much lower CMC, 0.3 mM, and this allows SCOR bicelles to be diluted to EM appropriate concentrations without vesiculation. SCOR bicelles were well behaved in cryo-EM and could be class averaged but were not compatible with negative stain EM when diluted, likely due to lipid-grid charge interactions. While not tested, it is likely that DDMB alone is compatible with cryo-EM since non-ionic detergents are currently used in many membrane protein cryo-EM studies (63). In an effort to study MPs in a lipid environment, many cryo-EM studies are now using Nano discs and SMALPs (63). The Sanders lab has previously tried to purify MPs in nanodiscs using the 4:2:1 lipid mixture and found extensive lipid vesiculation (rather than nanodisc assembly) following detergent removal to be a major impediment. SCOR bicelles are thus the only isotropic particle that can incorporate significant amounts of both cholesterol and sphingomyelin and are therefore an exciting option for those who want to study MP structure in a SCOR environment.

As mentioned above, SCOR bicelles can incorporate a wide range of lipid compositions. The ability to add or remove lipids to the membrane is especially important when trying to study MPs in a lipid raft-like environment. It is important to understand if observed changes in membrane protein structure or function are due to the cholesterol, sphingomyelin, the complex of cholesterol and sphingomyelin, or changes in membrane thickness. Traditional DMPC/DHPC bicelles have a bilayer thickness of ~4.2 nm (67) and SCOR bicelles have a bilayer thickness closer to ~5 nm, likely due to the ordering effect of cholesterol on DMPC (34). Comparative studies between complete SCOR bicelles and SCOR bicelles lacking lipid components, here referred to as degenerate bicelles, can allow for a nuanced understanding of how different lipid components or their complex can impact protein structure and function. As shown in **Figure 7.3**, degenerate bicelles and solution NMR were used to track C99 CSPs from removal of lipid components while maintaining the overall bicelle size. Native mass spec has implemented SCOR bicelles with great success when trying to understand the oligomeric state of both C99 and PMP22 (188,417). It would be very interesting to see a systematic study comparing the oligomeric states of MPs in the presence or absence of various lipid-raft components using degenerate and SCOR bicelles

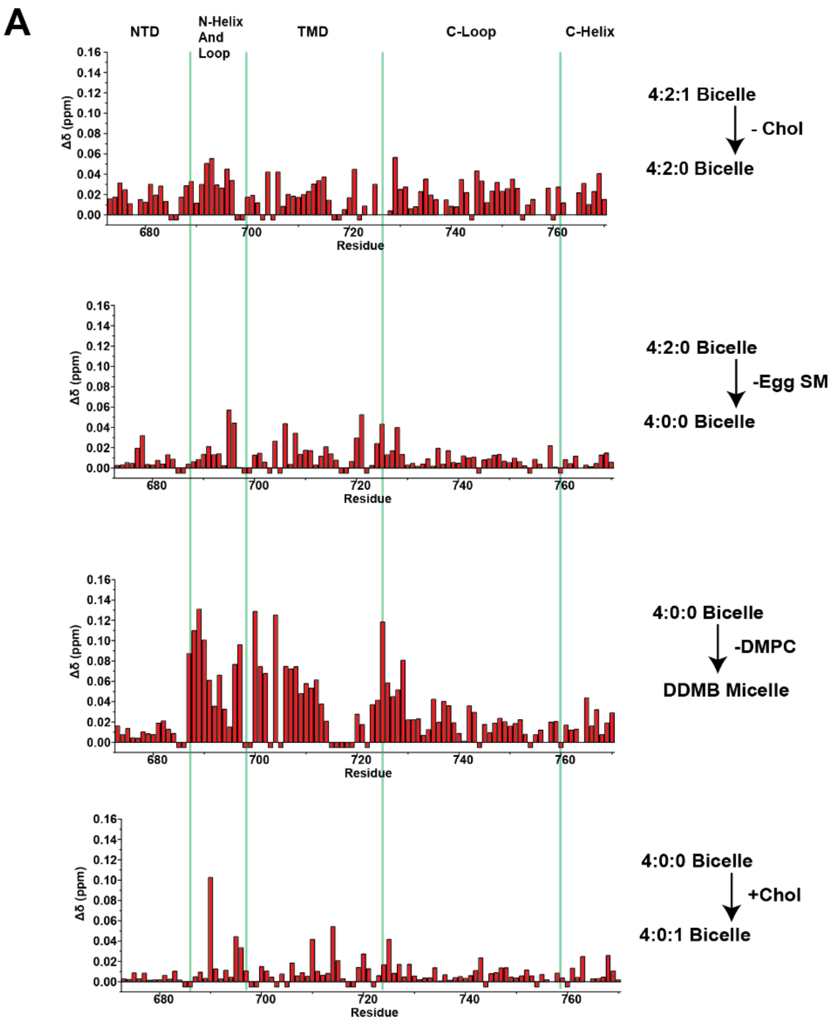

B

DMPC:EggSM:Chol at 4:2:1 Molar Ratios	Q ratio	Radius of Hydration
4:2:1	0.33	4.1
4:2:0	0.33	3.9
4:0:0	0.33	4.0
4:0:1	0.33	4.1
DDMB micelle	0	2.6

Figure 7.3: Degenerate bicelles can investigate the importance of individual SCOR lipids. *A) Combined proton and nitrogen chemical shift differences between membrane mimetics are plotted as a function of residue. Small negative bars represent residues that could not be accurately tracked between spectra or were unassigned. Green lines estimate boundaries for C99 structural regions identified in the main text. Samples were ~350 µM C99 in 10 wt % micelle/bicelle in matching buffer. B) Table showing DLS derived radius of hydration, R_h, for each degenerate bicelle. Notice how the bicelles do stay the same relative size if the q ratio is maintained.*

C99 structure in SCOR bicelles

Amyloidogenic C99 processing has many interesting connections to cholesterol and lipid rafts (186,204,205,207,208,418) and SCOR bicelles facilitated the first study of C99 structure in a SCOR environment. No obvious changes in C99 secondary structure or topology were observed when comparing SCOR bicelles to previous studies lacking sphingomyelin and cholesterol (186,232). This was initially disappointing but not surprising because C99 topology and secondary structure are resilient to changes in membrane composition (187). However, further characterization revealed C99 oligomeric interfaces and populations to be far more complex in SCOR bicelles than in LMPG or traditional bicelles.

Most methods used to determine oligomeric states of proteins were developed for soluble proteins and their translation to MPs can be problematic. Many methods such as size exclusion chromatography, DLS, and sedimentation analysis determine the oligomeric state of a protein based on the volume and mass of the protein particles (419). These size-based methods generally have a hard time observing small changes and the size of the membrane mimic can easily dwarf the size or density contributions of a small MP. SCOR bicelles are roughly ten times the mass of C99 and so these methods were not able to determine the C99 oligomeric state. We ultimately used native mass spectroscopy and chemical crosslinking do determine that C99 in SCOR bicelles was a mixture of monomer, dimer, and trimer because these techniques “remove” C99 from the SCOR bicelle.

Surprisingly, trimeric C99 was preferred over dimeric C99 in SCOR bicelles. The majority of the APP and C99 literature focus on the monomer *vs*. dimer relationship (212-214,238,243) since there is no precedent for a trimeric C99 *in vivo*. However, Higashide *et al.* showed via native PAGE that C99 is a mixture of monomer, dimer, and trimer when solubilizing mammalian cells with a non-ionic detergent, DDM (215). Furthering this point, the Sanders lab recently found that C99 is strongly excluded from the L_o phase in GPMVs derived from multiple human cell lines (223). The more ordered lipid environment of the SCOR bicelles likely forces the C99 into a higher energy state manifest as C99 trimers. The complicated oligomeric states of C99 in SCOR bicelles limits the biological conclusions that can be drawn from the structure, but the interfaces that made up these oligomeric states are rich in positing power (see below).

NMR amide backbone proton exchange and topology experiments identified regions of C99 that were believed to be oligomeric interfaces in SCOR bicelles. We identified residues 710-716 as the transmembrane oligomeric interface and this was in good agreement with *in vivo* studies that found residues 714-717 mediate C99 dimerization (238). These residues are especially exciting when considering recent studies that address topics other than C99 dimerization. A 2017 study from the Bowie lab with my advisor and myself as middle-authors looked at TM backbone hydrogen bond strength found that C99 residues T_{714} and V_{715} had backbone amide hydrogen bonds that were obviously weaker than the rest of the TM domain (420). This publication posits that these weak hydrogen bonds are weaker than water-water hydrogen bonds, but this is likely an underestimation of the true hydrogen bond strength (421). The weaker hydrogen bonds in the C99 TM domain are near the γ-secretase cleavage (GS) sites and the authors of the Bowie paper posit that the weak bonds are important for C99 function/processing. In 2019, a structure of chemically crosslinked C83 and catalytically inactive GS showed that GS unwinds the C99 TM helix prior to cleavage (373). It is not hard to imagine that backbone hydrogen bond strength plays a role in C99 unwinding during sequential GS cleavage. Weaker hydrogen bonds found in the Bowie study likely enhance the processivity of GS and encourage the production of shorter and less toxic AB peptides. It would be very interesting to look at the FAD mutations near the GS cleavage site and see if changes in backbone hydrogen bonds correlate with an increase in longer Aβ peptides.

The other oligomeric interfaces found within C99 in a SCOR environment were in the unstructured juxtamembrane regions. These regions were similarly characterized by their resistance to amide backbone proton exchange and lack of secondary structure as indicated by chemical shift analysis. The first cytosolic region consisted of residues 673–678 on the amino terminus of C99 and Aβ. These residues are known to form a β-sheet in amyloid aggregates (304), sample β-sheet structure in simulations (235), and were predicted by FTIR to participate in β-sheet formation in a truncated version of C99 lacking the cytosolic domains (372). Full length studies of monomeric C99 in LMPG did not observe any β-sheet for residues 673-678 and it is highly likely that the β-sheet structure previously observed by FTIR was due to homodimerization. This idea is supported by the fact that C99 is known to homodimerize with a K_D of ~0.5 Mol % in vesicles (204) and the FTIR experiment was done at a protein to lipid ratio of 1:50:2 Mol % (372).

As with the N-terminus, the cytosolic loop residues 735-745 of C99 appears to be unstructured when examined by chemical shift analysis but contains tertiary or quaternary structure upon closer inspection. Previous solution NMR studies looking at the soluble AICD peptide found that transient β-sheet structure was present in residues 742-747 (286,287) and NMR studies of monomeric full length C99 had difficulty assigning these peaks (186,187), an indication that these residues participate in complex dynamics. We failed to disrupt the cytosolic loop interface with mutation of key β-sheet cytosolic residues (286,287) indicating that the cytosolic loop interface is driven by colocalization of C99 transmembrane domains. The cytosolic loop of C99 is known to bind multiple regulatory soluble proteins and undergo significant post translational modifications (305). Phosphorylation at residue T743 and the resulting interaction between C99 and Pin1 has been shown to impact Aβ production (284,285,306). Moreover, the cytosolic loop of APP is likely critical for the *unknown* function of APP since it is highly resistant to mutations (422). The loop has no FAD mutations and has traditionally been eclipsed in the literature by intense focus on the Aβ peptide. I would personally like to see more research on the juxtamembrane region of APP, specifically the cytosolic loop and AICD. It is not obvious how a non-enzymatic protein like APP would transmit information about its oligomeric state into the cytosolic space. The cytosolic loop interface is only present in oligomeric C99 and likely alters the accessibility of cytosolic proteins to interface residues. It would be very interesting to quantify and compare the interaction between C99 and cytosolic binding partners as a function of C99 oligomeric state.

C99 and tau

Both APP and tau form insoluble aggregates that are widely recognized as defining hallmarks of AD (176). Several previous studies used *peptide fragments* of C99 to show APP transmembrane residues 713-724 of C99/APP bound to tau (183,184). The tau-binding C99 peptide sequences is always buried within the membrane during structural studies (186-188) and therefore the peptide is sequestered and unavailable to bind tau in *in vivo*. We carried out binding experiments between *full length* C99 and soluble tau with solution NMR and did not observe specific binding. It should be noted that both C99 and tau were expressed in bacteria and lacked any post translational modifications such as tau hyperphosphorylation. FAD mutants have recently been found to substantially increase the generation of Aβ fragments up to 49 amino acids in length and these "long-Aβs" contain significant portions of the APP 713-724 (172). While not done here, it would be interesting to see if these long-Aβ fragments are able to bind soluble tau.

Conclusions

This dissertation presents new methods for the study membrane proteins in complex and native environments. These methods were applied to disease relevant proteins and highlight the true usefulness of novel methods for addressing modern biomedical problems. There is a dearth of isotropic particles capable of solubilizing lipid raft forming lipids such as sphingomyelin and cholesterol. I characterized the first sphingolipid and cholesterol rich bicelles and showcased their suitability for a wide range of biochemical and biophysical methods by studying the structure of the Aβ precursor, C99. Ideally, all *in vitro* structural and function studies would be validated in native lipid environments but there is a lack of methods to deliver purified membrane proteins to eukaryotic cells. I developed methods to deliver recombinantly-expressed membrane proteins to mammalian cells with amphipathic polymers and model membrane free particles. These methods are unique in that they allow for *in vitro* labeling of membrane proteins before delivering them to biologically relevant membranes. It is my hope that the broader scientific community will use these methods to study their own membrane proteins and expand upon the methods described here. I am an apostle for these techniques and love discussing their future applications; feel free to contact me if you ever want to try out or are curious about the methods discussed here.

References:

1. Pfeffer, W. (1877) *Osmotische Untersuchungen; Studien zur Zellmechanik.*,
2. Robertson, J. D. (1959) The ultrastructure of cell membranes and their derivatives. *Biochemical Society symposium* **16**, 3-43
3. Singer, S. J., and Nicolson, G. L. (1972) The fluid mosaic model of the structure of cell membranes. *Science (New York, N.Y.)* **175**, 720-731
4. Bretscher, M. S. (1972) Asymmetrical Lipid Bilayer Structure for Biological Membranes. *Nature New Biology* **236**, 11-12
5. Wunderlich, F., Kreutz, W., Mahler, P., Ronai, A., and Heppeler, G. (1978) Thermotropic fluid goes to ordered "discontinuous" phase separation in microsomal lipids of Tetrahymena. An X-ray diffraction study. *Biochemistry* **17**, 2005-2010
6. van Meer, G., Voelker, D. R., and Feigenson, G. W. (2008) Membrane Lipids: Where They are and how They Behave. *Nat. Rev. Mol. Cell. Biol.* **9**, 112-124
7. Harayama, T., and Riezman, H. (2018) Understanding the diversity of membrane lipid composition. *Nat Rev Mol Cell Biol* **19**, 281-296
8. Slatter, D. A., Aldrovandi, M., O'Connor, A., Allen, S. M., Brasher, C. J., Murphy, R. C., Mecklemann, S., Ravi, S., Darley-Usmar, V., and O'Donnell, V. B. (2016) Mapping the Human Platelet Lipidome Reveals Cytosolic Phospholipase A2 as a Regulator of Mitochondrial Bioenergetics during Activation. *Cell metabolism* **23**, 930-944
9. Escribá, P. V., Busquets, X., Inokuchi, J., Balogh, G., Török, Z., Horváth, I., Harwood, J. L., and Vígh, L. (2015) Membrane lipid therapy: Modulation of the cell membrane composition and structure as a molecular base for drug discovery and new disease treatment. *Progress in lipid research* **59**, 38-53
10. Casares, D., Escribá, P. V., and Rosselló, C. A. (2019) Membrane Lipid Composition: Effect on Membrane and Organelle Structure, Function and Compartmentalization and Therapeutic Avenues. *International journal of molecular sciences* **20**
11. Pradas, I., Huynh, K., Cabré, R., Ayala, V., Meikle, P. J., Jové, M., and Pamplona, R. (2018) Lipidomics Reveals a Tissue-Specific Fingerprint. *Frontiers in physiology* **9**, 1165
12. Marlow, B., Kuenze, G., Li, B., Sanders, C. R., and Meiler, J. (2021) Structural determinants of cholesterol recognition in helical integral membrane proteins. *Biophysical journal* **120**, 1592-1604
13. Noy, N. (2007) Ligand specificity of nuclear hormone receptors: sifting through promiscuity. *Biochemistry* **46**, 13461-13467
14. Hansen, S. B. (2015) Lipid agonism: The PIP2 paradigm of ligand-gated ion channels. *Biochim Biophys Acta* **1851**, 620-628
15. Lee, A. G. (2004) How lipids affect the activities of integral membrane proteins. *Biochim Biophys Acta* **1666**, 62-87
16. London, E. (2019) Membrane Structure-Function Insights from Asymmetric Lipid Vesicles. *Acc Chem Res* **52**, 2382-2391
17. Lorent, J. H., Diaz-Rohrer, B., Lin, X., Spring, K., Gorfe, A. A., Levental, K. R., and Levental, I. (2017) Structural determinants and functional consequences of protein affinity for membrane rafts. *Nat Commun* **8**, 1219

18. Moeller, C. H., Mudd, J. B., and Thomson, W. W. (1981) Lipid phase separations and intramembranous particle movements in the yeast tonoplast. *Biochim Biophys Acta* **643**, 376-386
19. Nickels, J. D., Chatterjee, S., Stanley, C. B., Qian, S., Cheng, X., Myles, D. A. A., Standaert, R. F., Elkins, J. G., and Katsaras, J. (2017) The in vivo Structure of Biological Membranes and Evidence for Lipid Domains. *PLoS biology* **15**, e2002214
20. Veatch, S. L., and Keller, S. L. (2003) Separation of liquid phases in giant vesicles of ternary mixtures of phospholipids and cholesterol. *Biophysical journal* **85**, 3074-3083
21. Marsh, D. (2009) Cholesterol-induced fluid membrane domains: a compendium of lipid-raft ternary phase diagrams. *Biochim Biophys Acta* **1788**, 2114-2123
22. Kranenburg, M., and Smit, B. (2005) Phase behavior of model lipid bilayers. *J Phys Chem B* **109**, 6553-6563
23. Seelig, J. (1978) 31P Nuclear Magnetic Resonance and the Head Group Structure of Phospholipids in Membranes. *Biochim. Biophys. Acta* **515**, 105-140
24. Filippov, A., Orädd, G., and Lindblom, G. (2004) Lipid lateral diffusion in ordered and disordered phases in raft mixtures. *Biophysical journal* **86**, 891-896
25. Marsh, D. (2010) Structural and thermodynamic determinants of chain-melting transition temperatures for phospholipid and glycolipids membranes. *Biochim Biophys Acta* **1798**, 40-51
26. Wang, G., Li, S., Lin, H., Brumbaugh, E. E., and Huang, C. (1999) Effects of various numbers and positions of cis double bonds in the sn-2 acyl chain of phosphatidylethanolamine on the chain-melting temperature. *The Journal of biological chemistry* **274**, 12289-12299
27. Veatch, S. L., Soubias, O., Keller, S. L., and Gawrisch, K. (2007) Critical Fluctuations in Domain-forming Lipid Mixtures. *Proceedings of the National Academy of Sciences of the United States of America* **104**, 17650-17655
28. Clarke, J. A., Heron, A. J., Seddon, J. M., and Law, R. V. (2006) The Diversity of the Liquid Ordered (Lo) Phase of Phosphatidylcholine/Cholesterol Membranes: A Variable Temperature Multinuclear Solid-state NMR and X-ray Diffraction Study. *Biophys. J.* **90**, 2383-2393
29. Simons, K., and Ikonen, E. (1997) Functional Rafts in Cell Membranes. *Nature* **387**, 569-572
30. Brown, D. A., and London, E. (1998) Functions of Lipid Rafts in Biological Membranes. *Annu. Rev. Cell Dev. Biol.* **14**, 111-136
31. Sezgin, E., Levental, I., Mayor, S., and Eggeling, C. (2017) The Mystery of Membrane Organization: Composition, Regulation and Roles of Lipid Rafts. *Nat. Rev. Mol. Cell. Biol.* **18**, 361-374
32. Tsamaloukas, A., Szadkowska, H., and Heerklotz, H. (2006) Thermodynamic Comparison of the Interactions of Cholesterol with Unsaturated Phospholipid and Sphingomyelins. *Biophys. J.* **90**, 4479-4487
33. Endapally, S., Frias, D., Grzemska, M., Gay, A., Tomchick, D. R., and Radhakrishnan, A. (2019) Molecular Discrimination between Two Conformations of Sphingomyelin in Plasma Membranes. *Cell* **176**, 1040-1053.e1017
34. Pencer, J., Nieh, M. P., Harroun, T. A., Krueger, S., Adams, C., and Katsaras, J. (2005) Bilayer Thickness and Thermal Response of Dimyristoylphosphatidylcholine Unilamellar Vesicles Containing Cholesterol, Ergosterol and Lanosterol: A Small-angle Neutron Scattering Study. *Biochim. Biophys. Acta* **1720**, 84-91
35. Honerkamp-Smith, A. R., Veatch, S. L., and Keller, S. L. (2009) An Introduction to Critical Points for Biophysicists; Observations of Compositional Heterogeneity in Lipid Membranes. *Biochim. Biophys. Acta* **1788**, 53-63

36. Burns, M., Wisser, K., Wu, J., Levental, I., and Veatch, S. L. (2017) Miscibility Transition Temperature Scales with Growth Temperature in a Zebrafish Cell Line. *Biophysical journal* **113**, 1212-1222
37. Baumgart, T., Hammond, A. T., Sengupta, P., Hess, S. T., Holowka, D. A., Baird, B. A., and Webb, W. W. (2007) Large-scale fluid/fluid phase separation of proteins and lipids in giant plasma membrane vesicles. *Proc Natl Acad Sci U S A* **104**, 3165-3170
38. Heberle, F. A., Doktorova, M., Scott, H. L., Skinkle, A. D., Waxham, M. N., and Levental, I. (2020) Direct label-free imaging of nanodomains in biomimetic and biological membranes by cryogenic electron microscopy. *Proc Natl Acad Sci U S A* **117**, 19943-19952
39. Schuck, S., Honsho, M., Ekroos, K., Shevchenko, A., and Simons, K. (2003) Resistance of cell membranes to different detergents. *Proc Natl Acad Sci U S A* **100**, 5795-5800
40. Marinko, J. T., Kenworthy, A. K., and Sanders, C. R. (2020) Peripheral myelin protein 22 preferentially partitions into ordered phase membrane domains. *Proc Natl Acad Sci U S A* **117**, 14168-14177
41. Levental, I., Levental, K. R., and Heberle, F. A. (2020) Lipid Rafts: Controversies Resolved, Mysteries Remain. *Trends in cell biology* **30**, 341-353
42. Owen, D. M., Williamson, D. J., Magenau, A., and Gaus, K. (2012) Sub-resolution lipid domains exist in the plasma membrane and regulate protein diffusion and distribution. *Nat Commun* **3**, 1256
43. Gao, X., Lowry, P. R., Zhou, X., Depry, C., Wei, Z., Wong, G. W., and Zhang, J. (2011) PI3K/Akt signaling requires spatial compartmentalization in plasma membrane microdomains. *Proc Natl Acad Sci U S A* **108**, 14509-14514
44. Cheng, P. C., Brown, B. K., Song, W., and Pierce, S. K. (2001) Translocation of the B cell antigen receptor into lipid rafts reveals a novel step in signaling. *Journal of immunology (Baltimore, Md. : 1950)* **166**, 3693-3701
45. García-Sáez, A. J., Chiantia, S., and Schwille, P. (2007) Effect of line tension on the lateral organization of lipid membranes. *The Journal of biological chemistry* **282**, 33537-33544
46. Gray, E. M., Díaz-Vázquez, G., and Veatch, S. L. (2015) Growth Conditions and Cell Cycle Phase Modulate Phase Transition Temperatures in RBL-2H3 Derived Plasma Membrane Vesicles. *PloS one* **10**, e0137741
47. Seddon, A. M., Curnow, P., and Booth, P. J. (2004) Membrane proteins, lipids and detergents: not just a soap opera. *Biochim Biophys Acta* **1666**, 105-117
48. Dufourc, E. J. (2021) Bicelles and nanodiscs for biophysical chemistry. *Biochimica et biophysica acta. Biomembranes* **1863**, 183478
49. Ishchenko, A., Abola, E. E., and Cherezov, V. (2017) Crystallization of Membrane Proteins: An Overview. *Methods in molecular biology (Clifton, N.J.)* **1607**, 117-141
50. Kaplan, M., Narasimhan, S., de Heus, C., Mance, D., van Doorn, S., Houben, K., Popov-Čeleketić, D., Damman, R., Katrukha, E. A., Jain, P., Geerts, W. J. C., Heck, A. J. R., Folkers, G. E., Kapitein, L. C., Lemeer, S., van Bergen En Henegouwen, P. M. P., and Baldus, M. (2016) EGFR Dynamics Change during Activation in Native Membranes as Revealed by NMR. *Cell* **167**, 1241-1251.e1211
51. Miles, A. J., and Wallace, B. A. (2016) Circular dichroism spectroscopy of membrane proteins. *Chemical Society reviews* **45**, 4859-4872
52. Sanders, C. R., and Prosser, R. S. (1998) Bicelles: a Model Membrane System for All Seasons? *Structure* **6**, 1227-1234
53. Dürr, U. H., Gildenberg, M., and Ramamoorthy, A. (2012) The Magic of Bicelles Lights up Membrane Protein sStructure. *Chemical reviews* **112**, 6054-6074
54. Denisov, I. G., and Sligar, S. G. (2017) Nanodiscs in Membrane Biochemistry and Biophysics. *Chemical reviews* **117**, 4669-4713

55. Klopfer, K., and Hagn, F. (2019) Beyond Detergent Micelles: The Advantages and Applications of Non-micellar and Lipid-based Membrane Mimetics for Solution-state NMR. *Prog. Nucl. Magn. Reson. Spectrosc.* **114-115**, 271-283
56. Tribet, C., Audebert, R., and Popot, J. L. (1996) Amphipols: polymers that keep membrane proteins soluble in aqueous solutions. *Proc. Natl. Acad. Sci. U S A* **93**, 15047-15050
57. Popot, J. L., Berry, E. A., Charvolin, D., Creuzenet, C., Ebel, C., Engelman, D. M., Flotenmeyer, M., Giusti, F., Gohon, Y., Hong, Q., Lakey, J. H., Leonard, K., Shuman, H. A., Timmins, P., Warschawski, D. E., Zito, F., Zoonens, M., Pucci, B., and Tribet, C. (2003) Amphipols: polymeric surfactants for membrane biology research. *Cell Mol. Life Sci.* **60**, 1559-1574
58. Garavito, R. M., and Ferguson-Miller, S. (2001) Detergents as tools in membrane biochemistry. *The Journal of biological chemistry* **276**, 32403-32406
59. Lichtenberg, D., Ahyayauch, H., Alonso, A., and Goñi, F. M. (2013) Detergent solubilization of lipid bilayers: a balance of driving forces. *Trends in biochemical sciences* **38**, 85-93
60. Dominguez, A., Fernandez, A., Gonzalez, N., Iglesias, E., and Montenegro, L. (1997) Determination of Critical Micelle Concentration of Some Surfactants by Three Techniques. *Journal of Chemical Education* **74**, 1227
61. Tummino, P. J., and Gafni, A. (1993) Determination of the aggregation number of detergent micelles using steady-state fluorescence quenching. *Biophysical journal* **64**, 1580-1587
62. Lipfert, J., Columbus, L., Chu, V. B., Lesley, S. A., and Doniach, S. (2007) Size and Shape of Detergent Micelles Determined by Small-angle X-ray Scattering. *The journal of physical chemistry. B* **111**, 12427-12438
63. Choy, B. C., Cater, R. J., Mancia, F., and Pryor, E. E., Jr. (2021) A 10-year meta-analysis of membrane protein structural biology: Detergents, membrane mimetics, and structure determination techniques. *Biochimica et biophysica acta. Biomembranes* **1863**, 183533
64. Warschawski, D. E., Arnold, A. A., Beaugrand, M., Gravel, A., Chartrand, É., and Marcotte, I. (2011) Choosing membrane mimetics for NMR structural studies of transmembrane proteins. *Biochim Biophys Acta* **1808**, 1957-1974
65. Fuglestad, B., Marques, B. S., Jorge, C., Kerstetter, N. E., Valentine, K. G., and Wand, A. J. (2019) Reverse Micelle Encapsulation of Proteins for NMR Spectroscopy. *Methods Enzymol* **615**, 43-75
66. Valentine, K. G., Peterson, R. W., Saad, J. S., Summers, M. F., Xu, X., Ames, J. B., and Wand, A. J. (2010) Reverse micelle encapsulation of membrane-anchored proteins for solution NMR studies. *Structure* **18**, 9-16
67. Caldwell, T. A., Baoukina, S., Brock, A. T., Oliver, R. C., Root, K. T., Krueger, J. K., Glover, K. J., Tieleman, D. P., and Columbus, L. (2018) Low- q Bicelles are Mixed Micelles. *J. Phys. Chem. Lett.* **9**, 4469-4473
68. Hutchison, J. M., Lu, Z., Li, G. C., Travis, B., Mittal, R., Deatherage, C. L., and Sanders, C. R. (2017) Dodecyl-beta-melibioside Detergent Micelles as a Medium for Membrane Proteins. *Biochemistry* **56**, 5481-5484
69. Katsaras, J., Harroun, T. A., Pencer, J., and Nieh, M. P. (2005) "Bicellar" Lipid Mixtures as Used in Biochemical and Biophysical Studies. *Naturwissenschaften* **92**, 355-366
70. Sanders, C. R., 2nd, and Schwonek, J. P. (1992) Characterization of Magnetically Orientable Bilayers in Mixtures of Dihexanoylphosphatidylcholine and Dimyristoylphosphatidylcholine by Solid-state NMR. *Biochemistry* **31**, 8898-8905
71. Sanders, C. R., Hare, B. J., Howard, K. P., and Prestegard, J. H. (1994) Magnetically-oriented phospholipid micelles as a tool for the study of membrane-associated molecules. *Progress in Nuclear Magnetic Resonance Spectroscopy* **26**, 421-444
72. Sanders, C. R., 2nd, and Landis, G. C. (1995) Reconstitution of membrane proteins into lipid-rich bilayered mixed micelles for NMR studies. *Biochemistry* **34**, 4030-4040

73. Bax, A., and Tjandra, N. (1997) High-resolution heteronuclear NMR of human ubiquitin in an aqueous liquid crystalline medium. *Journal of biomolecular NMR* **10**, 289-292

74. Tjandra, N., and Bax, A. (1997) Direct measurement of distances and angles in biomolecules by NMR in a dilute liquid crystalline medium. *Science (New York, N.Y.)* **278**, 1111-1114

75. Ujwal, R., and Bowie, J. U. (2011) Crystallizing membrane proteins using lipidic bicelles. *Methods (San Diego, Calif.)* **55**, 337-341

76. Piai, A., Fu, Q., Dev, J., and Chou, J. J. (2017) Optimal Bicelle Size q for Solution NMR Studies of the Protein Transmembrane Partition. *Chemistry (Weinheim an der Bergstrasse, Germany)* **23**, 1361-1367

77. Schmidt, T., Situ, A. J., and Ulmer, T. S. (2016) Direct Evaluation of Protein-Lipid Contacts Reveals Protein Membrane Immersion and Isotropic Bicelle Structure. *J. Phys. Chem. Lett.* **7**, 4420-4426

78. Schmidt, M. L., and Davis, J. H. (2016) Liquid Disordered-liquid Ordered Phase Coexistence in Bicelles Containing Unsaturated Lipids and Cholesterol. *Biochim. Biophys. Acta* **1858**, 619-626

79. Cho, H. S., Dominick, J. L., and Spence, M. M. (2010) Lipid Domains in Bicelles Containing Unsaturated Lipids and Cholesterol. *The journal of physical chemistry. B* **114**, 9238-9245

80. Minto, R. E., Adhikari, P. R., and Lorigan, G. A. (2004) A 2H Solid-state NMR Spectroscopic Investigation of Biomimetic Bicelles Containing Cholesterol and Polyunsaturated Phosphatidylcholine. *Chemistry and physics of lipids* **132**, 55-64

81. Yamaguchi, T., Suzuki, T., Yasuda, T., Oishi, T., Matsumori, N., and Murata, M. (2012) NMR-based Conformational Analysis of Sphingomyelin in Bicelles. *Bioorganic & medicinal chemistry* **20**, 270-278

82. Kot, E. F., Arseniev, A. S., and Mineev, K. S. (2018) Behavior of Most Widely Spread Lipids in Isotropic Bicelles. *Langmuir : the ACS journal of surfaces and colloids* **34**, 8302-8313

83. Rouck, J. E., Krapf, J. E., Roy, J., Huff, H. C., and Das, A. (2017) Recent Advances in Nanodisc Technology for Membrane Protein Studies (2012-2017). *FEBS Lett.* **591**, 2057-2088

84. Postis, V., Rawson, S., Mitchell, J. K., Lee, S. C., Parslow, R. A., Dafforn, T. R., Baldwin, S. A., and Muench, S. P. (2015) The use of SMALPs as a Novel Membrane Protein Scaffold for Structure Study by Negative Stain Electron Microscopy. *Biochim. Biophys. Acta* **1848**, 496-501

85. Simon, K. S., Pollock, N. L., and Lee, S. C. (2018) Membrane Protein Nanoparticles: the Shape of Things to Come. *Biochemical Society transactions* **46**, 1495-1504

86. Bayburt, T. H., Grinkova, Y. V., and Sligar, S. G. (2002) Self-Assembly of Discoidal Phospholipid Bilayer Nanoparticles with Membrane Scaffold Proteins. *Nano Letters* **2**, 853-856

87. Denisov, I. G., Grinkova, Y. V., Lazarides, A. A., and Sligar, S. G. (2004) Directed self-assembly of monodisperse phospholipid bilayer Nanodiscs with controlled size. *Journal of the American Chemical Society* **126**, 3477-3487

88. Jamshad, M., Grimard, V., Idini, I., Knowles, T. J., Dowle, M. R., Schofield, N., Sridhar, P., Lin, Y. P., Finka, R., Wheatley, M., Thomas, O. R., Palmer, R. E., Overduin, M., Govaerts, C., Ruysschaert, J. M., Edler, K. J., and Dafforn, T. R. (2015) Structural analysis of a nanoparticle containing a lipid bilayer used for detergent-free extraction of membrane proteins. *Nano research* **8**, 774-789

89. Teo, A. C. K., Lee, S. C., Pollock, N. L., Stroud, Z., Hall, S., Thakker, A., Pitt, A. R., Dafforn, T. R., Spickett, C. M., and Roper, D. I. (2019) Analysis of SMALP co-extracted phospholipids shows distinct membrane environments for three classes of bacterial membrane protein. *Scientific Reports* **9**, 1813

90. Knowles, T. J., Finka, R., Smith, C., Lin, Y. P., Dafforn, T., and Overduin, M. (2009) Membrane proteins solubilized intact in lipid containing nanoparticles bounded by styrene maleic acid copolymer. *Journal of the American Chemical Society* **131**, 7484-7485

91. Tifrea, D. F., Pal, S., Le Bon, C., Giusti, F., Popot, J. L., Cocco, M. J., Zoonens, M., and de la Maza, L. M. (2018) Co-delivery of amphipol-conjugated adjuvant with antigen, and adjuvant

combinations, enhance immune protection elicited by a membrane protein-based vaccine against a mucosal challenge with Chlamydia. *Vaccine* **36**, 6640-6649

92. Tifrea, D. F., Pal, S., le Bon, C., Cocco, M. J., Zoonens, M., and de la Maza, L. M. (2020) Improved protection against Chlamydia muridarum using the native major outer membrane protein trapped in Resiquimod-carrying amphipols and effects in protection with addition of a Th1 (CpG-1826) and a Th2 (Montanide ISA 720) adjuvant. *Vaccine* **38**, 4412-4422
93. Nagy, J. K., Kuhn Hoffmann, A., Keyes, M. H., Gray, D. N., Oxenoid, K., and Sanders, C. R. (2001) Use of amphipathic polymers to deliver a membrane protein to lipid bilayers. *FEBS Lett.* **501**, 115-120
94. Mizrachi, D., Chen, Y., Liu, J., Peng, H. M., Ke, A., Pollack, L., Turner, R. J., Auchus, R. J., and DeLisa, M. P. (2015) Making water-soluble integral membrane proteins in vivo using an amphipathic protein fusion strategy. *Nat Commun* **6**, 6826
95. Slovic, A. M., Kono, H., Lear, J. D., Saven, J. G., and DeGrado, W. F. (2004) Computational design of water-soluble analogues of the potassium channel KcsA. *Proceedings of the National Academy of Sciences* **101**, 1828-1833
96. Ma, D., Tillman, T. S., Tang, P., Meirovitch, E., Eckenhoff, R., Carnini, A., and Xu, Y. (2008) NMR studies of a channel protein without membranes: Structure and dynamics of water-solubilized KcsA. *Proceedings of the National Academy of Sciences* **105**, 16537-16542
97. Mizrachi, D., Robinson, M.-P., Ren, G., Ke, N., Berkmen, M., and DeLisa, M. P. (2017) A water-soluble DsbB variant that catalyzes disulfide-bond formation in vivo. *Nature Chemical Biology* **13**, 1022-1028
98. Uebe, R., and Schüler, D. (2016) Magnetosome biogenesis in magnetotactic bacteria. *Nature Reviews Microbiology* **14**, 621-637
99. Arakaki, A., Webb, J., and Matsunaga, T. (2003) A novel protein tightly bound to bacterial magnetic particles in Magnetospirillum magneticum strain AMB-1. *The Journal of biological chemistry* **278**, 8745-8750
100. Feng, S., Wang, L., Palo, P., Liu, X., Mallapragada, S. K., and Nilsen-Hamilton, M. (2013) Integrated self-assembly of the Mms6 magnetosome protein to form an iron-responsive structure. *International journal of molecular sciences* **14**, 14594-14606
101. Kashyap, S., Woehl, T., Valverde-Tercedor, C., Sánchez-Quesada, M., Jiménez López, C., and Prozorov, T. (2014) Visualization of Iron-Binding Micelles in Acidic Recombinant Biomineralization Protein, MamC. *Journal of Nanomaterials* **2014**, 320124
102. Rawlings, A. E., Bramble, J. P., Walker, R., Bain, J., Galloway, J. M., and Staniland, S. S. (2014) Self-assembled MmsF proteinosomes control magnetite nanoparticle formation in vitro. *Proc Natl Acad Sci U S A* **111**, 16094-16099
103. Fuhrhop, J.-H., and Wang, T. (2004) Bolaamphiphiles. *Chemical reviews* **104**, 2901-2938
104. Polack, F. P., Thomas, S. J., Kitchin, N., Absalon, J., Gurtman, A., Lockhart, S., Perez, J. L., Perez Marc, G., Moreira, E. D., Zerbini, C., Bailey, R., Swanson, K. A., Roychoudhury, S., Koury, K., Li, P., Kalina, W. V., Cooper, D., Frenck, R. W., Jr., Hammitt, L. L., Tureci, O., Nell, H., Schaefer, A., Unal, S., Tresnan, D. B., Mather, S., Dormitzer, P. R., Sahin, U., Jansen, K. U., Gruber, W. C., and Group, C. C. T. (2020) Safety and Efficacy of the BNT162b2 mRNA Covid-19 Vaccine. *N. Engl. J. Med.* **383**, 2603-2615
105. Baden, L. R., El Sahly, H. M., Essink, B., Kotloff, K., Frey, S., Novak, R., Diemert, D., Spector, S. A., Rouphael, N., Creech, C. B., McGettigan, J., Kehtan, S., Segall, N., Solis, J., Brosz, A., Fierro, C., Schwartz, H., Neuzil, K., Corey, L., Gilbert, P., Janes, H., Follmann, D., Marovich, M., Mascola, J., Polakowski, L., Ledgerwood, J., Graham, B. S., Bennett, H., Pajon, R., Knightly, C., Leav, B., Deng, W., Zhou, H., Han, S., Ivarsson, M., Miller, J., Zaks, T., and Group, C. S. (2020) Efficacy and Safety of the mRNA-1273 SARS-CoV-2 Vaccine. *N. Engl. J. Med.*

106. V'Kovski, P., Kratzel, A., Steiner, S., Stalder, H., and Thiel, V. (2021) Coronavirus biology and replication: implications for SARS-CoV-2. *Nature reviews. Microbiology* **19**, 155-170
107. Mahdy, M. A. A., Younis, W., and Ewaida, Z. (2020) An Overview of SARS-CoV-2 and Animal Infection. *Front. Vet. Sci.* **7**, 596391
108. Zaki, A. M., van Boheemen, S., Bestebroer, T. M., Osterhaus, A. D., and Fouchier, R. A. (2012) Isolation of a novel coronavirus from a man with pneumonia in Saudi Arabia. *N. Engl. J. Med.* **367**, 1814-1820
109. Drosten, C., Gunther, S., Preiser, W., van der Werf, S., Brodt, H. R., Becker, S., Rabenau, H., Panning, M., Kolesnikova, L., Fouchier, R. A., Berger, A., Burguiere, A. M., Cinatl, J., Eickmann, M., Escriou, N., Grywna, K., Kramme, S., Manuguerra, J. C., Muller, S., Rickerts, V., Sturmer, M., Vieth, S., Klenk, H. D., Osterhaus, A. D., Schmitz, H., and Doerr, H. W. (2003) Identification of a novel coronavirus in patients with severe acute respiratory syndrome. *N. Engl. J. Med.* **348**, 1967-1976
110. Alluwaimi, A. M., Alshubaith, I. H., Al-Ali, A. M., and Abohelaika, S. (2020) The Coronaviruses of Animals and Birds: Their Zoonosis, Vaccines, and Models for SARS-CoV and SARS-CoV2. *Frontiers in veterinary science* **7**, 582287
111. Jia, H. P., Look, D. C., Shi, L., Hickey, M., Pewe, L., Netland, J., Farzan, M., Wohlford-Lenane, C., Perlman, S., and McCray, P. B., Jr. (2005) ACE2 receptor expression and severe acute respiratory syndrome coronavirus infection depend on differentiation of human airway epithelia. *J Virol* **79**, 14614-14621
112. Lan, J., Ge, J., Yu, J., Shan, S., Zhou, H., Fan, S., Zhang, Q., Shi, X., Wang, Q., Zhang, L., and Wang, X. (2020) Structure of the SARS-CoV-2 spike receptor-binding domain bound to the ACE2 receptor. *Nature* **581**, 215-220
113. Shang, J., Ye, G., Shi, K., Wan, Y., Luo, C., Aihara, H., Geng, Q., Auerbach, A., and Li, F. (2020) Structural basis of receptor recognition by SARS-CoV-2. *Nature* **581**, 221-224
114. Ke, Z., Oton, J., Qu, K., Cortese, M., Zila, V., McKeane, L., Nakane, T., Zivanov, J., Neufeldt, C. J., Cerikan, B., Lu, J. M., Peukes, J., Xiong, X., Kräusslich, H.-G., Scheres, S. H. W., Bartenschlager, R., and Briggs, J. A. G. (2020) Structures and distributions of SARS-CoV-2 spike proteins on intact virions. *Nature* **588**, 498-502
115. McBride, R., van Zyl, M., and Fielding, B. C. (2014) The coronavirus nucleocapsid is a multifunctional protein. *Viruses* **6**, 2991-3018
116. Neuman, B. W., Kiss, G., Kunding, A. H., Bhella, D., Baksh, M. F., Connelly, S., Droese, B., Klaus, J. P., Makino, S., Sawicki, S. G., Siddell, S. G., Stamou, D. G., Wilson, I. A., Kuhn, P., and Buchmeier, M. J. (2011) A structural analysis of M protein in coronavirus assembly and morphology. *J Struct Biol* **174**, 11-22
117. Corse, E., and Machamer, C. E. (2000) Infectious bronchitis virus E protein is targeted to the Golgi complex and directs release of virus-like particles. *J. Virol.* **74**, 4319-4326
118. Corse, E., and Machamer, C. E. (2003) The cytoplasmic tails of infectious bronchitis virus E and M proteins mediate their interaction. *Virology* **312**, 25-34
119. Vennema, H., Godeke, G. J., Rossen, J. W., Voorhout, W. F., Horzinek, M. C., Opstelten, D. J., and Rottier, P. J. (1996) Nucleocapsid-independent assembly of coronavirus-like particles by co-expression of viral envelope protein genes. *EMBO J.* **15**, 2020-2028
120. Venkatagopalan, P., Daskalova, S. M., Lopez, L. A., Dolezal, K. A., and Hogue, B. G. (2015) Coronavirus envelope (E) protein remains at the site of assembly. *Virology* **478**, 75-85
121. Stertz, S., Reichelt, M., Spiegel, M., Kuri, T., Martínez-Sobrido, L., García-Sastre, A., Weber, F., and Kochs, G. (2007) The intracellular sites of early replication and budding of SARS-coronavirus. *Virology* **361**, 304-315

122. Tooze, J., Tooze, S. A., and Fuller, S. D. (1987) Sorting of progeny coronavirus from condensed secretory proteins at the exit from the trans-Golgi network of AtT20 cells. *J Cell Biol* **105**, 1215-1226
123. Machamer, C. E. (2013) Accommodation of large cargo within Golgi cisternae. *Histochem Cell Biol* **140**, 261-269
124. Ghosh, S., Dellibovi-Ragheb, T. A., Kerviel, A., Pak, E., Qiu, Q., Fisher, M., Takvorian, P. M., Bleck, C., Hsu, V. W., Fehr, A. R., Perlman, S., Achar, S. R., Straus, M. R., Whittaker, G. R., de Haan, C. A. M., Kehrl, J., Altan-Bonnet, G., and Altan-Bonnet, N. (2020) beta-Coronaviruses Use Lysosomes for Egress Instead of the Biosynthetic Secretory Pathway. *Cell* **183**, 1520-1535 e1514
125. Mendonça, L., Howe, A., Gilchrist, J. B., Sun, D., Knight, M. L., Zanetti-Domingues, L. C., Bateman, B., Krebs, A. S., Chen, L., Radecke, J., Sheng, Y., Li, V. D., Ni, T., Kounatidis, I., Koronfel, M. A., Szynkiewicz, M., Harkiolaki, M., Martin-Fernandez, M. L., James, W., and Zhang, P. (2020) SARS-CoV-2 Assembly and Egress Pathway Revealed by Correlative Multi-modal Multi-scale Cryo-imaging. *bioRxiv*
126. Schoeman, D., and Fielding, B. C. (2019) Coronavirus envelope protein: current knowledge. *Virol. J.* **16**, 69
127. Lim, K. P., and Liu, D. X. (2001) The missing link in coronavirus assembly. Retention of the avian coronavirus infectious bronchitis virus envelope protein in the pre-Golgi compartments and physical interaction between the envelope and membrane proteins. *J. Biol. Chem.* **276**, 17515-17523
128. To, J., Surya, W., Fung, T. S., Li, Y., Verdia-Baguena, C., Queralt-Martin, M., Aguilella, V. M., Liu, D. X., and Torres, J. (2017) Channel-Inactivating Mutations and Their Revertant Mutants in the Envelope Protein of Infectious Bronchitis Virus. *J. Virol.* **91**
129. Raamsman, M. J., Locker, J. K., de Hooge, A., de Vries, A. A., Griffiths, G., Vennema, H., and Rottier, P. J. (2000) Characterization of the coronavirus mouse hepatitis virus strain A59 small membrane protein E. *J. Virol.* **74**, 2333-2342
130. Kuo, L., Hurst, K. R., and Masters, P. S. (2007) Exceptional flexibility in the sequence requirements for coronavirus small envelope protein function. *J Virol* **81**, 2249-2262
131. Westerbeck, J. W., and Machamer, C. E. (2015) A Coronavirus E Protein Is Present in Two Distinct Pools with Different Effects on Assembly and the Secretory Pathway. *J. Virol.* **89**, 9313-9323
132. Mandala, V. S., McKay, M. J., Shcherbakov, A. A., Dregni, A. J., Kolocouris, A., and Hong, M. (2020) Structure and drug binding of the SARS-CoV-2 envelope protein transmembrane domain in lipid bilayers. *Nat. Struct. Mol. Biol.* **27**, 1202-1208
133. Parthasarathy, K., Ng, L., Lin, X., Liu, D. X., Pervushin, K., Gong, X., and Torres, J. (2008) Structural flexibility of the pentameric SARS coronavirus envelope protein ion channel. *Biophys. J.* **95**, L39-41
134. Pervushin, K., Tan, E., Parthasarathy, K., Lin, X., Jiang, F. L., Yu, D., Vararattanavech, A., Soong, T. W., Liu, D. X., and Torres, J. (2009) Structure and inhibition of the SARS coronavirus envelope protein ion channel. *PLoS Pathog.* **5**, e1000511
135. Cady, S. D., Luo, W., Hu, F., and Hong, M. (2009) Structure and function of the influenza A M2 proton channel. *Biochemistry* **48**, 7356-7364
136. Pielak, R. M., and Chou, J. J. (2011) Influenza M2 proton channels. *Biochim. Biophys. Acta* **1808**, 522-529
137. Westerbeck, J. W., and Machamer, C. E. (2019) The Infectious Bronchitis Coronavirus Envelope Protein Alters Golgi pH To Protect the Spike Protein and Promote the Release of Infectious Virus. *J Virol* **93**

138. Cabrera-Garcia, D., Bekdash, R., Abbott, G. W., Yazawa, M., and Harrison, N. L. (2021) The envelope protein of SARS-CoV-2 increases intra-Golgi pH and forms a cation channel that is regulated by pH. *J Physiol*

139. Xia, B., Shen, X., He, Y., Pan, X., Liu, F.-L., Wang, Y., Yang, F., Fang, S., Wu, Y., Duan, Z., Zuo, X., Xie, Z., Jiang, X., Xu, L., Chi, H., Li, S., Meng, Q., Zhou, H., Zhou, Y., Cheng, X., Xin, X., Jin, L., Zhang, H.-L., Yu, D.-D., Li, M.-H., Feng, X.-L., Chen, J., Jiang, H., Xiao, G., Zheng, Y.-T., Zhang, L.-K., Shen, J., Li, J., and Gao, Z. (2021) SARS-CoV-2 envelope protein causes acute respiratory distress syndrome (ARDS)-like pathological damages and constitutes an antiviral target. *Cell Research*

140. Nieto-Torres, J. L., Verdiá-Báguena, C., Jimenez-Guardeño, J. M., Regla-Nava, J. A., Castaño-Rodriguez, C., Fernandez-Delgado, R., Torres, J., Aguilella, V. M., and Enjuanes, L. (2015) Severe acute respiratory syndrome coronavirus E protein transports calcium ions and activates the NLRP3 inflammasome. *Virology* **485**, 330-339

141. Surya, W., Li, Y., and Torres, J. (2018) Structural model of the SARS coronavirus E channel in LMPG micelles. *Biochim. Biophys. Acta Biomembr.* **1860**, 1309-1317

142. Torres, J., Parthasarathy, K., Lin, X., Saravanan, R., Kukol, A., and Liu, D. X. (2006) Model of a putative pore: the pentameric alpha-helical bundle of SARS coronavirus E protein in lipid bilayers. *Biophys. J.* **91**, 938-947

143. Park, S. H., Siddiqi, H., Castro, D. V., De Angelis, A. A., Oom, A. L., Stoneham, C. A., Lewinski, M. K., Clark, A. E., Croker, B. A., Carlin, A. F., Guatelli, J., and Opella, S. J. (2021) Interactions of SARS-CoV-2 envelope protein with amilorides correlate with antiviral activity. *PLoS pathogens* **17**, e1009519

144. Duart, G., García-Murria, M. J., Grau, B., Acosta-Cáceres, J. M., Martínez-Gil, L., and Mingarro, I. (2020) SARS-CoV-2 envelope protein topology in eukaryotic membranes. *Open biology* **10**, 200209

145. Lopez, L. A., Riffle, A. J., Pike, S. L., Gardner, D., and Hogue, B. G. (2008) Importance of conserved cysteine residues in the coronavirus envelope protein. *J Virol* **82**, 3000-3010

146. Corse, E., and Machamer, C. E. (2002) The cytoplasmic tail of infectious bronchitis virus E protein directs Golgi targeting. *J Virol* **76**, 1273-1284

147. Cohen, J. R., Lin, L. D., and Machamer, C. E. (2011) Identification of a Golgi complex-targeting signal in the cytoplasmic tail of the severe acute respiratory syndrome coronavirus envelope protein. *J. Virol.* **85**, 5794-5803

148. Javorsky, A., Humbert, P. O., and Kvansakul, M. (2021) Structural basis of coronavirus E protein interactions with human PALS1 PDZ domain. *Communications biology* **4**, 724

149. Chai, J., Cai, Y., Pang, C., Wang, L., McSweeney, S., Shanklin, J., and Liu, Q. (2021) Structural basis for SARS-CoV-2 envelope protein recognition of human cell junction protein PALS1. *Nat Commun* **12**, 3433

150. Boson, B., Legros, V., Zhou, B., Siret, E., Mathieu, C., Cosset, F. L., Lavillette, D., and Denolly, S. (2020) The SARS-CoV-2 envelope and membrane proteins modulate maturation and retention of the spike protein, allowing assembly of virus-like particles. *The Journal of biological chemistry* **296**, 100111

151. Hippius, H., and Neundörfer, G. (2003) The discovery of Alzheimer's disease. *Dialogues in clinical neuroscience* **5**, 101-108

152. Bekris, L. M., Yu, C. E., Bird, T. D., and Tsuang, D. W. (2010) Genetics of Alzheimer disease. *Journal of geriatric psychiatry and neurology* **23**, 213-227

153. Awada, A. A. (2015) Early and late-onset Alzheimer's disease: What are the differences? *Journal of neurosciences in rural practice* **6**, 455-456

154. Oxford, A. E., Stewart, E. S., and Rohn, T. T. (2020) Clinical Trials in Alzheimer's Disease: A Hurdle in the Path of Remedy. *International journal of Alzheimer's disease* **2020**, 5380346

155. Mullard, A. (2021) FDA approval for Biogen's aducanumab sparks Alzheimer disease firestorm. *Nature reviews. Drug discovery* **20**, 496

156. Hardy, J., and Allsop, D. (1991) Amyloid deposition as the central event in the aetiology of Alzheimer's disease. *Trends in pharmacological sciences* **12**, 383-388

157. Hardy, J., and Selkoe, D. J. (2002) The amyloid hypothesis of Alzheimer's disease: progress and problems on the road to therapeutics. *Science (New York, N.Y.)* **297**, 353-356

158. Jack, C. R., Jr., Knopman, D. S., Jagust, W. J., Petersen, R. C., Weiner, M. W., Aisen, P. S., Shaw, L. M., Vemuri, P., Wiste, H. J., Weigand, S. D., Lesnick, T. G., Pankratz, V. S., Donohue, M. C., and Trojanowski, J. Q. (2013) Tracking pathophysiological processes in Alzheimer's disease: an updated hypothetical model of dynamic biomarkers. *The Lancet. Neurology* **12**, 207-216

159. Selkoe, D. J., and Hardy, J. (2016) The amyloid hypothesis of Alzheimer's disease at 25 years. *EMBO molecular medicine* **8**, 595-608

160. Andrew, R. J., Kellett, K. A., Thinakaran, G., and Hooper, N. M. (2016) A Greek Tragedy: The Growing Complexity of Alzheimer Amyloid Precursor Protein Proteolysis. *The Journal of biological chemistry* **291**, 19235-19244

161. Chow, V. W., Mattson, M. P., Wong, P. C., and Gleichmann, M. (2010) An overview of APP processing enzymes and products. *Neuromolecular medicine* **12**, 1-12

162. Capone, R., Tiwari, A., Hadziselimovic, A., Peskova, Y., Hutchison, J. M., Sanders, C. R., and Kenworthy, A. K. (2020) The C99 domain of the amyloid precursor protein is a disordered membrane phase-preferring protein. *bioRxiv*, 2020.2011.2025.397893

163. Wu, L., Rosa-Neto, P., Hsiung, G. Y., Sadovnick, A. D., Masellis, M., Black, S. E., Jia, J., and Gauthier, S. (2012) Early-onset familial Alzheimer's disease (EOFAD). *The Canadian journal of neurological sciences. Le journal canadien des sciences neurologiques* **39**, 436-445

164. Benilova, I., Karran, E., and De Strooper, B. (2012) The toxic Aβ oligomer and Alzheimer's disease: an emperor in need of clothes. *Nature neuroscience* **15**, 349-357

165. Bertram, L., and Tanzi, R. E. (2008) Thirty years of Alzheimer's disease genetics: the implications of systematic meta-analyses. *Nature reviews. Neuroscience* **9**, 768-778

166. Iwatsubo, T., Odaka, A., Suzuki, N., Mizusawa, H., Nukina, N., and Ihara, Y. (1994) Visualization of A beta 42(43) and A beta 40 in senile plaques with end-specific A beta monoclonals: evidence that an initially deposited species is A beta 42(43). *Neuron* **13**, 45-53

167. Gravina, S. A., Ho, L., Eckman, C. B., Long, K. E., Otvos, L., Jr., Younkin, L. H., Suzuki, N., and Younkin, S. G. (1995) Amyloid beta protein (A beta) in Alzheimer's disease brain. Biochemical and immunocytochemical analysis with antibodies specific for forms ending at A beta 40 or A beta 42(43). *The Journal of biological chemistry* **270**, 7013-7016

168. Mak, K., Yang, F., Vinters, H. V., Frautschy, S. A., and Cole, G. M. (1994) Polyclonals to beta-amyloid(1-42) identify most plaque and vascular deposits in Alzheimer cortex, but not striatum. *Brain research* **667**, 138-142

169. Gregory, G. C., and Halliday, G. M. (2005) What is the dominant Abeta species in human brain tissue? A review. *Neurotoxicity research* **7**, 29-41

170. Devkota, S., Williams, T. D., and Wolfe, M. S. (2021) Familial Alzheimer's disease mutations in amyloid protein precursor alter proteolysis by γ-secretase to increase amyloid β-peptides of >45 residues. *The Journal of biological chemistry* **296**, 100281

171. Maloney, J. A., Bainbridge, T., Gustafson, A., Zhang, S., Kyauk, R., Steiner, P., van der Brug, M., Liu, Y., Ernst, J. A., Watts, R. J., and Atwal, J. K. (2014) Molecular mechanisms of Alzheimer disease protection by the A673T allele of amyloid precursor protein. *The Journal of biological chemistry* **289**, 30990-31000

172. Arendt, T., Stieler, J. T., and Holzer, M. (2016) Tau and tauopathies. *Brain research bulletin* **126**, 238-292

173. Maccioni, R. B., Farías, G., Morales, I., and Navarrete, L. (2010) The revitalized tau hypothesis on Alzheimer's disease. *Archives of medical research* **41**, 226-231

174. Kametani, F., and Hasegawa, M. (2018) Reconsideration of Amyloid Hypothesis and Tau Hypothesis in Alzheimer's Disease. *Frontiers in neuroscience* **12**, 25

175. Goedert, M. (1996) Tau protein and the neurofibrillary pathology of Alzheimer's disease. *Annals of the New York Academy of Sciences* **777**, 121-131

176. Bennett, R. E., DeVos, S. L., Dujardin, S., Corjuc, B., Gor, R., Gonzalez, J., Roe, A. D., Frosch, M. P., Pitstick, R., Carlson, G. A., and Hyman, B. T. (2017) Enhanced Tau Aggregation in the Presence of Amyloid β. *The American journal of pathology* **187**, 1601-1612

177. Götz, J., Chen, F., van Dorpe, J., and Nitsch, R. M. (2001) Formation of neurofibrillary tangles in P301l tau transgenic mice induced by Abeta 42 fibrils. *Science (New York, N.Y.)* **293**, 1491-1495

178. Lewis, J., Dickson, D. W., Lin, W. L., Chisholm, L., Corral, A., Jones, G., Yen, S. H., Sahara, N., Skipper, L., Yager, D., Eckman, C., Hardy, J., Hutton, M., and McGowan, E. (2001) Enhanced neurofibrillary degeneration in transgenic mice expressing mutant tau and APP. *Science (New York, N.Y.)* **293**, 1487-1491

179. Griner, S. L., Seidler, P., Bowler, J., Murray, K. A., Yang, T. P., Sahay, S., Sawaya, M. R., Cascio, D., Rodriguez, J. A., Philipp, S., Sosna, J., Glabe, C. G., Gonen, T., and Eisenberg, D. S. (2019) Structure-based inhibitors of amyloid beta core suggest a common interface with tau. *eLife* **8**

180. Maron, R., Armony, G., Tsoory, M., Wilchek, M., Frenkel, D., and Arnon, R. (2020) Peptide Interference with APP and Tau Association: Relevance to Alzheimer's Disease Amelioration. *International journal of molecular sciences* **21**

181. Smith, M. A., Siedlak, S. L., Richey, P. L., Mulvihill, P., Ghiso, J., Frangione, B., Tagliavini, F., Giaccone, G., Bugiani, O., Praprotnik, D., and et al. (1995) Tau protein directly interacts with the amyloid beta-protein precursor: implications for Alzheimer's disease. *Nature medicine* **1**, 365-369

182. Giaccone, G., Pedrotti, B., Migheli, A., Verga, L., Perez, J., Racagni, G., Smith, M. A., Perry, G., De Gioia, L., Selvaggini, C., Salmona, M., Ghiso, J., Frangione, B., Islam, K., Bugiani, O., and Tagliavini, F. (1996) beta PP and Tau interaction. A possible link between amyloid and neurofibrillary tangles in Alzheimer's disease. *The American journal of pathology* **148**, 79-87

183. Islam, K., and Levy, E. (1997) Carboxyl-terminal fragments of beta-amyloid precursor protein bind to microtubules and the associated protein tau. *The American journal of pathology* **151**, 265-271

184. Barrett, P. J., Song, Y., Van Horn, W. D., Hustedt, E. J., Schafer, J. M., Hadziselimovic, A., Beel, A. J., and Sanders, C. R. (2012) The amyloid precursor protein has a flexible transmembrane domain and binds cholesterol. *Science (New York, N.Y.)* **336**, 1168-1171

185. Song, Y., Mittendorf, K. F., Lu, Z., and Sanders, C. R. (2014) Impact of bilayer lipid composition on the structure and topology of the transmembrane amyloid precursor C99 protein. *Journal of the American Chemical Society* **136**, 4093-4096

186. Hutchison, J. M., Shih, K. C., Scheidt, H. A., Fantin, S. M., Parson, K. F., Pantelopulos, G. A., Harrington, H. R., Mittendorf, K. F., Qian, S., Stein, R. A., Collier, S. E., Chambers, M. G., Katsaras, J., Voehler, M. W., Ruotolo, B. T., Huster, D., McFeeters, R. L., Straub, J. E., Nieh, M. P., and Sanders, C. R. (2020) Bicelles Rich in both Sphingolipids and Cholesterol and Their Use in Studies of Membrane Proteins. *Journal of the American Chemical Society* **142**, 12715-12729

187. Müller, U. C., and Zheng, H. (2012) Physiological functions of APP family proteins. *Cold Spring Harbor perspectives in medicine* **2**, a006288

188. Castro, M. A., Hadziselimovic, A., and Sanders, C. R. (2019) The vexing complexity of the amyloidogenic pathway. *Protein science : a publication of the Protein Society* **28**, 1177-1193

189. Zheng, H., and Koo, E. H. (2006) The amyloid precursor protein: beyond amyloid. *Molecular neurodegeneration* **1**, 5
190. Bukhari, H., Glotzbach, A., Kolbe, K., Leonhardt, G., Loosse, C., and Muller, T. (2017) Small Things Matter: Implications of APP Intracellular Domain AICD Nuclear Signaling in the Progression and Pathogenesis of Alzheimer's Disease. *Prog. Neurobiol.* **156**, 189-213
191. Cupers, P., Orlans, I., Craessaerts, K., Annaert, W., and De Strooper, B. (2001) The amyloid precursor protein (APP)-cytoplasmic fragment generated by gamma-secretase is rapidly degraded but distributes partially in a nuclear fraction of neurones in culture. *Journal of neurochemistry* **78**, 1168-1178
192. Makin, S. (2018) The amyloid hypothesis on trial. *Nature* **559**, S4-s7
193. Checler, F., Afram, E., Pardossi-Piquard, R., and Lauritzen, I. (2021) Is γ-secretase a beneficial inactivating enzyme of the toxic APP C-terminal fragment C99? *The Journal of biological chemistry* **296**, 100489
194. Heston, L. L., and Mastri, A. R. (1977) The genetics of Alzheimer's disease: associations with hematologic malignancy and Down's syndrome. *Archives of general psychiatry* **34**, 976-981
195. Lott, I. T., and Head, E. (2019) Dementia in Down syndrome: unique insights for Alzheimer disease research. *Nature reviews. Neurology* **15**, 135-147
196. Jiang, Y., Mullaney, K. A., Peterhoff, C. M., Che, S., Schmidt, S. D., Boyer-Boiteau, A., Ginsberg, S. D., Cataldo, A. M., Mathews, P. M., and Nixon, R. A. (2010) Alzheimer's-related endosome dysfunction in Down syndrome is Abeta-independent but requires APP and is reversed by BACE-1 inhibition. *Proc Natl Acad Sci U S A* **107**, 1630-1635
197. Jiang, Y., Sato, Y., Im, E., Berg, M., Bordi, M., Darji, S., Kumar, A., Mohan, P. S., Bandyopadhyay, U., Diaz, A., Cuervo, A. M., and Nixon, R. A. (2019) Lysosomal Dysfunction in Down Syndrome Is APP-Dependent and Mediated by APP-betaCTF (C99). *J Neurosci* **39**, 5255-5268
198. Lauritzen, I., Pardossi-Piquard, R., Bourgeois, A., Pagnotta, S., Biferi, M. G., Barkats, M., Lacor, P., Klein, W., Bauer, C., and Checler, F. (2016) Intraneuronal aggregation of the β-CTF fragment of APP (C99) induces Aβ-independent lysosomal-autophagic pathology. *Acta neuropathologica* **132**, 257-276
199. Pulina, M. V., Hopkins, M., Haroutunian, V., Greengard, P., and Bustos, V. (2020) C99 selectively accumulates in vulnerable neurons in Alzheimer's disease. *Alzheimer's & dementia : the journal of the Alzheimer's Association* **16**, 273-282
200. Hetz, C. (2021) Adapting the proteostasis capacity to sustain brain healthspan. *Cell* **184**, 1545-1560
201. Lim, J., and Yue, Z. (2015) Neuronal aggregates: formation, clearance, and spreading. *Developmental cell* **32**, 491-501
202. Song, Y., Hustedt, E. J., Brandon, S., and Sanders, C. R. (2013) Competition Between Homodimerization and Cholesterol Binding to the C99 Domain of the Amyloid Precursor Protein. *Biochemistry* **52**, 5051-5064
203. Nierzwicki, L., and Czub, J. (2015) Specific Binding of Cholesterol to the Amyloid Precursor Protein: Structure of the Complex and Driving Forces Characterized in Molecular Detail. *J. Phys. Chem. Lett.* **6**, 784-790
204. Shepardson, N. E., Shankar, G. M., and Selkoe, D. J. (2011) Cholesterol level and statin use in Alzheimer disease: I. Review of epidemiological and preclinical studies. *Archives of neurology* **68**, 1239-1244
205. Jin, P., Pan, Y., Pan, Z., Xu, J., Lin, M., Sun, Z., Chen, M., and Xu, M. (2018) Alzheimer-like brain metabolic and structural features in cholesterol-fed rabbit detected by magnetic resonance imaging. *Lipids in health and disease* **17**, 61

206. Wood, W. G., Igbavboa, U., Eckert, G. P., Johnson-Anuna, L. N., and Müller, W. E. (2005) Is hypercholesterolemia a risk factor for Alzheimer's disease? *Molecular neurobiology* **31**, 185-192

207. Montesinos, J., Pera, M., Larrea, D., Guardia-Laguarta, C., Agrawal, R. R., Velasco, K. R., Yun, T. D., Stavrovskaya, I. G., Xu, Y., Koo, S. Y., Snead, A. M., Sproul, A. A., and Area-Gomez, E. (2020) The Alzheimer's disease-associated C99 fragment of APP regulates cellular cholesterol trafficking. *Embo j* **39**, e103791

208. Kienlen-Campard, P., Tasiaux, B., Van Hees, J., Li, M., Huysseune, S., Sato, T., Fei, J. Z., Aimoto, S., Courtoy, P. J., Smith, S. O., Constantinescu, S. N., and Octave, J. N. (2008) Amyloidogenic Processing but not Amyloid Precursor Protein (APP) Intracellular C-terminal Domain Production Requires a Precisely Oriented APP Dimer Assembled by Transmembrane GXXXG Motifs. *J. Biol. Chem.* **283**, 7733-7744

209. Khalifa, N. B., Van Hees, J., Tasiaux, B., Huysseune, S., Smith, S. O., Constantinescu, S. N., Octave, J. N., and Kienlen-Campard, P. (2010) What is the Role of Amyloid Precursor Protein Dimerization? *Cell adhesion & migration* **4**, 268-272

210. Decock, M., Stanga, S., Octave, J. N., Dewachter, I., Smith, S. O., Constantinescu, S. N., and Kienlen-Campard, P. (2016) Glycines from the APP GXXXG/GXXXA Transmembrane Motifs Promote Formation of Pathogenic Aβ Oligomers in Cells. *Frontiers in aging neuroscience* **8**, 107

211. Scheuermann, S., Hambsch, B., Hesse, L., Stumm, J., Schmidt, C., Beher, D., Bayer, T. A., Beyreuther, K., and Multhaup, G. (2001) Homodimerization of Amyloid Precursor Protein and its Implication in the Amyloidogenic Pathway of Alzheimer's Disease. *J. Biol. Chem.* **276**, 33923-33929

212. Munter, L. M., Voigt, P., Harmeier, A., Kaden, D., Gottschalk, K. E., Weise, C., Pipkorn, R., Schaefer, M., Langosch, D., and Multhaup, G. (2007) GxxxG Motifs Within the Amyloid Precursor Protein Transmembrane Sequence are Critical for the Etiology of Abeta42. *The EMBO journal* **26**, 1702-1712

213. Higashide, H., Ishihara, S., Nobuhara, M., Ihara, Y., and Funamoto, S. (2017) Alanine Substitutions in the GXXXG Motif alter C99 Cleavage by Gamma-secretase but not its Dimerization. *J. Neurochem.* **140**, 955-962

214. Simons, M., Keller, P., De Strooper, B., Beyreuther, K., Dotti, C. G., and Simons, K. (1998) Cholesterol depletion inhibits the generation of beta-amyloid in hippocampal neurons. *Proc Natl Acad Sci U S A* **95**, 6460-6464

215. Langness, V. F., van der Kant, R., Das, U., Wang, L., Chaves, R. D. S., and Goldstein, L. S. B. (2021) Cholesterol-lowering drugs reduce APP processing to Aβ by inducing APP dimerization. *Mol Biol Cell* **32**, 247-259

216. Osenkowski, P., Ye, W., Wang, R., Wolfe, M. S., and Selkoe, D. J. (2008) Direct and potent regulation of gamma-secretase by its lipid microenvironment. *The Journal of biological chemistry* **283**, 22529-22540

217. Cordy, J. M., Hooper, N. M., and Turner, A. J. (2006) The involvement of lipid rafts in Alzheimer's disease. *Molecular membrane biology* **23**, 111-122

218. Hicks, D., Nalivaeva, N., and Turner, A. (2012) Lipid Rafts and Alzheimer's Disease: Protein-Lipid Interactions and Perturbation of Signaling. *Frontiers in physiology* **3**

219. Harris, B., Pereira, I., and Parkin, E. (2009) Targeting ADAM10 to lipid rafts in neuroblastoma SH-SY5Y cells impairs amyloidogenic processing of the amyloid precursor protein. *Brain research* **1296**, 203-215

220. Schlebach, J. P., Barrett, P. J., Day, C. A., Kim, J. H., Kenworthy, A. K., and Sanders, C. R. (2016) Topologically Diverse Human Membrane Proteins Partition to Liquid-Disordered Domains in Phase-Separated Lipid Vesicles. *Biochemistry* **55**, 985-988

221. Capone, R., Tiwari, A., Hadziselimovic, A., Peskova, Y., Hutchison, J. M., Sanders, C. R., and Kenworthy, A. K. (2021) The C99 domain of the amyloid precursor protein resides in the disordered membrane phase. *Journal of Biological Chemistry* **296**, 100652
222. Wang, X., Wang, W., Li, L., Perry, G., Lee, H. G., and Zhu, X. (2014) Oxidative stress and mitochondrial dysfunction in Alzheimer's disease. *Biochim Biophys Acta* **1842**, 1240-1247
223. Reddy, P. H., Yin, X., Manczak, M., Kumar, S., Pradeepkiran, J. A., Vijayan, M., and Reddy, A. P. (2018) Mutant APP and amyloid beta-induced defective autophagy, mitophagy, mitochondrial structural and functional changes and synaptic damage in hippocampal neurons from Alzheimer's disease. *Human molecular genetics* **27**, 2502-2516
224. Vaillant-Beuchot, L., Mary, A., Pardossi-Piquard, R., Bourgeois, A., Lauritzen, I., Eysert, F., Kinoshita, P. F., Cazareth, J., Badot, C., Fragaki, K., Bussiere, R., Martin, C., Mary, R., Bauer, C., Pagnotta, S., Paquis-Flucklinger, V., Buée-Scherrer, V., Buée, L., Lacas-Gervais, S., Checler, F., and Chami, M. (2021) Accumulation of amyloid precursor protein C-terminal fragments triggers mitochondrial structure, function, and mitophagy defects in Alzheimer's disease models and human brains. *Acta neuropathologica* **141**, 39-65
225. Bugge, K., Lindorff-Larsen, K., and Kragelund, B. B. (2016) Understanding single-pass transmembrane receptor signaling from a structural viewpoint-what are we missing? *The FEBS journal* **283**, 4424-4451
226. Opella, S. J., and Marassi, F. M. (2017) Applications of NMR to membrane proteins. *Archives of biochemistry and biophysics* **628**, 92-101
227. Chen, W., Gamache, E., Rosenman, D. J., Xie, J., Lopez, M. M., Li, Y. M., and Wang, C. (2014) Familial Alzheimer's Mutations within APPTM Increase Aβ42 Production by Enhancing Accessibility of ε-Cleavage Site. *Nature communications* **5**, 3037
228. Nadezhdin, K. D., Bocharova, O. V., Bocharov, E. V., and Arseniev, A. S. (2012) Dimeric Structure of Transmembrane Domain of Amyloid Precursor Protein in Micellar Environment. *FEBS Lett.* **586**, 1687-1692
229. Howell, S. C., Mittal, R., Huang, L., Travis, B., Breyer, R. M., and Sanders, C. R. (2010) CHOBIMALT: a cholesterol-based detergent. *Biochemistry* **49**, 9572-9583
230. Beel, A. J., Mobley, C. K., Kim, H. J., Tian, F., Hadziselimovic, A., Jap, B., Prestegard, J. H., and Sanders, C. R. (2008) Structural Studies of the Transmembrane C-terminal Domain of the Amyloid Precursor Protein (APP): Does APP Function as a Cholesterol Sensor? *Biochemistry* **47**, 9428-9446
231. Dominguez, L., Foster, L., Meredith, S. C., Straub, J. E., and Thirumalai, D. (2014) Structural Heterogeneity in Transmembrane Amyloid Precursor Protein Homodimer is a Consequence of Environmental Selection. *J. Am. Chem. Soc.* **136**, 9619-9626
232. Dominguez, L., Foster, L., Straub, J. E., and Thirumalai, D. (2016) Impact of Membrane Lipid Composition on the Structure and Stability of the Transmembrane Domain of Amyloid Precursor Protein. *Proceedings of the National Academy of Sciences of the United States of America* **113**, E5281-5287
233. Pantelopulos, G. A., Straub, J. E., Thirumalai, D., and Sugita, Y. (2018) Structure of APP-C991-99 and Implications for Role of Extra-membrane Domains in Function and Oligomerization. *Biochim. Biophys. Acta Biomembr.* **1860**, 1698-1708
234. Dahms, S. O., Hoefgen, S., Roeser, D., Schlott, B., Gührs, K.-H., and Than, M. E. (2010) Structure and biochemical analysis of the heparin-induced E1 dimer of the amyloid precursor protein. *Proceedings of the National Academy of Sciences* **107**, 5381-5386
235. Hoefgen, S., Coburger, I., Roeser, D., Schaub, Y., Dahms, S. O., and Than, M. E. (2014) Heparin induced dimerization of APP is primarily mediated by E1 and regulated by its acidic domain. *J Struct Biol* **187**, 30-37

236. Yan, Y., Xu, T. H., Harikumar, K. G., Miller, L. J., Melcher, K., and Xu, H. E. (2017) Dimerization of the Transmembrane Domain of Amyloid Precursor Protein is Determined by Residues Around the Gamma-secretase Cleavage Sites. *J. Biol. Chem.* **292**, 15826-15837

237. Sun, F., Chen, L., Wei, P., Chai, M., Ding, X., Xu, L., and Luo, S. Z. (2017) Dimerization and Structural Stability of Amyloid Precursor Proteins Affected by the Membrane Microenvironments. *J. Chem. Inf. Model.* **57**, 1375-1387

238. Sato, T., Tang, T. C., Reubins, G., Fei, J. Z., Fujimoto, T., Kienlen-Campard, P., Constantinescu, S. N., Octave, J. N., Aimoto, S., and Smith, S. O. (2009) A Helix-to-coil Transition at the Epsilon-cut Site in the Transmembrane Dimer of the Amyloid Precursor Protein is Required for Proteolysis. *Proceedings of the National Academy of Sciences of the United States of America* **106**, 1421-1426

239. Itkin, A., Salnikov, E. S., Aisenbrey, C., Raya, J., Glattard, E., Raussens, V., Ruysschaert, J. M., and Bechinger, B. (2017) Structural Characterization of the Amyloid Precursor Protein Transmembrane Domain and Its γ-Cleavage Site. *ACS omega* **2**, 6525-6534

240. Pester, O., Barrett, P. J., Hornburg, D., Hornburg, P., Pröbstle, R., Widmaier, S., Kutzner, C., Dürrbaum, M., Kapurniotu, A., Sanders, C. R., Scharnagl, C., and Langosch, D. (2013) The Backbone Dynamics of the Amyloid Precursor Protein Transmembrane Helix Provides a Rationale for the Sequential Cleavage Mechanism of γ-Secretase. *J. Am. Chem. Soc.* **135**, 1317-1329

241. Gorman, P. M., Kim, S., Guo, M., Melnyk, R. A., McLaurin, J., Fraser, P. E., Bowie, J. U., and Chakrabartty, A. (2008) Dimerization of the Transmembrane Domain of Amyloid Precursor Proteins and Familial Alzheimer's Disease Mutants. *BMC neuroscience* **9**, 17

242. Li, C.-D., Junaid, M., Chen, H., Ali, A., and Wei, D.-Q. (2019) Helix-Switch Enables C99 Dimer Transition between the Multiple Conformations. *Journal of Chemical Information and Modeling* **59**, 339-350

243. Bayburt, T. H., and Sligar, S. G. (2010) Membrane protein assembly into Nanodiscs. *FEBS letters* **584**, 1721-1727

244. Dörr, J. M., Scheidelaar, S., Koorengevel, M. C., Dominguez, J. J., Schäfer, M., van Walree, C. A., and Killian, J. A. (2016) The styrene-maleic acid copolymer: a versatile tool in membrane research. *European biophysics journal : EBJ* **45**, 3-21

245. Raschle, T., Hiller, S., Etzkorn, M., and Wagner, G. (2010) Nonmicellar systems for solution NMR spectroscopy of membrane proteins. *Curr Opin Struct Biol* **20**, 471-479

246. Caffrey, M., and Cherezov, V. (2009) Crystallizing membrane proteins using lipidic mesophases. *Nature protocols* **4**, 706-731

247. Chae, P. S., Rasmussen, S. G., Rana, R. R., Gotfryd, K., Chandra, R., Goren, M. A., Kruse, A. C., Nurva, S., Loland, C. J., Pierre, Y., Drew, D., Popot, J. L., Picot, D., Fox, B. G., Guan, L., Gether, U., Byrne, B., Kobilka, B., and Gellman, S. H. (2010) Maltose-neopentyl glycol (MNG) amphiphiles for solubilization, stabilization and crystallization of membrane proteins. *Nature methods* **7**, 1003-1008

248. Sanders, C. R., 2nd, and Prestegard, J. H. (1990) Magnetically orientable phospholipid bilayers containing small amounts of a bile salt analogue, CHAPSO. *Biophysical journal* **58**, 447-460

249. da Graça Miguel, M., Eidelman, O., Ollivon, M., and Walter, A. (1989) Temperature dependence of the vesicle-micelle transition of egg phosphatidylcholine and octyl glucoside. *Biochemistry* **28**, 8921-8928

250. VanAken, T., Foxall-VanAken, S., Castleman, S., and Ferguson-Miller, S. (1986) Alkyl glycoside detergents: synthesis and applications to the study of membrane proteins. *Methods Enzymol* **125**, 27-35

251. Kegel, L. L., Szabó, L. Z., Polt, R., and Pemberton, J. E. (2016) Alkyl melibioside and alkyl cellobioside surfactants: effect of sugar headgroup and alkyl chain length on performance. *Green Chemistry* **18**, 4446-4460
252. Rosevear, P., VanAken, T., Baxter, J., and Ferguson-Miller, S. (1980) Alkyl glycoside detergents: a simpler synthesis and their effects on kinetic and physical properties of cytochrome c oxidase. *Biochemistry* **19**, 4108-4115
253. Oliver, R. C., Lipfert, J., Fox, D. A., Lo, R. H., Doniach, S., and Columbus, L. (2013) Dependence of Micelle Size and Shape on Detergent Alkyl Chain Length and Head Group. *PloS one* **8**, e62488
254. Zhou, Y., Lau, F. W., Nauli, S., Yang, D., and Bowie, J. U. (2001) Inactivation mechanism of the membrane protein diacylglycerol kinase in detergent solution. *Protein science : a publication of the Protein Society* **10**, 378-383
255. Czerski, L., and Sanders, C. R. (2000) Functionality of a membrane protein in bicelles. *Analytical biochemistry* **284**, 327-333
256. Van Horn, W. D., Kim, H. J., Ellis, C. D., Hadziselimovic, A., Sulistijo, E. S., Karra, M. D., Tian, C., Sönnichsen, F. D., and Sanders, C. R. (2009) Solution nuclear magnetic resonance structure of membrane-integral diacylglycerol kinase. *Science (New York, N.Y.)* **324**, 1726-1729
257. Koehler, J., Sulistijo, E. S., Sakakura, M., Kim, H. J., Ellis, C. D., and Sanders, C. R. (2010) Lysophospholipid micelles sustain the stability and catalytic activity of diacylglycerol kinase in the absence of lipids. *Biochemistry* **49**, 7089-7099
258. Gorzelle, B. M., Nagy, J. K., Oxenoid, K., Lonzer, W. L., Cafiso, D. S., and Sanders, C. R. (1999) Reconstitutive refolding of diacylglycerol kinase, an integral membrane protein. *Biochemistry* **38**, 16373-16382
259. Vinogradova, O., Sönnichsen, F., and Sanders, C. R., 2nd. (1998) On choosing a detergent for solution NMR studies of membrane proteins. *J Biomol NMR* **11**, 381-386
260. Li, Q., Mittal, R., Huang, L., Travis, B., and Sanders, C. R. (2009) Bolaamphiphile-class surfactants can stabilize and support the function of solubilized integral membrane proteins. *Biochemistry* **48**, 11606-11608
261. Walsh, J. P., and Bell, R. M. (1986) sn-1,2-Diacylglycerol kinase of Escherichia coli. Structural and kinetic analysis of the lipid cofactor dependence. *The Journal of biological chemistry* **261**, 15062-15069
262. Walsh, J. P., and Bell, R. M. (1986) sn-1,2-Diacylglycerol kinase of Escherichia coli. Mixed micellar analysis of the phospholipid cofactor requirement and divalent cation dependence. *The Journal of biological chemistry* **261**, 6239-6247
263. Sakakura, M., Hadziselimovic, A., Wang, Z., Schey, K. L., and Sanders, C. R. (2011) Structural basis for the Trembler-J phenotype of Charcot-Marie-Tooth disease. *Structure* **19**, 1160-1169
264. Mobley, C. K., Myers, J. K., Hadziselimovic, A., Ellis, C. D., and Sanders, C. R. (2007) Purification and initiation of structural characterization of human peripheral myelin protein 22, an integral membrane protein linked to peripheral neuropathies. *Biochemistry* **46**, 11185-11195
265. van Meer, G., and de Kroon, A. I. (2011) Lipid Map of the Mammalian Cell. *J. Cell. Sci.* **124**, 5-8
266. Kraft, M. L. (2013) Plasma Membrane Organization and Function: Moving Past Lipid Rafts. *Mol. Biol. Cell.* **24**, 2765-2768
267. Smrt, S. T., Draney, A. W., Singaram, I., and Lorieau, J. L. (2017) Structure and Dynamics of Membrane Proteins and Membrane Associated Proteins with Native Bicelles from Eukaryotic Tissues. *Biochemistry* **56**, 5318-5327
268. Barnaba, C., Sahoo, B. R., Ravula, T., Medina-Meza, I. G., Im, S. C., Anantharamaiah, G. M., Waskell, L., and Ramamoorthy, A. (2018) Cytochrome-P450-Induced Ordering of Microsomal Membranes Modulates Affinity for Drugs. *Angewandte Chemie (International ed. in English)* **57**, 3391-3395

269. Lemmin, T., Dimitrov, M., Fraering, P. C., and Dal Peraro, M. (2014) Perturbations of the Straight Transmembrane Alpha-helical Structure of the Amyloid Precursor Protein Affect its Processing by Gamma-secretase. *J. Biol. Chem.* **289**, 6763-6774

270. Scharnagl, C., Pester, O., Hornburg, P., Hornburg, D., Gotz, A., and Langosch, D. (2014) Side-chain to Main-chain Hydrogen Bonding Controls the Intrinsic Backbone Dynamics of the Amyloid Precursor Protein Transmembrane Helix. *Biophys. J.* **106**, 1318-1326

271. Lu, J. X., Yau, W. M., and Tycko, R. (2011) Evidence from Solid-state NMR for Nonhelical Conformations in the Transmembrane Domain of the Amyloid Precursor Protein. *Biophys. J.* **100**, 711-719

272. Audagnotto, M., Lemmin, T., Barducci, A., and Dal Peraro, M. (2016) Effect of the Synaptic Plasma Membrane on the Stability of the Amyloid Precursor Protein Homodimer. *J. Phys. Chem. Lett.* **7**, 3572-3578

273. Bunge, A., Müller, P., Stöckl, M., Herrmann, A., and Huster, D. (2008) Characterization of the Ternary Mixture of Sphingomyelin, POPC, and Cholesterol: Support for an Inhomogeneous Lipid Distribution at High Temperatures. *Biophys. J.* **94**, 2680-2690

274. Sani, M. A., Weber, D. K., Delaglio, F., Separovic, F., and Gehman, J. D. (2013) A Practical Implementation of de-Pake-ing via Weighted Fourier Transformation. *PeerJ* **1**, e30

275. Vogel, A., Reuther, G., Weise, K., Triola, G., Nikolaus, J., Tan, K. T., Nowak, C., Herrmann, A., Waldmann, H., Winter, R., and Huster, D. (2009) The Lipid Modifications of Ras that Sense Membrane Environments and Induce Local Enrichment. *Angewandte Chemie (International ed. in English)* **48**, 8784-8787

276. Huster, D., Paasche, G., Dietrich, U., Zschornig, O., Gutberlet, T., Gawrisch, K., and Arnold, K. (1999) Investigation of Phospholipid Area Compression Induced by Calcium-Mediated Dextran Sulfate Interaction. *Biophys. J.* **77**, 879-887

277. Feller, S. E., Gawrisch, K., and MacKerell, A. D., Jr. (2002) Polyunsaturated Fatty Acids in Lipid Bilayers: Intrinsic and Environmental Contributions to their Unique Physical Properties. *J. Am. Chem. Soc.* **124**, 318-326

278. Polozov, I. V., and Gawrisch, K. (2006) Characterization of the Liquid-ordered State by Proton MAS NMR. *Biophys. J.* **90**, 2051-2061

279. Mineev, K. S., Nadezhdin, K. D., Goncharuk, S. A., and Arseniev, A. S. (2016) Characterization of Small Isotropic Bicelles with Various Compositions. *Langmuir : the ACS journal of surfaces and colloids* **32**, 6624-6637

280. Wang, H., Barreyro, L., Provasi, D., Djemil, I., Torres-Arancivia, C., Filizola, M., and Ubarretxena-Belandia, I. (2011) Molecular Determinants and Thermodynamics of the Amyloid Precursor Protein Transmembrane Domain Implicated in Alzheimer's Disease. *Journal of molecular biology* **408**, 879-895

281. Hwang, T. L., van Zijl, P. C., and Mori, S. (1998) Accurate Quantitation of Water-Amide Proton Exchange Rates using the Phase-Modulated CLEAN Chemical EXchange (CLEANEX-PM) Approach with a Fast-HSQC (FHSQC) Detection Scheme. *Journal of biomolecular NMR* **11**, 221-226

282. De, S., Greenwood, A. I., Rogals, M. J., Kovrigin, E. L., Lu, K. P., and Nicholson, L. K. (2012) Complete Thermodynamic and Kinetic Characterization of the Isomer-specific Interaction Between Pin1-WW Domain and the Amyloid Precursor Protein Cytoplasmic Tail Phosphorylated at Thr668. *Biochemistry* **51**, 8583-8596

283. Pastorino, L., Sun, A., Lu, P. J., Zhou, X. Z., Balastik, M., Finn, G., Wulf, G., Lim, J., Li, S. H., Li, X., Xia, W., Nicholson, L. K., and Lu, K. P. (2006) The Prolyl Isomerase Pin1 Regulates Amyloid Precursor Protein Processing and Amyloid-beta Production. *Nature* **440**, 528-534

284. Ramelot, T. A., and Nicholson, L. K. (2001) Phosphorylation-induced Structural Changes in the Amyloid Precursor Protein Cytoplasmic Tail Detected by NMR. *Journal of molecular biology* **307**, 871-884
285. Ramelot, T. A., Gentile, L. N., and Nicholson, L. K. (2000) Transient Structure of the Amyloid Precursor Protein Cytoplasmic Tail Indicates Preordering of Structure for Binding to Cytosolic Factors. *Biochemistry* **39**, 2714-2725
286. Kroenke, C. D., Ziemnicka-Kotula, D., Xu, J., Kotula, L., and Palmer, A. G., 3rd. (1997) Solution Conformations of a Peptide Containing the Cytoplasmic Domain Sequence of the Beta Amyloid Precursor Protein. *Biochemistry* **36**, 8145-8152
287. Borgia, A., Borgia, M. B., Bugge, K., Kissling, V. M., Heidarsson, P. O., Fernandes, C. B., Sottini, A., Soranno, A., Buholzer, K. J., Nettels, D., Kragelund, B. B., Best, R. B., and Schuler, B. (2018) Extreme Disorder in an Ultrahigh-affinity Protein Complex. *Nature* **555**, 61-66
288. Decock, M., Stanga, S., Octave, J. N., Dewachter, I., Smith, S. O., Constantinescu, S. N., and Kienlen-Campard, P. (2016) Glycines from the APP GXXXG/GXXXA Transmembrane Motifs Promote Formation of Pathogenic Abeta Oligomers in Cells. *Frontiers in aging neuroscience* **8**, 107
289. Fu, Q., Piai, A., Chen, W., Xia, K., and Chou, J. J. (2019) Structure Determination Protocol for Transmembrane Domain Oligomers. *Nat. Protoc.* **14**, 2483-2520
290. Zhuang, T., Jap, B. K., and Sanders, C. R. (2011) Solution NMR Approaches for Establishing Specificity of Weak Heterodimerization of Membrane Proteins. *J. Am. Chem. Soc.* **133**, 20571-20580
291. Li, M., Reddy, L. G., Bennett, R., Silva, N. D., Jr., Jones, L. R., and Thomas, D. D. (1999) A Fluorescence Energy Transfer Method for Analyzing Protein Oligomeric Structure: Application to Phospholamban. *Biophys. J.* **76**, 2587-2599
292. Giannoulis, A., Ward, R., Branigan, E., Naismith, J. H., and Bode, B. E. (2013) PELDOR in Rotationally Symmetric Homo-oligomers. *Molecular physics* **111**, 2845-2854
293. Schmidt, T., Ghirlando, R., Baber, J., and Clore, G. M. (2016) Quantitative Resolution of Monomer-Dimer Populations by Inversion Modulated DEER EPR Spectroscopy. *Chemphyschem : a European journal of chemical physics and physical chemistry* **17**, 2987-2991
294. Marty, M. T., Hoi, K. K., and Robinson, C. V. (2016) Interfacing Membrane Mimetics with Mass Spectrometry. *Accounts of chemical research* **49**, 2459-2467
295. Osterlund, N., Moons, R., Ilag, L. L., Sobott, F., and Graslund, A. (2019) Native Ion Mobility-Mass Spectrometry Reveals the Formation of beta-Barrel Shaped Amyloid-beta Hexamers in a Membrane-Mimicking Environment. *J. Am. Chem. Soc.* **141**, 10440-10450
296. Lu, Z., Van Horn, W. D., Chen, J., Mathew, S., Zent, R., and Sanders, C. R. (2012) Bicelles at Low Concentrations. *Molecular pharmaceutics* **9**, 752-761
297. Cheng, Y. (2018) Membrane Protein Structural Biology in the Era of Single Particle cryo-EM. *Current opinion in structural biology* **52**, 58-63
298. Winkler, E., Julius, A., Steiner, H., and Langosch, D. (2015) Homodimerization Protects the Amyloid Precursor Protein C99 Fragment from Cleavage by gamma-Secretase. *Biochemistry* **54**, 6149-6152
299. Jung, J. I., Premraj, S., Cruz, P. E., Ladd, T. B., Kwak, Y., Koo, E. H., Felsenstein, K. M., Golde, T. E., and Ran, Y. (2014) Independent Relationship Between Amyloid Precursor Protein (APP) Dimerization and γ-Secretase Processivity. *PloS one* **9**, e111553
300. Decock, M., El Haylani, L., Stanga, S., Dewachter, I., Octave, J. N., Smith, S. O., Constantinescu, S. N., and Kienlen-Campard, P. (2015) Analysis by a Highly Sensitive Split Luciferase Assay of the Regions Involved in APP Dimerization and its Impact on Processing. *FEBS open bio* **5**, 763-773

301. Munter, L. M., Botev, A., Richter, L., Hildebrand, P. W., Althoff, V., Weise, C., Kaden, D., and Multhaup, G. (2010) Aberrant amyloid precursor protein (APP) processing in hereditary forms of Alzheimer disease caused by APP familial Alzheimer disease mutations can be rescued by mutations in the APP GxxxG motif. *The Journal of biological chemistry* **285**, 21636-21643

302. Kollmer, M., Close, W., Funk, L., Rasmussen, J., Bsoul, A., Schierhorn, A., Schmidt, M., Sigurdson, C. J., Jucker, M., and Fändrich, M. (2019) Cryo-EM Structure and Polymorphism of Aβ Amyloid Fibrils Purified from Alzheimer's Brain Tissue. *Nature communications* **10**, 4760

303. Bukhari, H., Glotzbach, A., Kolbe, K., Leonhardt, G., Loosse, C., and Müller, T. (2017) Small things matter: Implications of APP intracellular domain AICD nuclear signaling in the progression and pathogenesis of Alzheimer's disease. *Progress in neurobiology* **156**, 189-213

304. Akiyama, H., Shin, R. W., Uchida, C., Kitamoto, T., and Uchida, T. (2005) Pin1 Promotes Production of Alzheimer's Amyloid Beta from Beta-cleaved Amyloid Precursor Protein. *Biochem. Biophys. Res. Commun.* **336**, 521-529

305. Satarker, S., and Nampoothiri, M. (2020) Structural Proteins in Severe Acute Respiratory Syndrome Coronavirus-2. *Arch. Med. Res.* **51**, 482-491

306. Kim, D., Lee, J. Y., Yang, J. S., Kim, J. W., Kim, V. N., and Chang, H. (2020) The Architecture of SARS-CoV-2 Transcriptome. *Cell* **181**, 914-921 e910

307. Alam, I., Kamau, A. A., Kulmanov, M., Jaremko, L., Arold, S. T., Pain, A., Gojobori, T., and Duarte, C. M. (2020) Functional Pangenome Analysis Shows Key Features of E Protein Are Preserved in SARS and SARS-CoV-2. *Front. Cell Infect. Microbiol.* **10**, 405

308. Almazan, F., DeDiego, M. L., Sola, I., Zuniga, S., Nieto-Torres, J. L., Marquez-Jurado, S., Andres, G., and Enjuanes, L. (2013) Engineering a replication-competent, propagation-defective Middle East respiratory syndrome coronavirus as a vaccine candidate. *mBio* **4**, e00650-00613

309. Nieto-Torres, J. L., DeDiego, M. L., Verdia-Baguena, C., Jimenez-Guardeno, J. M., Regla-Nava, J. A., Fernandez-Delgado, R., Castano-Rodriguez, C., Alcaraz, A., Torres, J., Aguilella, V. M., and Enjuanes, L. (2014) Severe acute respiratory syndrome coronavirus envelope protein ion channel activity promotes virus fitness and pathogenesis. *PLoS Pathog.* **10**, e1004077

310. DeDiego, M. L., Alvarez, E., Almazan, F., Rejas, M. T., Lamirande, E., Roberts, A., Shieh, W. J., Zaki, S. R., Subbarao, K., and Enjuanes, L. (2007) A severe acute respiratory syndrome coronavirus that lacks the E gene is attenuated in vitro and in vivo. *J. Virol.* **81**, 1701-1713

311. Schoeman, D., and Fielding, B. C. (2020) Is There a Link Between the Pathogenic Human Coronavirus Envelope Protein and Immunopathology? A Review of the Literature. *Front. Microbiol.* **11**, 2086

312. Klumperman, J., Locker, J. K., Meijer, A., Horzinek, M. C., Geuze, H. J., and Rottier, P. J. (1994) Coronavirus M proteins accumulate in the Golgi complex beyond the site of virion budding. *J. Virol.* **68**, 6523-6534

313. Gorzelle, B. M., Hoffman, A. K., Keyes, M. H., Gray, D. N., Ray, D. G., and Sanders, C. R. (2002) Amphipols can support the activity of a membrane enzyme. *J. Am. Chem. Soc.* **124**, 11594-11595

314. Fernandez, A., Le Bon, C., Baumlin, N., Giusti, F., Cremel, G., Popot, J. L., and Bagnard, D. (2014) In vivo characterization of the biodistribution profile of amphipol A8-35. *J. Membr. Biol.* **247**, 1043-1051

315. Wilson, L., McKinlay, C., Gage, P., and Ewart, G. (2004) SARS coronavirus E protein forms cation-selective ion channels. *Virology* **330**, 322-331

316. Xia, B., Shen, X., He, Y., Pan, X., Wang, Y., Yang, F., Fang, S., Wu, Y., Zuo, X., Xie, Z., Jiang, X., Chi, H., Meng, Q., Zhou, H., Zhou, Y., Cheng, X., Chen, T., Xin, X., Jiang, H., Xiao, G., Zhao, Q., Zhang, L.-K., Shen, J., Li, J., and Gao, Z. (2020) SARS-CoV-2 envelope protein causes acute respiratory distress syndrome (ARDS)-like pathological damage and constitutes an antiviral target. *bioRxiv*, 2020.2006.2027.174953

317. Parthasarathy, K., Lu, H., Surya, W., Vararattanavech, A., Pervushin, K., and Torres, J. (2012) Expression and purification of coronavirus envelope proteins using a modified beta-barrel construct. *Protein Expr Purif* **85**, 133-141
318. Feryforgues, S., Fayet, J. P., and Lopez, A. (1993) Drastic Changes in the Fluorescence Properties of Nbd Probes with the Polarity of the Medium - Involvement of a Tict State. *J Photoch Photobio A* **70**, 229-243
319. Rezgui, R., Blumer, K., Yeoh-Tan, G., Trexler, A. J., and Magzoub, M. (2016) Precise quantification of cellular uptake of cell-penetrating peptides using fluorescence-activated cell sorting and fluorescence correlation spectroscopy. *Biochim Biophys Acta* **1858**, 1499-1506
320. Pocanschi, C. L., Dahmane, T., Gohon, Y., Rappaport, F., Apell, H. J., Kleinschmidt, J. H., and Popot, J. L. (2006) Amphipathic polymers: tools to fold integral membrane proteins to their active form. *Biochemistry* **45**, 13954-13961
321. Valyaeva, A. A., Zharikova, A. A., Kasianov, A. S., Vassetzky, Y. S., and Sheval, E. V. (2020) Expression of SARS-CoV-2 entry factors in lung epithelial stem cells and its potential implications for COVID-19. *Sci. Rep.* **10**, 17772
322. Lock, J. G., Hammond, L. A., Houghton, F., Gleeson, P. A., and Stow, J. L. (2005) E-cadherin transport from the trans-Golgi network in tubulovesicular carriers is selectively regulated by golgin-97. *Traffic* **6**, 1142-1156
323. Pusztai, A., Ewen, S. W. B., Grant, G., Brown, D. S., Stewart, J. C., Peumans, W. J., Vandamme, E. J. M., and Bardocz, S. (1993) Antinutritive Effects of Wheat-Germ-Agglutinin and Other N-Acetylglucosamine-Specific Lectins. *Brit J Nutr* **70**, 313-321
324. Czapla, T. H., and Lang, B. A. (1990) Effect of Plant-Lectins on the Larval Development of European Corn-Borer (Lepidoptera, Pyralidae) and Southern Corn-Rootworm (Coleoptera, Chrysomelidae). *J Econ Entomol* **83**, 2480-2485
325. Chazotte, B. (2011) Labeling membrane glycoproteins or glycolipids with fluorescent wheat germ agglutinin. *Cold Spring Harb Protoc* **2011**, pdb prot5623
326. Pavelka, M., Neumuller, J., and Ellinger, A. (2008) Retrograde traffic in the biosynthetic-secretory route. *Histochem Cell Biol* **129**, 277-288
327. Kanazawa, T., Takematsu, H., Yamamoto, A., Yamamoto, H., and Kozutsumi, Y. (2008) Wheat germ agglutinin stains dispersed post-golgi vesicles after treatment with the cytokinesis inhibitor psychosine. *J Cell Physiol* **215**, 517-525
328. Velasco, A., Hidalgo, J., Müller, M., and Garcia-Herdugo, G. (1988) Ultrastructural demonstration of lectin binding sites in the Golgi apparatus of rat epiphyseal chondrocytes. *Histochemistry* **89**, 177-184
329. Allen, R. D., Schroeder, C. C., and Fok, A. K. (1989) Intracellular binding of wheat germ agglutinin by Golgi complexes, phagosomes, and lysosomes of Paramecium multimicronucleatum. *The journal of histochemistry and cytochemistry : official journal of the Histochemistry Society* **37**, 195-202
330. Rohn, W. M., Rouille, Y., Waguri, S., and Hoflack, B. (2000) Bi-directional trafficking between the trans-Golgi network and the endosomal/lysosomal system. *J Cell Sci* **113 (Pt 12)**, 2093-2101
331. Wilson, J. M., de Hoop, M., Zorzi, N., Toh, B. H., Dotti, C. G., and Parton, R. G. (2000) EEA1, a tethering protein of the early sorting endosome, shows a polarized distribution in hippocampal neurons, epithelial cells, and fibroblasts. *Mol Biol Cell* **11**, 2657-2671
332. Ducatelle, R., and Hoorens, J. (1984) Significance of lysosomes in the morphogenesis of coronaviruses. *Arch Virol* **79**, 1-12
333. Johnston, J. A., Ward, C. L., and Kopito, R. R. (1998) Aggresomes: a cellular response to misfolded proteins. *J. Cell Biol.* **143**, 1883-1898

334. Wileman, T. (2006) Aggresomes and autophagy generate sites for virus replication. *Science (New York, N.Y.)* **312**, 875-878

335. Prentice, E., Jerome, W. G., Yoshimori, T., Mizushima, N., and Denison, M. R. (2004) Coronavirus replication complex formation utilizes components of cellular autophagy. *J. Biol. Chem.* **279**, 10136-10141

336. Maier, H. J., and Britton, P. (2012) Involvement of autophagy in coronavirus replication. *Viruses* **4**, 3440-3451

337. Zoonens, M., and Popot, J. L. (2014) Amphipols for each season. *The Journal of membrane biology* **247**, 759-796

338. Kurauskas, V., Hessel, A., Ma, P., Lunetti, P., Weinhäupl, K., Imbert, L., Brutscher, B., King, M. S., Sounier, R., Dolce, V., Kunji, E. R. S., Capobianco, L., Chipot, C., Dehez, F., Bersch, B., and Schanda, P. (2018) How Detergent Impacts Membrane Proteins: Atomic-Level Views of Mitochondrial Carriers in Dodecylphosphocholine. *J Phys Chem Lett* **9**, 933-938

339. Privé, G. G. (2007) Detergents for the stabilization and crystallization of membrane proteins. *Methods (San Diego, Calif.)* **41**, 388-397

340. Tate, C. G. (2010) Practical considerations of membrane protein instability during purification and crystallisation. *Methods in molecular biology (Clifton, N.J.)* **601**, 187-203

341. Schick, M. J. (1963) EFFECT OF TEMPERATURE ON THE CRITICAL MICELLE CONCENTRATION OF NONIONIC DETERGENTS. THERMODYNAMICS OF MICELLE FORMATION1. *The Journal of Physical Chemistry* **67**, 1796-1799

342. Tanford, C. (1974) Thermodynamics of Micelle Formation: Prediction of Micelle Size and Size Distribution. *Proceedings of the National Academy of Sciences of the United States of America* **71**, 1811-1815

343. Mineev, K. S., Lesovoy, D. M., Usmanova, D. R., Goncharuk, S. A., Shulepko, M. A., Lyukmanova, E. N., Kirpichnikov, M. P., Bocharov, E. V., and Arseniev, A. S. (2014) NMR-based approach to measure the free energy of transmembrane helix–helix interactions. *Biochimica et Biophysica Acta (BBA) - Biomembranes* **1838**, 164-172

344. Kotov, V., Bartels, K., Veith, K., Josts, I., Subhramanyam, U. K. T., Günther, C., Labahn, J., Marlovits, T. C., Moraes, I., Tidow, H., Löw, C., and Garcia-Alai, M. M. (2019) High-throughput stability screening for detergent-solubilized membrane proteins. *Scientific Reports* **9**, 10379

345. Lefèvre, C. T., and Bazylinski, D. A. (2013) Ecology, diversity, and evolution of magnetotactic bacteria. *Microbiology and molecular biology reviews : MMBR* **77**, 497-526

346. Iwadate, M., Asakura, T., and Williamson, M. P. (1998) The structure of the melittin tetramer at different temperatures--an NOE-based calculation with chemical shift refinement. *European journal of biochemistry* **257**, 479-487

347. van den Bogaart, G., Guzmán, J. V., Mika, J. T., and Poolman, B. (2008) On the mechanism of pore formation by melittin. *The Journal of biological chemistry* **283**, 33854-33857

348. Song, Y., Mittendorf, K. F., Lu, Z., and Sanders, C. R. (2014) Impact of Bilayer Lipid Composition on the Structure and Topology of the Transmembrane Amyloid Precursor C99 Protein. *J. Am. Chem. Soc.* **136**, 4093-4096

349. Deatherage, C. L., Lu, Z., Kim, J.-H., and Sanders, C. R. (2015) Notch Transmembrane Domain: Secondary Structure and Topology. *Biochemistry* **54**, 3565-3568

350. Hutchison, J. M., Capone, R., Luu, D. D., Shah, K. H., Hadziselimovic, A., Van Horn, W. D., and Sanders, C. R. (2021) Recombinant SARS-CoV-2 envelope protein traffics to the trans-Golgi network following amphipol-mediated delivery into human cells. *The Journal of biological chemistry*, 100940

351. Kang, C., Vanoye, C. G., Welch, R. C., Van Horn, W. D., and Sanders, C. R. (2010) Functional delivery of a membrane protein into oocyte membranes using bicelles. *Biochemistry* **49**, 653-655

352. Tian, C., Vanoye, C. G., Kang, C., Welch, R. C., Kim, H. J., George, A. L., Jr., and Sanders, C. R. (2007) Preparation, functional characterization, and NMR studies of human KCNE1, a voltage-gated potassium channel accessory subunit associated with deafness and long QT syndrome. *Biochemistry* **46**, 11459-11472
353. Bragin, P. E., Kuznetsov, A. S., Bocharova, O. V., Volynsky, P. E., Arseniev, A. S., Efremov, R. G., and Mineev, K. S. (2018) Probing the effect of membrane contents on transmembrane protein-protein interaction using solution NMR and computer simulations. *Biochimica et Biophysica Acta (BBA) - Biomembranes* **1860**, 2486-2498
354. Linse, S. (2019) Mechanism of amyloid protein aggregation and the role of inhibitors. *Pure and Applied Chemistry* **91**, 211-229
355. Das, A., and Mukhopadhyay, C. (2009) Urea-Mediated Protein Denaturation: A Consensus View. *The Journal of Physical Chemistry B* **113**, 12816-12824
356. Lim, W. K., Rösgen, J., and Englander, S. W. (2009) Urea, but not guanidinium, destabilizes proteins by forming hydrogen bonds to the peptide group. *Proceedings of the National Academy of Sciences* **106**, 2595-2600
357. Broecker, J., and Keller, S. (2013) Impact of Urea on Detergent Micelle Properties. *Langmuir : the ACS journal of surfaces and colloids* **29**, 8502-8510
358. Holzwarth, G., and Doty, P. (1965) The Ultraviolet Circular Dichroism of Polypeptides1. *Journal of the American Chemical Society* **87**, 218-228
359. Greenfield, N. J., and Fasman, G. D. (1969) Computed circular dichroism spectra for the evaluation of protein conformation. *Biochemistry* **8**, 4108-4116
360. Lees, J. G., Miles, A. J., Wien, F., and Wallace, B. A. (2006) A reference database for circular dichroism spectroscopy covering fold and secondary structure space. *Bioinformatics* **22**, 1955-1962
361. Cascio, M., and Wallace, B. A. (1995) Effects of local environment on the circular dichroism spectra of polypeptides. *Analytical biochemistry* **227**, 90-100
362. Chen, Y., and Wallace, B. A. (1997) Secondary solvent effects on the circular dichroism spectra of polypeptides in non-aqueous environments: influence of polarisation effects on the far ultraviolet spectra of alamethicin. *Biophysical chemistry* **65**, 65-74
363. Sreerama, N., and Woody, R. W. (2004) On the analysis of membrane protein circular dichroism spectra. *Protein science : a publication of the Protein Society* **13**, 100-112
364. Demirdöven, N., Cheatum, C. M., Chung, H. S., Khalil, M., Knoester, J., and Tokmakoff, A. (2004) Two-dimensional infrared spectroscopy of antiparallel beta-sheet secondary structure. *Journal of the American Chemical Society* **126**, 7981-7990
365. Moran, S. D., Woys, A. M., Buchanan, L. E., Bixby, E., Decatur, S. M., and Zanni, M. T. (2012) Two-dimensional IR spectroscopy and segmental ¹³C labeling reveals the domain structure of human γD-crystallin amyloid fibrils. *Proceedings of the National Academy of Sciences* **109**, 3329-3334
366. Zhang-Haagen, B., Biehl, R., Nagel-Steger, L., Radulescu, A., Richter, D., and Willbold, D. (2016) Monomeric Amyloid Beta Peptide in Hexafluoroisopropanol Detected by Small Angle Neutron Scattering. *PloS one* **11**, e0150267
367. Stine, W. B., Jungbauer, L., Yu, C., and LaDu, M. J. (2011) Preparing synthetic Aβ in different aggregation states. *Methods in molecular biology (Clifton, N.J.)* **670**, 13-32
368. Jahn, T. R., and Radford, S. E. (2005) The Yin and Yang of protein folding. *The FEBS journal* **272**, 5962-5970
369. Nagarajan, R. (2002) Molecular Packing Parameter and Surfactant Self-Assembly: The Neglected Role of the Surfactant Tail. *Langmuir : the ACS journal of surfaces and colloids* **18**, 31-38

370. Yan, Y., Xiong, W., Li, X., Lu, T., Huang, J., Li, Z., and Fu, H. (2007) Molecular Packing Parameter in Bolaamphiphile Solutions: Adjustment of Aggregate Morphology by Modifying the Solution Conditions. *The Journal of Physical Chemistry B* **111**, 2225-2230
371. Hu, Y., Kienlen-Campard, P., Tang, T.-C., Perrin, F., Opsomer, R., Decock, M., Pan, X., Octave, J.-N., Constantinescu, S. N., and Smith, S. O. (2017) β-Sheet Structure within the Extracellular Domain of C99 Regulates Amyloidogenic Processing. *Scientific Reports* **7**, 17159
372. Zhou, R., Yang, G., Guo, X., Zhou, Q., Lei, J., and Shi, Y. (2019) Recognition of the amyloid precursor protein by human γ-secretase. *Science (New York, N.Y.)* **363**, eaaw0930
373. Zhao, G., Cui, M. Z., Mao, G., Dong, Y., Tan, J., Sun, L., and Xu, X. (2005) gamma-Cleavage is dependent on zeta-cleavage during the proteolytic processing of amyloid precursor protein within its transmembrane domain. *The Journal of biological chemistry* **280**, 37689-37697
374. Colacurcio, D. J., Pensalfini, A., Jiang, Y., and Nixon, R. A. (2018) Dysfunction of autophagy and endosomal-lysosomal pathways: Roles in pathogenesis of Down syndrome and Alzheimer's Disease. *Free Radic Biol Med* **114**, 40-51
375. Hoffmann, C., Gaietta, G., Zürn, A., Adams, S. R., Terrillon, S., Ellisman, M. H., Tsien, R. Y., and Lohse, M. J. (2010) Fluorescent labeling of tetracysteine-tagged proteins in intact cells. *Nature protocols* **5**, 1666-1677
376. Plácido, A. I., Pereira, C. M., Duarte, A. I., Candeias, E., Correia, S. C., Santos, R. X., Carvalho, C., Cardoso, S., Oliveira, C. R., and Moreira, P. I. (2014) The role of endoplasmic reticulum in amyloid precursor protein processing and trafficking: implications for Alzheimer's disease. *Biochim Biophys Acta* **1842**, 1444-1453
377. Jung, E. S., Hong, H., Kim, C., and Mook-Jung, I. (2015) Acute ER stress regulates amyloid precursor protein processing through ubiquitin-dependent degradation. *Scientific Reports* **5**, 8805
378. Isbert, S., Wagner, K., Eggert, S., Schweitzer, A., Multhaup, G., Weggen, S., Kins, S., and Pietrzik, C. U. (2012) APP dimer formation is initiated in the endoplasmic reticulum and differs between APP isoforms. *Cellular and molecular life sciences : CMLS* **69**, 1353-1375
379. Selkoe, D. J. (1991) The molecular pathology of Alzheimer's disease. *Neuron* **6**, 487-498
380. van der Kant, R., Goldstein, L. S. B., and Ossenkoppele, R. (2020) Amyloid-β-independent regulators of tau pathology in Alzheimer disease. *Nature reviews. Neuroscience* **21**, 21-35
381. Nhan, H. S., Chiang, K., and Koo, E. H. (2015) The multifaceted nature of amyloid precursor protein and its proteolytic fragments: friends and foes. *Acta neuropathologica* **129**, 1-19
382. Goedert, M., Spillantini, M. G., Jakes, R., Rutherford, D., and Crowther, R. A. (1989) Multiple isoforms of human microtubule-associated protein tau: sequences and localization in neurofibrillary tangles of Alzheimer's disease. *Neuron* **3**, 519-526
383. Espinoza, M., de Silva, R., Dickson, D. W., and Davies, P. (2008) Differential incorporation of tau isoforms in Alzheimer's disease. *Journal of Alzheimer's disease : JAD* **14**, 1-16
384. Shankar, G. M., Li, S., Mehta, T. H., Garcia-Munoz, A., Shepardson, N. E., Smith, I., Brett, F. M., Farrell, M. A., Rowan, M. J., Lemere, C. A., Regan, C. M., Walsh, D. M., Sabatini, B. L., and Selkoe, D. J. (2008) Amyloid-beta protein dimers isolated directly from Alzheimer's brains impair synaptic plasticity and memory. *Nature medicine* **14**, 837-842
385. Mattsson-Carlgren, N., Andersson, E., Janelidze, S., Ossenkoppele, R., Insel, P., Strandberg, O., Zetterberg, H., Rosen, H. J., Rabinovici, G., Chai, X., Blennow, K., Dage, J. L., Stomrud, E., Smith, R., Palmqvist, S., and Hansson, O. (2020) Aβ deposition is associated with increases in soluble and phosphorylated tau that precede a positive Tau PET in Alzheimer's disease. *Science advances* **6**, eaaz2387
386. Vasconcelos, B., Stancu, I. C., Buist, A., Bird, M., Wang, P., Vanoosthuyse, A., Van Kolen, K., Verheyen, A., Kienlen-Campard, P., Octave, J. N., Baatsen, P., Moechars, D., and Dewachter, I.

(2016) Heterotypic seeding of Tau fibrillization by pre-aggregated Abeta provides potent seeds for prion-like seeding and propagation of Tau-pathology in vivo. *Acta neuropathologica* **131**, 549-569

387. Manczak, M., and Reddy, P. H. (2013) Abnormal interaction of oligomeric amyloid-β with phosphorylated tau: implications to synaptic dysfunction and neuronal damage. *Journal of Alzheimer's disease : JAD* **36**, 285-295
388. Pickett, E. K., Herrmann, A. G., McQueen, J., Abt, K., Dando, O., Tulloch, J., Jain, P., Dunnett, S., Sohrabi, S., Fjeldstad, M. P., Calkin, W., Murison, L., Jackson, R. J., Tzioras, M., Stevenson, A., d'Orange, M., Hooley, M., Davies, C., Colom-Cadena, M., Anton-Fernandez, A., King, D., Oren, I., Rose, J., McKenzie, C. A., Allison, E., Smith, C., Hardt, O., Henstridge, C. M., Hardingham, G. E., and Spires-Jones, T. L. (2019) Amyloid Beta and Tau Cooperate to Cause Reversible Behavioral and Transcriptional Deficits in a Model of Alzheimer's Disease. *Cell reports* **29**, 3592-3604.e3595
389. Fein, J. A., Sokolow, S., Miller, C. A., Vinters, H. V., Yang, F., Cole, G. M., and Gylys, K. H. (2008) Co-localization of amyloid beta and tau pathology in Alzheimer's disease synaptosomes. *The American journal of pathology* **172**, 1683-1692
390. Chen, G. F., Xu, T. H., Yan, Y., Zhou, Y. R., Jiang, Y., Melcher, K., and Xu, H. E. (2017) Amyloid beta: structure, biology and structure-based therapeutic development. *Acta pharmacologica Sinica* **38**, 1205-1235
391. Brody, A. H., and Strittmatter, S. M. (2018) Synaptotoxic Signaling by Amyloid Beta Oligomers in Alzheimer's Disease Through Prion Protein and mGluR5. *Advances in pharmacology (San Diego, Calif.)* **82**, 293-323
392. Benilova, I., and De Strooper, B. (2013) Neuroscience. Promiscuous Alzheimer's amyloid: yet another partner. *Science (New York, N.Y.)* **341**, 1354-1355
393. Xia, M., Cheng, X., Yi, R., Gao, D., and Xiong, J. (2016) The Binding Receptors of Aβ: an Alternative Therapeutic Target for Alzheimer's Disease. *Molecular neurobiology* **53**, 455-471
394. Fogel, H., Frere, S., Segev, O., Bharill, S., Shapira, I., Gazit, N., O'Malley, T., Slomowitz, E., Berdichevsky, Y., Walsh, D. M., Isacoff, E. Y., Hirsch, J. A., and Slutsky, I. (2014) APP homodimers transduce an amyloid-β-mediated increase in release probability at excitatory synapses. *Cell reports* **7**, 1560-1576
395. Ghosal, K., Fan, Q., Dawson, H. N., and Pimplikar, S. W. (2016) Tau Protein Mediates APP Intracellular Domain (AICD)-Induced Alzheimer's-Like Pathological Features in Mice. *PloS one* **11**, e0159435
396. Puzzo, D., Piacentini, R., Fá, M., Gulisano, W., Li Puma, D. D., Staniszewski, A., Zhang, H., Tropea, M. R., Cocco, S., Palmeri, A., Fraser, P., D'Adamio, L., Grassi, C., and Arancio, O. (2017) LTP and memory impairment caused by extracellular Aβ and Tau oligomers is APP-dependent. *eLife* **6**
397. Xu, X. (2009) Gamma-secretase catalyzes sequential cleavages of the AbetaPP transmembrane domain. *Journal of Alzheimer's disease : JAD* **16**, 211-224
398. Olsson, F., Schmidt, S., Althoff, V., Munter, L. M., Jin, S., Rosqvist, S., Lendahl, U., Multhaup, G., and Lundkvist, J. (2014) Characterization of intermediate steps in amyloid beta (Aβ) production under near-native conditions. *The Journal of biological chemistry* **289**, 1540-1550
399. Bourré, G., Cantrelle, F.-X., Kamah, A., Chambraud, B., Landrieu, I., and Smet-Nocca, C. (2018) Direct Crosstalk Between O-GlcNAcylation and Phosphorylation of Tau Protein Investigated by NMR Spectroscopy. *Frontiers in Endocrinology* **9**
400. Harbison, N. W., Bhattacharya, S., and Eliezer, D. (2012) Assigning backbone NMR resonances for full length tau isoforms: efficient compromise between manual assignments and reduced dimensionality. *PloS one* **7**, e34679

401. Aránzazu Partearroyo, M., Ostolaza, H., Goñi, F. M., and Barberá-Guillem, E. (1990) Surfactant-induced cell toxicity and cell lysis. A study using B16 melanoma cells. *Biochemical pharmacology* **40**, 1323-1328

402. Qi, L., and Gao, X. (2008) Quantum dot-amphipol nanocomplex for intracellular delivery and real-time imaging of siRNA. *ACS nano* **2**, 1403-1410

403. Kim, T. K., and Eberwine, J. H. (2010) Mammalian cell transfection: the present and the future. *Analytical and bioanalytical chemistry* **397**, 3173-3178

404. Remington, S. J. (2011) Green fluorescent protein: a perspective. *Protein science : a publication of the Protein Society* **20**, 1509-1519

405. Zacharias, D. A., Violin, J. D., Newton, A. C., and Tsien, R. Y. (2002) Partitioning of lipid-modified monomeric GFPs into membrane microdomains of live cells. *Science (New York, N.Y.)* **296**, 913-916

406. Lafranchi, L., Schlesinger, D., Kimler, K. J., and Elsässer, S. J. (2020) Universal Single-Residue Terminal Labels for Fluorescent Live Cell Imaging of Microproteins. *Journal of the American Chemical Society* **142**, 20080-20087

407. Bonucci, A., Ouari, O., Guigliarelli, B., Belle, V., and Mileo, E. (2020) In-Cell EPR: Progress towards Structural Studies Inside Cells. *Chembiochem : a European journal of chemical biology* **21**, 451-460

408. Xiong, Y., Tian, X., and Ai, H. W. (2019) Molecular Tools to Generate Reactive Oxygen Species in Biological Systems. *Bioconjugate chemistry* **30**, 1297-1303

409. Gohon, Y., Dahmane, T., Ruigrok, R. W., Schuck, P., Charvolin, D., Rappaport, F., Timmins, P., Engelman, D. M., Tribet, C., Popot, J. L., and Ebel, C. (2008) Bacteriorhodopsin/amphipol complexes: structural and functional properties. *Biophysical journal* **94**, 3523-3537

410. Diab, C., Tribet, C., Gohon, Y., Popot, J. L., and Winnik, F. M. (2007) Complexation of integral membrane proteins by phosphorylcholine-based amphipols. *Biochim Biophys Acta* **1768**, 2737-2747

411. Sharma, K. S., Durand, G., Gabel, F., Bazzacco, P., Le Bon, C., Billon-Denis, E., Catoire, L. J., Popot, J. L., Ebel, C., and Pucci, B. (2012) Non-ionic amphiphilic homopolymers: synthesis, solution properties, and biochemical validation. *Langmuir : the ACS journal of surfaces and colloids* **28**, 4625-4639

412. Teoh, K. T., Siu, Y. L., Chan, W. L., Schlüter, M. A., Liu, C. J., Peiris, J. S., Bruzzone, R., Margolis, B., and Nal, B. (2010) The SARS coronavirus E protein interacts with PALS1 and alters tight junction formation and epithelial morphogenesis. *Mol Biol Cell* **21**, 3838-3852

413. Park, S. H., Siddiqi, H., Castro, D. V., De Angelis, A. A., Oom, A. L., Stoneham, C. A., Lewinski, M. K., Clark, A. E., Croker, B. A., Carlin, A. F., Guatelli, J., and Opella, S. J. (2021) Interactions of SARS-CoV-2 envelope protein with amilorides correlate with antiviral activity. *PLoS pathogens* **17**, e1009519

414. Deatherage, C. L., Lu, Z., Kroncke, B. M., Ma, S., Smith, J. A., Voehler, M. W., McFeeters, R. L., and Sanders, C. R. (2017) Structural and biochemical differences between the Notch and the amyloid precursor protein transmembrane domains. *Science advances* **3**, e1602794

415. Schmidt, P., Bender, B. J., Kaiser, A., Gulati, K., Scheidt, H. A., Hamm, H. E., Meiler, J., Beck-Sickinger, A. G., and Huster, D. (2018) Improved in Vitro Folding of the Y2 G Protein-Coupled Receptor into Bicelles. *Frontiers in Molecular Biosciences* **4**

416. Fantin, S. M., Parson, K. F., Yadav, P., Juliano, B., Li, G. C., Sanders, C. R., Ohi, M. D., and Ruotolo, B. T. (2021) Ion mobility–mass spectrometry reveals the role of peripheral myelin protein dimers in peripheral neuropathy. *Proceedings of the National Academy of Sciences* **118**, e2015331118

417. Simons, M., Keller, P., De Strooper, B., Beyreuther, K., Dotti, C. G., and Simons, K. (1998) Cholesterol depletion inhibits the generation of beta-amyloid in hippocampal neurons. *Proceedings of the National Academy of Sciences of the United States of America* **95**, 6460-6464

418. Gell, D. A., Grant, R. P., and Mackay, J. P. (2012) The Detection and Quantitation of Protein Oligomerization. in *Protein Dimerization and Oligomerization in Biology* (Matthews, J. M. ed.), Springer New York, New York, NY. pp 19-41

419. Cao, Z., Hutchison, J. M., Sanders, C. R., and Bowie, J. U. (2017) Backbone Hydrogen Bond Strengths Can Vary Widely in Transmembrane Helices. *Journal of the American Chemical Society* **139**, 10742-10749

420. Lessen, H. J., Majumdar, A., and Fleming, K. G. (2020) Backbone Hydrogen Bond Energies in Membrane Proteins Are Insensitive to Large Changes in Local Water Concentration. *Journal of the American Chemical Society* **142**, 6227-6235

421. Li, G. C., Forster-Benson, E. T. C., and Sanders, C. R. (2020) Genetic intolerance analysis as a tool for protein science. *Biochimica et Biophysica Acta (BBA) - Biomembranes* **1862**, 183058

Appendix 1. Dodecyl-β-Melibioside Detergent Micelles as a Medium for Membrane Proteins

Contents:

Supporting Materials and Methods

Materials. n-Decyl-β-D-Maltoside (β-DM), n-Dodecyl-ß-D-maltoside (β-DDM), β-n-Dodecyl Melibioside (β-DDMB), n-Dodecylphosphocholine (DPC), 1-Myristoyl-2-Hydroxy-sn-Glycero-3-Phosphocholine (LMPC), and 1-Myristoyl-2-Hydroxy-sn-Glycero-3-Phospho-(1'-rac-Glycerol) (LMPG) were purchased from Anatrace. High grade imidazole, leucine, lysozyme, DNase, and RNase were purchased from Sigma. Amicon Ultracel 10 kDa and 30 kDa molecular weight cut-off (MWCO) spin filters were purchased from Millipore. D_2O (99 %) and $^{15}NH_4Cl$ were purchased from Cambridge Isotopes Lab. Lauryl betaine (Empigen), 30% solution, was purchased from BOC Sciences. PerfectPro Ni-NTA Superflow nickel resin was purchased from 5-Prime. DTT and IPTG were purchased from Research Products International.

Preparation of n-Dodecyl-β-Meliboside (β-DDMB). β-DDMB was synthesized and purified in-using a common glycosyl donor intermediate. The synthesis scheme is shown in Supporting Figure 2.1. The glycosyl donor was synthesized in two steps with an overall yield of 85%. Sequentially, the melibiose hydroxyl groups were protected, followed by bromination of the anomeric position to create a suitable leaving group. These two steps were carried out with minimum requisite workup protocols while the resultant donor, perbenzoyl bromomelibiose, was used for glycosylation without further purification.

The Lewis-acid catalyzed glycosylation reaction of the aforementioned glycosyl donor with the acceptor, n-dodecanol, provided the protected glycoside with a yield of approximately 80%. The respective β-isomer was separated at this stage by silica gel column chromatography using a suitable ratio of ethyl acetate in hexanes. Finally, the global deprotection of the hydroxyl protecting groups in a basic medium provided the β-DDMB target in 70% yield. β-DDMB was purified by reverse phase C18 chromatography using a linear gradient of 50-100% methanol in deionized water.

Supporting Figure 2.1

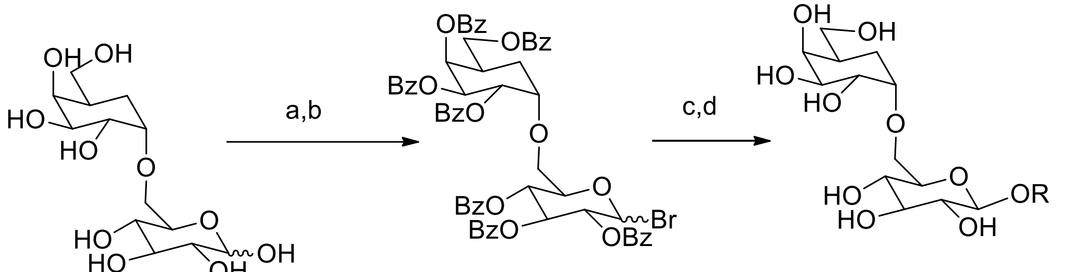

Melibiose

perbenzoyl bromomelibiose
BBMeli

n-Dodecyl-beta-D-Melibioside
R= $C_{12}H_{25}OH$; ME12

a. Pyridine, BzCl, 0°C to RT, 24 hrs; b. DCM, 33%HBr in AcOH, 4°C to RT, 6 hrs;
c. BBMeli, DCM, dodecanol, AgOTf, -20°C to RT, 24 hrs; d. NaOMe, MeOH, RT, 48hrs

Scheme 1. Synthesis of Melibiosides via benzoyl group protection

Dynamic Light Scattering. Stock solutions of each detergent were created by dissolving powdered detergent in ultrapure water. The stock solutions were flash frozen in liquid nitrogen and stored at -20 °C. All samples were mixed before ~300 µL was passed through a 0.2 µm syringe filter into a DLS-specific disposable cuvette. The sample chamber in the cuvette held roughly 100 µL and the excess 200 µL was used to compensate for evaporation from the sample chamber during heating. The disposable cuvette was covered with a disposable cap and placed into the Wyatt Technologies DynaPro NanoStar instrument for thermal equilibration. The samples were generally subjected to a temperature ramp from ~22 °C to 55 °C with a ramp rate of 1 °C/min, with 5 acquisitions of 5 second integration time for 80-90 points. The micelles were typically monodisperse, but at lower detergent concentrations (< 1 mM) aberrant readings were common. Acquisitions with a 25 % or higher polydispersity were not subjected to further analysis. The Stokes-Einstein equation (Eq. 1) was used to determine the hydrodynamic radius (R_h) via derived diffusion constants; k is Boltzmann's constant, T is the absolute temperature, η is sample viscosity, and D_t is the diffusion coefficient. Temperature and NaCl concentration effects on viscosity were taken into account by the Dynamics 7.1.9 software when determining R_h. It is important to note that the R_h determined by DLS is based on several assumptions and serves as an approximate measure of size.

$$R_h = \frac{kT}{6\pi\eta D_t} \qquad (1)$$

The DLS method was evaluated by taking well characterized detergents and analyzing the data to determine the micellar radius of hydration. The apparent micelle molecular weight was determined based on the assumption that the micelles at 25 °C have a density and shape similar to globular proteins, an option built into the Dynamics 7.1.9 software. This approach leads to an apparent aggregate molecular weight, from which the detergent aggregation number can be calculated. The aggregation number values from the DLS, found in Supporting Table 1, were usually in agreement with previously reported aggregation numbers determined with other methods.

Static Light Scattering. DLS-derived R_h and aggregate molecular weight values are reasonable approximations, however there are significant assumptions which must be made to extract micelle molecular weight and aggregation number. Static light scattering (SLS) can directly determine molecular weight and was used to confirm the DLS results. The Wyatt DynaPro NanoStar is capable of single angle static light scattering and was used to confirm the DLS-determined molecular weight for β-DM; the refractive index increment (dn/dc) value needed for the SLS analysis was previously reported to be 0.133 (1). An inline Wyatt Technologies DAWN8+ multi angle static light scattering instrument coupled to an Agilent 1200 series refractive index detector was used to determine the molecular weight of DPC and β-DDMB micelles. The β-DDM dn/dc of 0.133 was used for β-DDMB, which is reasonable in light of the chemical similarity of these detergents. A dn/dc of 0.139 was determined for DPC. The β-DDM and β-DDMB static light scattering results (Table 1) are in good agreement with the DLS results and the discrepancy for DPC is likely due to differences in DPC concentration and buffer composition.

NMR Spectroscopy. Two-dimensional $^{1}H,^{15}N$-TROSY spectra were collected at 318 K with the trosyetf3gpsi pulse program of the Bruker library. Experiments were conducted using 800 MHz or 900 MHz Bruker Avance spectrometers equipped with cryoprobes. Data was processed in TopSpin v3.2 and visualized with NMRFAM-SPARKY v3.115. Linewidths were determined with NMRview software with spectra that were processed in an identical manner.

Expression and Purification of E. coli Diacylgycerol Kinase (DAGK). DAGK was expressed and purified using methods similar to those described previously(2). His_6-tagged forms of wild type (WT) and of a stability enhanced triple mutant (I53C, I70L, V107D) form of DAGK (3) ("triple super DAGK") were expressed using *pTrc*-based pSD005 vectors(4) transformed into *E. coli* WH1061 cells, which lack endogenous DAGK and are leucine auxotrophs (5). DAGK was expressed and purified as previously reported(6). In brief, WH1061 cells were grown in M9, Leu-supplemented media and induced with 1 mM IPTG after reaching an OD_{600nm} of 0.8. Induced cells were cultured for 24 hours at RT before being pelleted and frozen in liquid nitrogen. Frozen cell pellets were thawed on ice and 20 mL of lysis buffer (300 mM NaCl, 75 mM Tris pH 7.8, 0.2 mg/mL PMSF, 5 mM MgAcetate, and 0.2 mM EDTA) was added per gram of wet cell pellet followed by addition of lysozyme (to 2 mg/ml), RNase (to 0.2 mg/ml), and DNase (to 0.2 mg/ml). After tumbling at RT for ~1hr, the lysis mixture was sonicated on ice and Empigen was added to 3%, followed by tumbling for ~1 hr at 4 °C. This solution was then centrifuged at 20,000 x g for 20 min at 4 °C and the supernatant was combined with buffer A-equilibrated Ni(II)-NTA "Superflow" resin at a ratio of 1 mL Ni-NTA per 1 gram starting wet cell mass (buffer A is 40 mM Tris pH 7.8, 300 mM NaCl, plus 0.5 mM fresh DTT). The resin and lysate supernatant were tumbled at RT for 1 hr before being centrifuged at 1000 x g for 5 min. The supernatant was removed and the resin was loaded into a gravity column and washed with buffer A containing 3% Empigen. To remove impurities, resin was washed with buffer A containing 1.5% Empigen and 40 mM imidazole until absorbance at 280 nm returned to baseline, reflecting completion of elution of non-His_6 tagged protein impurities from the resin. The detergent was exchanged by 10 X 1 column volume washes using a solution containing 0.5% w/v of the desired final detergent (β-DDMB, β-DM, or β-DDM) and 25 mM Tris pH 7.8. DAGK was eluted from the column using a buffer containing 250 mM imidazole pH 7.8 and 0.5% (w/v) of the detergent of choice. Following elution, the A280 of the purified DAGK solution was measured to determine the DAGK concentration based on 1.8 OD/(mg/ml·cm).

Purification of C99. The His_6-tagged 99 residue C-terminal domain of the human amyloid precursor protein has previously been expressed and purified into LMPG micelles(7,8) such that only a brief overview is given here. C99 was expressed from pET-21a in BL21(DE3) cells*,* which were grown in $^{15}NH_4Cl$-supplemented M9 medium to an OD600 of 0.6-0.7 before being induced with 1 mM IPTG. Induced cells were grown overnight at 18 °C. The cells were pelleted and enzymatically lysed (RNase, DNase, and lysozyme) in lysis buffer (75 mM Tris pH 7.8, 300 mM NaCl, 5 mM MgAcetate and 0.2 mM EDTA) by tumbling the mixture for 2 hours at RT. The lysate was then probe-sonicated on ice and then centrifuged at 20,000 x g for 20 minutes at 4 °C. The resulting pellet containing ^{15}N-labled C99 was resuspended in lysis buffer and sonicated/centrifuged two more times. The inclusion body pellet was then dissolved by urea/SDS (8 M urea, 300 mM NaCl, and 0.2 % sodium dodecyl sulfate) and tumbled overnight at room temperature. The dissolved inclusion body solution was centrifuged at 30,000 x g for 45 minutes at 25 °C and the supernatant was added to urea/SDS-equilibrated Ni-NTA at a ratio of 1 mL Ni resin per original 1 gram wet cells. The resin and supernatant were then tumbled for ~2 hours at room temperature and the resin was loaded onto a gravity column. On the column the resin was washed with 4 CV of urea-SDS followed by 6 CV of 0.2 % SDS in Tris buffered saline at pH 7.8. Impurities were washed off the column with 8 X 1 CV of 10 mM Imidazole pH 7.8 containing 0.05% (w/v) of the final detergent (LMPG, β-DDMB, or β-DDM). This was followed by elution with by 6 X 1 CV of 30 mM Imidazole pH 7.8 containing 0.05% of the final detergent. C99 was eluted off the column with 250 mM imidazole pH 7.8 containing 0.5 % of the final detergent. The pH of the pure C99 solution was adjusted to 4.5 or 6.5 with acetic acid. The protein was both buffer-exchanged and concentrated to 300-400 µM by repeated centrifugal ultrafiltration at 1000 x g in an Amicon 10 kDa MWCO spin filter followed by buffer dilution and re-concentration. The compositions of the final buffers used were either (i) 25 mM imidazole at pH 6.5, 10% D20, 0.5 mM EDTA, and 9% detergent when LMPG was the detergent used in elution or (ii) 25 mM Na acetate pH 4.5 or 6.5, 75 mM NaCl, 1 mM EDTA, 9% detergent, and 10% D20 when β-DDM or β-DDMB where used as the detergent in the elution. Concentrated samples were stored at room temperature.

Purification of the Notch 1 Transmembrane Domain. The purification of the His$_6$-Notch1 construct used in this paper has previously been published (9) (10) . The TM/JM domain (1721-1771) of Notch1 was expressed using a pTrcHis vector in *E. coli* BL21(DE3). Cells were grown at 37 °C in 2.8 L Fernbach flasks with 500 mL ^{15}NH$_4$Cl-labeled M9 media to an OD600 of 0.8, followed by induction with 1 mM IPTG at 25 °C for 20 hours. The harvested cells were subjected to enzymatic lysis for 30 minutes at 4 °C after being suspended in lysis buffer with 1 mM PMSF, protease inhibitor cocktail (Sigma P8849), and 1 mM DTT. Lysate was then probe-sonicated and the recombinant Notch1 was extracted by adding 3% Empigen to the lysate and tumbling for 4 hrs at 4 °C. The solubilized lysate was centrifuged at 30,000 x g for 45 minutes at 4 °C to remove insoluble components. 0.2 mL of Ni-NTA per liter of starting M9 media was equilibrated with 1X buffer A (40 mM Tris pH 7.8, 300 mM NaCl, and 1 mM DTT) and then added to the supernatant and tumbled overnight at 4 °C. Tumbled resin was loaded onto a small gravity column and rinsed with 10 CV of buffer A with 3% Empigen and then 10 X 1 CV of buffer A with 1.5% Empigen. The column detergent was swapped to LMPG to remove contaminants by washing with buffer A containing 0.2 % LMPG and the column was successively eluted with this buffer at imidazole concentrations 0 mM (12 CV), 25 mM (25 CV), and 65 mM (25 CV). LMPG was then either replaced by the final detergent of choice by re-equilibrating with 20 column volumes of 0.25% buffer A containing either 0.5% β-DDMB, β-DDM, or LMPC; Notch1 was eluted off the column with 300 mM IMD pH 7.8 containing either 0.5% β-DDMB, β-DDM, or LMPC (10 CV). Acetic acid was used to adjust the pH of eluted protein solution to 5.5 and the protein was both buffer-exchanged and concentrated using concentrated 200-300 µM by repeated centrifugal ultrafiltration at 1000 x g in an Amicon 10 kDa MWCO spin filter followed by buffer dilution and re-concentration. The compositions of the final buffers used were either (1) 65 mM imidazole at pH 5.5, 2 mM DTT, 10% D2O, 1 mM EDTA, and 1% LMPC or (2) 25 mM Na acetate pH 5.5, 75 mM NaCl, 1 mM EDTA, 10% D2O, and approximately 5% β-DDMB or β-DDM. Concentrated samples were stored at room temperature.

Expression and Purification of PMP22. Wild-type PMP22 was expressed and purified according to previously published protocol(11) with slight modifications. Briefly, the His$_{10}$-tagged PMP22 fusion protein was expressed recombinantly in *Escherichia coli* BL21(DE3) Star grown in minimal media at 20°C.

Protein expression was initiated by the addition of IPTG when the OD$_{600}$ reaches 1.0-1.2 and cells were grown for an additional 24 hours at 20°C before harvesting. After cell lysis, the fusion protein was extracted from the membrane using Empigen (Sigma) and was bound to Ni(II) resin. After washing with 40 mM imidazole to remove nonspecific binding, Empigen was then exchanged with the desired detergent by washing the resin containing the bound protein extensively with 25 mM phosphate buffer (pH 7.2), 1.0 mM TCEP, and 0.5% (w/v) of the desired detergent. The fusion protein was then eluted with buffer containing 50 mM TRIS, pH 8.0, 250 mM imidazole, 1.0 mM TCEP, and 0.5% of the desired detergent, and was then subsequently cleaved using thrombin.

After thrombin cleavage, the cleaved PMP22 is separated from the uncleaved fusion protein by again conducting Ni(II) affinity chromatography where the post-cleavage mixture was buffer-exchanged and resuspended in 50 mM TRIS, pH 8.0, 40 mM imidazole, 1.0 mM TCEP before incubation with Ni(II) resin for an hour. The resin was then washed with increasing concentration of imidazole. The cleaved PMP22 is mostly present in the flow through and the first wash eluate of the resin with 40 mM imidazole. These two solutions contain a few contaminants, so they are pooled together and buffer-exchanged with buffer containing 50 mM acetate (pH 5.0) and 1 mM DTT for further purification by cation exchange chromatography using a Hi-Trap SP-sepharose FF cation exchange column (GE Healthcare Life Sciences). For the sample in TDPC, PMP22 elutes at around 0.20 M NaCl, while for the samples at DDM and DDMB, PMP22 elutes at both 0.20 M and 0.40 M NaCl. The fractions containing PMP22 were pooled, buffer-exchanged, and concentrated using a 30 kDa MWCO Amicon Ultra centrifugal filters (Millipore). The final NMR buffer contains 50 mM acetate (pH 5.0), 10 mM DTT, 1 mM EDTA, 5% D_2O.

DAGK Enzyme Activity Assays. Assays were conducted using variations of a previously reported assay(12,13). 0.2 mg/mL DAGK stock solutions in the detergent-containing elution buffer from above were prepared, from which aliquots were used to start DAGK activity assay reaction. The DAGK activity assay couples the production of ADP by DAGK upon phosphorylation of DAG to the conversion of NADH to NAD+ by excess lactate dehydrogenase and pyruvate kinase. One mL of assay mix (75 mM PIPES pH 6.9, 50 mM LiCl, 0.1 mM EGTA, 0.1 mM EDTA, 0.2 mM DTT, 1 % (w/v) β-DM, β-DDM, or β-DDMB, 3 mol % cardiolipin, 4.5 mol% dihexanoylglycerol, 20 units each of lactate dehydrogenase and pyruvate kinase, 1 mM phosphoenolpyruvate, 3 mM ATP, 0.25 mM NADH, and 15 mM MgAcetate) were pipetted into a quartz cuvette and then incubated in a 30 °C temperature-controlled UV-Vis spectrophotometer sample cell. The β-DDM and β-DDMB assay mixes contained roughly slightly less cardiolipin than the traditional β-DM assay mixes due to the increased molecular weight of DDM. A ~2 µL aliquot of purified DAGK at 0.2 mg/mL was thoroughly mixed with the assay solution to start the assay, which was monitored at 340 nm. The linear decrease of absorbance at 340 nm signifies conversion of NADH to NAD+ and was quantitated to determine the DAGK activity as in previous work (12). Error bars reflect standard deviations calculated based on 3-4 replicates per condition.

Expanded Figure Captions (see main paper):

Figure 2.1. Use of dynamic light scattering (DLS) to characterize the mean radius of hydration (Rh) of β-DDMB and β-DDM micelles. A) 10mM DDMB (black) or 10mM DDM (red) detergent was dissolved in water and subjected to a 1°C/min temperature ramp; apparent micelle size was tracked by DLS. Each mean hydrodynamic radius value is the average over a temperature range indicated. For mean radius of 27 °C

the temperature range is 22-32 °C and for 50 °C the temperature range is 45-50 °C. B) Example of a temperature ramp used in panel A. C) β-DDMB micelle size as a function of pH (average value of the temperature range from 22 to 70 °C. The buffer was either 25mM imidazole buffered at pH 7.5 or 6.5 or 25mM sodium acetate at pH 5.5 or 4.5. The total β-DDMB concentration was 10 mM. D) β-DDMB micelle size (average value over the temperature range from 22 to 55 °C) as a function of salt concentration at 10 mM total β-DDMB.

Figure 2.2. Thermal stability of DAGK in β-DDMB and other detergents. DAGK samples (0.2 mg/ml) were incubated at 70°C, with aliquots being removed at time points and flash frozen prior to later assay in the standard DM/cardiolipin mixed miceller DAGK activity assay (12). The β-DDMB, β-DDM, β-DM, and DPC concentrations were 0.5 wt% (5 mg/ml) and samples were buffered with 250mM imidazole at pH 7.8.

Figure 2.3. DAGK activity assays started with detergent aliquots of DAGK diluted various micelle and mixed micelle assay mixtures. DAGK was purified into DDMB, DM, or DDM micelles. The long-established "standard" assay condition is labeled DM1XCL and contains 21 mM β-DM and 0.66 mM (3 mol%) CL. "1XCL" refers to the fact that the mole fraction of CL in the mixture is the same (1X) that as in the traditional assay procedure(12). All assays contained 1 wt% detergent (β-DDMB, β-DDM or β-DM) and either no lipid (0CL), 0.66 mM CL (1CL), or 1.32 mM CL (2CL). The β-DDM and β-DDMB assay mixes contain ~6 % less mol % cardiolipin than the DM assay mix.

Figure 2.4. NMR spectra of single span membrane proteins in β-DDMB and in other detergents. ^{15}N,^{1}H-TROSY-HSQC spectra were collected at 45°C on a 900MHz or 800MHz cryoprobe-equipped Bruker Avance III. A) 400µM C99 in 9% β-DDMB 25mM sodium acetate pH 6.5 (black) and 400µM C99 in 9% LMPG plus 25mM Imidazole pH 6.5 (red). C) 230µM Notch-TMD in 5% β-DDMB plus 25mM sodium acetate pH 5.5 (black) and 300µM Notch-TMD in 1% LMPC 65mM imidazole pH 5.5 (red). B) 400µM C99 in 9% β-DDMB plus 25mM sodium acetate pH 4.5 (black) and 300 µM C99 in 9% β-DDM 25mM sodium acetate pH 4.5 (red). D) 230µM Notch-TMD in 5% β-DDMB plus 25mM sodium acetate pH 5.5 (black) and 300µM Notch-TMD in 4.5% β-DDM plus 25mM sodium acetate pH 5.5 (red). E) 350µM PMP22 in 20% β-DDMB plus 50 mM acetate (pH 5.0), 10 mM DTT, 1 mM EDTA (black) and 700µM PMP22 in 20% TDPC plus 50 mM acetate (pH 5.0), 10 mM DTT, 1 mM EDTA (red). F) 350µM PMP22 in 20% β-DDMB plus 50 mM acetate (pH 5.0), 10 mM DTT, 1 mM EDTA (black) and 400µM PMP22 in 20% β-DDM plus 50 mM acetate (pH 5.0), 10 mM DTT, 1 mM EDTA (red).

Table S2.1. Micelle molecular weights determined by DLS and SLS for β-DDMB and for selected other previously well-characterized detergents.

Detergent	DLS Micelle MW(Da)[b]	SLS Micelle MW(Da)	Aggregation Number	Aggregation Number (Literature)
β-DM	33,000 ± 700	31,500 ± 200[b]	67-70 (DLS) 65-66 (SLS)	69[a], 82-90 (14)
β-DDM	59,000 ± 3000	N/A	109-121 (DLS)	78-149 (15), 135-145 (14) (1)
DPC	26,500 ± 1000	19,500 ± 400[c]	73-78 (DLS) 54-57 (SLS)	54[a] 60-80(14)
β-DDMB	42,000 ± 2000	44,400 ± 300[b]	80-88 (DLS) 87-89 (SLS)	65 (α/β anomeric mixture) (16)

a. Values previously reported by Anatrace in their catalog.
b. DLS values were conducted at 25 °C with a detergent concentration of 10mM in water.
c. Values calculated at 10% DPC w/v in phosphate buffer solution pH 6.5.

Supporting References

[1] Strop, P., and Brunger, A. T. (2005) Refractive index-based determination of detergent concentration and its application to the study of membrane proteins, *Protein Sci 14*, 2207-2211.

[2] Van Horn, W. D., Kim, H. J., Ellis, C. D., Hadziselimovic, A., Sulistijo, E. S., Karra, M. D., Tian, C., Sonnichsen, F. D., and Sanders, C. R. (2009) Solution nuclear magnetic resonance structure of membrane-integral diacylglycerol kinase, *Science 324*, 1726-1729.

[3] Zhou, Y. F., and Bowie, J. U. (2000) Building a thermostable membrane protein, *Journal of Biological Chemistry 275*, 6975-6979.

[4] Lau, F. W., and Bowie, J. U. (1997) A method for assessing the stability of a membrane protein, *Biochemistry 36*, 5884-5892.

[5] Miller, K. J., McKinstry, M. W., Hunt, W. P., and Nixon, B. T. (1992) Identification of the diacylglycerol kinase structural gene of Rhizobium meliloti 1021, *Mol Plant Microbe Interact 5*, 363-371.

[6] Oxenoid, K., Kim, H. J., Jacob, J., Sonnichsen, F. D., and Sanders, C. R. (2004) NMR assignments for a helical 40 kDa membrane protein, *J Am Chem Soc 126*, 5048-5049.

[7] Beel, A. J., Mobley, C. K., Kim, H. J., Tian, F., Hadziselimovic, A., Jap, B., Prestegard, J. H., and Sanders, C. R. (2008) Structural studies of the transmembrane C-terminal domain of the amyloid precursor protein (APP): Does APP function as a cholesterol sensor?, *Biochemistry 47*, 9428-9446.

[8] Barrett, P. J., Song, Y., Van Horn, W. D., Hustedt, E. J., Schafer, J. M., Hadziselimovic, A., Beel, A. J., and Sanders, C. R. (2012) The amyloid precursor protein has a flexible transmembrane domain and binds cholesterol, *Science 336*, 1168-1171.

[9] Deatherage, C. L., Lu, Z. W., Kroncke, B. M., Ma, S., Smith, J. A., Voehler, M. W., McFeeters, R. L., and Sanders, C. R. (2017) Structural and biochemical differences between the Notch and the amyloid precursor protein transmembrane domains, *Sci Adv 3*.

[10] Deatherage, C. L., Lu, Z. W., Kim, J. H., and Sanders, C. R. (2015) Notch Transmembrane Domain: Secondary Structure and Topology, *Biochemistry 54*, 3565-3568.

[11] Sakakura, M., Hadziselimovic, A., Wang, Z., Schey, K. L., and Sanders, C. R. (2011) Structural Basis for the Trembler-J Phenotype of Charcot-Marie-Tooth Disease, *Structure 19*, 1160-1169.

[12] Czerski, L., and Sanders, C. R. (2000) Functionality of a membrane protein in bicelles, *Anal Biochem 284*, 327-333.

[13] Van Horn, W. D., Kim, H. J., Ellis, C. D., Hadziselimovic, A., Sulistijo, E. S., Karra, M. D., Tian, C. L., Sonnichsen, F. D., and Sanders, C. R. (2009) Solution Nuclear Magnetic Resonance Structure of Membrane-Integral Diacylglycerol Kinase, *Science 324*, 1726-1729.

[14] Lipfert, J., Columbus, L., Chu, V. B., Lesley, S. A., and Doniach, S. (2007) Size and shape of detergent micelles determined by small-angle X-ray scattering, *J Phys Chem B 111*, 12427-12438.

[15] VanAken, T., Foxall-VanAken, S., Castleman, S., and Ferguson-Miller, S. (1986) Alkyl glycoside detergents: synthesis and applications to the study of membrane proteins, *Methods Enzymol 125*, 27-35.

[16] Kegel, L. L., Szabó, L. Z., Polt, R., and Pemberton, J. E. (2016) Alkyl melibioside and alkyl cellobioside surfactants: effect of sugar headgroup and alkyl chain length on performance, *Green Chem. 18*, 4446-4460.

Appendix 2. Bicelles Rich in both Sphingolipids and Cholesterol and Their Use in Studies of Membrane Proteins

The document includes:

Materials and Methods

Supplementary Figures S3.1-S3.6

Supplementary Table S3.1

Supplementary References

Materials and Methods.

Materials: β-n-Dodecyl melibioside (DDMB), 1-myristoyl-2-hydroxy-sn-glycero-3-phosphocholine (LMPC), and 1-myristoyl-2-hydroxy-sn-glycero-3-phospho-(1'-rac-glycerol) (LMPG) were purchased from Anatrace. 1,2-dimyristoyl-sn-glycero-3-phosphocholine (DMPC) and 1,2-dimyristoyl-sn-glycero-3-phospho-(1'-rac-glycerol) (DMPG) were purchased from Avanti Polar Lipids or CardenPharma. High purity cholesterol, imidazole, isoleucine, valine, alanine, phenylalanine, leucine, lysozyme, DNase, and RNase were purchased from Sigma-Aldrich. Amicon Ultracel 10 kDa and 30kDa molecular weight cut-off (MWCO) spin filters were purchased from Millipore. D_2O (99%), ^{15}N-amino acids, and $^{15}NH_4Cl$ were purchased from Cambridge Isotopes Lab. Lauryl betaine (Empigen), 30% solution, was purchased from BOC Sciences. PerfectPro Ni-NTA Superflow nickel resin was purchased from 5-Prime. Dithiothreitol (DTT) and isopropylthiogalactoside (IPTG) were purchased from Research Products International. (S-(1-oxyl-2,2,5,5-tetramethyl-2,5-dihydro-1H-pyrrol-3-yl)methyl methanesulfonothioate) (MTSL), 2-(14-carboxytetradecyl)-2-ethyl-4,4-dimethyl-3-oxazolidinyloxy (16-DSA), and Gd-diethylenetriamine penta-acetic acid (Gd-DTPA) were purchased from Santa Cruz Biotechnology. Egg Sphingomyelin was purchased from NOF Corporation. (N,N'-Dimethyl-N-(iodoacetyl)-N'-(7-nitrobenz-2-oxa-1,3-diazol-4-yl)ethylenediamine) (IANBD) and (1,5-IAEDANS, 5-((((2-iodoacetyl)amino)ethyl)amino)naphthalene-1-sulfonic acid) (IAEDANS) were purchased from Thermo Fisher.

Detergent Solubilization Tests for Cholesterol and/or Sphingomyelin-Containing Lipid Mixtures. 50 mgs of various cholesterol and/or sphingomyelin-containing lipid mixtures (see Table S1) were mixed with any one of 35 different detergents at the desired lipid-to-detergent mole ratio (q) in sealable glass vials with 1 ml of 50 mM phosphate buffer plus 1 mM EDTA at pH 7.0. The final detergent+lipid concentration was therefore 5% wt/vol. A cross-section of 35 different detergents were selected and a total of over 200 mixtures were tested. Samples were mixed vigorously by vortexing and then subjected to repeated heating (up to 100 °C) and cooling (including ice bath) cycles, flash freeze-thaw cycles with thawing first at room temperature and then via warm bath sonication (Fisher Scientific Solid-State Ultrasonic FS-9), and 10 day incubation at 37 °C to test in a robust manner if it was possible to form fully dissolved mixtures of mixed micelles or bicelles, depending on q ratio. Results are summarized in Table S1.

SCOR Bicelle Formation

Powdered DMPC, sphingomyelin, and cholesterol were warmed in sealed container from -30 °C to room temperature before being weighed out into a sealable ~15 mL glass vial. A benzene and ethanol mixture (95:5 v/v) was used to fully dissolve the lipid mixture with the aid of vortexing. Once fully dissolved, the majority of the solvent was evaporated at 45 °C with a Smart Evaporator C1 (BioChromato) equipped with a small roughing pump. The resulting gel-like mixture was then frozen and lyophilized overnight to remove remaining solvent. A 15 wt % stock solution of DDMB in ultrapure water was added to the lyophilized lipids to the desired DDMB-to-total lipid mole ratio to create a proto-bicelle mixture. Additional ultrapure water with ~1mM EDTA pH 7.8 was added to bring the proto-bicelle mixture to the desired final volume, with a typical final detergent+lipid weight-% value being 4%. The mixture was then extensively vortexed and flash frozen in liquid nitrogen. The frozen mixture was then placed in a warm sonication bath (Fisher Scientific Solid-State Ultrasonic FS-9) until it thawed and warmed to the bath temperature. This cycle of vortexing, freezing, and sonicated thawing was repeated at least three times, but some lipid mixtures required over 30 cycles to become completely clear. Generally, the final bicelle solution was a 4 wt % bicelle solution of 10 mL volume. Dynamic light scattering (see below) was used to confirm that the bicelles were present and of the expected size. Bicelles were always prepared in advance and stored at -30 °C after being flash frozen. The primary **s**phingolipid and **c**h**o**lesterol-**r**ich (**SCOR**) bicelles referred to in the paper contain an overall lipid:detergent mole ratio of 1:3 (q=0.33) with the lipid component consisting of DMPC:Egg Sphingomyelin:Cholesterol at a molar ratio of 4:2:1. Other mixtures that were tested for possible bicelle formation are listed in Supplemental Table 1. Egg SM is predominantly (~86 mole %) composed of the saturated C16-amidated form (*https://avantilipids.com/product/860061*), with minor compositions of other saturated forms, including the C18-amidated form (~6 mole %) and the C22-amidated form (3 mole %); the C24:1 unsaturated form is also present (~3 mole %).

Solid State NMR of 4:2:1 DMPC:eggSphingomyelin:Cholesterol Bilayered Vesicles

DMPC or DMPC-d_{54}, egg SM, and cholesterol were mixed in a chloroform/methanol mixture at a molar ratio of 4:2:1. After evaporating the solvent, the samples were re-dissolved in cyclohexane and lyophilized overnight. The obtained fluffy powder was hydrated with 50 wt% D_2O for ^1H MAS NMR or with deuterium-depleted H_2O to generate multilamellar vesicles for the other solid state NMR measurements.

Static ^2H and ^{31}P NMR experiments were carried out on a Bruker Avance I 750 MHz spectrometer (Bruker Biospin, Rheinstetten, Germany) operating at resonance frequencies of 114.9 MHz for ^2H and 303.1 MHz for ^{31}P. A double channel solids probe equipped with a 5 mm solenoid coil was used.

For the ^{31}P NMR spectra, a Hahn-echo pulse sequence was used. A ^{31}P 90˚ pulse length of 14 μs, a Hahn-echo delay of 30 μs, a spectral width of 100 kHz, and a recycle delay of 2.5 s were used. Continuous-wave proton decoupling was applied during signal acquisition. The measured NMR spectra were simulated using a program written in Mathcad 2001 to obtain the chemical shift anisotropy. The ^2H NMR spectra were accumulated with a spectral width of ±250 kHz using quadrature phase detection. A phase-cycled quadrupolar echo sequence was used.(17) The typical length of a 90° pulse was 5.0 μs, and a relaxation delay of 1 s was applied. NMR spectra were dePaked using the algorithm of McCabe and Wassall(18) and the order parameter profiles of the acyl chains were determined.(19)

^1H magic-angle spinning (MAS) NMR measurements were conducted on a Bruker 600 Avance III NMR spectrometer at a resonance frequency of 600.1 MHz using a triple channel 3.2 mm MAS probe. The ^1H 90° pulse length was 4 μs and the relaxation delay was 3 s. The MAS frequency was 10 kHz.

Small Angle X-Ray and Neutron Scattering

SCOR bicelle stocks were prepared at Vanderbilt and checked by DLS before being flash frozen and shipped on dry ice to the ORNL Bio-SANS and NSLS II LiX beamlines, where they were stored frozen and subjected to small angle scattering experiments, both X-ray and neutron. On arrival, SANS bicelle samples were checked for homogeneity and radius of gyration with a BioSAXS-2000 (Rigaku). Bicelle samples were diluted to 0.5 or 1.0 wt % to suppress inter-particle interactions (i.e. structure factor) to scattering curves while maintaining signal. It is known from DLS that SCOR bicelles of a given DDMB/lipid composition maintain their size over a range of concentrations spanning 0.25 wt% to 20.0 wt%. Bicelle samples were buffered with 10 mM imidazole pH 6.5, 0.1 mM EDTA, and 0.3 mM DDMB (0.3 mM being the CMC of DDMB). Samples were syringe-filtered through a 0.1µm filter before being placed in a banjo cell on the beamline. SANS scans of fully protonated SCOR bicelles at lipid:detergent mole-to-mole ratios (q) of 0.25, 0.33, 0.5, and 1.0, as well as of DDMB-only micelles scans, were collected in ~100 % D_2O buffer.

SAXS experiments were performed on the 16ID-LiX beamline at the National Synchrotron Light Source II (NSLS II), located at the Brookhaven National Laboratory (Upton, NY), with the standard flow-cell-based solution scattering setup and the X-ray energy of 13.5 keV with Q range from 0.005 to 2.5 $Å^{-1}$ Radial averaging and Q-conversion of data were performed using the standard software, merging data from all three detectors used in the measurements. The background subtraction was performed based on the water scattering (hydrogen bond) at $\sim$2.0 $Å^{-1}$.

All SANS experiments were conducted at Oak Ridge National Lab on the Bio-SANS(20) beamline at a sample-to-detector distance of 7 m using an average neutron wavelength of 6 Å with a wavelength spread of 15%. The combination of small-angle and wide-angle detectors allowed detection of **Q** ranging from 0.003 to 0.7 $Å^{-1}$ where **Q** is the scattering vector, defined as **Q**$\equiv 4n\pi/\lambda \sin \theta/2$, with θ and λ being the scattering angle and wavelength, respectively. The radius of gyration was determined from bicelles with the ATSAS software. Appropriate background of buffer was subtracted and data reduction was carried out before fitting following the standard procedure provided by facility-supplied reduction software.

Small Angle Scattering Analysis

SANS data analysis was performed using SASView 4.2.0 software (http://www.sasview.org/). The core-shell bicelle model used here is defined by the following equations. The scattering length density of the bicelle core (ρ_c), face (ρ_f) and rim (ρ_r) are defined as the follows:

$$\rho(r) = \begin{cases} \rho_c \;\; 0 < r < R;\; -L < z < L \\ \rho_f \;\; 0 < r < R;\; -(L + t_f) < z < -L; L < z < (L + t_f) \\ \rho_r \;\; R < r < R + 2t_r;\; -(L + t_f) < z < (L + t_f) \end{cases} \quad (1)$$

Where *R*, *2L*, t_f, and t_r stand for the radius, length, thickness of face and rim of the bicelle, respectively. Accordingly, the form factor of the bicelle could be presented in the following equations.

$$I(q,\alpha) = \frac{scale}{V_t} \int_0^{\pi/2} F(q,\alpha)^2 \sin(\alpha)\, d\alpha + BKG \quad (2)$$

$$F(q,\alpha)=\begin{bmatrix} (\rho_c-\rho_f)V_c\dfrac{2J_1(qR\sin\alpha)}{(qR\sin\alpha)}\dfrac{\sin(qL\cos\alpha)}{qL\cos\alpha} \\ +(\rho_f-\rho_r)V_{c+f}\dfrac{2J_1(qR\sin\alpha)}{(qR\sin\alpha)}\dfrac{\sin\left(q\left(L+t_f\right)\cos\alpha\right)}{q\left(L+t_f\right)\cos\alpha} \\ +(\rho_r-\rho_s)V_t\dfrac{2J_1(q(R+t_r)\sin\alpha)}{(q(R+t_r)\sin\alpha)}\dfrac{\sin\left(q\left(L+t_f\right)\cos\alpha\right)}{q\left(L+t_f\right)\cos\alpha} \end{bmatrix} \quad (3)$$

where *α* is the angle between *q* and the bilayer normal, whereas V_t, V_c and V_{c+f} are the total volume of the bicelle, core, and core + faces, respectively. R is the core radius, 2L is the length of the core, and J_1 is first order Bessel function.(21)

Bicelle Transbilayer Bilayer Head Group-to-Head Group Span

SAXS scattering curves for DDMB micelles and SCOR bicelles at various q (Lipid:Detergent mole-to-mole ratios) were plotted in Origin v8.6. The peak, indicated in Figure 3.2D, was fit to a bi-Gaussian peak to obtain the peak maximum (Q_{max}) while accounting for peak asymmetry. Qmax was converted into a headgroup-headgroup distance, L, in a model independent manner using equation 4.(22)

$$L=2\pi/Q_{max} \quad (4)$$

Modeling of Bicelle Structure/Composition Based on Small Angle Scattering Data

The SCOR bicelle dimensions at a q of 0.33 were determined from the SAXS and SANS global fitting. The surface area and volume of the bicelles were calculated via equations 5 and 6, respectively, where a, b, and c are radii and a=b. The surface area of a lipid or detergent head group was assumed to be 70Å^2. Average lipid/detergent weights and volumes were calculated based on the overall mol % as shown in equation 7. The total number of lipid and detergent molecules in a bicelle assembly was determined via volume and surface area arguments based on the population average (μ) shown in equations 8 and 9. Multiplying the aggregation number by the average molecular weight reveals the bicelles to be ~98000-106000 Daltons. This value is in agreement with the ~105000 Daltons estimate provided by DLS (will be described below).

$$SA_{bicelle}=4\pi\left(\frac{(ab)^{1.6}+(ac)^{1.6}+(bc)^{1.6}}{3}\right)^{1/1.6} \quad (5)$$

$$V_{bicelle}=\frac{4}{3}\pi abc \quad (6)$$

$$MW_{\mu\,(q=0.33)}=\frac{1}{3}\left(\left(MW_{DMPC}*\frac{4}{7}\right)+\left(MW_{EggSM}*\frac{2}{7}\right)+\left(MW_{Chol}*\frac{1}{7}\right)\right)+\frac{2}{3}\left(MW_{DDMB}\right) \quad (7)$$

Lipid Parameters Used for These Calculations

Component	Molecular Weight	Volume (Å^3)
DDMB	510.6	453*(23)
DMPC	677.9	1099(24)
Egg Sphingomyelin	711	1232(25)
Cholesterol	386.7	630(24)
μ (q=0.33)	555	658

* Volume of DDM (which is chemically similar to DDMB)

$$N_{agg}=\frac{V_{bicelle}}{V_{\mu}}=\sim 191\ molecules \quad (8)$$

$$N_{agg}=\frac{SA_{bicelle}}{70Å^2}=\sim 177\ molecules \quad (9)$$

Cryo-EM data collection

3.0 µl of 0.64 wt % bicelle samples (at both q = 1 and q = 0.33) in 75 mM NaCl, 1 mM EDTA, 25 mM sodium acetate, pH 4.5 were applied to a 200 mesh Quantifoil R1.2/1.3 that was glow discharged for 2 min at 25 milliamperes. The grid was blotted for 2s with a blot force of 5 or 6 before being plunged into liquid ethane using a Thermo Scientific Vitrobot Mark IV at 22°C and 100% humidity. The bicelle micrographs were collected using a Thermo Scientific Polara TF30 microscope at Vanderbilt operated at 300 keV. Micrographs were recorded using counted mode on a K2 Summit direct electron detector (Gatan) at a nominal magnification of 31,000× in a defocus range of −1.5 to −3.5 µm at a low-dose condition with a calibrated magnification of 1.24 Å/pixel. The bicelle samples were exposed for 8 s over 40 frames, resulting in a total dose of 75 e−/Å2. Data were collected both manually and with automation using SerialEM.

Image processing of the Polara datasets

All images were motion-corrected using motioncor2 with a dose weighting parameter of 2.3 e^-/angstrom/frame and a total dose of 40e^-/Å2. The contrast transfer function for each image was determined using Gctf(26) and used to remove micrographs with low maximum resolution or high astigmatism. Further processing was carried out using RELION2.(27) Putative particles were identified by autopicking, using representative class averages obtained from manually picked particles as templates. q = 1.0 Bicelle particles were extracted at a box size of 250 × 250 pixels and q = 0.33 bicelle particles were extracted at a box size of 128 x 128. 2D class averages were determined using 25 iterations of classification. Bicelle dimensions were determined from 50 particles using ImageJ.

Dynamic Light Scattering

SCOR bicelle solutions were allowed to equilibrate at room temperature and visually checked for transparency and diluted to 0.5 wt % solutions [(100X weight (lipid+detergent)/volume] unless noted. The buffer used for dilution contained a critical micelle concentration of DDMB (0.3 mM), 10 mM buffer (either sodium acetate for pH 4.5 or imidazole for pH 6.5 and 7.8), and varying NaCl concentration. Solutions were filtered through 0.1 µm syringe filters to remove dust and trace residual lipid vesicles. The bicelle solution was then added to the inner and overflow chamber of a disposable cuvette, which helps to suppress evaporation from the experimentally observable inner chamber. Finally, the disposable DLS cuvette was capped before being loaded in the DLS instrument. Experiments were generally carried out at 25 °C, with temperature-dependent experiments involving ramping from 22 °C to 55 °C at a rate of 1 °C/minute. Possible changes in viscosity occurring when ionic strength and/or temperature were varied were taken into account by the Dynamics 7.5 software (Wyatt Technologies). The DLS software calculates an apparent hydrodynamic radius (R_h) via the Stokes-Einstein equation (Eq. 10):

$$R_h = \frac{kT}{6\pi\eta D_t} \qquad (10)$$

where k is Boltzmann's constant, T is the absolute temperature, η is sample viscosity, and D_t is the diffusion coefficient. The apparent molecular weight of the SCOR bicelles was calculated in the Dynamics software, as based on the measured apparent radius of hydration, using the assumption that the density of the bicelle is similar to that of a globular protein.

Recombinant Expression of the C99 Protein

The C99 construct used in this study has been previously purified into, variously, LMPG micelles, DDMB micelles, and DMPC/DHPC bicelles, as reported.(8,28,29) Therefore, only a brief explanation will be given here. Unless otherwise stated, the construct used in this study had a tryptophan incorporated in the C-terminal purification tag at position 109 to aid in UV-Vis based protein quantification. For ^{15}N-labeled C99 samples, protein was expressed based on a pET-21a vector in BL21(DE3) cells, which were grown in $^{15}NH_4Cl$-supplemented M9 medium to an OD_{600} of ~ 0.6 before being induced with 1 mM IPTG. Induced cells were incubated overnight with shaking at 18 °C and harvested in the morning by centrifugation. The cells were flash frozen in liquid nitrogen and stored at -80 °C. Uniformly triple-labeled C99 (^{2}H, ^{13}C, and ^{15}N) was produced following the gradual conditioning of *E. coli* cells to deuterated media as follows: a single colony was picked and allowed to grow overnight at 37 °C in 50 mL of protonated LB media containing ampicillin. The next morning, 1 mL of the LB media was transferred to 30 mL of protonated M9 media and allowed to grow to an O.D. of ~0.8 at 37 °C, at which point 1 mL was placed in 30 mL of 70 % D_20 M9 media containing ampicillin. The 70 % D_2O medium was allowed to grow overnight to an O.D. of ~0.8 and then one mL was placed in 30 mL of triple labeled (U-^{13}C,^{15}N, plus 99 % D_2O) M9 media at 37 °C. If the cells were able to grow in the 99 % D_2O aliquot to an OD_{600} approaching 1.0 or above, 8 mL of the aliquot was transferred into ~1 L triple-labeled M9 media at 37 °C containing ampicillin. This culture was induced when the OD_{600} reached ~0.4 with 1.1 mM IPTG and then incubated with continued shaking at 18 °C for 28 hours before being harvested and flash frozen.

Amino acid-specific labeling was achieved through the use of an auxotrophic *E. coli* strain, CT19. The CT19 strain is deficient with regard to synthesis of specific amino acids (Val, Ala, Tyr, Leu, Ile, Asp, Phe, and Trp), such that these amino acids must be added to the medium to enable growth.(30) The "CT19 medium" was similar to traditional M9 except that 0.5g/L of Val, Ala, Leu, Ile, and Phe are added directly to the medium before autoclave-based sterilization. Additionally, 0.5g of Tyr and Asp and 0.1g of Trp were added to the media when adding other traditional M9 reagents (vitamins, glucose, etc.) before inoculation. The C99 plasmid used above was transformed into CT19 cells and plated on an ampicillin, kanamycin, and tetracycline supplemented agar plate. The next day, a colony was picked and placed in 100 mL of antibiotic-supplemented LB, which was allowed to grow overnight at 37 °C. The next morning, 12 mL of the overnight LB was placed in unlabeled CT19 medium and allowed to grow to an O.D. of ~ 0.7 at 37 °C. The CT19 cells were then harvested by centrifugation at 3000xg for 20 minutes at 25 °C before being resuspended in fresh CT19 medium with a single ^{15}N-supplemented amino acid. The cells and media were then incubated with shaking at 18 °C and induced with 1mM IPTG for 13 hours before being harvested and flash frozen.

Purification of C99 into SCOR Bicelles

Frozen cell pellets were thawed, suspended in lysis buffer (75 mM Tris pH 7.8, 300 mM NaCl, 5 mM MgAcetate and 0.2 mM EDTA), and then enzymatically lysed (RNase, DNase, and lysozyme) by tumbling the mixture for at least 2 hours at RT. The lysate was then probe-sonicated on ice for 10 minutes with a 50% duty cycle followed by centrifugaton at 20,000 x g for 20 minutes at 4 °C. The resulting inclusion body pellet containing isotopically-labeled C99 was resuspended in lysis buffer with a Dounce homogenizer and sonicated/centrifuged two more times to remove cytosolic and membrane contaminants. The inclusion body pellet was dissolved in lysis buffer without EDTA and containing 3% Empigen detergent and allowed to tumble overnight at 4 °C. The insoluble fraction was removed by centrifuging the solution at 25,000xg for 45 minutes at 4 °C. The supernatant was combined with pre-equilibrated Ni-NTA at a ratio of 1 mL of resin for every 7 grams of original wet cell mass. The resin and supernatant were allowed to tumble at room temperature for 1-2 hours. The suspension was centrifuged at 200xg to pellet the protein-laden resin, which was loaded into a gravity column and washed with 20 column volumes (CV) of EDTA-free lysis buffer with 3 % Empigen. To remove weakly bound impurities and change the membrane mimetic, the column was washed with 20 CV of 0.25 wt % SCOR bicelles in 30 mM imidazole pH 7.8. C99 was eluted from the column with 0.5 wt % SCOR bicelles in 500 mM imidazole pH 7.8. Protein elution was tracked my monitoring the absorbance at 280nm and only the main peak was collected. The C99 concentration was determined via UV absorption at 280 nm using a molar extinction coefficient of 11,400 $M^{-1}cm^{-1}$; this value is different from previously reported coefficients due to the inclusion of a tryptophan in the purification tag. The purity of C99 was assessed by SDS-PAGE. The C99-SCOR bicelle complex was found to remain soluble for several months at moderately acidic pH, such that glacial acetic acid was used to adjust the pH of the C99 solution to pH 4.5 soon after purification. The protein-bicelle complex was then buffer-swapped into NMR buffer (25 mM sodium acetate pH 4.5 with 75 mM sodium chloride, 1 mM EDTA, and a critical micelle concentration of DDMB 0.3 mM) by 2 rounds of 10-20X concentration via centrifugal ultra-filtration using an Amicon Ultra-4 30KDa molecular weight cut-off filter (Millipore) followed by 10X-20X dilution with the NMR buffer before a final concentration step. The final bicelle concentration was in the 5-10 wt-% range. The concentrated sample was stored at 4 °C for short term storage or frozen in liquid nitrogen for long term storage at -80 °C.

Backbone NMR Resonance Assignments for C99 in SCOR Bicelles

The NMR resonance assignment process for C99 in SCOR bicelles was challenging due to the large size (roughly 100 kDa, minus protein) of the q =0.33 SCOR bicelles. All NMR experiments reported here were measured on a 900 MHz Bruker Avance III spectrometer equipped with a cryoprobe in a Bruker shaped sample tube (Z106898) and at 45 °C. TROSY-based HSQC, HNCO, HNCA, and HNCB spectra were acquired on 400-µM C99 samples in 10 wt % SCOR bicelles q=0.33 in NMR buffer. Non-transmembrane segments of the protein were easily and confidently assigned, but ^{13}C resonances from transmembrane sites tended to be very broad even though C99 was perdeuterated. We therefore also incorporated a strategy in which we collected NMR data for C99 in DDMB micelles, a condition that yields spectra that are similar to those for C99 in SCOR bicelles, only much more highly resolved (and therefore easier to assign). TROSY-based HSQC, HNCO, HN(CA)CO, HNCA, and HNCB spectra were acquired on a 350-µM perdeuterated U-^{13}C,^{15}N-C99 sample in 10 wt % DDMB in NMR buffer. These spectra were used to help complete the assignment of the ^{1}H,^{15}N-TROSY resonances of C99 in DDMB, as shown in supplemental Figure S3.4. It was possible to transfer many of these assignments to previously unassigned peaks from C99 in SCOR bicelles, a process that was facilitated by drawing upon previously completed assignments for C99 in conventional DMPC/DHPC bicelles.(8) The assignment process was also facilitated by collection of TROSY spectra from C99 prepared with amino acid type-specific ^{15}N-labeling. Spectra were processed in TOPSPIN 3.2 and analyzed using NMRFAM-SPARKY version 1.413. Chemical shift values for C99 in SCOR bicelles are listed under BMRB ascension number 50083.

Nitroxide Spin-Labeling of C99

C99 was purified and labeled with the paramagnetic probe MTSL as previously reported.(31) C99 with a L723C or K699C mutation was purified in a similar manner as WT C99, with the following exceptions. To remove impurities, the initial C99-bound Ni(II)-resin was washed extensively with 10mM imidazole pH 7.8, 0.05% LMPG in 1x Tris-buffered saline (TBS) followed by an extensive wash with 30mM imidazole, pH 7.8, 0.05% LMPG in 1x TBS. Next, the mutant C99 was eluted from the resin in 20 mM Tris, 200 mM NaCl, 0.05% LMPG, 250 mM imidazole at pH 7.8, such that the final C99 concentration for the whole elution fraction was ~50 µM. The pH of the eluate was adjusted to 6.5 with 1M HCl and 1 mM EDTA was added before the solution was concentrated 10X to ~0.5 mL using centrifugal ultrafiltration with an Amicon Ultra-4 30KDa molecular weight cut-off filter cartridge. The retentate was transferred to a 1.5 mL Eppendorf tube and fresh DTT was added to 2.5 mM after replacing the air in the tube with Ar gas. The sample was gently tumbled at room temperature overnight to reduce disulfide bonds. The next morning, 250 mM MTSL dissolved in DMSO was added to 10 mM in the L723C or K699C C99 in LMPG solution, and the sample was gently tumbled at room temperature for 30 minutes before being transferred to 37 °C for three hours. The sample was stored at room temperature overnight. The sample was then buffer-exchanged using the same type of Amicon filter as used above with 50 mM phosphate buffer pH 7.8 until the final imidazole concentration was 2.5 mM. The MTSL-labeled C99 was then re-associated to 1 mL of fresh Ni resin by tumbling the resin and protein together for one hour at 4 °C. The C99-bound resin was then loaded into a gravity column and extensively washed with 50 mM phosphate buffer pH 7.8 with 0.05 wt % LMPG to remove MTSL-modified DTT and unreacted MTSL. The resin-associated spin-labeled C99 protein was then re-equilibrated with a SCOR bicelles solution and eluted from the column as described previously for WT C99 in SCOR bicelles. The spin labeling efficiency for each C99 sample was quantified by double integrating EPR. The estimated spin label concentration was then compared to the protein concentration determined by UV absorbance at 280 nm using an extinction coefficient of 11400 $M^{-1}cm^{-1}$. In both cases, the spin labeling efficiency was observed by EPR to be ~30-40%.

Measurement of NMR ^{15}N Relaxation Times and ^{1}H-^{15}N Steady State NOEs (ssNOEs)

TROSY-based ^{15}N T1, T2, and ^{1}H-^{15}N ssNOE were collected on a U-^{15}N 300 μM C99 sample in 5 wt % SCOR bicelles at q=0.33 in NMR buffer at 45 °C. Steady-state heteronuclear NOE values were determined from peak intensity ratios between interleaved spectra collected with and without 3 second presaturation. An interleaved T1 experiment was run with ⍰ values of 0.1, 0.25, 0.5, 0.8, 1.1, 1.4, 2.5, and 4.5 seconds. The interleaved T2 experiment was run with ⍰ times of 17, 34, 51, 68, 85, 102, 119, and 136 milliseconds. Spectra and relaxation times were analyzed with SPARKY, using its peak height analysis extension. The reported error for each measurement represents the uncertainty of the fit. For SCOR bicelle samples T2 relaxation rates were too short for many transmembrane C99 sites. Therefore, relaxation times could not be measured, reflecting the >100 kDa molecular weight of the C99/SCOR bicelle assemblies.

Probing the Membrane Topology of C99 in SCOR Bicelles

Lipophilic (16-DSA) and aqueous (Gd-DTPA) paramagnetic probes have previously been used in conjunction with NMR to probe the membrane topology of sites within C99 and other membrane proteins.(29) A 900 MHz Bruker Avance III spectrometer equipped with a cryoprobe was used to collect ^{1}H,^{15}N-TROSY spectra on 200-400 μM U-^{15}N-C99 samples in 5-10 wt % q=0.33 SCOR bicelles in NMR buffer at 45 °C. The exposure of amide sites to the paramagnetic probes was determined by comparing residue peak heights between matched reference and probe-containing C99 samples. The optimal probe concentration was in each case determined empirically. Due to lipid solubility issues, 16-DSA experiments required that 16-DSA be added at the early organic solvent step of bicelle preparation (see previous section). With the exception of the experiment summarized in Figure 3.6C, all Gd(III)-DTPA and 16-DSA addition experiments were completed in triplicate, with probe-induced reductions in peak intensity being averaged for the three replicates. In this case, the uncertainty of each measurement was determined to be the standard deviation calculated for the replicates. One replicate of each experiment involved a construct of C99 where the purification tag was moved from the C-terminus to the N-terminus, referred to as NT2, which revealed that results were independent of which terminus the purification tag was attached to. A non-paramagnetic 16-DSA reference spectrum was collected following addition of ascorbic acid in NMR buffer to 10 mM as a nitroxide reducing agent, followed by 1-hour incubation before collecting the reference spectrum. Gd-DTPA experiments were carried out by collecting TROSY spectra using matched acquisition parameters, first in the absence of the chelate and then following addition of Gd-DTPA dissolved in NMR buffer to 1 mM.

Water-protein NH proton chemical exchange was also tracked by NMR. CLEANEX-PM(32) HSQC spectra was acquired on 350 μM U-^{15}N-C99 samples in 10 wt % SCOR bicelles q=0.33 in NMR buffer at 45 °C. Peak intensities acquired with 100, 50, and 10 ms mixing times were compared to a reference spectrum. It was found that the 50 ms mixing time result exhibited the highest dynamic range of peak intensities.

Förster Resonance Energy Transfer (FRET) of C99 in SCOR Bicelles

L732C C99 was overexpressed in a large culture (12 L) and was purified into q = 0.33 SCOR bicelles, followed by adjustment of the pH to 4.5 with glacial acetic acid. EDTA and fresh DTT were added to the protein solution to 1 mM and 2.5 mM, respectively, and the solution was tumbled overnight at room temperature. The reduced protein was checked using SDS-PAGE to verify that L732C C99 was monomeric. The L732C-C99 in SCOR bicelle solution was then buffer-swapped into NMR buffer to remove DTT and concentrated 10X with an Amicon Ultra-4 30KDa filter cartridge, repeated three times. The protein concentration was determined by UV spectrophotometry at 280 nm before being split into two aliquots. To each aliquot was added either fresh DMSO-dissolved IANBD or IAEDANS from 200 mM stocks to a molar concentration 10 times that of C99. The mixture was covered in foil and allowed to react with the dyes for two days at room temperature with gentle tumbling. To remove excess dye, the samples were extensively buffer exchanged into fresh NMR buffer. Labeling efficiency was determined using UV-Vis by comparing the protein concentration and dye concentrations using extinction coefficients of 5600 $M^{-1}cm^{-1}$ at 337 nm for IAEDANS and 23700 $M^{-1}cm^{-1}$ at 472 nm for IANBD. While the extent of IAEDANS labeling was found to be ~100 %, the IANBD labeling efficiency was found to be only ~25 %.

All FRET experiments were conducted at 25 °C and samples were mixed for at least 1 hour before collection of a spectrum. IAEDANS (donor) was excited at 336 nm and IANBD (acceptor) was excited at 463 nm while emission spectra were collected from 346 to 700 nm. FRET experiments were carried out on a Fluoromax-3 (Horiba) spectrometer. Experiments with increasing acceptor-labeled C99 maintained a constant protein-to-lipid ratio. FRET efficiency (E) was determined according to equations 11 and 12 and then normalized from 0 to 1 so the methods of determining efficiency could be compared. I_{DA} is the intensity of the donor in the presence of acceptor and I_D is the intensity of the same concentration of donor in the absence of acceptor.

$$(E) = 1 - \frac{I_{DA}}{I_D} \tag{11}$$

I_A is the intensity of the acceptor and I_D is the intensity of the donor.

$$(E) = \frac{I_A}{I_A + I_D} \tag{12}$$

Both methods yielded similar efficiency values when normalized from 0 to 1 and were linear in nature.

Electron Paramagnetic Resonance (EPR) Double Electron Electron Resonance (DEER) of C99 in SCOR Bicelles.

X-band (9.5 GHz) CW-EPR spectra were collected at room temperature using a Bruker EMX spectrometer at an incident power of 10 mW and 1.6-gauss modulation amplitude. DEER experiments were performed at 83 K on a Bruker 580 pulsed EPR spectrometer at Q-band frequency (34 GHz) using a standard four-pulse protocol.(33) Samples were diluted with NMR buffer from ~200 M K699C or L723C C99 in NMR buffer and 5 % SCOR bicelles (q = 0.33). Analysis of the DEER data to determine the distance probability distribution (P(r)) was carried out using in house software running in MATLAB.(34)

Glutaraldehyde Crosslinking of C99 in SCOR Bicelles

Glutaraldehyde (GA) crosslinking followed by SDS-PAGE was used to probe the oligomerization of C99. C99 was purified into SCOR bicelles as described above. A stock protein sample of 250 µM C99 in 2.5 wt-% bicelles q =0.33 was aliquoted into a 50-µL volume containing freshly diluted glutaraldehyde, 50 M C99, SCOR bicelle q=0.33 from 0.5 to 4.0 wt % and 0.1 mM EDTA. Chemical crosslinking and other biophysical techniques below require a lower protein and bicelle concentration than the NMR experiments, but the ratio of C99 to lipid is similar between all experiments. Samples were mixed and then allowed to react at room temperature for 30 minutes before 15 µL was removed and quenched with 2 µL of 1 M tris-glycine. Samples were then subjected to SDS-PAGE stained with SimplyBlue and imaged on a Kodak Gel Logic 112. Images were checked for oversaturation. Oligomeric band signals were integrated and analyzed using ImageJ. This process was repeated for three separate C99 purifications.

Ion mobility - mass spectrometry (IM-MS) experiments.

All IM-MS data were collected using a Synapt G2 HDMS IM-Q-ToF mass spectrometer (Waters, Milford, MA), with a direct infusion nESI source set to positive ion mode. The instrument settings were tuned to generate intact C99 and C99 complex ions while completely dissociating them from SCOR bicelles, including appropriately tuned settings for the sampling cone (80 V), trap cell accelerating potential (200V) and the transfer cell accelerating potential (70V).(35,36) The trapping cell wave velocity and height were 116 m/s and 0.1 V. The IMS wave velocity and height were 250 m/s and 15 V. The transfer cell wave velocity and height were 300 m/s and 10 V. Prior to analysis, C99 in SCOR bicelles at a protein concentration of 29 µM was exchanged from buffer containing 25 mM sodium acetate, 75 mM NaCl, 1 mM EDTA, 500 mM imidazole, and 1 x CMC (0.3 mM) of DDMB to 200 mM ammonium acetate containing 1 x CMC of DDMB detergent using 30 kDa Amicon Ultra-0.5 centrifugal filter cartridges (MilliporeSigma, Burlington, MA). For bicelle dilution experiments, C99 was bound to Ni resin as described above and the resin was split into equal aliquots. Different wt/v percentages of bicelles were used to elute C99 from each aliquot of resin and each dilution was buffer exchanged and analyzed via IM-MS the same way. For all SCOR bicelles measured at varying wt %, C99 was observed as monomeric, dimeric, and trimeric species, with charge state distributions of 4+ - 6+, 7+ - 12+, and 11+ - 13+ respectively. These charge states were observed to persist across all bicelle weight percentages, and were extracted into a text-based format using TWIM Extract to compute the relative intensity of each species at a given bicelle weight percentage.(37)

Supplementary Figures.

Figure S3.1

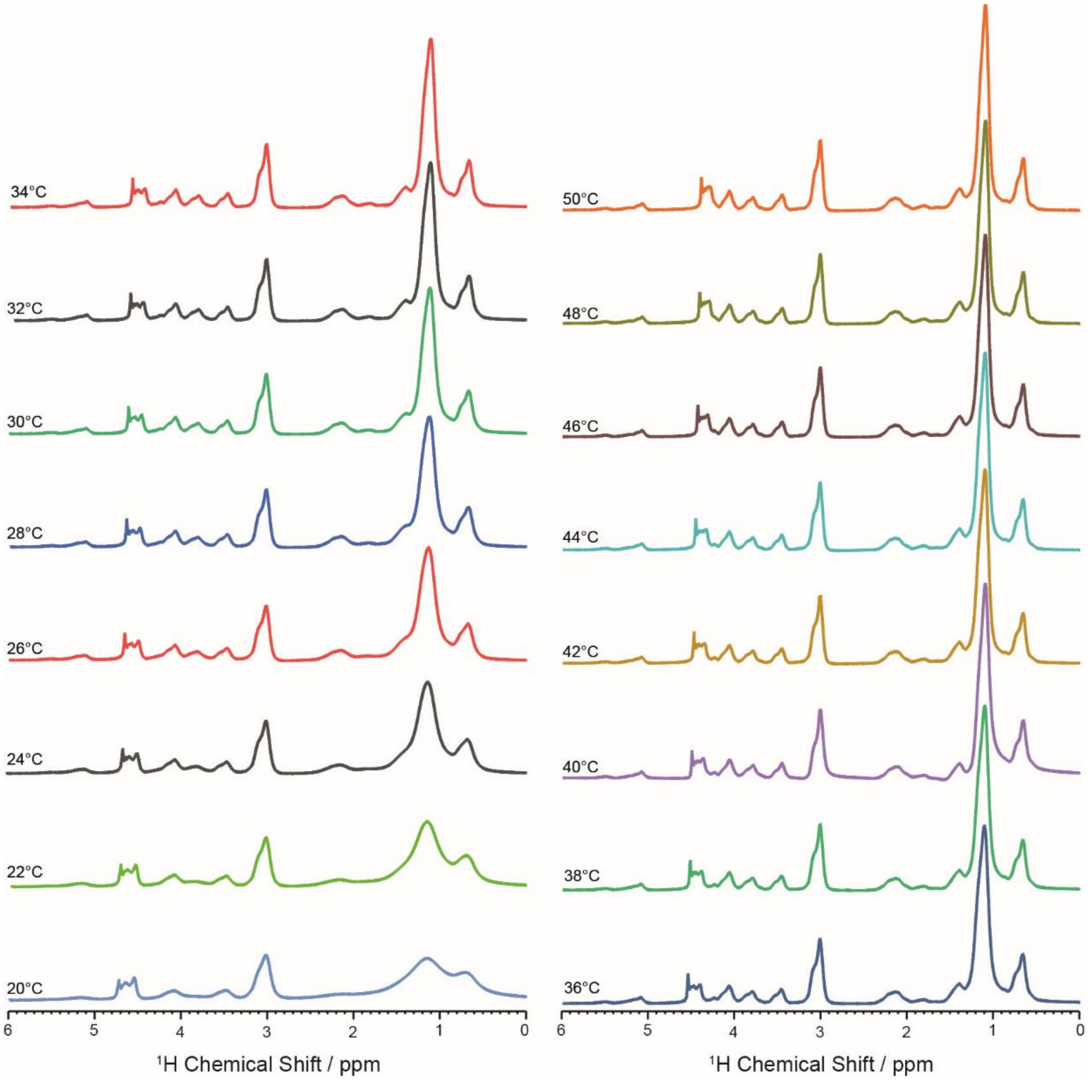

Figure S3.1. ^{1}H magic angle spinning (MAS) NMR spectra of hydrated DMPC/egg-SM/cholesterol (4/2/1 mol/mol/mol) vesicles at various temperatures. NMR spectra were recorded at a MAS frequency of 10 kHz.

Figure S3.2

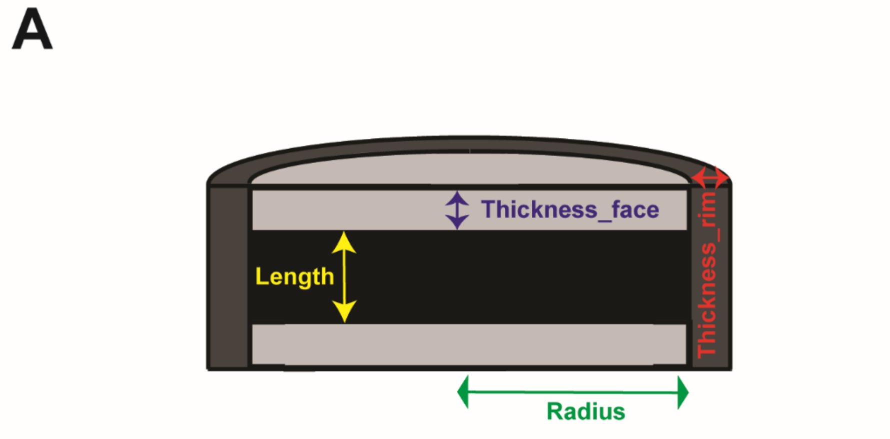

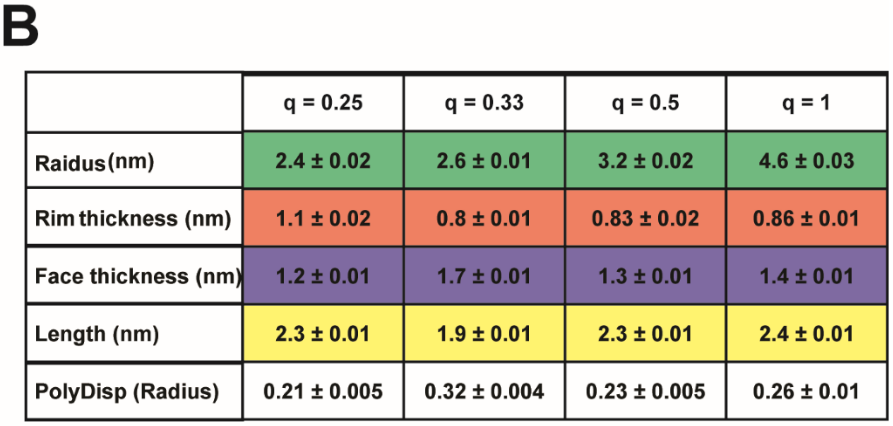

	q = 0.25	q = 0.33	q = 0.5	q = 1
Raidus (nm)	2.4 ± 0.02	2.6 ± 0.01	3.2 ± 0.02	4.6 ± 0.03
Rim thickness (nm)	1.1 ± 0.02	0.8 ± 0.01	0.83 ± 0.02	0.86 ± 0.01
Face thickness (nm)	1.2 ± 0.01	1.7 ± 0.01	1.3 ± 0.01	1.4 ± 0.01
Length (nm)	2.3 ± 0.01	1.9 ± 0.01	2.3 ± 0.01	2.4 ± 0.01
PolyDisp (Radius)	0.21 ± 0.005	0.32 ± 0.004	0.23 ± 0.005	0.26 ± 0.01

Figure S3.2. Fitting of small angle scattering data for SCOR Bicelles. (A) Descriptive dimensions for the core-shell bicelle model. **(B)** Bicelle dimensions as a function of q, based on fitting the SAXS and SANS data to the core-shell bicelle model shown in A.

Figure S3.3

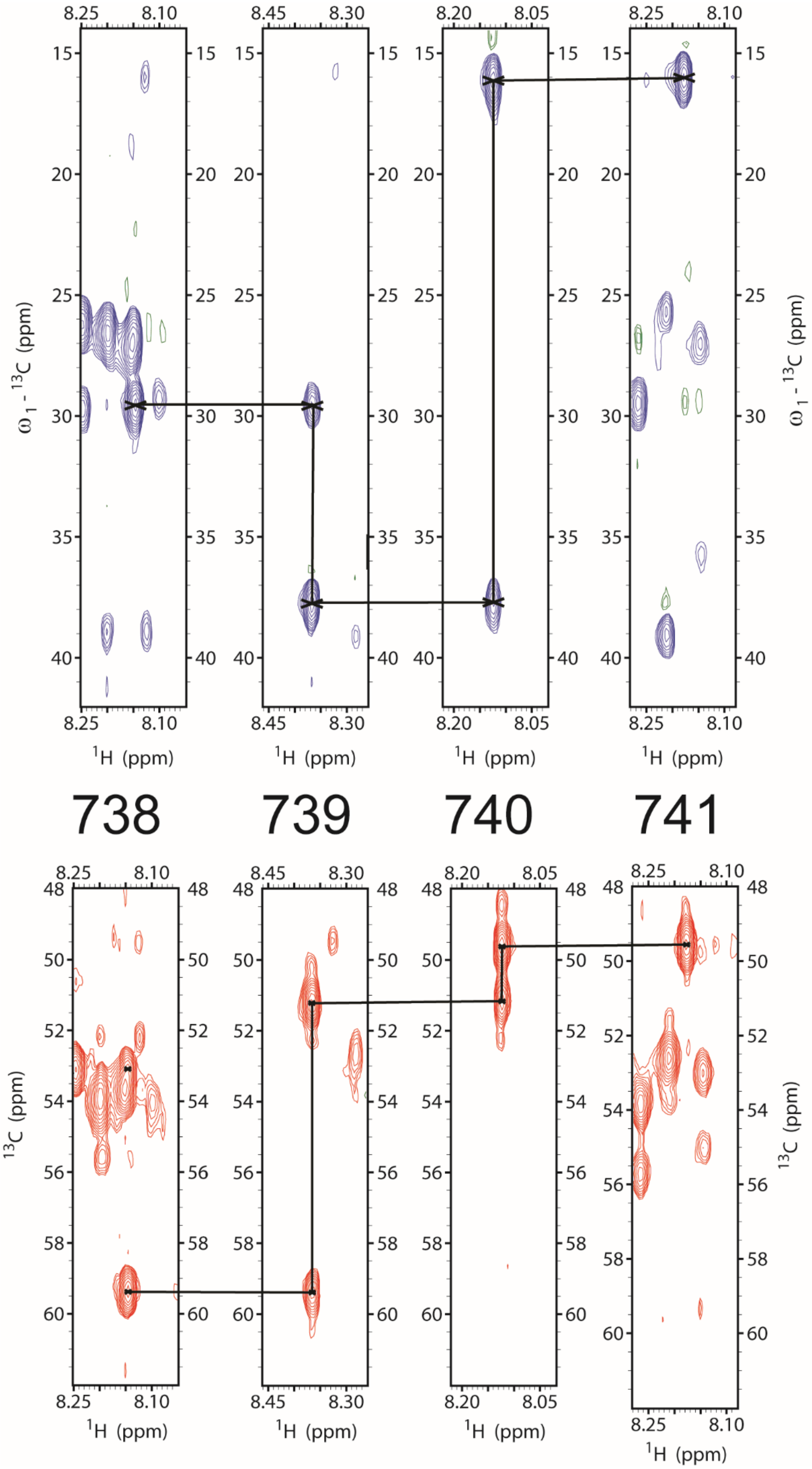
8.25
8.10
8.45
8.30
8.20
8.05
15
20
25
30
35
40
ω1 - 13C (ppm)
1H (ppm)
738
739
740
741
48
50
52
54
56
58
60
13C (ppm)

Figure S3.3. Example of use of 3-D NMR data to assign backbone resonances for C99 in SCOR bicelles. C α peaks are shown in red and C β peaks are shown in blue for residues 738-741. This spectrum was collected on a 400-μM C99 sample in 10 wt % SCOR bicelles, q=0.33, in NMR buffer at 45 °C in a shaped tube at 900 MHz.

Figure S3.4

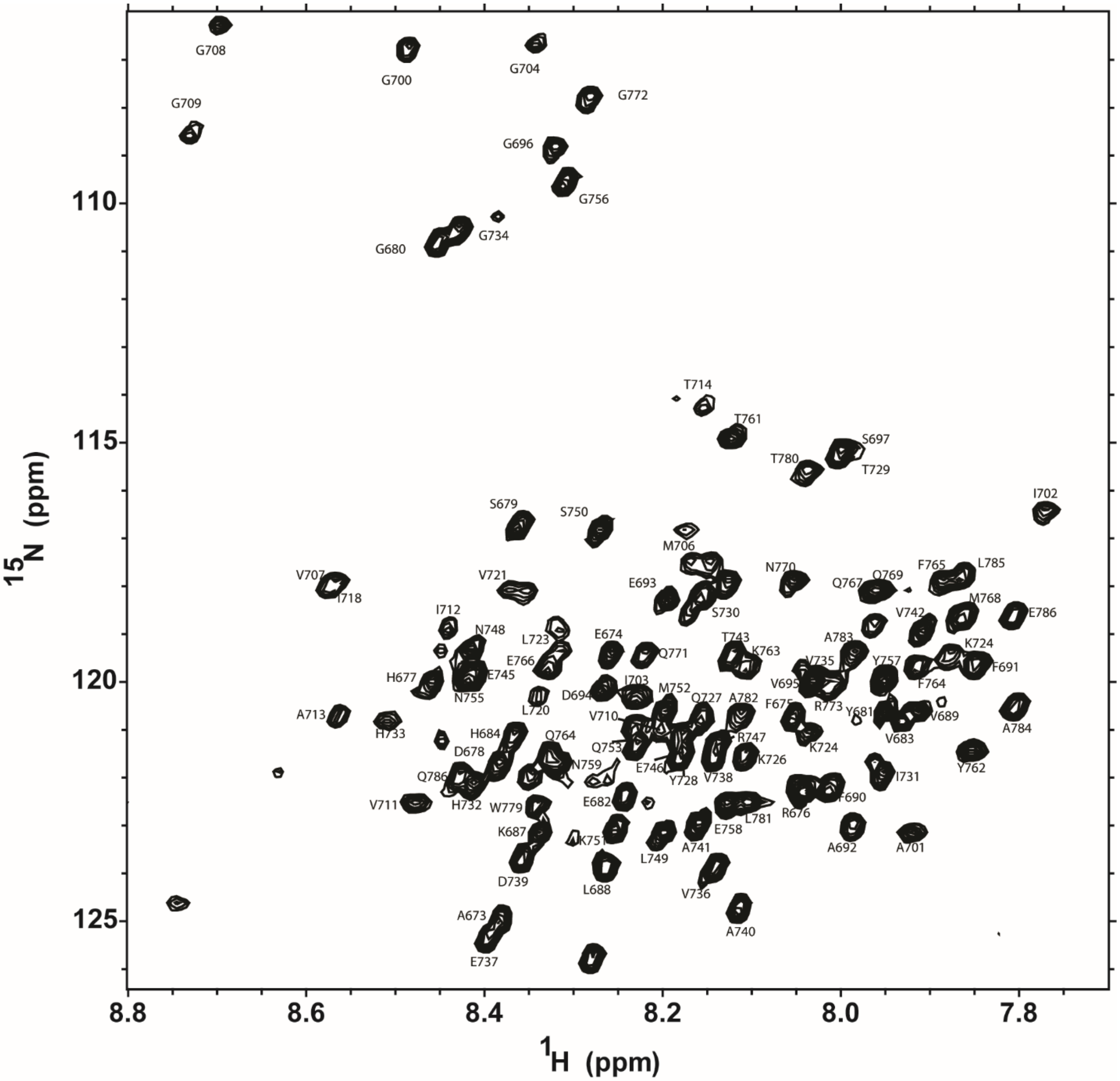

Figure S3.4. Assigned ^{1}H,^{15}N-TROSY NMR spectrum of C99 in DDMB Micelles. The backbone amide ^{1}H-^{15}N peaks are labeled according to amino acid number. This spectrum was collected using a 350-µM C99 sample in 10 wt % DDMB in NMR buffer at 45 °C in a shaped tube at 900 MHz.

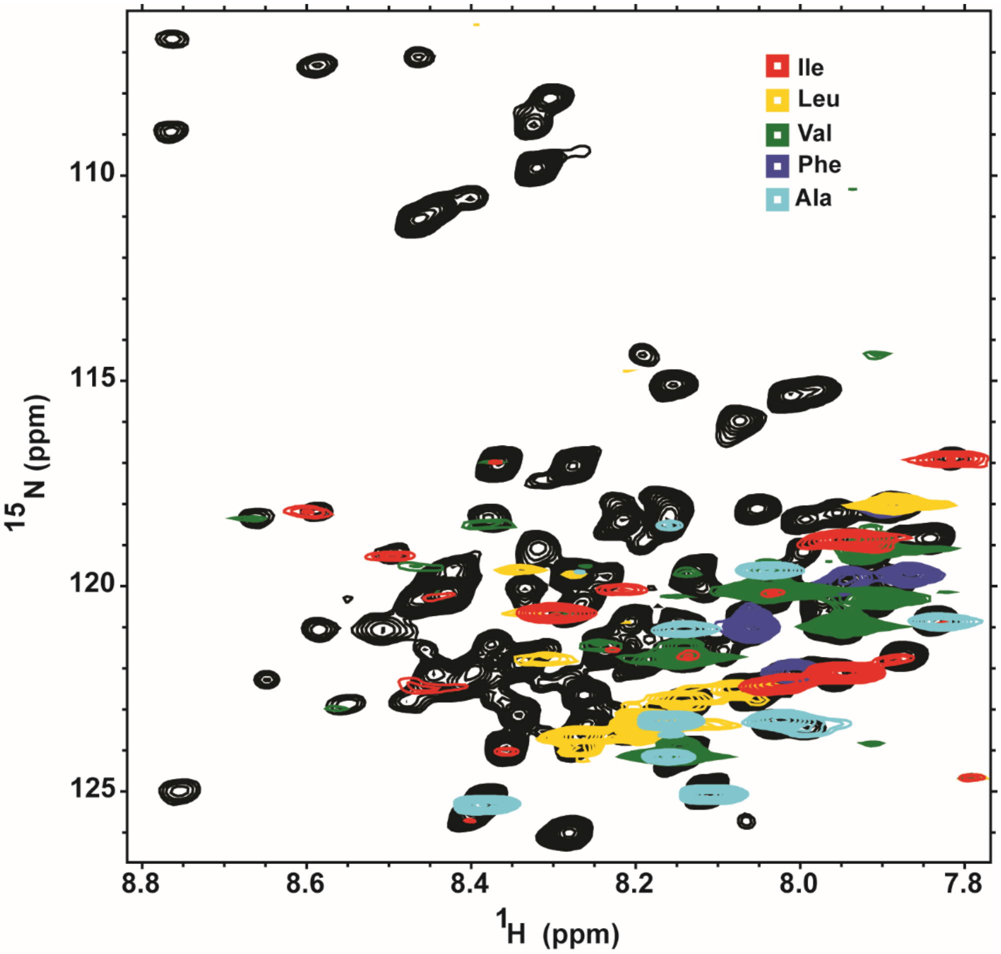

Figure S3.5. Using of specific ^{15}N-amino acid labeling to help resolve ambiguous resonance assignments in SCOR bicelles. ^{15}N-specifically labeled amino acid TROSY spectra are overlaid on top of the black spectrum (900 MHz) from U-^{15}N-C99 (the latter from a sample containing) 500 µM C99 in 10 wt % SCOR bicelles, q=0.33, in NMR buffer and a shaped tube at 45 °C. Spectra from C99 samples labeled, respectively, with ^{15}N-Phe (500 µM, navy), ^{15}N-Leu (400 µM, yellow), ^{15}N-Val (400 µM, green), ^{15}N-Ile (600 µM, red), and ^{15}N-Ala (400 µM, cyan) were all collected in 20 wt % SCOR bicelles, q=0.33, in NMR buffer, using an 800MHz magnet at 45 °C.

Figure S3.6

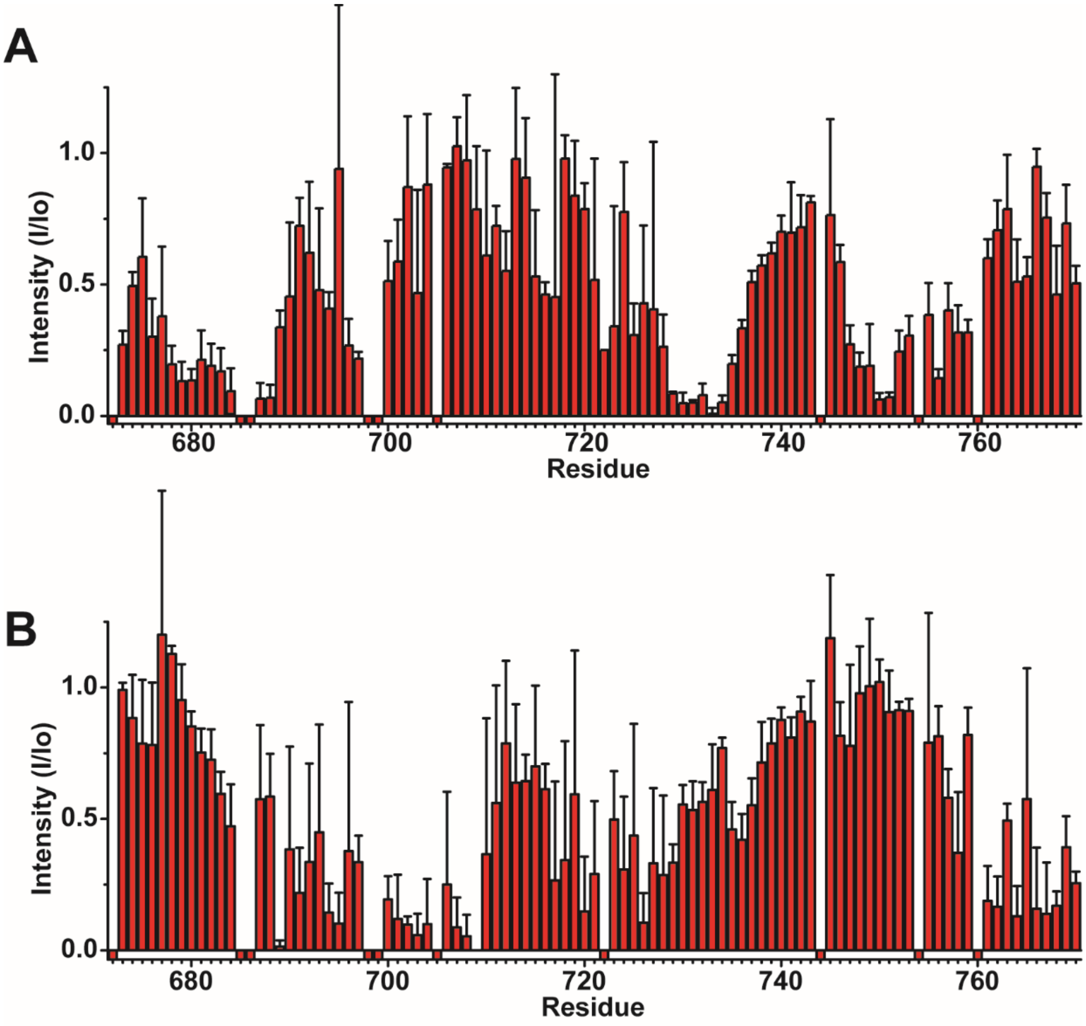

Figure S3.6. Replot of the Gd(III)-DTPA and 16-DSA paramagnetic probe NMR experiments presented in Figure 3.6B of the main paper. *The plot is the same except that n=3 <u>error bars</u> for each data point are now shown.* **(A)** Mean intensity reduction for residues of C99 in topology experiments with 1mM Gd-DTPA present. **(B)** Mean intensity reduction for residues of C99 in topology experiments with 6-9 lipid mol % 16-DSA present. Both panels represent three independent experiments, in each case with one of the three experiments using a C99 construct with the purification tag moved from the C-terminus to the N-terminus. Error is the standard deviation, and small negative peaks indicate unassigned residues (no data). C99 concentrations for all experiments were between ~200 and 400 µM in 5-10 wt% SCOR bicelles, q=0.33.

Table S3.1. Detergent Solubilization Tests for Various Cholesterol and/or Sphingomyelin-Containing Lipid Mixtures.

Lipid Mixture	Detergent	q ratio	CMC (mM)	Observations
2:1 DPPC:Cholesterol	Dodecylphosphocholine (DPC)	0.33	1.5	Did not solubilize after ice-bath, boiling, vortexing, freeze thawing, or being placed in the warm room for a week. Final solution is milky at RT.
6:1:1 POPC:ESM:Cholesterol	Sodium Dodecylsulfate (SDS)	0.33	7	Did not solubilize with boiling, ice bath, or freeze thaw, became clearer in warm room after 10 days. Still somewhat cloudy
6:1:1 POPC:ESM:Cholesterol	Dodecylphosphocholine (DPC)	0.33	1.5	Solubilized after two cycles of ice bath, vortexing and boiling, remains clear at RT
6:1:1 POPC:ESM:Cholesterol	Decylphosphocholine (DecPC)	0.33	11	Solubilized after two cycles of ice bath, vortexing and boiling, remains clear at RT
6:1:1 POPC:ESM:Cholesterol	Fenfos-5	0.33		Did not solubilize with boiling, ice bath, or freeze-thaw, became clearer in warm room after 10 days. milky at RT
6:1:1 POPC:ESM:Cholesterol	Tetradecylphosphocoline (TDPC)	0.33	0.12	Did not solubilize with boiling, ice bath, or freeze thaw, became clearer in warm room after 10 days. Still somewhat cloudy, better than SDS
6:1:1 POPC:ESM:Cholesterol	Lyso-myristoylphosphatidylcholine (LMPC)	0.33	0.07	Did not solubilize with boiling, ice bath, or freeze thaw, became clearer in warm room after 10 days. Cloudy at RT
6:1:1 POPC:ESM:Cholesterol	Lyso-myristoylphosphatidylglycerol (LMPG)	0.33	1.8	Did not solubilize with boiling, ice bath, freeze thaw or warm room. Cloudy and viscous at RT
6:1:1 POPC:ESM:Cholesterol	Lauryl sarcosine (LSC)	0.33	14	Did not solubilize with boiling, ice bath, or freeze thaw, became clearer in warm room after 10 days. Cloudy at RT

6:1:1 POPC:ESM:Cholesterol	Lubrol 17A17 10%	0.33		Solubilized after two cycles of ice bath, vortexing and boiling, remains clear at RT
6:1:1 POPC:ESM:Cholesterol	Brij 97 (Brij 010)	0.33	0.04	Became cloudy and solid after going through cycles of the boiling, ice bath and vortexing, it also went through a freeze thaw and was in the warm room for 10 days. It remains in a solid gel like state at RT
6:1:1 POPC:ESM:Cholesterol	Brij 35	0.33	0.09	Solubilized after one cycles of ice bath, vortexing and boiling, remains clear at RT
6:1:1 POPC:ESM:Cholesterol	Brij 58 10%	0.33	0.08	Solubilized after three cycles of ice bath, vortexing and boiling, remains clear at RT
6:1:1 POPC:ESM:Cholesterol	Cymal-4	0.33	7.6	Solubilized after one cycles of ice bath, vortexing and boiling, remains clear at RT
6:1:1 POPC:ESM:Chol	Dodecylmelibioside (DDMB)	0.33	0.3	Solubilized after one cycles of ice bath, vortexing and boiling, remains clear at RT
6:1:1 POPC:ESM:Cholesterol	Decylmaltoside (DM)	0.33	2	Solubilized after one cycles of ice bath, vortexing and boiling, remains clear at RT
6:1:1 POPC:ESM:Cholesterol	Dodecylmaltoside (DDM)	0.33	0.17	Solubilized after one cycles of ice bath, vortexing and boiling, remains clear at RT
6:1:1 POPC:ESM:Cholesterol	Octylglucoside (OGC)	0.33	19	Solubilized after one cycles of ice bath, vortexing and boiling, remains clear at RT
6:1:1 POPC:ESM:Cholesterol	Lauryl Maltoside Neopentylglycol (LMN)	0.33	0.01	Did not solubilize with boiling, ice bath, or freeze thaw, became clearer in warm room after 10 days. Cloudy and viscous at RT
6:1:1 POPC:ESM:Cholesterol	Octyl Glucose Neopentyl Glycol (OGNG)	0.33	1	Solubilized after two cycles of ice bath, vortexing and boiling, remains clear at RT
6:1:1 POPC:ESM:Cholesterol	Cymal-5 Neopentylglycol	0.33	0.0058	Solubilized after two cycles of ice bath, vortexing and boiling, remains clear at RT
6:1:1 POPC:ESM:Cholesterol	Tween 20	0.33	0.06	did not solubilize with boiling, ice bath, or freeze thaw, became clearer in warm room after 10 days. Cloudy at RT

6:1:1 POPC:ESM:Cholesterol	Zwittergent-3-14	0.33	0.4	Solubilized after one cycles of ice bath, vortexing and boiling, remains clear at RT
6:1:1 POPC:ESM:Cholesterol	Zwittergent-3-10	0.33	25	Solubilized after one cycles of ice bath, vortexing and boiling, remains clear at RT
6:1:1 POPC:ESM:Cholesterol	FOSMEA-10	0.33	5	Solubilized after one cycles of ice bath, vortexing and boiling, remains clear at RT
6:1:1 POPC:ESM:Cholesterol	FOSMEA-12	0.33	0.43	Did not solubilize with boiling, ice bath, or freeze thaw, became clearer in warm room after 10 days. Milky and viscous at RT
6:1:1 POPC:ESM:Cholesterol	TRIPAO 10%	0.33	4.5	Did not solubilize with boiling, ice bath, or freeze thaw, became clearer in warm room after 10 days. Somewhat cloudy at RT
6:1:1 POPC:ESM:Cholesterol	ASB-14	0.33	8	Did not solubilize with boiling, ice bath, or freeze thaw, became clearer in warm room after 10 days. Still somewhat cloudy, better than SDS
6:1:1 POPC:ESM:Cholesterol	ANAPOE-C12E8 10%	0.33	0.09	Did not solubilize with boiling, ice bath, or freeze thaw, became clearer in warm room after 10 days. Milky and viscous at RT
6:1:1 POPC:ESM:Cholesterol	ANAPOE-C8E4	0.33	8	Did not solubilize with boiling, ice bath, or freeze thaw, became clearer in warm room after 10 days. Somewhat cloudy at RT
6:1:1 POPC:ESM:Cholesterol	Cyclophos-5	0.33	4.5	Did not solubilize with boiling, ice bath, or freeze thaw, became clearer in warm room after 10 days. Somewhat cloudy at RT
6:1:1 POPC:ESM:Cholesterol	Cyclophos-7	0.33	0.63	Did not solubilize with boiling, ice bath, or freeze thaw, became clearer in warm room after 10 days. Somewhat cloudy at RT
6:1:1 POPC:ESM:Cholesterol	Fluorinated Octyl Maltoside (FOM)	0.33	1	Did not solubilize with boiling, ice bath, or freeze thaw, became clearer in warm room after 10 days. Cloudy at RT
6:1:1 POPC:ESM:Cholesterol	C-HEGA-11	0.33	12	Solubilized after two cycles of ice bath, vortexing and boiling, remains clear at RT
6:1:1 POPC:ESM:Cholesterol	LDAO	0.33	1	Solubilized after two cycles of ice bath, vortexing and boiling, remains clear at RT

6:1:1 POPC:ESM:Cholesterol	Sodium Dodecylsulfate (SDS)	2.5	7	Did not solubilize upon adding detergent solution, Boiling-ice bath cycles, freeze thaw, or after placing in warm room for 10 days. Final Solution is milky with large particulate.
6:1:1 POPC:ESM:Cholesterol	Dodecylphosphocholine (DPC)	2.5	1.5	Did not solubilize upon adding detergent solution, Boiling-ice bath cycles, freeze thaw, or after placing in warm room for 10 days. Final solution is milky with large particulate.
6:1:1 POPC:ESM:Cholesterol	Decylphosphocholine (DecPC)	2.5	11	Did not solubilize upon adding detergent solution, Boiling-ice bath cycles, freeze thaw, or after placing in warm room for 10 days. Final solution is milky with large particulate.
6:1:1 POPC:ESM:Cholesterol	Fenfos-5	2.5		Did not solubilize upon adding detergent solution, Boiling-ice bath cycles, freeze thaw, or after placing in warm room for 10 days. Final Solution is milky with large particulate.
6:1:1 POPC:ESM:Cholesterol	Tetradecylphosphocoline (TDPC)	2.5	0.12	Did not solubilize upon adding detergent solution, Boiling-ice bath cycles, freeze thaw, or after placing in warm room for 10 days. Final solution is consistently milky
6:1:1 POPC:ESM:Cholesterol	Lyso-myristoylphosphatidylcholine (LMPC)	2.5	0.07	Did not solubilize upon adding detergent solution, Boiling-ice bath cycles, freeze thaw, or after placing in warm room for 10 days. Final solution is milky with large particulate.
6:1:1 POPC:ESM:Cholesterol	Lyso-myristoylphosphatidylglycerol (LMPG)	2.5	1.8	Did not solubilize upon adding detergent solution, Boiling-ice bath cycles, freeze thaw, or after placing in warm room for 10 days. Final Solution is consistently milky
6:1:1 POPC:ESM:Cholesterol	Lauryl sarcosine (LSC)	2.5	14	Solubilized after one cycle of ice bath/boiling. Looks cloudy, but like a tradtional 2.5 bicelle.
6:1:1 POPC:ESM:Cholesterol	Lubrol 17A17 10%	2.5		Did not solubilize upon adding detergent solution, Boiling-ice bath cycles, freeze thaw, or after placing in warm room for 10 days. Final solution is milky with large particulate.
6:1:1 POPC:ESM:Cholesterol	Brij 97 (Brij 010)	2.5	0.04	Did not solubilize upon adding detergent solution, Boiling-ice bath cycles, freeze thaw, or after placing in warm room for 10 days. Final solution is milky with large particulate.
6:1:1 POPC:ESM:Cholesterol	Brij 35	2.5	0.09	Did not solubilize upon adding detergent solution, Boiling-ice bath cycles, freeze thaw, or after placing in warm room for 10 days. Final solution is milky with large particulate.

6:1:1 POPC:ESM:Cholesterol	Brij 58	2.5	0.08	Did not solubilize upon adding detergent solution, Boiling-ice bath cycles, freeze thaw, or after placing in warm room for 10 days. Final solution is consistently milky
6:1:1 POPC:ESM:Cholesterol	Cymal-4	2.5	7.6	Did not solubilize upon adding detergent solution, Boiling-ice bath cycles, freeze thaw, or after placing in warm room for 10 days. Final solution is milky with large particulate.
6:1:1 POPC:ESM:Cholesterol	Dodecyl Melibioside (DDMB)	2.5	0.3	Did not solubilize upon adding detergent solution, Boiling-ice bath cycles, freeze thaw, or after placing in warm room for 10 days. Final solution is milky/
6:1:1 POPC:ESM:Cholesterol	Decylmaltoside (DM)	2.5	2	Did not solubilize upon adding detergent solution, Boiling-ice bath cycles, freeze thaw, or after placing in warm room for 10 days. Final solution is milky with large particulate.
6:1:1 POPC:ESM:Cholesterol	Dodecylmaltoside (DDM)	2.5	0.17	Did not solubilize upon adding detergent solution, Boiling-ice bath cycles, freeze thaw, or after placing in warm room for 10 days. Final solution is milky.
6:1:1 POPC:ESM:Cholesterol	Octylglucoside (OGC)	2.5	19	Did not solubilize upon adding detergent solution, Boiling-ice bath cycles, freeze thaw, or after placing in warm room for 10 days. Final solution is milky.
6:1:1 POPC:ESM:Cholesterol	Lauryl Maltoside Neopentylglycol (LMN)	2.5	0.01	Did not solubilize upon adding detergent solution, Boiling-ice bath cycles, freeze thaw, or after placing in warm room for 10 days. Final solution is milky.
6:1:1 POPC:ESM:Cholesterol	Octyl Glucose Neopentyl Glycol (OGNG)	2.5	1	Did not solubilize upon adding detergent solution, Boiling-ice bath cycles, freeze thaw, or after placing in warm room for 10 days. Final solution is milky.
6:1:1 POPC:ESM:Cholesterol	Cymal-5 Neopentylglycol	2.5	0.0058	Did not solubilize upon adding detergent solution, boiling-ice bath cycles, freeze thaw, or after placing in warm room for 10 days. Final solution is consistently milky.
6:1:1 POPC:ESM:Cholesterol	Tween 20	2.5	0.06	Did not solubilize upon adding detergent solution, Boiling-ice bath cycles, freeze thaw, or after placing in warm room for 10 days. Final solution is consistently milky.
6:1:1 POPC:ESM:Cholesterol	Zwittergent-3-14	2.5	0.4	Did not solubilize upon adding detergent solution, Boiling-ice bath cycles, freeze thaw, or after placing in warm room for 10 days. Final solution is milky.

6:1:1 POPC:ESM:Cholesterol	Zwittergent-3-10	2.5	25	Did not solubilize upon adding detergent solution, Boiling-ice bath cycles, freeze thaw, or after placing in warm room for 10 days. Final solution is milky.
6:1:1 POPC:ESM:Cholesterol	FOSMEA-10	2.5	5	Did not solubilize upon adding detergent solution, Boiling-ice bath cycles, freeze thaw, or after placing in warm room for 10 days. Final solution is milky.
6:1:1 POPC:ESM:Cholesterol	FOSMEA-12	2.5	0.43	Did not solubilize upon adding detergent solution, Boiling-ice bath cycles, freeze thaw, or after placing in warm room for 10 days. Final solution is milky.
6:1:1 POPC:ESM:Cholesterol	TRIPAO 10%	2.5	4.5	Did not solubilize upon adding detergent solution, Boiling-ice bath cycles, freeze thaw, or after placing in warm room for 10 days. Final solution is milky.
6:1:1 POPC:ESM:Cholesterol	ASB-14	2.5	8	Did not solubilize upon adding detergent solution, Boiling-ice bath cycles, freeze thaw, or after placing in warm room for 10 days. Final solution is milky.
6:1:1 POPC:ESM:Cholesterol	ANAPOE-C12E8 10%	2.5	0.09	Did not solubilize upon adding detergent solution, Boiling-ice bath cycles, freeze thaw, or after placing in warm room for 10 days. Final solution is consistently milky.
6:1:1 POPC:ESM:Cholesterol	ANAPOE-C8E4	2.5	8	Did not solubilize upon adding detergent solution, Boiling-ice bath cycles, freeze thaw, or after placing in warm room for 10 days. Final solution is consistently milky.
6:1:1 POPC:ESM:Cholesterol	Cyclophos-5	2.5	4.5	Did not solubilize upon adding detergent solution, Boiling-ice bath cycles, freeze thaw, or after placing in warm room for 10 days. Final solution is milky.
6:1:1 POPC:ESM:Cholesterol	Cyclophos-7	2.5	0.63	Did not solubilize upon adding detergent solution, Boiling-ice bath cycles, freeze thaw, or after placing in warm room for 10 days. Final solution is milky.
6:1:1 POPC:ESM:Cholesterol	Fluorinated Octyl Maltoside (FOM)	2.5	1	Did not solubilize upon adding detergent solution, Boiling-ice bath cycles, freeze thaw, or after placing in warm room for 10 days. Final solution is milky.
6:1:1 POPC:ESM:Cholesterol	C-HEGA-11	2.5	12	Did not solubilize upon adding detergent solution, Boiling-ice bath cycles, freeze thaw, or after placing in warm room for 10 days. Final solution is milky.
6:1:1 POPC:ESM:Cholesterol	LDAO	2.5	1	Did not solubilize upon adding detergent solution, Boiling-ice bath cycles, freeze thaw, or after placing in warm room for 10 days. Final solution is milky.

2:1 DPPC:Cholesterol	Decylphosphocholine (DecPC)	0.33	11	Did not solubilize after ice-bath, boiling, vortexing, freeze thawing, or being placed in the warm room for a week. Final solution is milky at RT.
2:1 DPPC:Cholesterol	Lauryl sarcosine (LSC)	2.5	14	Did not solubilize after ice-bath, boiling, vortexing, freeze thawing, or being placed in the warm room for a week. Final solution is milky at RT.
2:1 DPPC:Cholesterol	Lubrol 17A17 10%	0.33		Did not solubilize after ice-bath, boiling, vortexing, freeze thawing, or being placed in the warm room for a week. Final solution is milky at RT.
2:1 DPPC:Cholesterol	Brij 35	0.33	0.09	Did not solubilize after ice-bath, boiling, vortexing, freeze thawing, or being placed in the warm room for a week. Final solution is milky at RT.
2:1 DPPC:Cholesterol	Brij 58	0.33	0.08	Did not solubilize after ice-bath, boiling, vortexing, freeze thawing, or being placed in the warm room for a week. Final solution is milky at RT.
2:1 DPPC:Cholesterol	Cymal-4	0.33	7.6	Did not solubilize after ice-bath, boiling, vortexing, freeze thawing, or being placed in the warm room for a week. Final solution is milky at RT.
2:1 DPPC:Cholesterol	Beta-Decylmaltoside (DM)	0.33	2	Did not solubilize after ice-bath, boiling, vortexing, freeze thawing, or being placed in the warm room for a week. Final solution is milky at RT.
2:1 DPPC:Cholesterol	Beta-Dodecylmaltoside (DDM)	0.33	0.17	Did not solubilize after ice-bath, boiling, vortexing, freeze thawing, or being placed in the warm room for a week. Final solution is milky at RT.
2:1 DPPC:Cholesterol	Beta-Octylglucoside (OGC)	0.33	19	Did not solubilize after ice-bath, boiling, vortexing, freeze thawing, or being placed in the warm room for a week. Final solution is milky at RT.
2:1 DPPC:Cholesterol	Beta-Octyl Glucose Neopentyl Glycol (OGNG)	0.33	1	Did not solubilize after ice-bath, boiling, vortexing, freeze thawing, or being placed in the warm room for a week. Final solution is milky at RT.
2:1 DPPC:Cholesterol	Cymal-5 Neopentylglycol	0.33	0.0058	Did not solubilize after ice-bath, boiling, vortexing, freeze thawing, or being placed in the warm room for a week. Final solution is milky at RT.
2:1 DPPC:Cholesterol	Zwittergent-3-14	0.33	0.4	Did not solubilize after ice-bath, boiling, vortexing, freeze thawing, or being placed in the warm room for a week. Final solution is milky at RT.
2:1 DPPC:Cholesterol	Zwittergent-3-10	0.33	25	Did not solubilize after ice-bath, boiling, vortexing, freeze thawing, or being placed in the warm room for a week. Final solution is milky at RT.

2:1 DPPC:Cholesterol	Beta-Dodecyl Melibioside (DDMB)	0.33	0.3	Did not solubilize after ice-bath, boiling, vortexing, freeze thawing, or being placed in the warm room for a week. Final solution is milky at RT.
2:1 DPPC:Cholesterol	FOSMEA-10	0.33	5	Did not solubilize after ice-bath, boiling, vortexing, freeze thawing, or being placed in the warm room for a week. Final solution is milky at RT.
2:1 DPPC:Cholesterol	C-HEGA-11	0.33	12	Did not solubilize after ice-bath, boiling, vortexing, freeze thawing, or being placed in the warm room for a week. Final solution is milky at RT.
2:1 DPPC:Cholesterol	LDAO	0.33	1	Did not solubilize after ice-bath, boiling, vortexing, freeze thawing, or being placed in the warm room for a week. Final solution is milky at RT.
2:1 DPPC:Cholesterol	Brij 97 (Brij 010)	0.33	0.04	Did not solubilize after ice-bath, boiling, vortexing, freeze thawing, or being placed in the warm room for a week. Final solution is milky at RT.
6:3:1 DMPC:ESM:Cholesterol	Dodecylphosphocholine (DPC)	0.33	1.5	Solubilized after two cycles of ice-bath, boiling, and vortexing. Final solution is clear at RT
6:3:1 DMPC:ESM:Cholesterol	Decylphosphocholine (DecPC)	0.33	11	Solubilized after two cycles of ice-bath, boiling, and vortexing. Final solution is clear at RT
6:3:1 DMPC:ESM:Cholesterol	Lauryl sarcosine (LSC)	2.5	14	Did not solubilize after ice-bath, boiling, vortexing, freeze thawing, or being placed in the warm room for a week. Final solution is cloudy at RT.
6:3:1 DMPC:ESM:Cholesterol	Brij 35	0.33	0.09	
6:3:1 DMPC:ESM:Cholesterol	Cymal-4	0.33	7.6	Solubilized after two cycles of ice-bath, boiling, and vortexing. This solution showed viscosity above RT. Final Solution is clear at RT
6:3:1 DMPC:ESM:Cholesterol	Beta-Decylmaltoside (DM)	0.33	2	Solubilized after two cycles of ice-bath, boiling, and vortexing. This solution showed viscosity above RT. Final Solution is clear at RT
6:3:1 DMPC:ESM:Cholesterol	Beta-Octylglucoside (OGC)	0.33	19	Did not solubilize after ice-bath, boiling, vortexing, freeze thawing, or being placed in the warm room for a week. Final solution is milky at RT.
6:3:1 DMPC:ESM:Cholesterol	Beta-Octyl Glucose Neopentyl Glycol (OGNG)	0.33	1	Did not solubilize after ice-bath, boiling, vortexing, freeze thawing, or being placed in the warm room for a week. Final solution is milky at RT.

6:3:1 DMPC:ESM:Cholesterol	Cymal-5 Neopentylglycol	0.33	0.006	Solubilized after two cycles of ice-bath, boiling, and vortexing. Final Solution is clear at RT
6:3:1 DMPC:ESM:Cholesterol	Zwittergent-3-14	0.33	0.4	Did not solubilize after ice-bath, boiling, vortexing, freeze thawing, or being placed in the warm room for a week. Final solution is milky at RT.
6:3:1 DMPC:ESM:Cholesterol	Zwittergent-3-10	0.33	25	Solubilized after two cycles of ice-bath, boiling, and vortexing. This solution showed viscosity above RT. Final Solution is clear at RT
6:3:1 DMPC:ESM:Cholesterol	Dodecyl Melibioside (DDMB)	0.33	0.3	Solubilized after two cycles of ice-bath, boiling, and vortexing. Final Solution is clear at RT
6:3:1 DMPC:ESM:Cholesterol	FOSMEA-10	0.33	5	Solubilized after two cycles of ice-bath, boiling, and vortexing. This solution showed viscosity above RT. Final Solution is clear at RT
6:3:1 DMPC:ESM:Cholesterol	C-HEGA-11	0.33	11	Solubilized after two cycles of ice-bath, boiling, and vortexing. This solution showed viscosity above RT. Final Solution is clear at RT
6:3:1 DMPC:ESM:Cholesterol	LDAO	0.33	1	Did not solubilize after ice-bath, boiling, vortexing, freeze thawing, or being placed in the warm room for a week. Final solution is cloudy and slighty viscous at RT.
6:3:1 DMPC:ESM:Cholesterol	Brij 97 (Brij 010)	0.33	0.04	Solubilized after two cycles of ice-bath, boiling, and vortexing. This solution showed viscosity above RT. Final Solution is clear at RT
2:1:1 POPC:ESM:Cholesterol	Dodecylphosphocholine (DPC)	0.33	1.5	Did not solubilize after ice-bath, boiling, vortexing, freeze thawing, or being placed in the warm room for a week. Final solution is consistently milky at RT.
2:1:1 POPC:ESM:Cholesterol	Decylphosphocholine (DecPC)	0.33	11	Did not solubilize after ice-bath, boiling, vortexing, freeze thawing, or being placed in the warm room for a week. Final solution is consistently milky at RT.
2:1:1 POPC:ESM:Cholesterol	Lauryl sarcosine (LSC)	2.5	14	Did not solubilize after ice-bath, boiling, vortexing, freeze thawing, or being placed in the warm room for a week. Final solution is consistently milky and slightly viscous at RT.
2:1:1 POPC:ESM:Cholesterol	Lubrol 17A17 10%	0.33		Did not solubilize after ice-bath, boiling, vortexing, freeze thawing, or being placed in the warm room for a week. Final solution is slightly milky/consistent at RT.

2:1:1 POPC:ESM:Cholesterol	Brij 35	0.33	0.09	Did not solubilize after ice-bath, boiling, vortexing, freeze thawing, or being placed in the warm room for a week. Final solution is consistently milky at RT.
2:1:1 POPC:ESM:Cholesterol	Brij 58	0.33	0.08	Did not solubilize after ice-bath, boiling, vortexing, freeze thawing, or being placed in the warm room for a week. Final solution is slightly milky/consistent at RT.
2:1:1 POPC:ESM:Cholesterol	Cymal-4	0.33	7.6	Did not solubilize after ice-bath, boiling, vortexing, freeze thawing, or being placed in the warm room for a week. Final solution is very cloudy and slightly viscous at RT.
2:1:1 POPC:ESM:Cholesterol	Decylmaltoside (DM)	0.33	2	Did not solubilize after ice-bath, boiling, vortexing, freeze thawing, or being placed in the warm room for a week. Final solution is milky/soapy at RT.
2:1:1 POPC:ESM:Cholesterol	Dodecylmaltoside (DDM)	0.33	0.17	Did not solubilize after ice-bath, boiling, vortexing, freeze thawing, or being placed in the warm room for a week. Final solution is very soapy at RT.
2:1:1 POPC:ESM:Cholesterol	Octylglucoside (OGC)	0.33	19	Did not solubilize after ice-bath, boiling, vortexing, freeze thawing, or being placed in the warm room for a week. Final solution is consistently milky at RT.
2:1:1 POPC:ESM:Cholesterol	Octyl Glucose Neopentyl Glycol (OGNG)	0.33	1	Did not solubilize after ice-bath, boiling, vortexing, freeze thawing, or being placed in the warm room for a week. Final solution is soapy and viscous at RT.
2:1:1 POPC:ESM:Cholesterol	Cymal-5 Neopentylglycol	0.33	0.0058	Did not solubilize after ice-bath, boiling, vortexing, freeze thawing, or being placed in the warm room for a week. Final solution is consistently milky at RT.
2:1:1 POPC:ESM:Cholesterol	Zwittergent-3-14	0.33	0.4	Did not solubilize after ice-bath, boiling, vortexing, freeze thawing, or being placed in the warm room for a week. Final solution is consistently milky at RT.
2:1:1 POPC:ESM:Cholesterol	Zwittergent-3-10	0.33	25	Did not solubilize after ice-bath, boiling, vortexing, freeze thawing, or being placed in the warm room for a week. Final solution is consistently cloudy at RT.
2:1:1 POPC:ESM:Cholesterol	Dodecyl Melibioside (DDMB)	0.33	0.3	Did not solubilize after ice-bath, boiling, vortexing, freeze thawing, or being placed in the warm room for a week. Final solution is soapy and viscous at RT.

2:1:1 POPC:ESM:Cholesterol	FOSMEA-10	0.33	5	Did not solubilize after ice-bath, boiling, vortexing, freeze thawing, or being placed in the warm room for a week. Final solution is Consistently very cloudy at RT.
2:1:1 POPC:ESM:Cholesterol	C-HEGA-11	0.33	12	Did not solubilize after ice-bath, boiling, vortexing, freeze thawing, or being placed in the warm room for a week. Final solution is consistently slightly milky at RT.
2:1:1 POPC:ESM:Cholesterol	LDAO	0.33	1	Did not solubilize after ice-bath, boiling, vortexing, freeze thawing, or being placed in the warm room for a week. Final solution is consistently very cloudy at RT.
2:1:1 POPC:ESM:Cholesterol	Brij 97 (Brij 010)	0.33	0.04	Did not solubilize after ice-bath, boiling, vortexing, freeze thawing, or being placed in the warm room for a week. Final solution is milky and slightly viscous at RT.
2:1:1 DPPC:ESM:Cholesterol	Dodecylphosphocholine (DPC)	0.33	1.5	Did not solubilize after ice-bath, boiling, vortexing, freeze thawing, or being placed in the warm room for a week. Final solution is consistently cloudy at RT.
2:1:1 DPPC:ESM:Cholesterol	Decylphosphocholine (DecPC)	0.33	11	Did not solubilize after ice-bath, boiling, vortexing, freeze thawing, or being placed in the warm room for a week. Final solution is consistently milky at RT.
2:1:1 DPPC:ESM:Cholestrol	Lauryl sarcosine (LSC)	2.5	14	Did not solubilize after ice-bath, boiling, vortexing, freeze thawing, or being placed in the warm room for a week. Final solution is consistently milky at RT.
2:1:1 DPPC:ESM:Cholesterol	Lubrol 17A17 10%	0.33		Did not solubilize after ice-bath, boiling, vortexing, freeze thawing, or being placed in the warm room for a week. Final solution is consistently very cloudy at RT.
2:1:1 DPPC:ESM:Cholesterol	Brij 35	0.33	0.09	Did not solubilize after ice-bath, boiling, vortexing, freeze thawing, or being placed in the warm room for a week. Final solution is consistently milky at RT.
2:1:1 DPPC:ESM:Cholesterol	Brij 58	0.33	0.08	Did not solubilize after ice-bath, boiling, vortexing, freeze thawing, or being placed in the warm room for a week. Final solution is consistently milky at RT.
2:1:1 DPPC:ESM:Cholesterol	Cymal-4	0.33	7.6	Did not solubilize after ice-bath, boiling, vortexing, freeze thawing, or being placed in the warm room for a week. Final solution is consistently milky at RT.

2:1:1 DPPC:ESM:Cholesterol	Decylmaltoside (DM)	0.33	2	Did not solubilize after ice-bath, boiling, vortexing, freeze thawing, or being placed in the warm room for a week. Final solution is consistently milky at RT.
2:1:1 DPPC:ESM:Cholesterol	Dodecylmaltoside (DDM)	0.33	0.17	Did not solubilize after ice-bath, boiling, vortexing, freeze thawing, or being placed in the warm room for a week. Final solution was part gel part liquid but only liquid and somewhat clear at RT.
2:1:1 DPPC:ESM:Cholesterol	Octylglucoside (OGC)	0.33	19	Did not solubilize after ice-bath, boiling, vortexing, freeze thawing, or being placed in the warm room for a week. Final solution is milky/soapy at RT.
2:1:1 DPPC:ESM:Cholesterol	Octyl Glucose Neopentyl Glycol (OGNG)	0.33	1	Did not solubilize after ice-bath, boiling, vortexing, freeze thawing, or being placed in the warm room for a week. Final solution is milky/soapy at RT.
2:1:1 DPPC:ESM:Cholesterol	Zwittergent-3-14	0.33	0.4	Did not solubilize after ice-bath, boiling, vortexing, freeze thawing, or being placed in the warm room for a week. Final solution was part gel part liquid but only liquid and cloudy at RT.
2:1:1 DPPC:ESM:Cholesterol	Zwittergent-3-10	0.33	25	Did not solubilize after ice-bath, boiling, vortexing, freeze thawing, or being placed in the warm room for a week. Final solution is consistently very cloudy at RT.
2:1:1 DPPC:ESM:Cholesterol	Dodecyl Melibioside (DDMB)	0.33	0.3	Did not solubilize after ice-bath, boiling, vortexing, freeze thawing, or being placed in the warm room for a week. Final solution is consistently milky at RT.
2:1:1 DPPC:ESM:Cholesterol	FOSMEA-10	0.33	5	Did not solubilize after ice-bath, boiling, vortexing, freeze thawing, or being placed in the warm room for a week. Final solution is consistently milky at RT.
2:1:1 DPPC:ESM:Cholesterol	C-HEGA-11	0.33	12	Did not solubilize after ice-bath, boiling, vortexing, freeze thawing, or being placed in the warm room for a week. Final solution is consistently milky at RT.
2:1:1 DPPC:ESM:Cholesterol	Brij 97 (Brij 010)	0.33	0.04	Did not solubilize after ice-bath, boiling, vortexing, freeze thawing, or being placed in the warm room for a week. Final solution is milky and slightly viscous at RT.
2:1 EMS:Cholesterol	Dodecylphosphocholine (DPC)	0.33	1.5	Did not solubilize after ice-bath, boiling, vortexing, freeze thawing, or being placed in the warm room for a week. Final solution is consistently milky at RT.

2:1 EMS:Cholesterol	Decylphosphocholine (DecPC)	0.33	11	Did not solubilize after ice-bath, boiling, vortexing, freeze thawing, or being placed in the warm room for a week. Final solution is consistently milky at RT.
2:1 EMS:Cholesterol	Lauryl sarcosine (LSC)	2.5	14	Did not solubilize after ice-bath, boiling, vortexing, freeze thawing, or being placed in the warm room for a week. Final solution is consistently milky at RT.
2:1 EMS:Cholesterol	Lubrol 17A17 10%	0.33		Did not solubilize after ice-bath, boiling, vortexing, freeze thawing, or being placed in the warm room for a week. Final solution is consistently milky at RT.
2:1 EMS:Cholesterol	Brij 35	0.33	0.09	Did not solubilize after ice-bath, boiling, vortexing, freeze thawing, or being placed in the warm room for a week. Final solution is consistently milky at RT.
2:1 EMS:Cholesterol	Brij 58 10%	0.33	0.08	Did not solubilize after ice-bath, boiling, vortexing, freeze thawing, or being placed in the warm room for a week. Final solution is consistently milky and slightly viscous at RT.
2:1 EMS:Cholesterol	Cymal-4	0.33	7.6	Did not solubilize after ice-bath, boiling, vortexing, freeze thawing, or being placed in the warm room for a week. Final solution is consistently milky at RT.
2:1 EMS:Cholesterol	Decylmaltoside (DM)	0.33	2	Did not solubilize after ice-bath, boiling, vortexing, freeze thawing, or being placed in the warm room for a week. Final solution is consistently milky at RT.
2:1 EMS:Cholesterol	Dodecylmaltoside (DDM)	0.33	0.17	Did not solubilize after ice-bath, boiling, vortexing, freeze thawing, or being placed in the warm room for a week. Final solution is consistently very cloudy at RT
2:1 EMS:Cholesterol	Octylglucoside (OGC)	0.33	19	Did not solubilize after ice-bath, boiling, vortexing, freeze thawing, or being placed in the warm room for a week. Final solution is consistently milky at RT.
2:1 EMS:Cholesterol	Octyl Glucose Neopentyl Glycol (OGNG)	0.33	1	Did not solubilize after ice-bath, boiling, vortexing, freeze thawing, or being placed in the warm room for a week. Final solution is consistently milky at RT.
2:1 EMS:Cholesterol	Zwittergent-3-14	0.33	0.4	Did not solubilize after ice-bath, boiling, vortexing, freeze thawing, or being placed in the warm room for a week. Final solution is cconsistently milky at RT.

2:1 EMS:Cholesterol	Zwittergent-3-10	0.33	25	Did not solubilize after ice-bath, boiling, vortexing, freeze thawing, or being placed in the warm room for a week. Final solution is consistently milky at RT.
2:1 EMS:Cholesterol	Dodecyl Melibioside (DDMB)	0.33	0.3	Did not solubilize after ice-bath, boiling, vortexing, freeze thawing, or being placed in the warm room for a week. Final solution is milky with particles at RT
2:1 EMS:Cholesterol	FOSMEA-10	0.33	5	Did not solubilize after ice-bath, boiling, vortexing, freeze thawing, or being placed in the warm room for a week. Final solution is consistently milky at RT.
2:1 EMS:Cholesterol	C-HEGA-11	0.33	12	Did not solubilize after ice-bath, boiling, vortexing, freeze thawing, or being placed in the warm room for a week. Final solution is consistently milky at RT.
2:1 EMS:Cholesterol	LDAO	0.33	1	Did not solubilize after ice-bath, boiling, vortexing, freeze thawing, or being placed in the warm room for a week. Final solution is consistently very cloudy at RT.
2:1 EMS:Cholesterol	Brij 97 (Brij 010)	0.33	0.04	Did not solubilize after ice-bath, boiling, vortexing, freeze thawing, or being placed in the warm room for a week. Final solution is milky/soapy and slightly viscous at RT.
1:1:1 POPC:ESM:Cholesterol	Dodecylphosphocholine (DPC)	0.33	1.5	Did not solubilize after ice-bath, boiling, vortexing, freeze thawing, or being placed in the warm room for a week. Final solution is consistently milky at RT.
1:1:1 POPC:ESM:Cholesterol	Decylphosphocholine (DecPC)	0.33	11	Did not solubilize after ice-bath, boiling, vortexing, freeze thawing, or being placed in the warm room for a week. Final solution is consistently milky at RT.
1:1:1 POPC:ESM:Cholesterol	Lauryl sarcosine (LSC)	2.5	14	Did not solubilize after ice-bath, boiling, vortexing, freeze thawing, or being placed in the warm room for a week. Final solution is consistently milky at RT.
1:1:1 POPC:ESM:Cholesterol	Lubrol 17A17 10%	0.33		Did not solubilize after ice-bath, boiling, vortexing, freeze thawing, or being placed in the warm room for a week. Final solution is consistently milky at RT.
1:1:1 POPC:ESM:Cholesterol	Brij 35	0.33	0.09	Did not solubilize after ice-bath, boiling, vortexing, freeze thawing, or being placed in the warm room for a week. Final solution is consistently very cloudy at RT.

1:1:1 POPC:ESM:Cholesterol	Brij 58 10%	0.33	0.08	Did not solubilize after ice-bath, boiling, vortexing, freeze thawing, or being placed in the warm room for a week. Final solution is consistently milky at RT.
1:1:1 POPC:ESM:Cholesterol	Cymal-4	0.33	7.6	Did not solubilize after ice-bath, boiling, vortexing, freeze thawing, or being placed in the warm room for a week. Final solution is consistently milky at RT.
1:1:1 POPC:ESM:Cholesterol	Decylmaltoside (DM)	0.33	2	Did not solubilize after ice-bath, boiling, vortexing, freeze thawing, or being placed in the warm room for a week. Final solution is consistently milky at RT.
1:1:1 POPC:ESM:Cholesterol	Dodecylmaltoside (DDM)	0.33	0.17	Did not solubilize after ice-bath, boiling, vortexing, freeze thawing, or being placed in the warm room for a week. Final solution is consistently milky at RT.
1:1:1 POPC:ESM:Cholesterol	Octylglucoside (OGC)	0.33	19	Did not solubilize after ice-bath, boiling, vortexing, freeze thawing, or being placed in the warm room for a week. Final solution is consistently milky at RT.
1:1:1 POPC:ESM:Cholesterol	Octyl Glucose Neopentyl Glycol (OGNG)	0.33	1	Did not solubilize after ice-bath, boiling, vortexing, freeze thawing, or being placed in the warm room for a week. Final solution is consistently milky at RT.
1:1:1 POPC:ESM:Cholesterol	Cymal-5 Neopentylglycol	0.33	0.0058	Did not solubilize after ice-bath, boiling, vortexing, freeze thawing, or being placed in the warm room for a week. Final solution is consistently milky at RT.
1:1:1 POPC:ESM:Cholesterol	Zwittergent-3-14	0.33	0.4	Did not solubilize after ice-bath, boiling, vortexing, freeze thawing, or being placed in the warm room for a week. Final solution is consistently milky at RT.
1:1:1 POPC:ESM:Cholesterol	Zwittergent-3-10	0.33	25	Did not solubilize after ice-bath, boiling, vortexing, freeze thawing, or being placed in the warm room for a week. Final solution is consistently milky at RT.
1:1:1 POPC:ESM:Cholesterol	B-Dodecyl Melibioside (DDMB)	0.33	0.3	Did not solubilize after ice-bath, boiling, vortexing, freeze thawing, or being placed in the warm room for a week. Final solution is consistently milky at RT.
1:1:1 POPC:ESM:Cholesterol	FOSMEA-10	0.33	5	Did not solubilize after ice-bath, boiling, vortexing, freeze thawing, or being placed in the warm room for a week. Final solution is consistently milky at RT.

1:1:1 POPC:ESM:Cholesterol	C-HEGA-11	0.33	12	Did not solubilize after ice-bath, boiling, vortexing, freeze thawing, or being placed in the warm room for a week. Final solution is consistently milky at RT.
1:1:1 POPC:ESM:Cholesterol	LDAO	0.33	1	Did not solubilize after ice-bath, boiling, vortexing, freeze thawing, or being placed in the warm room for a week. Final solution is consistently milky at RT.
1:1:1 POPC:ESM:Cholesterol	Brij 97 (Brij 010)	0.33	0.04	Did not solubilize after ice-bath, boiling, vortexing, freeze thawing, or being placed in the warm room for a week. Final solution is milky/soapy and slightly viscous at RT.
4:1:1 POPC:ESM:Chol	DDMB	0.33	0.3	Solution is clear after one cycles.
6:2:1 POPC:ESM:Chol	DDMB	0.33	0.3	Solution is clear after two cycles.
6:1:2 POPC:ESM:Chol	DDMB	0.33	0.3	Solution is cloudy after three cycles.
6:3:1 DMPC:ESM:Chol	DDMB	0.33	0.3	Solution is clear after two cycles.
4:1:1 DMPC:ESM:Chol	DDMB	0.33	0.3	Solution is clear after three cycles.
4:2:1 DMPC:ESM:Chol	DDMB	0.33	0.3	Solution is clear after three cycles.
2:1:1 DMPC:ESM:Chol	DDMB	0.33	0.3	Solution is cloudy after three cycles.
4:1:2 DMPC:ESM:Chol	DDMB	0.33	0.3	Solution is cloudy after three cycles.
6:3:1 DPPC:ESM:Chol	DDMB	0.33	0.3	Solution is clear after three cycles.

4:1:1 POPC:ESM:Chol	DDMB (alpha anomer)	0.33	ND	Solution is clear after three cycles.
6:2:1 POPC:ESM:Chol	DDMB (alpha anomer)	0.33	ND	Solution is clear after three cycles.
6:1:2 POPC:ESM:Chol	DDMB (alpha anomer)	0.33	ND	Solution is clear after three cycles.
4:1:1 DMPC:ESM:Chol	DDMB (alpha anaomer)	0.33	ND	Solution is clear after three cycles.
6:3:1 DMPC:ESM:Chol	Tetradecyl Melibioside	0.33	0.4	Solution is clear after two cycles.
4:1:1 DMPC:ESM:Chol	Tetradecyl Melibioside	0.33	0.14	Solution is clear after three cycles.
4:2:1 DMPC:ESM:Chol	Tetradecyl Melibioside	0.33	0.14	Solution is clear after three cycles.
2:1:1 DMPC:ESM:Chol	Tetradecyl Melibioside	0.33	0.14	Solution is cloudy after three cycles.
4:1:2 DMPC:ESM:Chol	Tetradecyl Melibioside	0.33	0.14	Solution is clear after two cycles.
6:3:1 DPPC:ESM:Chol	Tetradecyl Melibioside	0.33	0.14	Solution is clear after three cycles.

Appendix 3. Recombinant SARS-CoV-2 envelope protein traffics to the trans-Golgi network following amphipol-mediated delivery into human cells

Contents

Supporting Materials and Methods

Recombinant SARS-CoV-2 Envelope protein construct

DNA encoding the SARS CoV-2 envelope protein (S2-E) sequence followed by a C-terminal linker with a thrombin cleavage site and 10X His tag was inserted into a pET-21b plasmid vector. The encoded S2-E sequence is as shown below, with the added linker/thrombin site/tag indicated in blue font:

> MYSFVSEETGTLIVNSVLLFLAFVVFLLVTLAILTALRLCAYCCNIVNVSLVKPSFYVYS-
> RVKNLNSSRVPDLLVLESSGGGSILVPRGSGGSHHHHHHHHHH

Multiple constructs were tested for expression in several bacterial strains and the inclusion of the linker with thrombin cut site significantly increased expression levels.

Recombinant expression of the SARS-CoV-2 Envelope protein

The expression plasmid indicated above was transformed into Rosetta 2(DE3) pLysS cells. Transformed cells were then spread on agar LB plates supplemented with ampicillin and chloramphenicol before overnight growth at 37 °C. Colonies were picked the next afternoon and used to inoculate LB medium (150 mL in 500 mL baffled flask) supplemented with 100 µM ampicillin and 34 µM chloramphenicol before culturing the bacteria overnight with rotary shaking at 37 °C at 230 rotations per minute (RPM). The next morning, 20 mL of overnight culture was added to 1 L of antibiotic-supplemented M9 medium with added MEM vitamins (Corning) in a 2 L baffled flask and grown at 37 °C at 230 RPM. After ~5-8 hours, when the cultures had grown to an OD_{600} of 0.6-0.8 they were induced with 1 mM isopropyl β-D-1-thiogalactopyranoside. Induced cultures were allowed to incubate overnight at 37 °C at 230 RPM to facilitate production of S2-E inclusion bodies. Cultures were harvested the next morning by spinning cultures down at 3500 × g for 20 min at 4 °C and the pelleted cells were flash frozen in liquid nitrogen before being stored at –80 °C. Six liters of culture typically resulted in a wet cell mass of 10-14 g.

Purification of the SARS-CoV-2 Envelope protein

10-14 grams of frozen cells were thawed at room temperature and suspended in 140 mL of lysis buffer—75mM tris(hydroxymethyl)aminomethane (Tris) pH 7.8, 300 mL NaCl, and 0.2 mM ethylenediaminetetraacetic acid (EDTA)—supplemented with 0.5 mM magnesium acetate, lysozyme, ribonuclease, deoxyribonuclease, and 50 µL/gram wet cell mass protease inhibitor (P8849 Sigma). The lysis slurry was tumbled for two hours at 4 °C before being sonicated with a (Fisher Scientific, model FB705) on ice for 12 minutes at 60% power with alternating 5 second pulses and pauses (total power imparted on the slurry was ~ 80 kJ). The sonicated slurry was centrifuged at 25,000 × g for 20 minutes at 4 °C and the supernatant was discarded. The inclusion body pellets were resuspended with a Dounce homogenizer in 140 mL of lysis buffer. The sonication and centrifugation steps were repeated once in order to further clean the inclusion bodies. Clean inclusion body pellets were resuspended in 140 mL of lysis buffer supplemented with 3 % w/v N-dodecyl-N,N-dimethylglycine (Empigen), 0.5 mM dithiothreitol (DTT), and 25 µL/gram wet cell mass protease inhibitor before being tumbled overnight at 4 °C. The next morning, persistently insoluble materials were removed from the dissolved inclusion bodies by spinning at 25,000 × g for 45 minutes at 4 °C. The supernatant was saved.

2 mL of HisPur Ni-NTA Superflow agarose resin (Thermo Scientific) was equilibrated in lysis buffer before being mixed with the supernatant. The resin and supernatant were tumbled 1-2 hours at 4 °C before the resin was loaded onto a gravity column connected to an A_{280} detector. To wash away unbound impurities, 15 column volumes (CV) of 0.3% Empigen, 1×Tris-buffered saline (TBS, 20 mM Tris pH 7.5 140 mM NaCl), plus 0.25 mM DTT were passed through the resin. Low-affinity impurities were washed away with 15 CV washes of 30 mM imidazole, 1× TBS, 0.1% 1-myristoyl-2-hydroxy-sn-glycero-3-phosphocholine (LMPC), and 0.25 mM DTT. This was repeated for 75, 90, and 120 mM imidazole washes in order to remove the remaining impurities. A 10 CV solution of 0.2 wt% PMAL-C8 (Anatrace, Maumee, OH) in 1X TBS was washed over the resin in 2 CV pulses in order to remove the majority of the detergent and exchange the resin-bound envelope protein into amphipols. Excess amphipols and residual detergent were then removed by washing the column with 10 CV of 1× TBS. Amphipol-complexed envelope protein was then eluted from the column with 5 CV of 250 mM imidazole in 1× TBS pH 7.8. It was seen that envelope protein could be eluted in either amphipol PMAL-C8 or A8-35 (Anatrace), but PMAL-C8 was chosen because it is zwitterionic and easier to work with than the anionic A8-35. The S2-E construct tag can be proteolytically removed with thrombin in detergent solutions for structural and biochemical studies, but this was not carried out here because the thrombin precipitated the S2-E in PMAL-C8 amphipols solutions.

Fluorescent labeling of S2-E

Immediately after the envelope protein was eluted in complex with PMAL-C8, 1.5 mg of thiol-reactive N,N'-dimethyl-N-(iodoacetyl)-N'-(7-nitrobenz-2-oxa-1,3-diazol-4-yl)ethylenediamine (IA-NBD) (Thermo Fisher) or AFDye 488 Maleimide (Flouroprobes) was dissolved into 300 µL of dimethyl sulfoxide (DMSO) and added to the ~10 mL of eluted protein for labeling of one or more of its 3 cysteine residues (which are sequentially proximal within the S2-E extramembrane C-terminus). The reaction tube was covered in foil and tumbled at room temperature for one hour before being filtered through a 0.8 µm Acrodisc low-protein binding filter (PALL PN 4618). The filtered amphipol/S2-E solution was then extensively dialyzed against 1× TBS pH 7.8 with 0.25 mM tris(2-carboxyethyl)phosphine hydrochloride (TCEP) and EDTA in 6-8 kD molecular weight cut-off (MWCO) dialysis tubing from Spectra/Por (part number 132660). On the morning of tissue culture treatment, the dialyzed protein was concentrated ~10× in a 10kD MWCO Amicon Ultra-15 filter cartridge by centrifuging at 2500 × g at room temperature (RT). Protein purity was checked by sodium dodecylsulfate polyacrylamide gel electrophoresis (SDS-PAGE) and the concentration was determined by measuring absorbance at 280 nm using an extinction coefficient of 6000 $M^{-1}cm^{-1}$. AFDye 488 Maleimide dye has absorbance at A280 and so the protein concetration was determined by reference on SDS-PAGE against unlabeled or NBD labeled E. Dye labeling efficiency was checked by measuring absorbance at 472 nm or 493 nm with an excitation coefficient of 23700 $M^{-1}cm^{-1}$ or 72000 $M^{-1}cm^{-1}$ for NBD or AF488 respectively. It was seen that the labeling efficiency was usually ~0.7 flourophore per protein, indicating that, on the average, only one of three wild type cysteine residues was modified. Dye-modified S2-E (S2-E-Dye) was normally used within one week (with storage at 4 °C) following completion of preparation. Indeed, we observed that preparations that were stored for longer than 3 weeks at 4 °C led to cellular results in which S2-E-NBD was seen to traffic as usual to the perinuclear space but did not then obviously segregate to one side of the nucleus at longer timepoints (16/24h), as was seen when freshly prepared samples were employed. Starting with six liters of culture, this protocol yields roughly 500 µg of fluorescently labeled S2-E protein.

Functional delivery of SARS-CoV-2 envelope protein from amphipols to planar bilayers

Planar lipid bilayers were formed from a solution of synthetic 1-palmitoyl-2-oleoyl-glycero-3-phosphocoline (POPC) and 1-palmitoyl-2-oleoyl-glycero-3-phosphoethanolamine (POPE, Avanti Polar Lipids) in a 3:1 mole ratio in *n*-decane (Sigma-Aldrich). A glass bulb was used to apply the POPC/POPE solution in a 150 µm aperture of a Delrin cup (Warner Instruments), separating the *cis* and *trans* chambers. Asymmetric buffers were used, with 5 mM 4-(2-hydroxyethyl)-1-piperazineethanesulfonic acid (HEPES), 500 mM NaCl, pH 7.2 for the *cis* chamber, and 5 mM HEPES, 50 mM NaCl, pH 7.2 for the *trans* chamber as done in previous studies for comparison.(38,39) The bilayer capacitance ranged between 50-65 pF.

Delivery of the SARS-CoV-2 envelope protein (S2-E) complexed by PMAL-C8 amphipols to pre-formed planar bilayers was achieved spontaneously by pipette addition of ~1 µL of ~3 µM of the S2-E–amphipol complex and accompanied by stirring of the chambers. Each chamber (cis/trans) had 2.5 mL of buffer (5mL total volume). Incorporation of S2-E was achieved by addition of PMAL-C8 complexed S2-E to either the cis or to both cis and trans chambers. The final concentration of protein varied from ~5 nM–15 nM. S2-E unitary currents were collected from a BC-535 amplifier (Warner Instruments) at 23 ± 1°C, 10 mV/pA gain and low-pass filtered by a 4-pole Bessel filter at 1 kHz. The resulting data were digitized using an analog-to-digital converter (Digidata 1550A, Molecular Devices) at 1 kHz using the pClamp10.7 software suite (Molecular Devices). The single-channel data were collected over separate amphipol delivery experiments carried out on different days, with three-minute recordings for each voltage. Recordings were analyzed using the single-channel search in ClampFit 10.7 (Molecular Devices) filtered with a 100 Hz low pass Gaussian filter and ignoring short level changes of 25 ms duration to obtain the number of events, open probability, reversal potential, and single-channel conductance. Similar conditions were conducted with the S2-E-NBD. Control experiments where PMAL-C8 only (no S2-E) was added to the planar bilayers did not exhibit channel activity at 1x or 50x amphipol concentrations relative to those used in S2-E and S2-E-NBD planar bilayer experiments.

Maintenance of cell cultures

Human cell lines HeLa (ATCC cat# CCL-2) and alveolar SW1573 (ATCC cat# CRL-2170) cells were obtained from ATCC. HeLa cells were maintained in a tissue culture incubator with humidified air supplemented with 5% CO_2 at 37 °C. HeLa cells were grown in low glucose Dulbecco's Modified Eagles Medium (DMEM, Gibco cat# 11885-084) supplemented with 10% fetal bovine serum (FBS, Gibco 26140-079), 1% penicillin/streptomycin (P/S, Corning, Ref 30-0020CI). SW1573 cells were kept in a tissue culture incubator with humidified air without added CO_2 at 37°C. The SW1573 were grown and maintained in (Leibovitz's medium # 15, or L-15; ATCC cat # 30-2008) supplemented with 10% FBS and 1% P/S. Both cell lines were passaged 2 times a week and seeded such as to always remain below 95% confluency.

Cell culture treatments

The underlying idea of our S2-E-to-cell experiments was to treat cells with aliquots of fluorescently-tagged S2-E/amphipol and then to follow cell association and intracellular trafficking of the flurorescently-taged protein over time. These experiments were conducted with healthy growing cells that are well attached to a glass coverslip surface. These cells were treated with various concentrations of SE-2 protein/amphipol for differing amounts of time. This is achieved with freshly concentrated, and preferably freshly made, SE-2 protein complexed with amphipol PMAL-C8 in TBS. In order not to perturb the cells by changes in osmotic pressure, pH, or temperature the stock S2-E amphipol solution was processed prior to addition to the cells. S2-E was first dialyzed against TBS. Further, the resulting S2-E/amphipol solution was added to fresh 37 °C pre-warmed cell media and mixed before aliquots were then added to cells. The added volume of the S2-E/amphipol solution added to the cell culture never exceeded 10% of the culture volume and was often less (4-6%). At the chosen time points, the coverslip containing attached cells was rinsed to discard floating cell debris and then 'fixed' with paraformaldehyde. Fixing is intended to chemically freeze cells. The procedure kills the cells but preserves their plasma membrane surface and intracellular structures. After discarding excess fixative, cells are treated differently depending on the cell structures we wished to observe in relation to S2-E protein. When the goal was to see S2-E in relation to the plasma membrane we used WGA a lecithin conjugated to a fluorophore together with a cell nucleus dye DRAQ5 which preferentially binds double-stranded DNA. When the intent was to observe intracellular organelles Golgi, ERGIC, and others the fixed cells were permeabilized by incubation with detergent with the goal being to make small holes of sufficient size, for antibodies specific to those structures, to enter the cell surface and gain access to Golgi,ERGIC, and other cell organelles.

Exponentially growing cells were plated in the wells of a 12-well plate with 1.5 thickness glass coverslips (Fisherbrand cat # 12-545-81) at a cell density of 20-23,000 live cells/well in 2mL cell media. After a day, the cells destined for 24h and 16-18h time points were treated by rinsing once with Dulbecco's phosphate buffered saline without calcium and magnesium (DPBS, Corning cat 21-031-CV) and by adding 1 mL of fresh medium with no more than 5-10 % volume of freshly concentrated S2-E protein (labelled or not) with amphipol in the dialysis buffer at the concentrations stated in the figure captions. Cells were protected from light. The remaining and undiluted S2-E/amphipol stock was stored at 4 °C overnight protected from light and used in the same way the next morning for the remaining time points. At the appropriate time, each coverslip was transferred into a fresh 12-well plate well facing upwards containing 2 mL of 37 °C pre-warmed DPBS. DPBS was discarded by suction, and cell fixation was started by adding gently 1 mL/well of pre-warm 4% paraformaldehyde (PFA, EMS cat #15714) dissolved in DPBS for 15 min at 37 °C. After fixation in 4% PFA, all steps were carried out with gentle mixing and at room temperature and with plates protected from light by being kept wrap in aluminum foil. All solutions were filtered prior to addition to coverslips to avoid addition or formation of aggregates. Fixation was stopped by discarding the 4% PFA solution by suction and by gently rinsing 2 times with 2 mL/well with DPBS for 15 min/each. The cell membrane was labeled with wheat germ agglutinin conjugated to Alexa Fluor-555 (WGA-AF555 Invitrogen cat# W32464) at a final concentration of 5 µg/mL for 15 min using 1 mL/well. Coverslips were then rinsed from excess WGA-AF555 by rinsing 2 times with 2 mL/well in DPBS for 15 min for each time point and once using 100mM glycine in DPBS. The times of cell treatment were imperfectly staggered. After the 100 mM glycine rinse, the timepoint samples were set aside without shaking until other time points were completed. When all time points had finished the 100 mM glycine rinse, all coverslips were transferred into a common 12-well plate, and the following treatments proceeded as a group.

For time-course S2-E-NBD trafficking course experiments without antibodies (Figs. 4.2 and S4.6) cells were cell nucleus-labeled using freshly opened of DRAQ5 (Invitrogen cat #65-0880), an anthraquinone membrane permeable dye with high affinity for double-stranded DNA. DRAQ5 was used diluted 1:2500 in DPBS using 2 mL/well and incubated for 1 h. Excess DRAQ5 was then rinsed away twice with 2mL/well 5-10 min each DPBS +0.01% Triton X-100 (TX-100) and once with DPBS only. Coverslips were mounted in glass slides using Prolong Gold antifade (Invitrogen, cat # P10144) and cured, typically for 2 days, before imaging.

For experiments requiring antibody detection of organelle-specific marker proteins (Figs. 4.3, S10-S12, and S14-S16) or anti-E (Figs. S4.5 and S4.7), cells were permeabilized with 1 mL/well containing 0.1% TX-100 dissolved in DPBS for 15 min. Permeabilization was stopped by rinsing twice in 2 mL/well DPBS and blocking overnight with 2 mL/well of 1% BSA dissolved in DPBS with 0.01% TX-100. The day after, plates were allowed to reach RT for 30-40 min without mixing and then treated with specific antibodies for detection of Golgin97 (1 mL/well, diluted 1: 500; Invitrogen, cat #A21270), or ERGIC53 (40) (1 mL/well, diluted 1:500; ENZO cat# ENZ-ABS300), or for E protein detection (1:1000 dilution of rabbit polyclonal antibody ProSci cat# 10-518, (this polyclonal was not very specific and weakly reacts to a nuclear protein in HeLa cells, see Fig. S4.5 panel E) or KDEL (1mL/well diluted 1:400; Abcam, cat# EPR12668) or GM130 (1mL/well diluted 1:500; Cell Signaling, cat #12480S) or EEA1 (1mL/well diluted 1:450; Invitrogen, cat # MA5-14794) or Lamp1 (1mL/well diluted 1:400; Encorbio, cat # MCA-5H6) or vimentin (1mL/well diluted 1:500; Cell Signaling, cat #5741S. All antibodies were diluted in freshly made and 0.2 µm filtered 1% BSA dissolved in DPBS + 0.01% TX100 (1%BSA)and incubated for 2 h at RT with gentle mixing. Each coverslip was treated to remove unbound primary antibody by rinsing 3 times with 2mL/well DPBS + 0.01% TX-100, 15 min each. Samples were then incubated with a secondary antibody conjugated to a fluorescent dye using 1 mL/well for 1 hr in 1% bovine serum albumin (BSA) using 1:1000 dilution of goat anti-mouse conjugated to Alexa Fluor 546 (AF546; Invitrogen cat# A11030), against mouse mAb for Golgin-97 and ERGIC53. For samples treated with rabbit anti-E polyclonal (in Fig. S4.7) we used donkey anti-rabbit conjugated Alexa Fluor 488 (AF488; Invitrogen cat# A32790). For Figures S4.5, S4.10-S4.12, S4.14 and S4.16 where samples were treated with rabbit antibodies and we used donkey anti-rabbit conjugated Alexa Fluor 555 (Invitrogen cat # A31572),while for anti-Lamp1 (Fig. S4.15) we used goat anti-mouse conjugated Alexa Fluor 555 (Invitrogen cat # A32727). After 1 h incubation with gentle shaking the samples were rinsed twice for 15 min with 2 mL/well DPBS + 0.01% TX100 and treated in the same way as above for nuclear counter-staining using DRAQ5 and coverslip mounting.

For live-cell imaging experiments, HeLa cells exponentially growing and maintained as above were split into a 12-well plate (Corning # 3512) or 35 mm glass bottom petri dishes (MatTek Part No. P35G-1.5-12-C) at a density of 5000 cells/cm^2 the day before treatment and grown overnight in 5% CO_2 atmosphere. The next day, cells were rinsed once with RT DPBS and their cell culture media was exchanged for 1 mL pre-warmed L15 complete medium and placed in a 0% CO_2 incubator for 30 minutes. After thermal equilibration to L15 media, samples imaged within 3 hours were treated with 10 µg /mL of WGA-555, and for nuclear labeling used 1-drop/mL Hoechst 33342 (Invitrogen, cat # R37605), and 2.5 µM of either AF488 or NBD labeled S2-E in PMAL-C8 was added before being placed back in the 0% CO2 incubator for the first hour. For samples imaged 24 h after after treatment with S2-E-label (data not shown), WGA-AF555, and the nuclear stain were added one hour before imaging. Samples were imaged both before and after washing away labeling media (S2-E, WGA-555, and NucBlue) in order to determine if free S2-E interfered with imaging (see Fig. S4.4).

For live cell imaging with cysteine-NBD (Fig. S4.8), HeLa cells growing in low glucose DMEM were split into 35 mm glass bottom petri dishes (MatTek Part No. P35G-1.5-12-C) at a density of 5000 cells/cm^2 and grown for ~36 hours in 5% CO_2. The cysteine-NBD was created the morning before the HeLa cell treatment. One mg of IA-NBD amine was reacted with two mg of L-cysteine amino acid in one mL of 80/20 water/DMSO and reacted in the dark at RT for one hour. The resulting mixture was filtered with a 0.8 µm Acrodisc low-protein binding filter and the NBD concentration was determined by UV-Vis as with S2-E. Cells were treated with 5 µM cysteine-NBD and placed back in the incubator before imaging. Prior to imaging, media was replaced with 1 mL of dye-free pre-warmed complete DMEM low glucose media.

Cell imaging

All confocal experiments shown were imaged using a LSM 510 confocal microscope, with a Plan-Neofluar 40x/1.30 Oil DIC objective. The confocal pinholes were set at 84µm for the 633 nm HeNe1 laser line, at 80µm, for the 543 nm HeNe1 laser line, and at 86µm for the Argon laser. These settings correspond to a pinhole diameter of 1.00 Airy units for the HeNe2 laser (633 nm), and the same optical slice of 1.1 µm for all three lines. These settings were kept for all channels in all experiments. The fluorophores were excited using the 488 nm line of a 40 mW Argon laser set at 10% power (reduced at source to 50%, for a final 5%) for NBD and AF488 signal. The 543 nm line was set at 10% power for WGA-AF555 and for anti-mouse AF546, whereas the 633 nm line of a HeNe laser was set to 15-50% power for DRAQ5 depending on the dye emission intensity. Images were collected at 1-2× and occasionally 3× zoom. The frame size was set usually to 1024, data depth was 8 bit, and Multi track/frame mode was used, for each channel. The scan average parameter was usually set to 4, but sometimes to 8 or 16. For presentation purposes, images were processed using ImageJ software.

Live cell imaging was done with an ECHO Revolve equipped with a ELWD Universal Condenser; NA 0.30 WD 73m and using a 40x PLAN Fluorite LWD CC Phase Ph2 NA 0.60 objective. LED light cubes used were: DAPI - EX:385/30 EM:450/50 DM:425, for the nuclear stain; FITC - EX:470/40 EM:525/50 DM:495 for the E-labeled protein, and TxRED - EX:560/40 EM:635/60 DM:600 for WGA-AF555.

Statistics

The numbers of replicates, validation of reagents, software, and statistical approaches are detailed in the above methods and/or in the relevant figure captions.

Supporting References

1. Wilson, L., McKinlay, C., Gage, P., and Ewart, G. (2004) SARS coronavirus E protein forms cation-selective ion channels. *Virology* **330**, 322-331
2. Xia, B., Shen, X., He, Y., Pan, X., Wang, Y., Yang, F., Fang, S., Wu, Y., Zuo, X., Xie, Z., Jiang, X., Chi, H., Meng, Q., Zhou, H., Zhou, Y., Cheng, X., Chen, T., Xin, X., Jiang, H., Xiao, G., Zhao, Q., Zhang, L.-K., Shen, J., Li, J., and Gao, Z. (2020) SARS-CoV-2 envelope protein causes acute respiratory distress syndrome (ARDS)-like pathological damage and constitutes an antiviral target. *bioRxiv*, 2020.2006.2027.174953
3. Venkatagopalan, P., Daskalova, S. M., Lopez, L. A., Dolezal, K. A., and Hogue, B. G. (2015) Coronavirus envelope (E) protein remains at the site of assembly. *Virology* **478**, 75-85
4. Feryforgues, S., Fayet, J. P., and Lopez, A. (1993) Drastic Changes in the Fluorescence Properties of Nbd Probes with the Polarity of the Medium - Involvement of a Tict State. *J Photoch Photobio A* **70**, 229-243
5. Rezgui, R., Blumer, K., Yeoh-Tan, G., Trexler, A. J., and Magzoub, M. (2016) Precise quantification of cellular uptake of cell-penetrating peptides using fluorescence-activated cell sorting and fluorescence correlation spectroscopy. *Biochim Biophys Acta* **1858**, 1499-1506
6. Pavelka, M., Neumuller, J., and Ellinger, A. (2008) Retrograde traffic in the biosynthetic-secretory route. *Histochem Cell Biol* **129**, 277-288
7. Kanazawa, T., Takematsu, H., Yamamoto, A., Yamamoto, H., and Kozutsumi, Y. (2008) Wheat germ agglutinin stains dispersed post-golgi vesicles after treatment with the cytokinesis inhibitor psychosine. *J Cell Physiol* **215**, 517-525

Supporting Figures

Figure S4.1

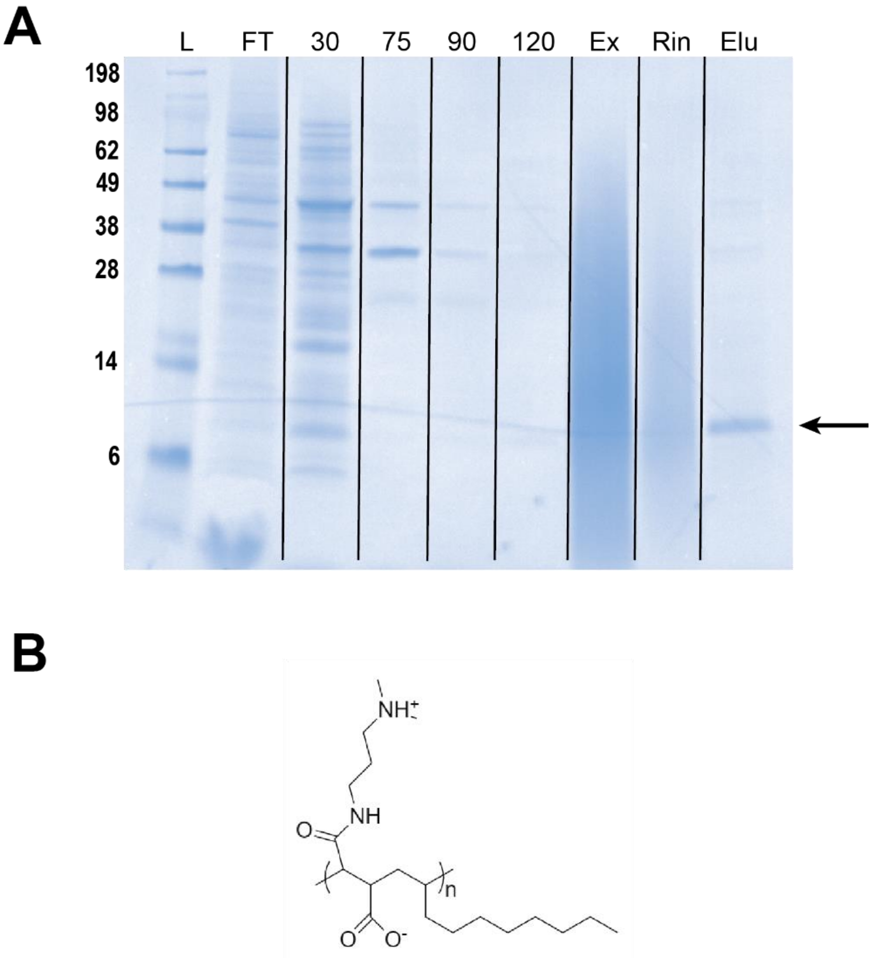

Figure S4.1. Representative SDS-PAGE of SARS-CoV-2 envelope protein (S2-E) purified into PMAL-C8. A) Each lane represents a step in the purification protocol after passing detergent-solubilized inclusion bodies over the column. SDS-PAGE samples were boiled and reduced with 5mM DTT before being run. Gels were stained with the SimplyBlue coomassie alternative (Invitrogen). Lanes from left to right are: Molecular Weight Standard **L**adder SeeBlue Plus2, **F**low-**T**hrough, **30** mM imidazole wash, **75** mM imidazole wash, **90** mM imidazole wash, **120** mM imidazole wash, **Ex**change into PMAL-C8, **Rin**se unbound PMAL-C8, and **Elu**tion. The black arrow points to the purified S2-E protein in the final elution. **B)** Chemical structure of PMAL-C8.

Figure S4.2

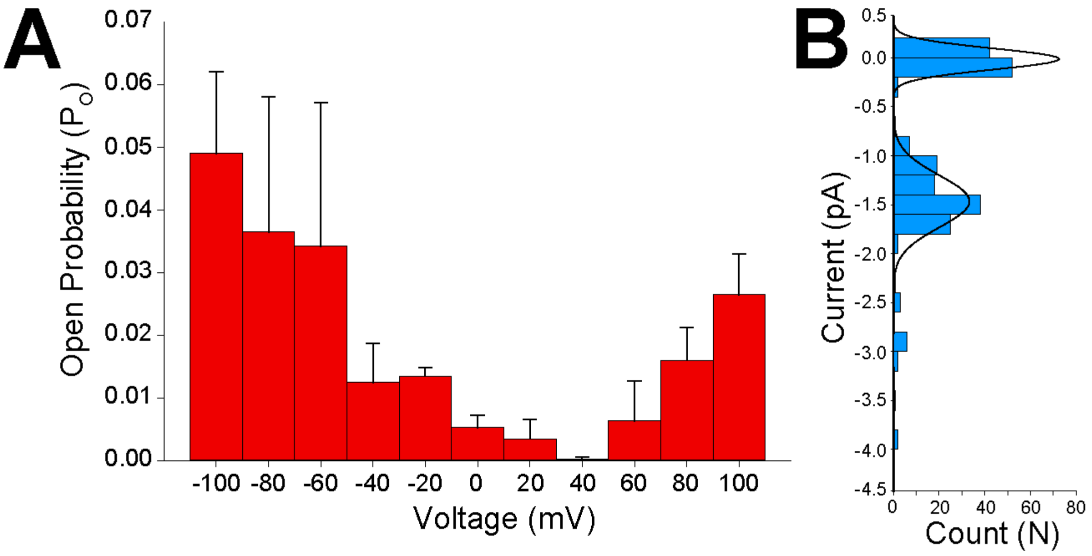

Figure S4.2. S2-E ion channel open probability and current amplitude distribution from planar bilayer electrophysiology measurements after amphipol delivery. Previous studies of CoV E proteins indicate that the channel has low open probabilities and current amplitudes. **(A)** Shows the open probability as a function of voltage for the data in Fig. 4.1*C*. Error bars are SEM from three distinct delivery experiments on different days and in total correspond to 9 min of measurement. **(B)** Identifies the number of events and the respective currents recorded at -100 mV. The historgram was fit to a 3 polynomial Gaussian fit with an average amplitude of 1.47 ± 0.05 pA for the open state. As in panel A, these data are from three separate recordings.

Figure S4.3

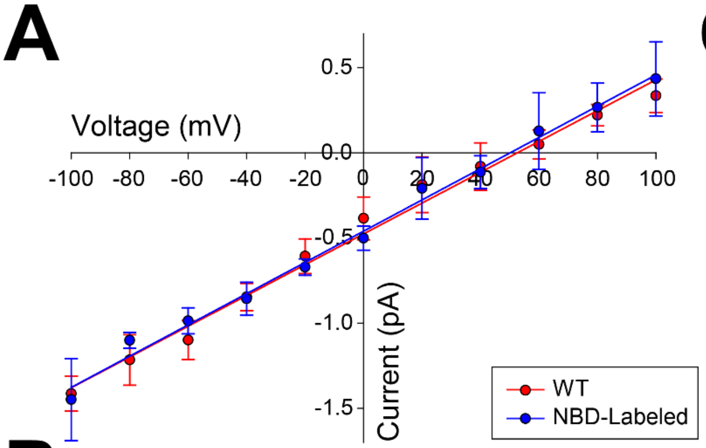

B

	Conductance (pS)	Reversal Potential (mV)
WT	9.0 ± 0.3	53 ± 3
NBD-Labeled	9.2 ± 0.2	50 ± 2

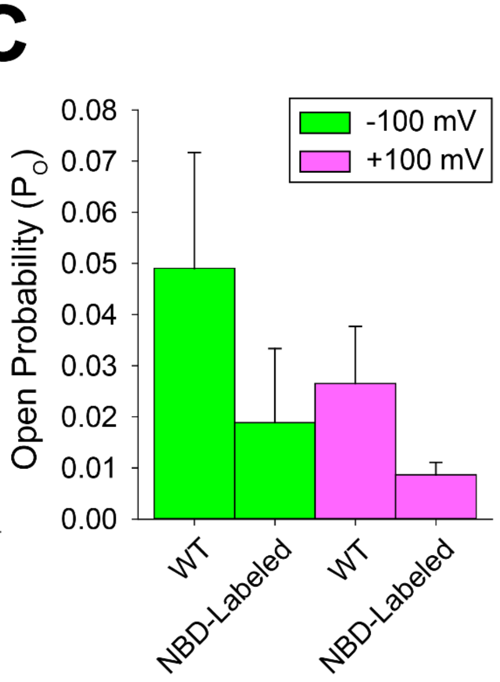

Figure S4.3. Planar lipid bilayer electrophysiology characterization of NBD-labeled SARS-CoV-2 envelope protein delivered from amphipols. (A) Comparison of unlabeled (WT) and NBD-labeled S2-E current-voltage relationship shows that NBD-labeling has no meaningful impact on conductance and reversal potential (B). (C) NBD-labeling of S2-E results in a nonstatistically significant decrease in open probability relative to the WT based on calculations of an unpaired t-test with P-values of 0.125 at -100 mV and 0.055 at 100 mV. Data represent three replicates. Error bars are standard deviations from three distinct delivery experiments on different days and correspond to a total measurement time of 9 min.

Figure S4.4

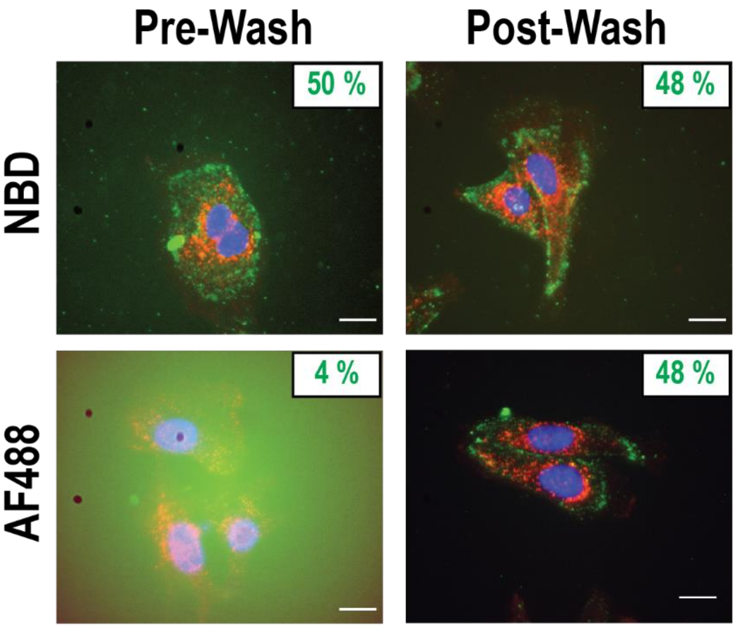

Figure S4.4. Comparison of live cell imaging when S2-E is labeled with either NBD or AF488. Top Left: The solvatochromic properties of NBD allows for live cell imaging of amphipol-mediated S2-E-NBD delivery to the plasma membrane. The S2-E-NBD has a low fluorescent intensity in bulk solution and this facilitates live cell imaging with the S2-E-NBD containing media--supplemental reference (41). While this is an undesirable characteristic for soluble targets it is suited for use with membrane proteins where the intensity of NBD is orders of magnitude higher when associated with the lipid bilayer. **Bottom Left:** AF488 is not solvatochromic and thus has a constant high fluorescent intensity, supplemental reference (42). The high background from S2-E-AF488 prevents live cell imaging of S2-E-AF488 delivery to the plasma membrane. **Top Right:** Washing away the S2-E-NBD containing medium and replacing it with fresh S2-E-NBD-free media does not significantly impact visualization of S2-E-NBD delivery to cells. **Bottom Right:** Washing away the S2-E-AF488 containing media and replacing it with fresh S2-E-AF488 free media drastically reduces background and allows adequate visualization of S2-E-AF488 delivery to cells. DAPI and TxRED settings were 110 ms at 16 % power and 620 ms at 81 % power respectively for all images. FITC settings were 570 ms, with power levels are indicated on each panel in the upper right hand corner. This experiment was performed twice with identical overall results. Scale bars are 25µm. Since S2-E is a membrane protein and given the ease of use, lower molecular weight, and lower cost of NBD; we preferencially used this label for most experiments. NBD use in membrane proteins appears validated by the comparable Pearson correlation coefficients results obtained using either S2-E-NBD and S2-E-AF488 (see captions for Figs. S4.5 and S4.10).

Figure S4.5 (First Page of Three-Page Figure)

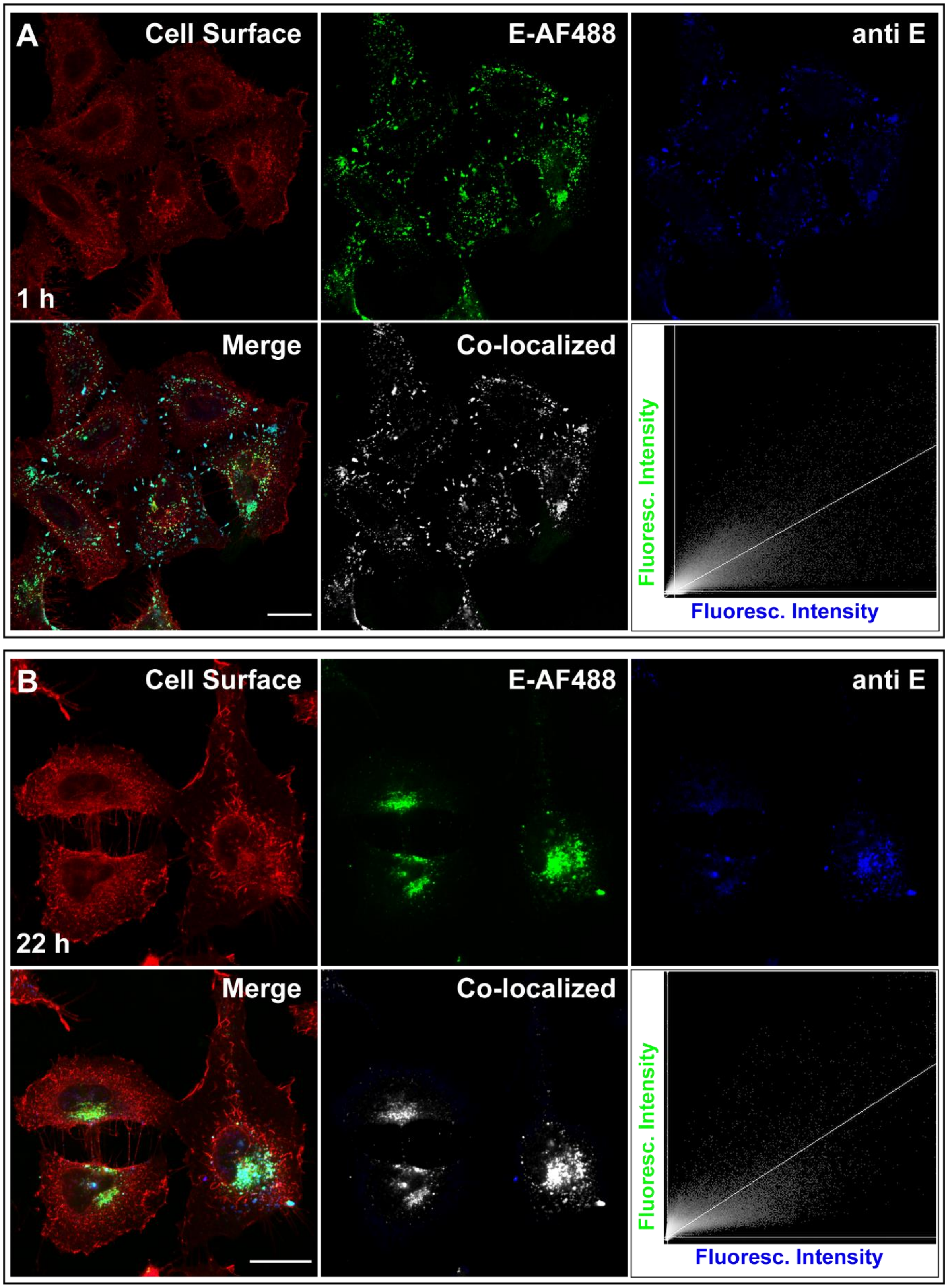
A
Cell Surface
1 h
E-AF488
anti E
Merge
Co-localized
Fluoresc. Intensity
Fluoresc. Intensity
B
Cell Surface
22 h
E-AF488
anti E
Merge
Co-localized
Fluoresc. Intensity
Fluoresc. Intensity

Figure S4.5. panels C and D (Second Page of Three-Page Figure)

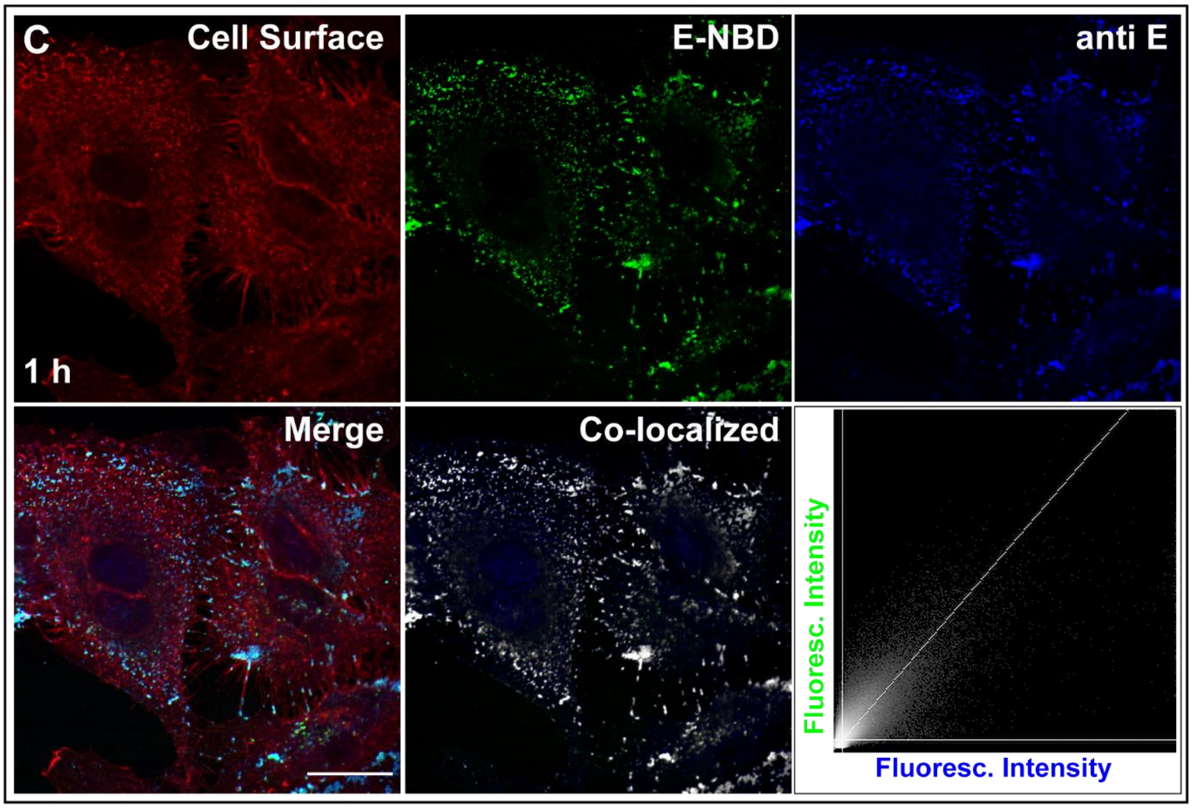
C
Cell Surface
E-NBD
anti E
1 h
Merge
Co-localized
Fluoresc. Intensity
Fluoresc. Intensity

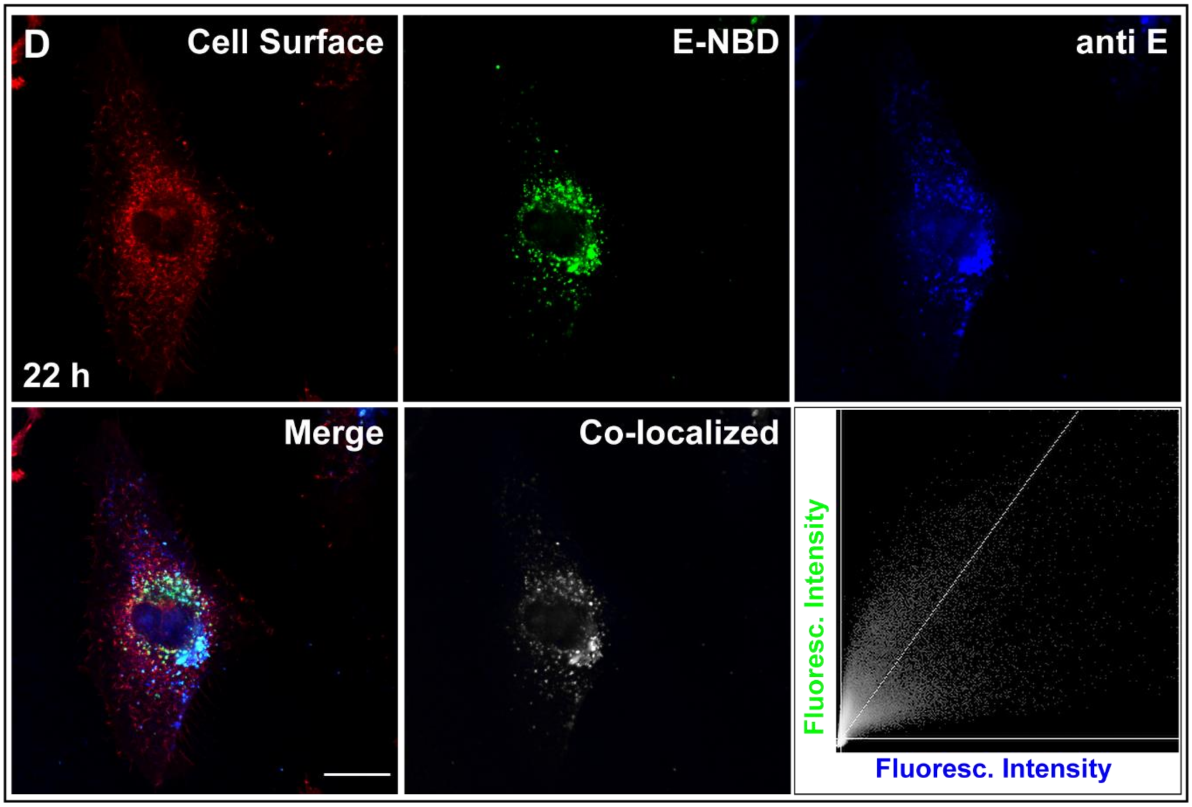
D
Cell Surface
E-NBD
anti E
22 h
Merge
Co-localized
Fluoresc. Intensity
Fluoresc. Intensity

Figure S4.5. panel E (Third Page of Three-Page Figure)

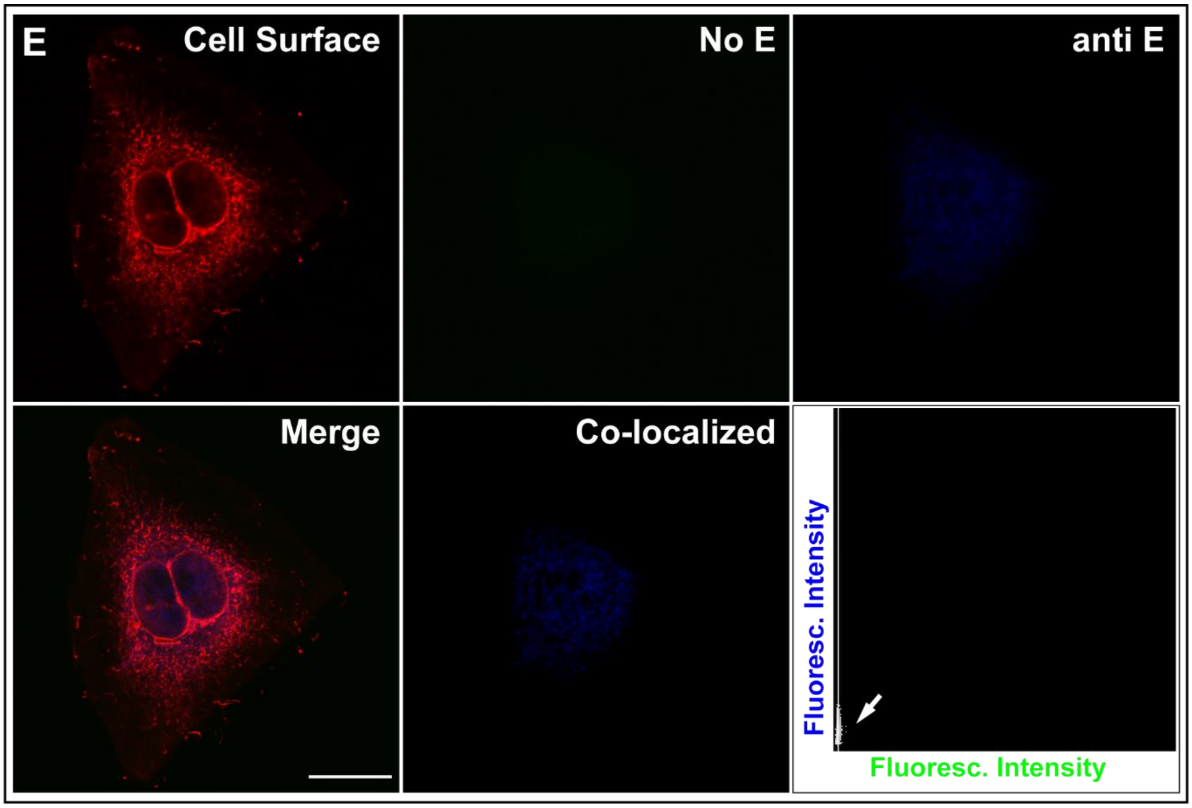

Fig. S4.5. (This page and 2 preceding pages). SARS-CoV-2 envelope protein labeling in cysteines with NBD or AF488 does not affect E retrograde trafficking. To validate the integrity of the fluorescent signals from S2-E-NBD or S2-E-AF488 over time, HeLa cell samples were treated with each labeled protein for 1 h or 24 h. After the indicated times,samples were fixed, membrane stained with WGA-AF555, and probed with polyclonal anti-E antibodies (ProSci cat#10-518; dilution1:1000). Panel **A** shows HeLa cells treated with 2.5µM S2-E-AF488 after 1 h. First row, individual color channels used to detect cell surface (red), S2-E-AF488 (green) and anti-E (blue). Second row shows the merged image of the above three channels, followed by the co-localized image in white between S2-E-AF488 (green) and anti-E (blue) images. The last image is the intensity plot between green and blue images. Colocalization image and intensity plots were obtained using the Image-J plugin Colocalization Threshold, without ROIs. Panel **B** shows cells treated with S2-E-AF488 for 24 h. Both rows in B are presented as in panel A. Panel **C** shows HeLa cells treated with 2.5µM E-NBD after 1 h. First row in C shows individual color channels used to detect cell surface (red), E-NBD (green) and anti-E (blue). Second row in C shows the merged image, followed by the co-localized image between S2-E-AF488 and anti-E, and the intensity plot between green and blue images. Panel **D** shows cells treated with S2-E-AF488 after 24 h. Both rows in D are presented as in panel C. Experiments shown in panels A-D were performed 3 independent times, twice using E-NBD and once with S2-E-AF488. For each E-labeled time point, at least 5 images were recorded and analyzed for colocalization, using four Image-J plugins (Colocalization Test, Colocalization Threshold, Coloc-2, and JACoP). As expected, all colocalized images in panels A-D show strong Pearson correlation with comparable coefficients. Using the colocalization-threshold plugin, average Pearson correlation coefficients with standard deviations for each experiment were: S2-E-NBD#1; 1 h, 0.72 ± 0.05 and 24 h, 0.68 ± 0.03; for S2-E-AF488; 1 h, 0.73 ± 0.09

and 24 h, 0.68 ± 0.05 and for S2-E-NBD#2; 1 h, 0.77 ± 0.05, 24 h, 0.70 ± 0.11. Panel **E** is HeLa cells non-treated with S2-E but probed with anti-E antibodies showing that the antibodies used exhibit non-specific binding to a nuclear target. Note that the anti-E and co-localized images are enhanced to show the unspecific binding of the anti-E, and that HeLa cells treated with S2-E-NBD or S2-E-AF488 do not show green fluorescence in the cell nuclei. Scale bars are 20 µm. For more details see online Materials and Methods.

Figure S4.6

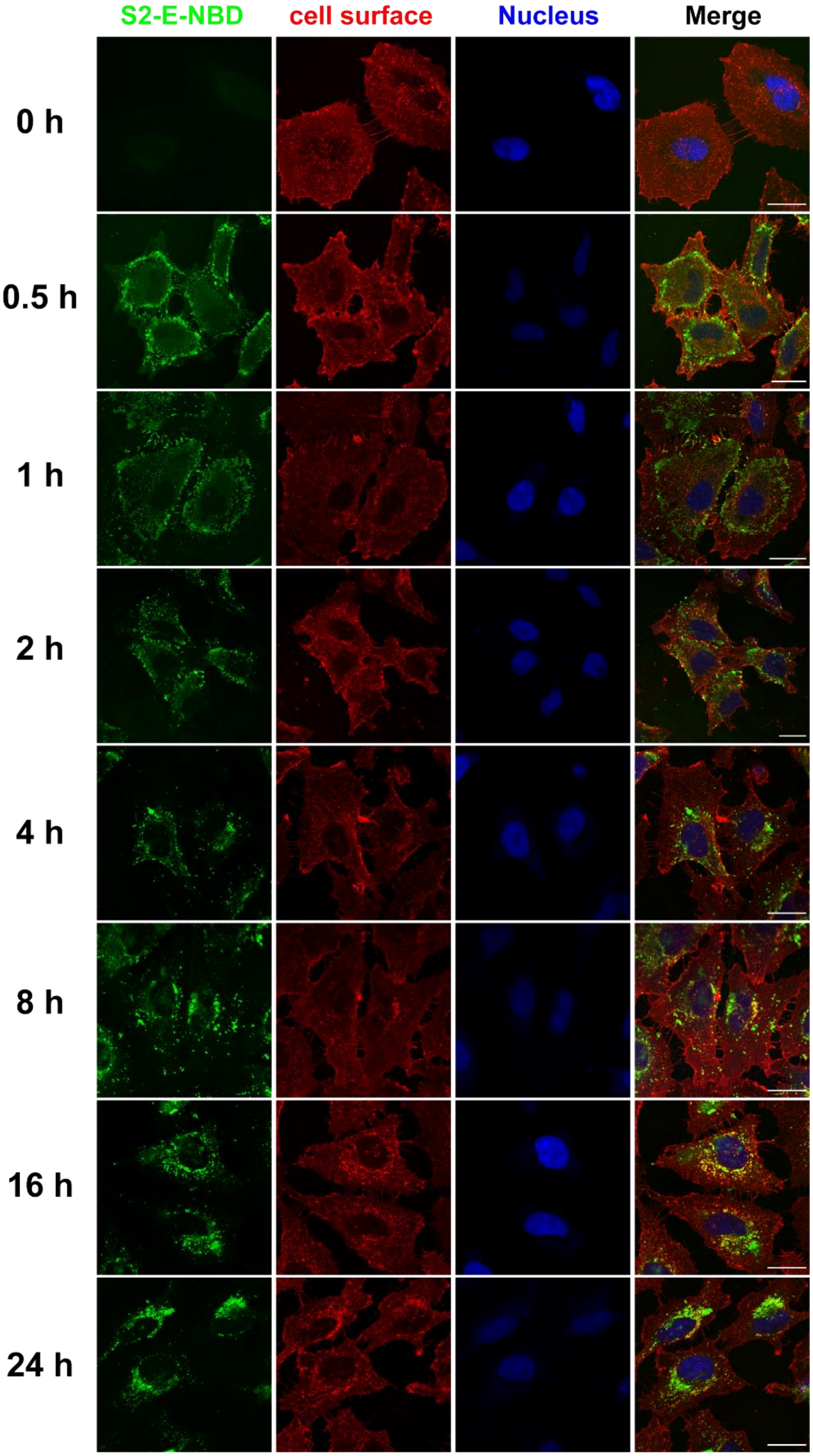

Figure S4.6. Individual channels for each composite image shown in Fig. 4.2 of the main text. Color scheme: green, NBD-labeled S2-E; red, cell surface plasma membrane (WGA-AF555); and blue, cell nuclei

(DRAQ5). Note the movement over time of the S2-E-NBD signal towards one side of the cell nucleus while the red signal remains constant. Scale bar 25 µm.

Figure S4.7 (Four-Page Figure)

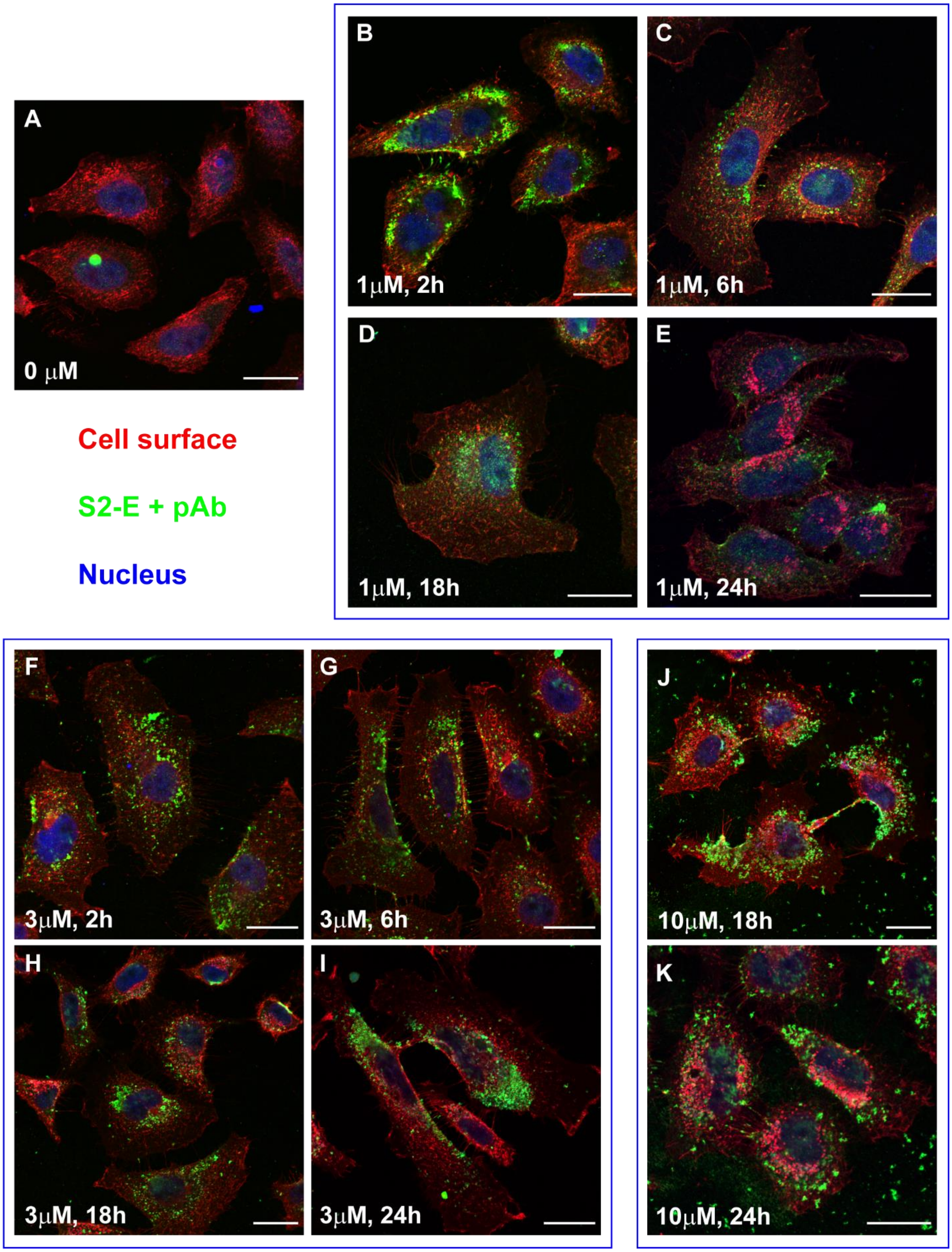
A
0 μM
Cell surface
S2-E + pAb
Nucleus
B
1μM, 2h
C
1μM, 6h
D
1μM, 18h
E
1μM, 24h
F
3μM, 2h
G
3μM, 6h
H
3μM, 18h
I
3μM, 24h
J
10μM, 18h
K
10μM, 24h

Figure S4.7. Lower Panel I. Individual channels and composite of upper panels A and B-E

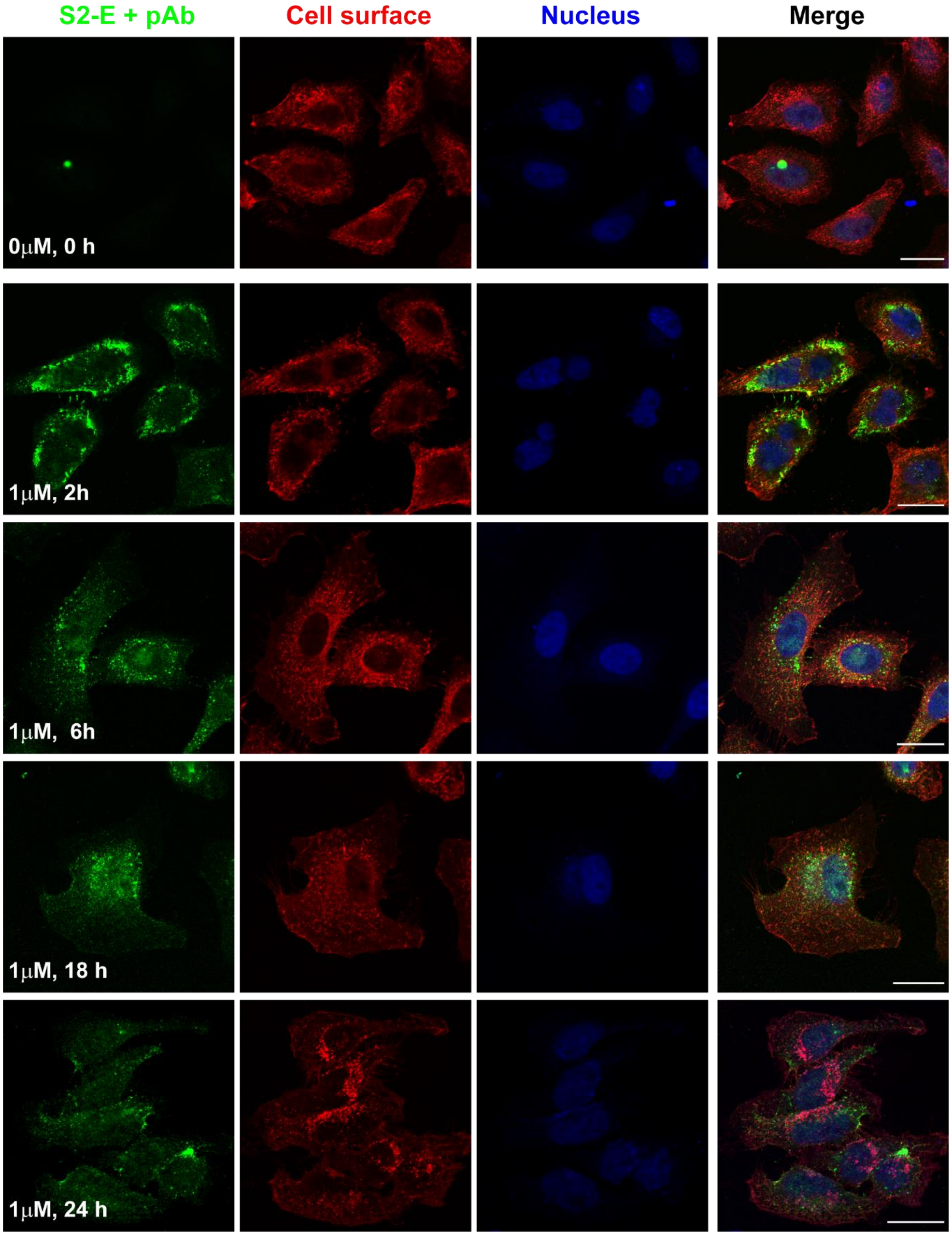

Figure S4.7. Lower Panel II. Individual channels and composite of upper panels A, F-I

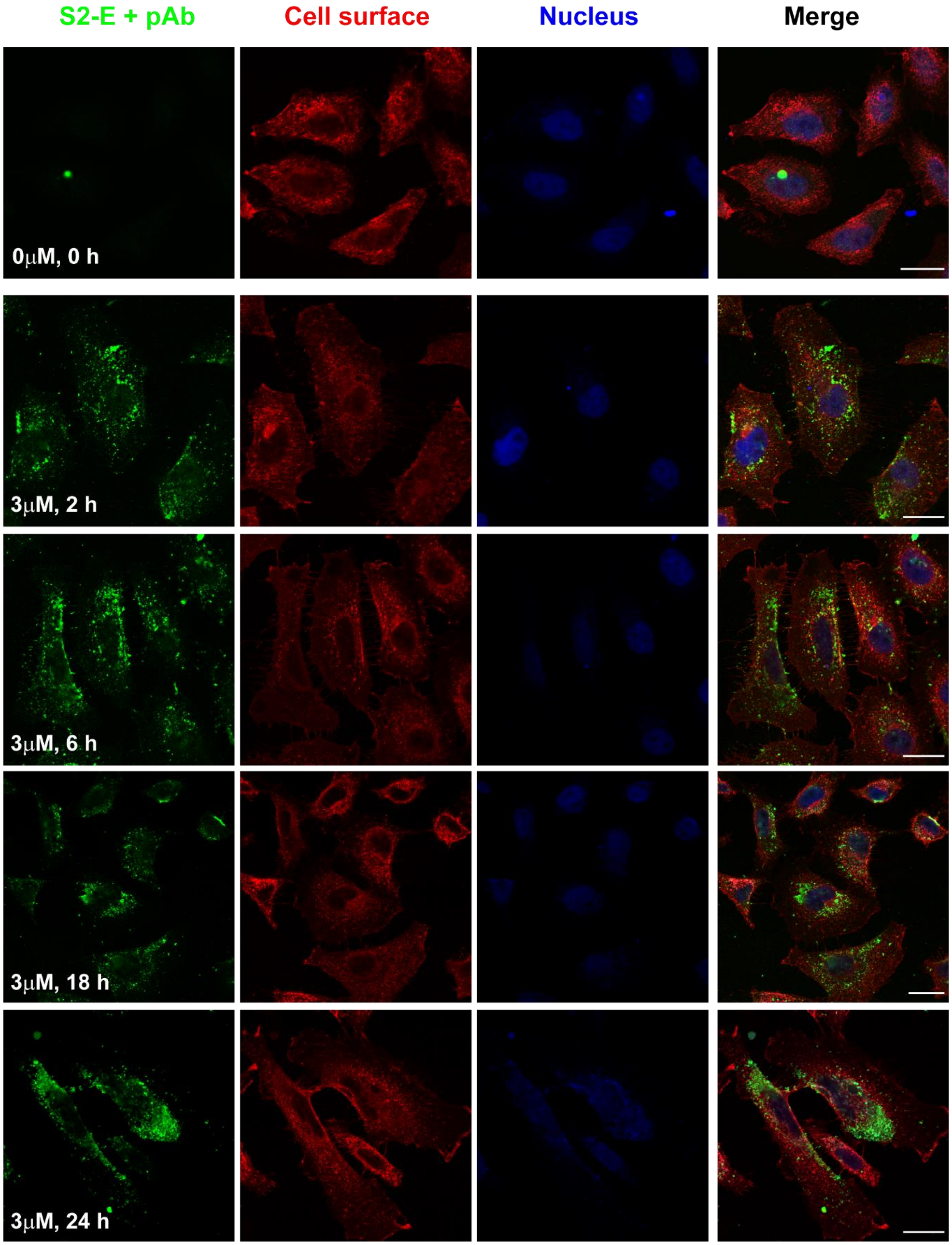
S2-E + pAb
Cell surface
Nucleus
Merge
0μM, 0 h
3μM, 2 h
3μM, 6 h
3μM, 18 h
3μM, 24 h

Figure S4.7. Lower Panel III. Individual channels and composite of upper panels A and J-K

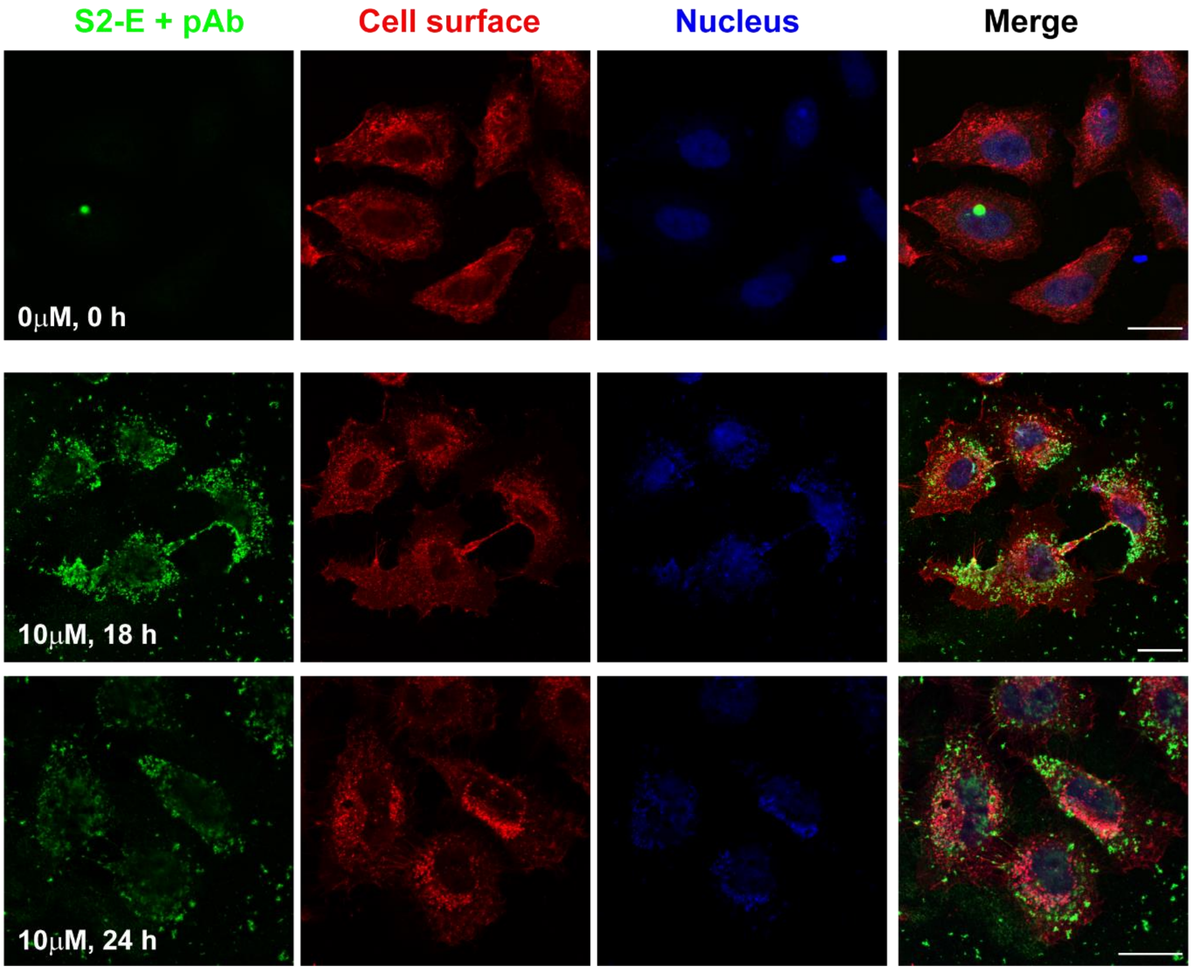

Figure S4.7 (This page and 3 preceding pages). Unmodified S2-E protein delivered to cells from PMAL-C8 amphipol shows similar cell membrane localization and retrograde kinetics as for the NBD-tagged S2-E protein. The time course and concentration dependency of unmodified S2-E was followed using rabbit anti-E polyclonal antibodies. Rabbit antibodies were detected using anti-rabbit conjugated AF488 (green). Hela cell surface plasma membranes (red) were detected using WGA-AF555, while cell nuclei (blue) were labeled using DRAQ5. Applied unlabeled S2-E concentrations were 1 µM for panels B-E, 3µM for panels F-I, and 10µM in panels J and K. Time points are: 0h and untreated sample (A); for the 1µM series: 2h (B), 6h (C) 18h (D) and 24h (E); for 3µM series: 2h (F), 6h (G) 18h (H) and 24h (I); for cells treated with 10µM unlabeled E: 18h (D) and 24h (E). At 10µM, S2-E observation of cell debris suggest cellular toxicity. Overall, delivery and retrograde transport of unmodified S2-E follows a similar time course as for NBD-labeled S2-E; however, the control sample without added E but treated with anti-E (panel A) did exhibit a weak unspecific binding on the green channel (see also Fig. S4.5 panel E). The lower panels I (2nd page of Fig.) , II (3rd page), and III (4th page) of the figure show the individual channels of each composite image presented in the upper panel. For comparison purposes, we re-used the untreated control (panel A) at each S2-E concentration 1 µM, 3 µM and 10 µM. For lower panel I (A-D), lower panel II (A, G-I) and panel III (A, J and K). All scale bars are 25 µm. This experiment was independently repeated twice. For further experimental details see the above Supporting Materials and Methods.

Figure S4.8

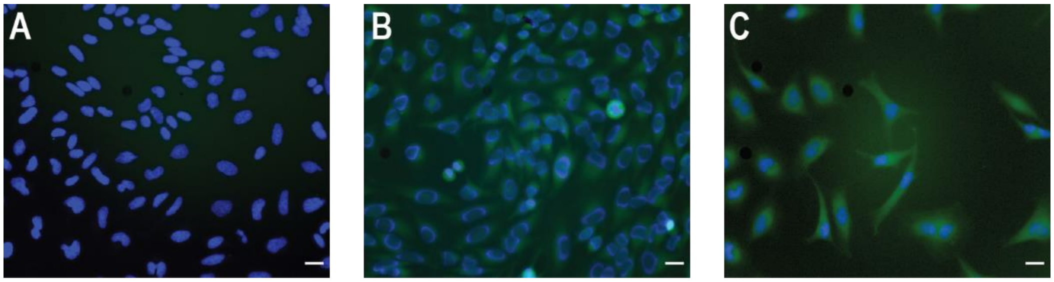

Figure S4.8. Cysteine-NBD uniformly stains membranes in HeLa cells. A) HeLa cells stained with only NucBlue. **B)** Hela cells stained with NucBlue and 5 µM cysteine-NBD for one hour. **C)** Hela cells stained with NucBlue and 5 µM cysteine-NBD after 18 hours. Note that cysteine-NBD stains all membranes in HeLa cells and this does not occur with S2-E-NBD, even after 18 hours. This indicates that S2-E-NBD is not degraded to the point of liberating NBD dye. This experiment was repeated twice. Scale bars 25 µm.

Figure S4.9. (2 Page Figure)

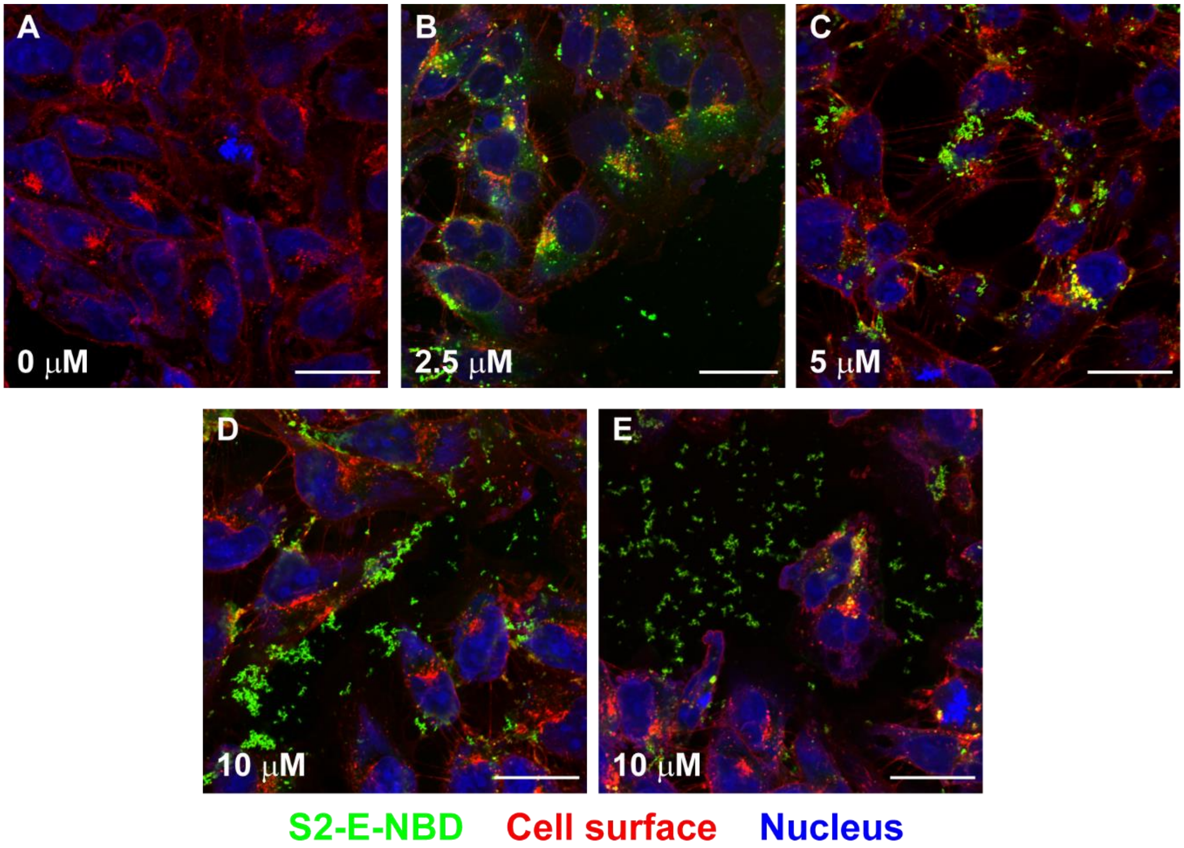

Figure S4.9. Lower Panel. Individual channels and composite of upper panels A-D. (Figure Page 2 of 2)

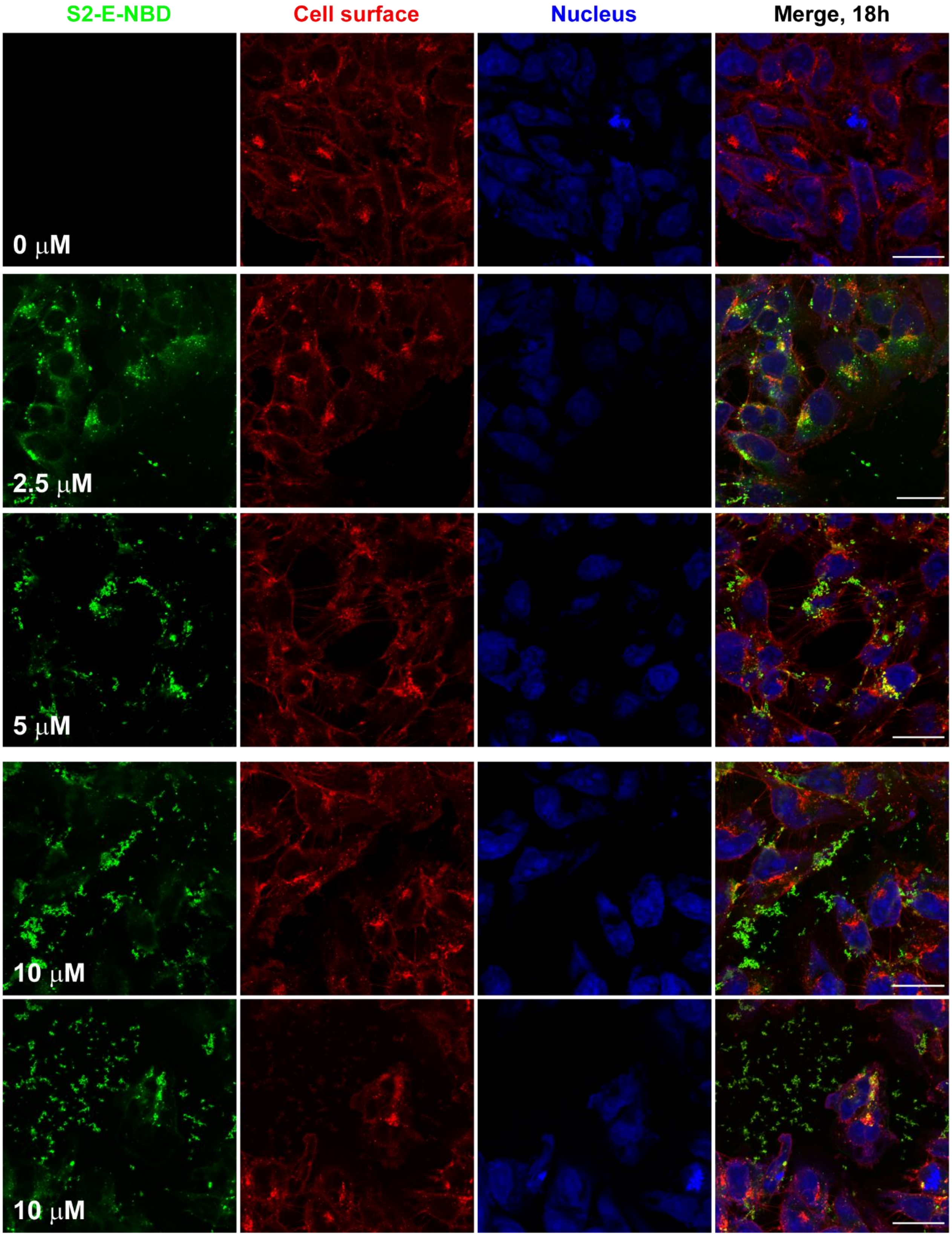
S2-E-NBD
Cell surface
Nucleus
Merge, 18h
0 μM
2.5 μM
5 μM
10 μM
10 μM

Figure S4.9 (above 2 pages). Cell membrane delivery and uptake of the SARS-CoV-2 envelope protein with PMAL-C8 amphipol in a human alveolar cell line. Representative confocal microscopy images showing SW1573 cells treated with increasing concentrations of added NBD-labeled S2-E. All time points were collected at 18h. **(A)** untreated control 0µM, **(B)** 2.5µM S2-E in the cell culture, **(C)** 5µM, and 10µM **(D and E)**. Color scheme is: green, NBD-labeled S2-E; red, cell plasma membrane (WGA-AF555); blue, cell nuclei (DRAQ5). As in HeLa cells, at 18hrs after cell treatment the S2-E-NBD signal is primarily at a perinuclear location (panels B and C). For cells incubated with the highest level (10µM) of S2-E-NBD, some of the protein appears to be aggregated (D) while in panel E—top left side, SW1573 shows signs of co-localization of S2-E with the plasma membrane label, indicating cell membrane fragments, possibly suggesting cellular toxicity at 10µM S2-E-NBD. The lower panel (2nd page) of the figure shows the individual channels of each composite image presented in the upper panel. Scale bars are 25 µm. This experiment was conducted once. For further experimental details see the Supporting Materials and Methods.

Figure S4.10 (2 Page Figure)

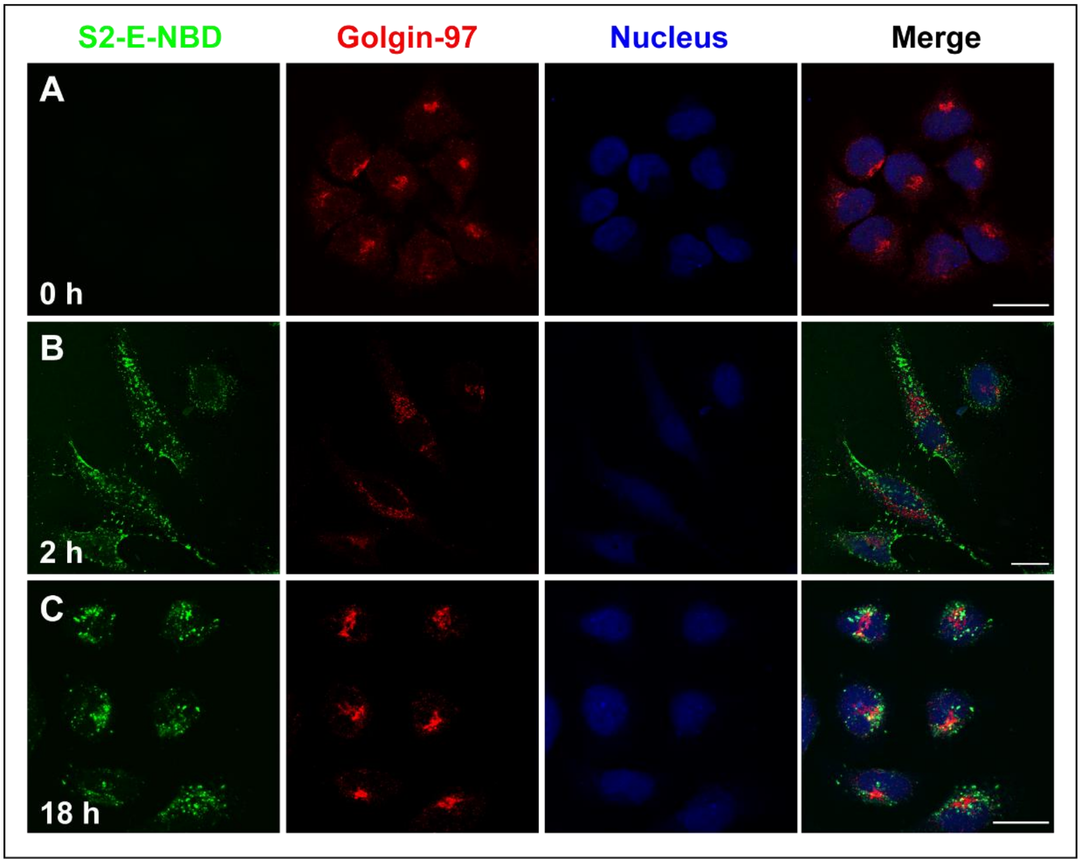

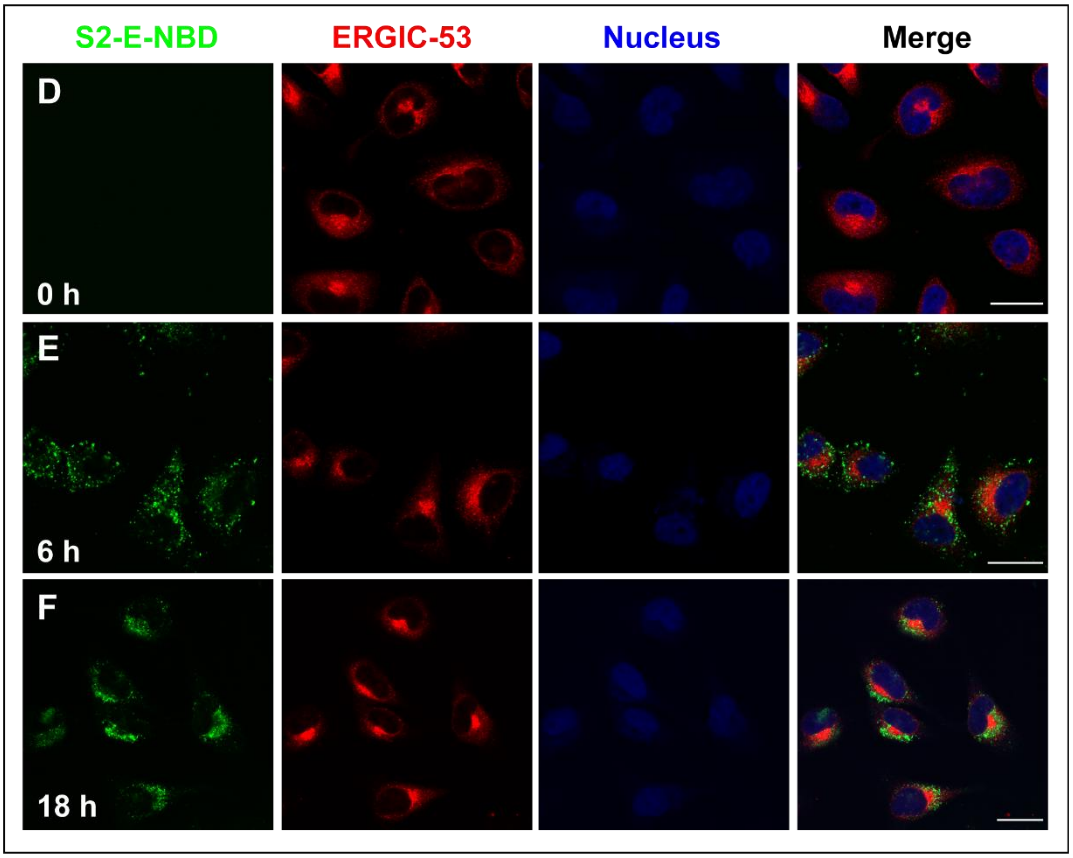

Figure S4.10 (Page 2 of 2 Page Figure)

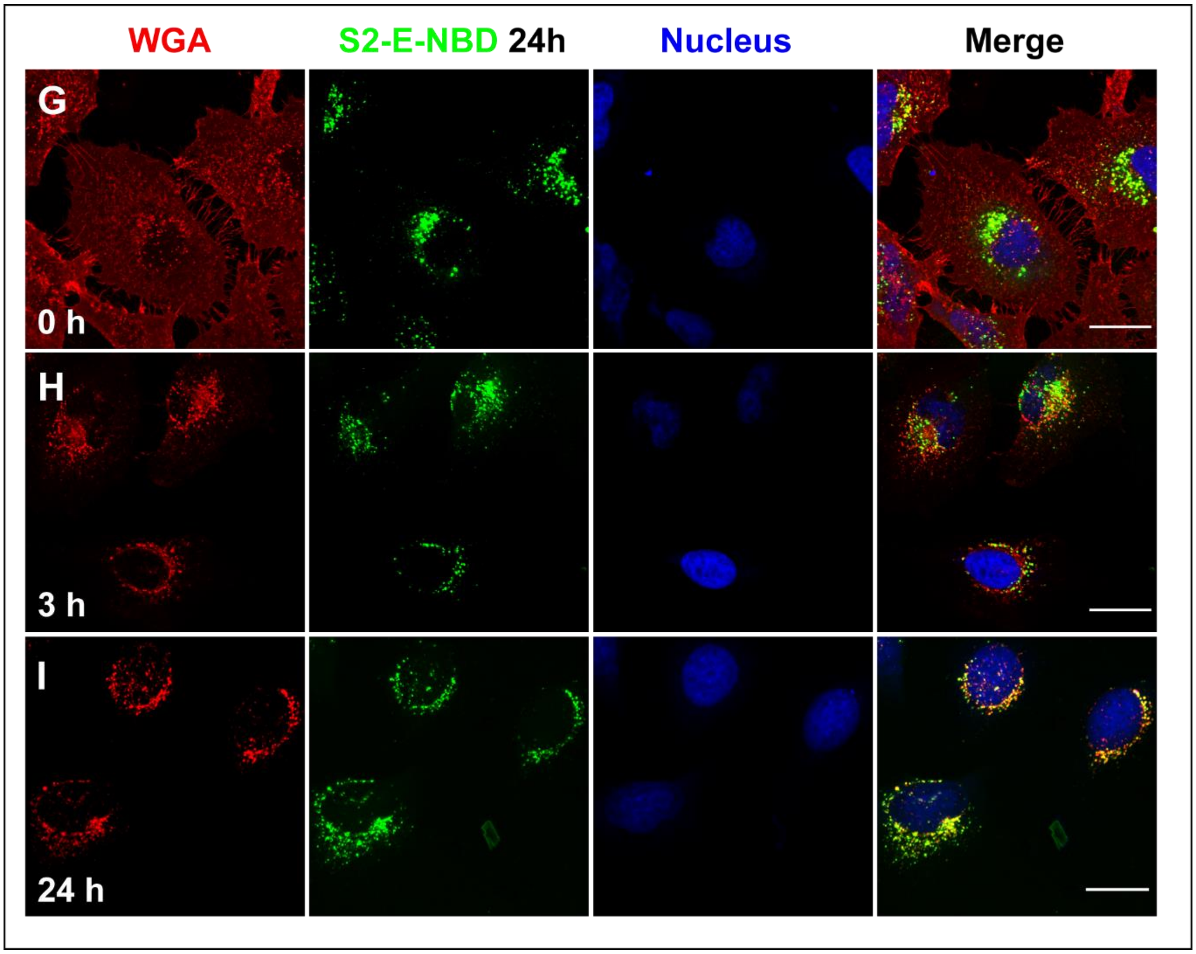

Fig S4.10. Individual channels for merged images from Figure 4.3. (above 2 pages) Rows **A** to **C**; HeLa cells treated with 2.5µM E-NBD (green), for 0, 2 and 18 h were tested for Golgi localization (red) using anti-Golgin-97 (Invitrogen cat# A21270 diluted 1:500). Golgin-97 was detected using anti-mouse conjugated AlexaFluor546. Cellular nuclei (blue) were detected using DRAQ5. Notice how the S2-E-NBD signal (green) moves towards the perinuclear space over time; and poorly overlap with the Golgin-97 signal. Correlation analysis using ImageJ plugin Colocalization Threshold for row C: 18h S2-E-NBD (green) versus Golgin-97 (red) yields poor Pearson correlation coefficient. Analysis of several other S2-E-NBD 16-21 h and Golgin-97 confirm further poor correlation (~ 0-0.2). Rows **D** to **F**; HeLa cells treated with 2.5µM S2-E-NBD (green) for 0, 6 and 18 h were tested for ERGIC localization (red) using monoclonal antibody against ERGIC-53 protein. Anti -ERGIC-53 antibodies and cell nuclei were detected using the same conditions used for Golgin-97 in panels A-C. Notice how the S2-E-NBD signal (green) moves toward the perinuclear space over time and appears to overlap with part of the ERGIC-53 signal. Correlation analysis using ImageJ Colocalization Threshold for row F: 18h S2-E-NBD (green) versus ERGIC-53 (red) yields poor Pearson correlation coefficients. Analysis of several other E-NBD 16-24 h and ERGIC-53 confirm further this poor correlation (~ 0-0.2). Rows **G** to **I**; HeLa cells treated with 2.5µM S2-E-AF488 (green) for 24 h were tested for wheat germ agglutinin co-localization (red) using WGA-AF555 at 10µg/mL for the indicates times. In panel G, WGA was added after cell fixation marking the cell membrane, while in panel H, WGA was added 3 h before cell fixation. In panel I, S2-E-AF488 and WGA-AF555 were added together 24 h before cell fixation. Notice how the WGA signal (red) moves towards the perinuclear space over time and overlaps well with the S2-E-AF488 in the merged image (panel I). Correlation analysis using ImageJ Colocalization Threshold between row I: 24 h S2-E-AF488 (green) versus 24h WGA-AF555 (red) yields a strong Pearson correlation coefficient; this remains the case with either S2-E-AF488 or S2-E-NBD. Analysis of several other equally 24h treated S2-E-AF488 or S2-E-NBD and 24h WGA-AF555 confirm the strong correlation (3 experiments, 2 with S2-E-NBD and one with S2-E-AF488; analyzed cells = 13, 19, 12, for Pearson correlation coefficient averages with standard deviations for 5 images of each experiment were: 0.67 ± 0.15; 0.73 ± 0.16; 0.68 ± 0.097. Scale bars are 25 µm. For further details see online Materials and Methods.

Figure S4.11

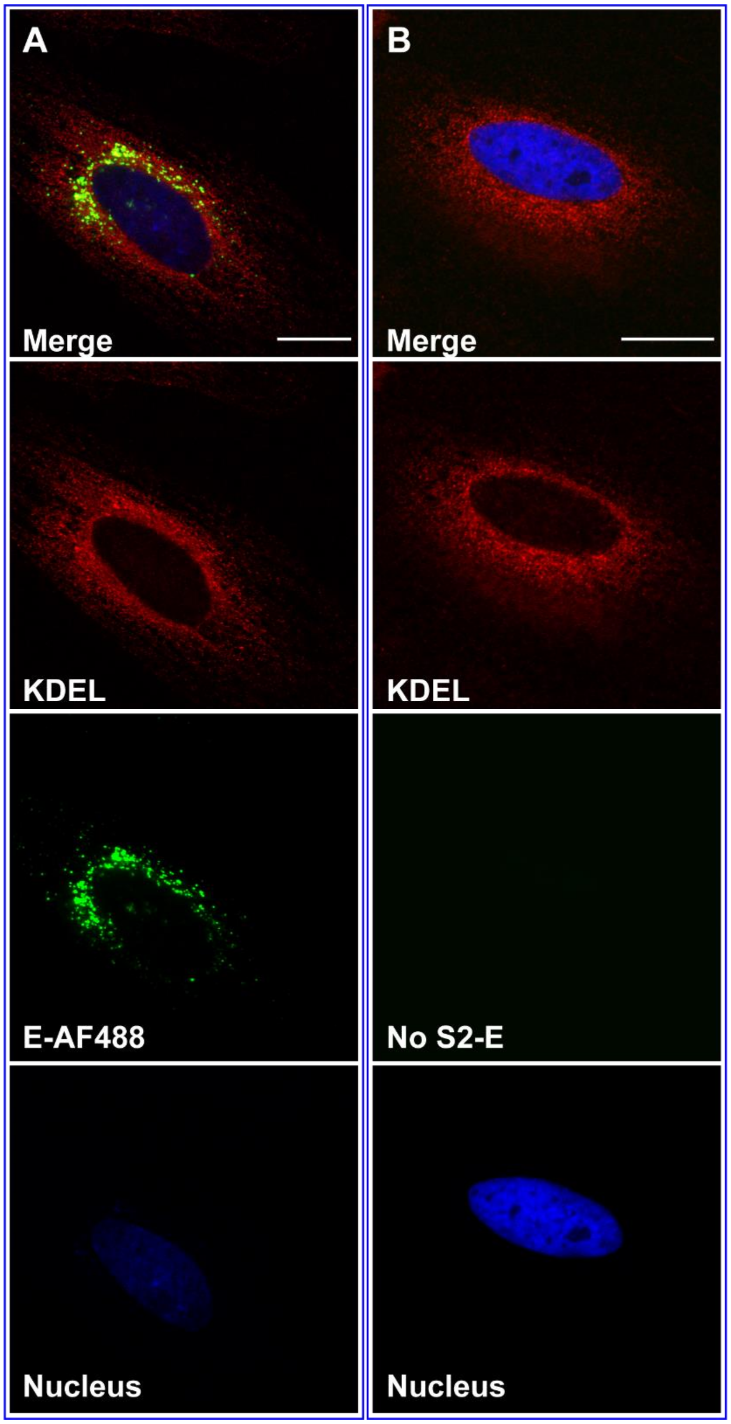

Fig. S4.11. SARS-CoV-2 envelope protein traffics to the perinuclear space and does not accumulate in the endoplasmic reticulum. Representative confocal microscopy images showing HeLa cells treated for 24 h with 2.5 µM S2-E labeled with AF488 (**A**) or without S2-E (**B**), and probed with the KDEL antibody conjugated to AF555 (Abcam, cat# EPR12668), a known marker for the endoplasmic reticulum. For each column, the first image is the Merge of the below 3 channels, in red anti-KDEL, in green for A, is S2-E-AF488 and in column B no added S2-E, in blue cell nuclei. This experiment was repeated twice once with S2-E-NBD and once with S2-E-AF488. No significant colocalization was observed between KDEL and S2-E-AF488 after 24 h treatment. Scale bars are 20 µm. For more details see online Materials and Methods.

Figure S4.12

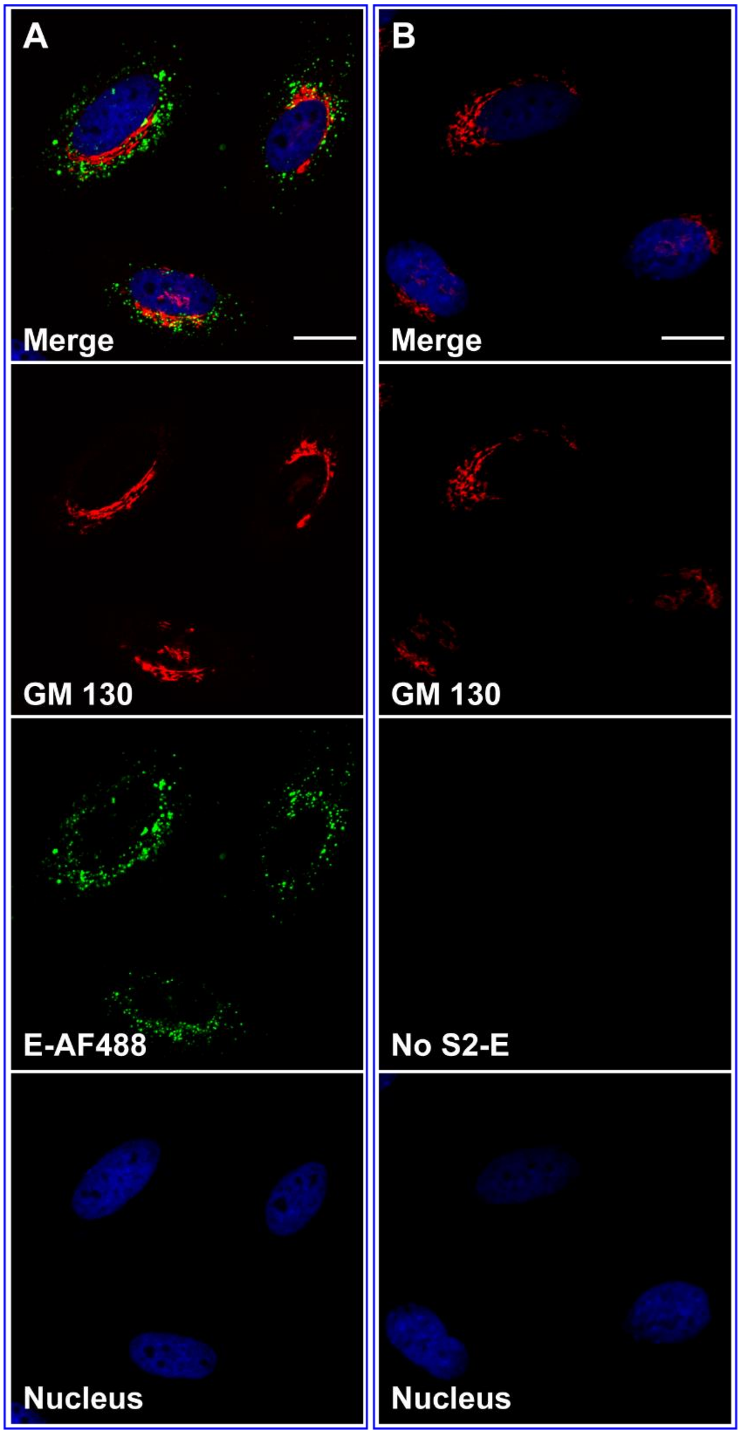

Fig. S4.12. SARS-CoV-2 envelope protein traffics to the perinuclear space and does not accumulate in the cis-Golgi. Representative confocal microscopy images showing HeLa cells treated for 24h with 2.5 µM S2-E labeled with AF488 (**A**) or without S2-E (**B**) and probed with the GM130 antibody (Cell Signaling, cat #12480S), a known marker for the *cis*-Golgi. For each column, the first image is the Merge of the below 3 channels, red (anti-GM130), green (for A only, S2-E-AF488) and blue (cell nuclei). This experiment was repeated twice, once with S2-E-NBD and once with S2-E-AF488. No significant colocalization was observed between GM130 and S2-E-AF488. Scale bars are 20 µm. For more details see online Materials and Methods.

Figure S4.13

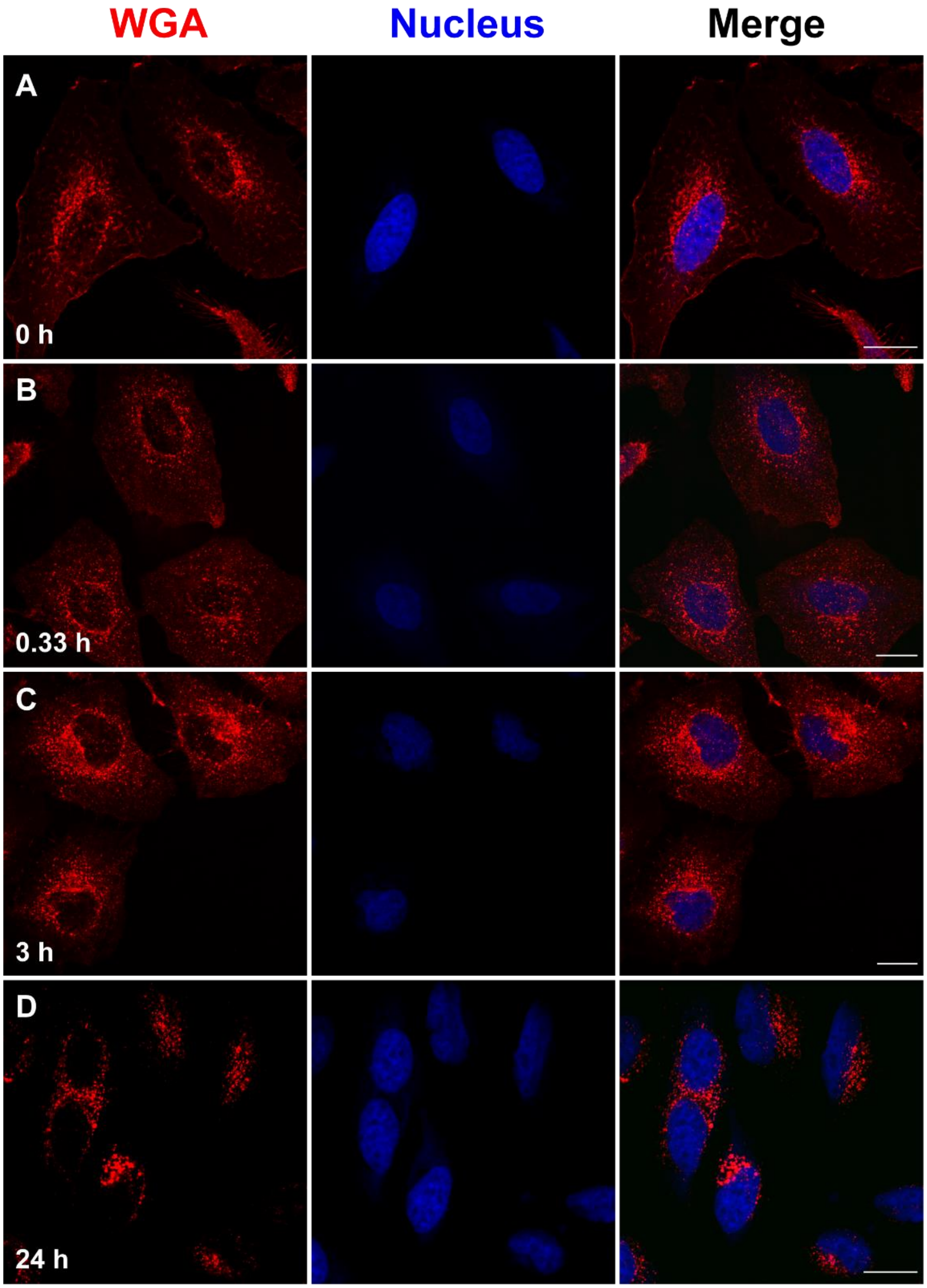

Fig. S4.13. Wheat germ agglutinin (WGA) protein retrograde traffics and accumulates in the perinuclear space. Representative confocal microscopy images showing HeLa cells treated with 10 µg/mL WGA conjugated to

AlexaFluor-555. For each row, the first image in red is WGA-AF555, the second show the blue cell nuclei, and the third is the merge image of both channels. In row **A** cell were WGA-AF555 treated post fixation or 0 h, while in panels B-D cells were treated with WGA and fixed after 20 min (**B**), 3 h (**C**), 24 h (**D**). Notice how, over time, WGA accumulates in the perinuclear space. WGA has been shown in prior studies to be quickly internalized and accumulate in the trans-Golgi network (TGN) See supplemental references (43,44). Experiments were independently repeated three times, twice using S2-E-NBD and once with S2-E-AF488. Scale bars are 20 µm. For more details see online Materials and Methods.

Figure S4.14

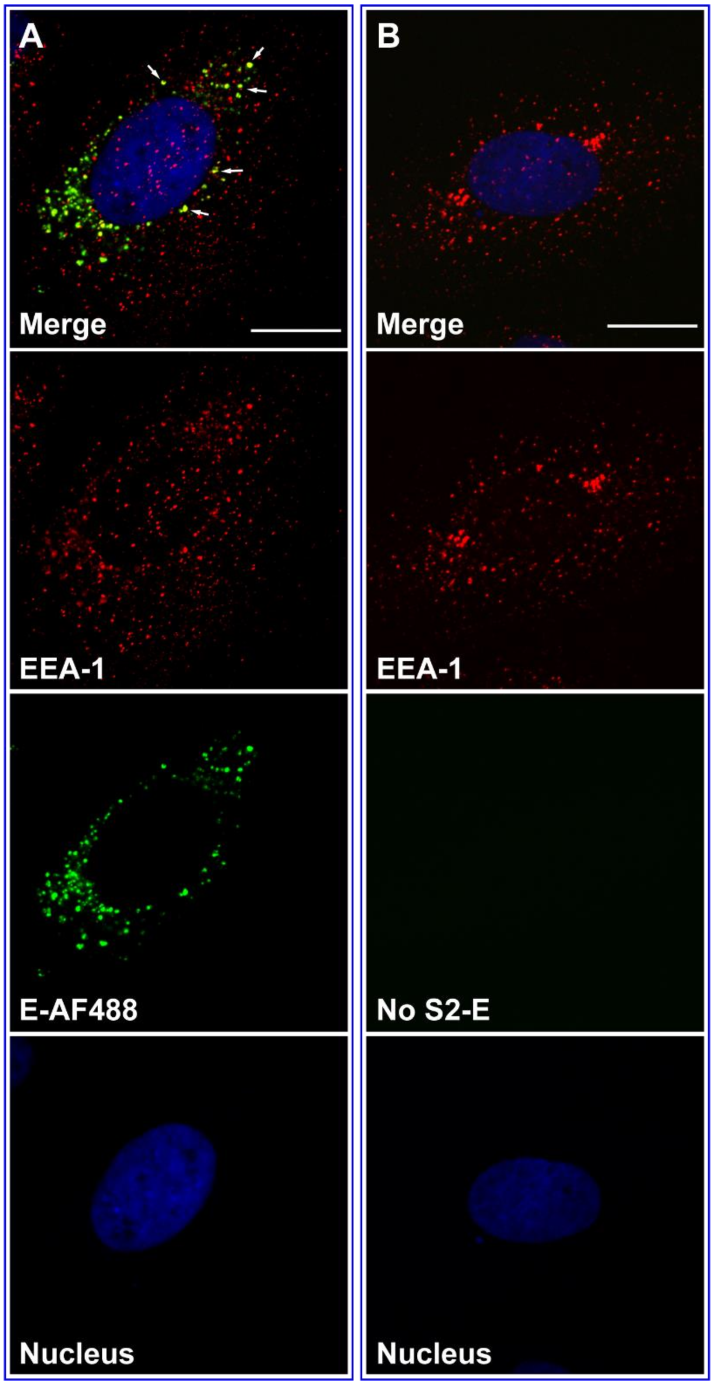

Fig. S4.14. Some SARS-CoV-2 envelope protein is found in early endosomes at late time points. Representative confocal microscopy images showing HeLa cells treated for 24 h with 2.5 µM S2-E labeled with AF488 (**A**) or without S2-E (**B**) and probed with anti-EEA1 antibody (Invitrogen, cat # MA5-14794), a well establish marker for early endosomes. For each column, the first image is the merge of 3 channels: red (anti-EEA1), green (for A only, S2-E-AF488), and blue (cell nuclei). This experiment was repeated twice, once with S2-E-NBD and once with S2-E-AF488. Some EEA1 vesicles show colocalization with S2-E, most colocalized vesicles appear also as enlarged vesicles. Examples of this are shown with white arrows in panel A merge. Using the image-J plugin colocalization-threshold, the Pearson correlation coefficient between green and red images in column A was determined to be 0.45, suggesting a weak to moderate correlation. Scale bars are 20 µm. For more details see online Materials and Methods.

Figure S4.15

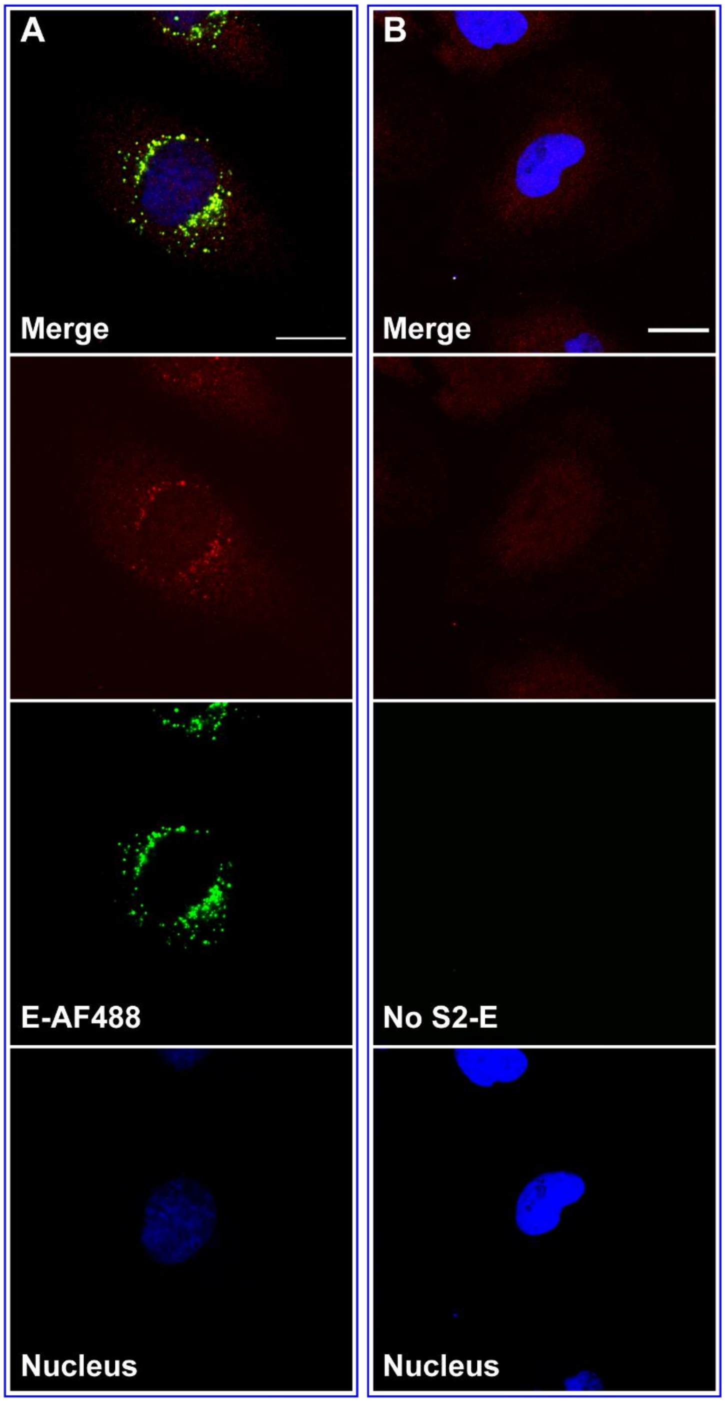

Fig. S4.15. SARS-CoV-2 envelope protein is also found in late endosomes at late time points. Representative confocal microscopy images showing HeLa cells treated for 24 h with 2.5 µM S2-E labeled with AF488 (**A**) or without S2-E (**B**) and probed with anti-Lamp1 antibody (Encorbio, cat # MCA-5H6), an established marker for late endosomes, endolysosomes, and lysosomes. For each column, the first image is the merge of 3 channels: red (anti-Lamp1), green (for A only, S2-E-AF488) and blue (cell nuclei). This experiment was carried out once. Notice how cells treated with S2-E show enlarged vesicles in the red channel, and how these vesicles overlap with the S2-E-AF488 signal. Using the Image-J plugin colocalization-threshold without ROI, the Pearson correlation coefficient between panel A, green and red images, was determined to be 0.64, suggesting good correlation. Scale bars are 20 µm. For more details see online Materials and Methods.

Figure S4.16

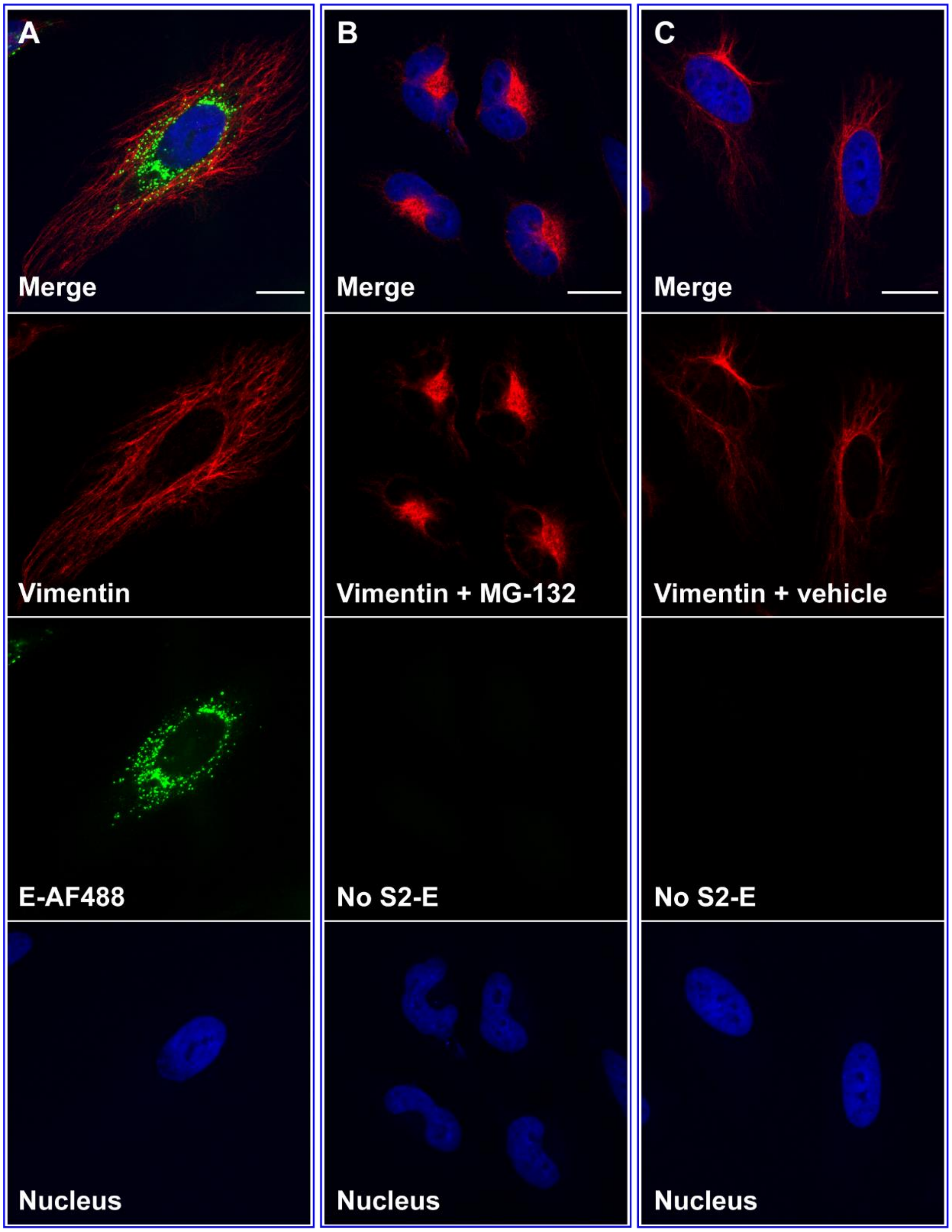

Fig. S4.16. SARS-CoV-2 envelope protein traffics to the perinuclear space and does not accumulate in aggresome vimentin-cages. Representative confocal microscopy images showing HeLa cells treated for 24 h with 2.5 µM S2-E labeled with AF488 (**A**) and two control samples. As the positive control HeLa cells were treated with 12 µM MG-132 for 21 h (**B**). MG-132 is a protease inhibitor known to induce formation of perinuclear, typically one sided, vimentin cages containing denatured proteins. As a negative control (**C**) show cells treated only with DMSO vehicle. For each column, the first image is the merge of 3 channels: red (anti-vimentin, Cell Signaling, cat #5741S)], green (panel A only, S2-E-AF488), and blue (cell nuclei). This experiment was repeated twice once with S2-E-NBD and once with S2-

E-AF488. No vimentin cages were observed, suggesting that the majority of S2-E is not in aggresomes. Scale bars are 20 µm. For more details see online Materials and Methods.